Attitude & orbital control system design for near-Earth asteroid exploration using autonomous miniature satellites

Master Thesis Aerospace Engineering:
Space Engineering

Steven Verwer

Delft University of Technology

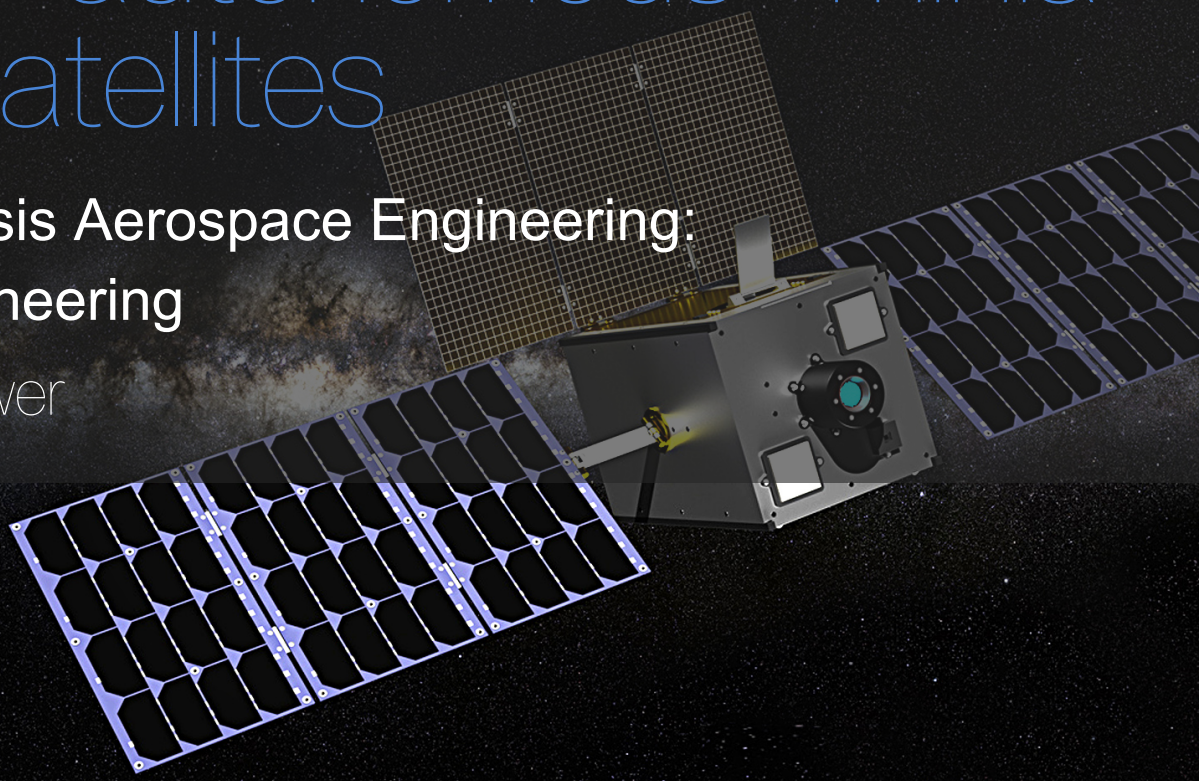

TU Delft

Attitude & orbital control system design for near-Earth asteroid exploration using autonomous miniature satellites

by

Steven Verwer

to obtain the degree of Master of Science
at the Delft University of Technology,
to be defended publicly on Wednesday May 10, 2022 at 10:00 AM.

Student number:	4354362	
Project duration:	June 6, 2022 – May 10, 2023	
Thesis committee:	Ir. S. Casini,	TU Delft
	Dr. ir. A. Cervone,	TU Delft

Cover: Deep-space CubeSat by ESA-Jacky Huart (Modified)

An electronic version of this thesis is available at `http://repository.tudelft.nl/`.

TU Delft

Preface

The following pages represent the culmination of years of study, research, and dedication, and it is with great pride and gratitude that I present this master's thesis which explores the design of an attitude and orbital control system for a general autonomous 6U CubeSat near-Earth asteroid fly-by mission. As near-Earth asteroid exploration gains increasing attention and interest for scientific exploration, planetary protection, and in situ resource utilization, the miniaturization of missions has become an attractive option due to decreased costs and volume. It was during the course on micro-propulsion systems that I first had the opportunity to meet my supervisor, Angelo Cervone, and later on, he introduced me to his colleague Stefano Casini. At that time Stefano was in the middle of his Ph.D. studies about autonomous miniature satellite missions with a focus on navigation. It was then that he and Angelo introduced me to the idea of designing an attitude and orbital control system for these missions because currently there is no standard available for these missions. However, designing a control system for these missions presents significant challenges. This thesis addresses these challenges by simulating different combinations of commercially available off-the-shelf components to conceptualize a feasible design for a propulsion system, an attitude determination and control system, and a secondary propulsion system for desaturation. However, these systems are very much entangled with the rest of the spacecraft. The mass, volume, and power available come from the design of the rest of the spacecraft. Also, a larger total mass needs a larger propellant mass. Since there are no missions that come close to autonomous miniature satellite missions that start in an Earth orbit and end close to a near-Earth asteroid, the complete satellite design had to be done from scratch.

Luckily, Stefano Casini and Angelo Cervone could give me helpful insights and suggestions that were great most of the time but sometimes could turn the master's thesis into a Ph.D. scale research. It was at that time that I learned that research, such as this master thesis, cannot be seen as a project, but as something that is almost always prematurely ended because there is always more that can be investigated. And also, you never know how much effort and time goes into a single extra research question before you try to answer it.

From the results of this thesis, I am proud to say that from my perspective as a member of the scientific community, the work I have done could serve as a valuable starting point for the standardization of attitude and orbital control systems for future autonomous miniature satellite missions.

To end this preface, I would like to express my deepest gratitude to my girlfriend, Demi Zoet, for her endless support through these years, my family, Walter, Thea, and Quirien Verwer, best friends Alex Remmelzwaal, Casper Kerkhove, and Erik Le Blansch, and supervisors Angelo Cervone and Stefano Casini for their support and helpful insights.

Steven Verwer
Delft, April 2023

Summary

Exploration of near-Earth asteroids has become an interesting and challenging target for the next decades due to scientific exploration, planetary protection, and in situ resource utilization. The miniaturization of these missions has gained interest due to decreased costs and volume. Autonomous miniature satellites enable the use of limited support for mission operations and navigation, leading to further cost reductions. However, designing an attitude and orbital control system for near-Earth asteroid autonomous miniature satellite missions presents a significant challenge. This thesis aims to design an attitude and orbital control system for a general autonomous 6U CubeSat near-Earth asteroid fly-by mission starting from a super synchronous geostationary transfer orbit by simulating different combinations of commercially available off-the-shelf components. Currently, no off-the-shelf solution is available for these systems which this thesis aims to conceptualize. The thesis addresses the following research questions: What is a feasible design for a propulsion system for interplanetary travel to the near-Earth asteroid? What is a feasible design for a propulsion system to desaturate reaction wheels? And what is a feasible design for an attitude control system including a control algorithm to perform the different mission segments such as detumbling, Earth escape, deep-space cruise, and the near-Earth asteroid close encounter?

Using an indirect single-shooting calculus-of-variations-based fuel-efficient trajectory optimization framework incorporating a particle swarm or artificial intelligence-based optimization algorithm, different interplanetary propulsion systems were simulated. From the results, ThrustMe's NPT30-I2 gridded-ion thruster was found to be a feasible solution that required 4.850 kilograms of propellant for a 13.041 kg 6U CubeSat to the most ambitious target asteroid.

For the desaturation of the reaction wheels, GomSpace's Nanoprop CGP3 warm gas propulsion system was found to be a feasible solution because of its exceptionally high total impulse-to-total mass ratio. In combination with the thruster configuration problem which was solved by a super-ellipsoid approximation of the satellite combined with a particle swarm optimization method, a feasible secondary propulsion system for desaturation was found.

Finally, the ClydeSpace iADCS400 attitude determination and control system designed for 6U CubeSats in combination with the reaction control thruster system Nanoprop CGP3, a Lyapunov control controller, and a linear quadratic regulator controller were simulated for the different mission segments. The results show that each mission segment is possible for the complete system design. The complete attitude and orbital control system design can be considered a starting point for the standardization of these systems for future missions.

Contents

List of Figures

List of Tables

Nomenclature

Abbreviations

Abbreviation	Definition
ACS	Attitude control system
ADCS	Attitude determination and control system
AOCS	Attitude and orbital control system
BC	Blended control
BWG	Beam-wave guide (antenna)
COE	Classical orbital elements or Kepler elements
COTS	Commercially off-the-shelf
COV	Calculus of variations
CSV	Cartesian state vector
CubeSat	A miniaturized satellite characterized by a modular form factor, defined by 10cm cubic units (3.9 inches)
DART	Double asteroid redirection test
DSN	Deep space network
DSS-24	Deep space 34-m antenna in Goldstone
DSS-34	Deep space 34-m antenna in Canberra
DSS-54	Deep space 34-m antenna in Madrid
EKF	Extended Kalman filter
EOM	Equations of motion
FFS	Finite Fourier series control
GCR	Galactic cosmic rays
LC	Lyapunov control
LIT	Linear energy transfer
LQGR	Linear quadratic guassian regulator
LQR	Linear quadratic regulator
LVLH	Local vertical local horizon frame
MEE	Modified equinoctial elements
MISO	Multiple-input-single-output
MRP	Modified Rodrigues parameter
NASA	National aeronautics and space administration
NC	Neurocontroller
NEA	Near-Earth asteroid
NLP	Nonlinear programming
NRLMSISE-00	The mathematical representation of the 2001 United States naval research laboratory mass spectrometer and incoherent scatter radar exosphere

Abbreviation	Definition
OCP	Optimal control problem
OSIRIS-REx	Origins, spectral interpretation, resource identification, security and regolith explorer
PSV3	Cylindrical coordinates
RAM	Random access memory
RP	Rodrigues parameter
SB	Shape-based control
SC	Spherical coordinates
SEE	Single event effects
SEP	Solar energetic particles
SOTA	State-of-the-art
SPICE toolkit	Spacecraft, planet, instrument, c-matrix, events toolkit
SSGTO	Super synchronous geostationary transfer orbit
TID	Total ionizing doze
TPBVP	Two-point boundary value problem

Symbols

Symbol	Definition	Unit
A	Satellite reference surface area	[m^2]
AU	Astronomical unit 149,597,871	[km]
A_{zen}	Zenith atmospheric attenuation	[dB]
B	Signal bandwidth	[Hz]
C	Channel capacity	[bits/s]
C	Direction cosine matrix	[-]
CD	Cumulative weather distribution factor	[-]
C_3	Characteristic orbital energy	[km^2/s^4]
C_D	Aerodynamic drag coefficient	[-]
C_R	Effective reflectivity of the satellite	[-]
DCL	Signal power loss due to data conversion	[dBi]
E_b/N_0	Energy per bit to noise power density ratio	[dBi]
$FSPL$	Free space path loss	[dB]
F_L	Lorentz force	[N]
$F_{T,corr}$	Corrected thrust force for available power	[N]
F_T	Thrust force	[N]
G	Gravitational constant, $6\,6743\text{E}-11$	[m^3/(kg s^2)]
G_{RX}	Receiver gain	[dBi]
G_{TX}	Transmitter gain	[dBi]
$HPBW$	Half-power beam width	[deg]
I_{sp}	Mass specific impulse	[s]
J	Inertia tensor	[kg/m^2]

Symbol	Definition	Unit
J_s	Satellite inertia tensor	[kg/m^2]
J_w	Reaction wheel inertia tensor	[kg/m^2]
J_{zz}	Reaction wheel z-axis moment of inertia	[kg/m^2]
K	Control gain matrix	[-]
L_{RX}	Signal power losses between receiving antenna and receiver	[dBi]
L_{TX}	Signal power losses between transmitter and antenna	[dBi]
L_{atm}	Signal power loss due to the atmosphere	[dBi]
L_{fs}	Signal power loss in free space	[dBi]
L_p	Signal power loss due to the antenna pointing error	[dBi]
M	Moment or torque	[Nm]
N	Noise spectral density	[W/Hz]
N_0	Spectral noise density	[dBi/Hz]
P_0	Electric power at a distance of 1 AU from the Sun	[W]
P_e	Effective electric power	[W]
P_{RX}	Received power	[mW]
P_{TX}	Transmitted power	[mW]
$P_{n,m}$	Legendre polynomials	[-]
P_{noise}	Power of the system noise	[dBm]
P_{prop}	Propulsion system power requirement	[W]
Q	Skew symmetric rotation matrix	[-]
SF	Switching function for low-thrust trajectory control law	[-]
SNR	Signal-to-noise ratio	[-]
T	Noise temperature	[K]
T'_{CMB}	Effective cosmic background noise temperature	[K]
T_{CMB}	Cosmic background noise temperature, 2.725	[K]
T_{max}	Maximum thrust	[-]
T_{op}	Operational noise temperature	[K]
U	CubeSat form factor $10 \times 10 \times 10$	[cm^3]
U	Gravitational potential	[J/kg]
V	Lyapunov energy function	[-]
W	Energy flux of incoming solar radiation	[W/m^2]
W	Reaction wheel rotation matrix	[-]
$\mathbb{I}_{n\times n}$	$n \times n$ Identity matrix	[-]
$\mathcal{J}$	Performance parameter	[-]
$\mathcal{L}$	Path cost function	[-]
$\mathcal{L}_n$	Optimization objective function	[-]
$\mathcal{N}$	(Pseudo) inertial reference frame	[-]
$\mathcal{O}$	Arbitrary reference point	[-]
$\mathcal{P}_n$	Optimization penalty function	[-]
$\vec{B}$	Magnetic induction of the geomagnetic field	[T]

Symbol	Definition	Unit
$\vec{F}_{RCT}$	Reaction control thruster force	[N]
$\vec{H}$	Absolute angular momentum	[kg m/s^2]
$\vec{M}_{RCT}$	Reaction control thruster torque	[Nm]
$\vec{T}$	Reaction wheel torque	[Nm]
$\vec{T}_m$	Magnetic torquer torque	[Nm]
$\vec{a}_p$	Perturbation accelerations	$\begin{bmatrix} m/s^2 & m/s^2 & m/s^2 \end{bmatrix}^\top$
$\vec{g}$	Rodrigues parameters or Gibbs parameters	[-]
$\vec{h}$	Relative angular momentum	[kg m/s^2]
$\vec{p},\ \vec{\rho},\ \vec{r}$	position vector $\begin{bmatrix} x & y & z \end{bmatrix}^\top$	$\begin{bmatrix} m & m & m \end{bmatrix}^\top$
$\vec{q}$	Quaternions	[-]
$\vec{u}$	Control vector	[-]
$\vec{v}$	velocity vector $\dot{\vec{r}}$	$\begin{bmatrix} m/s & m/s & m/s \end{bmatrix}^\top$
a	Semi-major axis of the orbit	[km]
c	Speed of light in vacuum, 299792458	[m/s]
e	Eccentricity of the elliptical orbit	[-]
f	Frequency	[Hz]
f	time-derivative function	[-]
f_s	Symbol rate	[bit/s]
g_0	Gravitational acceleration at sea level, 9 80665	[m/s^2]
i	Inclination of the orbit with respect to the reference frame	[rad]
k_B	Stefan Boltzmann constant, 1 380649E $-$ 23	[J/K]
m	Mass	[kg]
$p,\ f,\ g,\ h,\ k,\ L$	Modified equinoctial elements	[km, - ,-, -, -, rad]
q	Electric charge of the satellite	[V]
r	Spherical can polar coordinates radius	[m]
$r_{Earth},\ R$	Average radius of the Earth, 6378.1363	[km]
t	Time	[s, years]
t_0	Start time	[s, years]
t_f	Final time	[s, years]
v	Velocity	[m/s]
v_{∞_e}	Earth escape velocity at infinity	[km/s]
$x,\ y,\ z$	Cartesian coordinates	[m]
$\Phi\|_{t=t_f}$	Terminal cost function	[-]
Υ	Vernal equinox	[-]
Ω	Longitude of the ascending node	[rad]
Ω	Skew symmetric angular velocity matrix	[-]
γ	Elevation angle offset	[deg]
$\mathcal{H}$	Hamiltonian	[-]
μ	Standard gravitational parameter	[km^3/s^2]
μ_m	Magnetic torquer magnetic moment	[A m^2]

Symbol	Definition	Unit
μ_{Earth}	Standard gravitational parameter of Earth, 98,600.4415	[km^3/s^2]
ν	True anomaly	[rad]
ω	Argument of periapsis	[rad]
ω_w	Reaction wheel angular velocity	[rad/s]
ϕ	Longitude	[rad]
ψ	Terminal constraint function	[-]
ρ	Density	[kg/m^3]
σ	Standard deviation	[-]
θ	Co-latitude	[rad]
θ	Elevation angle	[deg]
$\theta_1,\ \theta_2,\ \theta_3$	Euler angles	[rad]
ε	fuel-to-energy-optimality-ratio	[-]
ε	specific orbital energy	[J/kg]
$\vec{\beta}$	Control steering vector	[-]
$\vec{\chi}$	State vector	[-]
$\vec{\lambda}$	Lagrange multipliers or co-variables	[-]
$\vec{\omega}$	Angular velocity vector	$\begin{bmatrix} rad/s & rad/s & rad/s \end{bmatrix}^\top$
$\vec{\psi}$	Modified Rodrigues parameters	[-]
$\vec{\psi}_s$	Shadow modified Rodrigues parameters	[-]
$\vec{\xi}$	Design parameters	[-]

1

Introduction

One of the next decades' most challenging and interesting objectives is the exploration of near-Earth Asteroids (NEAs). The main reasons for this deep interest are related to scientific exploration [1], planetary protection [2], and *in situ* resource utilization [3, Part 5]. Missions to NEAs are not new, in fact, there are many past and current satellite missions to asteroids. Some examples are the double asteroid redirection test or DART, a kinetic impact test mission to the asteroids Didymos and Dimorphos launched in 2021 [4], and origins, spectral interpretation, resource identification, security, regolith explorer or OSIRIS-REx, which is a sample return mission to the asteroid Bennu in 2016 [4]. Of these missions, OSIRIS-REx proves the interest of major space organizations in asteroids for their resources and DART proves the interest in planetary protection of NEAs.

Along with this interest in the exploration of NEAs, there is gaining interest in the miniaturization of these missions because it decreases the total mission cost. These miniature satellite missions often come in a standard form factor of 1U or $10 \times 10 \times 10$ centimeter. These 'cubes' can be stacked to form bigger satellites which are a multiple of 1U units. The miniaturization decreases the required mass and volume of a mission and the standard shape of CubeSats enables the development, production, and use of standard components, which reduces the mission cost. Additionally, Casini, Fodde, Monna, *et al.* [1] proposes to use autonomous miniature satellites to decrease the total mission cost of NEA exploration missions even further because it enables the use of limited support for mission operations and navigation. According to Casini, Fodde, Monna, *et al.* [1], one of the biggest challenges of NEA autonomous miniature satellite missions is the design of an attitude & orbital control system (AOCS). The AOCS serves several essential functions, including attitude control, orbit control, and stabilization. Attitude control involves using the measured orientation of the spacecraft and to make adjustments to ensure it is pointing in the right direction. Orbit control, on the other hand, involves controlling the spacecraft's position and velocity in orbit through the use of thrusters or other mechanisms. Finally, stabilization involves counteracting external forces that may cause the spacecraft to spin or drift off course. Overall, the AOCS is a vital component that ensures the success of any space mission by maintaining the spacecraft's stability, orientation, and trajectory. For satellites, this is primarily done by a combination of a propulsion system, magnetic torquers, reaction wheels, and sensors. Of these sub-systems, the magnetic torquer only works in well-known, and significantly strong magnetic fields such as the Earth's magnetic field. Operations such as detumbling and desaturation are mainly done

by the magnetic torquer in Earth's orbit. Beyond Earth's orbit, other methods have to be used such as reaction control thrusters (RCTs).

Currently, commercially available off-the-shelf (COTS) CubeSat AOCSs are exclusively designed for miniature satellite missions which remain in Earth orbit. Using these AOCS systems directly for NEA missions leads to problems such as the problem that magnetic torquers cannot be used without the presence of well-known, and significantly strong magnetic fields. Designing an AOCS for NEA missions, therefore, increases the performance of these missions and deals with specific problems which occur outside of an Earth orbit. Ideally, an AOCS design for these missions eventually leads to standardization which further reduces their cost and increases their reliability and performance.

1.1. Thesis scope

The scope of this thesis is focused on a specific type of autonomous miniature satellite NEA exploration mission that is deployed in a super synchronous geostationary transfer orbit (SSGTO) and only performs a NEA fly-by trajectory within 5 years. The satellite used in this mission is a 6U CubeSat and only COTS components are utilized. The choice of using SSGTO orbit, a fly-by mission type, and a 6U CubeSat with COTS components is based on the following reasons:

- SSGTOs are a viable option for miniature satellite NEA missions due to their high energy and commercial nature as they have a perigee at 295 km and an apogee at 90,000 km and are often used by larger satellites as a piggyback ride [1].
- Fly-by missions are chosen because they are relevant and more common than rendezvous missions for miniature satellites.
- The mission duration of 5 years is chosen because it is comparable to other NEA missions. Miniature satellite missions such as NEAScout and Hayabusa2 have primarily had mission durations of less than 3 years, but all these missions used staging rockets to reduce the Earth's escape phase duration. To be conservative, a mission duration of 5 years is reasonable [4].
- A 6U CubeSat is chosen since it is considered innovative while still being achievable with the current state-of-the-art COTS components.

This narrowed scope allows for a more focused study while still maintaining relevance to the field of NEA exploration using CubeSats.

1.2. Thesis goal and research questions

Since there is a need and proven interest in NEA exploration missions using an autonomous miniature satellite and one of the main challenges which have to be solved is to design an AOCS for these missions, the goal of the thesis is to design an AOCS for an autonomous 6U satellite NEA fly-by mission starting from an SSGTO by simulating different combinations of COTS components. As mentioned in the introduction, a feasible combination is an AOCS which is a combination of a propulsion system for interplanetary travel, desaturation of reaction wheels and orbital corrections, and an attitude determination and control system (ADCS). This leads to the following research questions and sub-questions for this thesis:

RQ1: What is a feasible design for a propulsion system for interplanetary travel to perform an autonomous 6U satellite near-Earth asteroid fly-by mission starting from a super synchronous geostationary transfer orbit within 5 years?

In order to answer this research question, the state-of-the-art (SOTA) for micro propulsion systems has been investigated to be able to select a feasible propulsion system. This leads to the following research sub-question:

RQ1.1: What state-of-the-art propulsion systems meet the requirements for a near-Earth asteroid fly-by mission?

Additionally, a practical framework to simulate a fuel-efficient trajectory to a NEA starting from an SS-GTO within 5 years is developed to verify the feasibility of the propulsion systems selected in sub-research question RQ1.1. This trajectory should be fuel-efficient because it promotes miniaturization. This leads to the sub-research question:

RQ1.2: What is a practical framework to simulate a fuel-efficient trajectory to a near-Earth asteroid within 5 years?

In this case, a practical framework is defined as a framework that uses a fast and simplified model to evaluate a system while still being accurate. This enables the simulation of the different systems even when the computing power available is limited. Notice that the term fuel-efficient is not the correct term for all systems such as electric propulsion systems that only use propellant. Propellant-efficient is the proper formulation for these propulsion systems. However, for this thesis, the name fuel-efficient is mentioned instead of propellant-efficient because it is more well-known literature when discussing this particular problem.

The second research question focuses on the reaction control thrusters (RCTs) required to desaturate the onboard reaction wheels and perform small orbital corrections. This leads to the following research question:

RQ2: What is a feasible design for a propulsion system to desaturate reaction wheels for an autonomous 6U satellite near-Earth asteroid fly-by mission starting from a super synchronous geostationary transfer orbit for 5 years?

To answer this research question, the SOTA for micro propulsion systems for desaturation of reaction wheels and orbital corrections has been investigated to be able to select a feasible propulsion system. This leads to the following research sub-question:

RQ2.1: What state-of-the-art propulsion systems meet the requirements for the desaturation of reaction wheels for a CubeSat near-Earth asteroid fly-by mission?

Furthermore, the number of thrusters, the position, and the direction to maximize the amount of torque per propellant mass have been found as well because this leads to a propellant-optimal propulsion system configuration for momentum-dumping maneuvers. This leads to the following research sub-question:

RQ2.2: What number of thrusters, their position, and direction are required to perform momentum dumping maneuvers?

The final and third research question focuses on the attitude control system including a control algorithm to detumble, track the asteroid, and correct the orientation of the satellite. This leads to the following research question:

RQ3: What is a feasible design for an attitude control system including a control algorithm for an autonomous 6U satellite near-Earth asteroid fly-by mission starting from a super synchronous geostationary transfer orbit?

To answer this research question, a framework to simulate the attitude of the spacecraft must be developed to verify the feasibility of the AOCS system with respect to attitude control. This leads to the following sub-research question:

RQ3.1: What is a practical framework to simulate the attitude of a CubeSat?

A practical framework in this case is a model which is simplified, but accurate enough to decide on which system requires the least mass, volume, and power to control the attitude of the satellite and meets the requirements of a CubeSat fly-by mission.

The research goal and questions presented are of scientific significance for several reasons. Firstly, the focus on NEA exploration using an autonomous miniature satellite in a specific mission configuration (i.e., a fly-by mission type, 6U CubeSat with COTS components, and deployed in an SSGTO) is a novel approach that can potentially pave the way for low-cost and efficient space exploration using off-the-shelf components. This approach is particularly relevant given the current surge of interest in space exploration and the potential commercial benefits that NEA exploration can bring.

Secondly, the research questions proposed in the thesis are specific and measurable, which makes the research more manageable and achievable. The research questions focus on the design of the AOCS of the CubeSat, which is a crucial component in any space mission. The selection and customization of a feasible propulsion system for interplanetary travel and the optimal configuration for reaction wheel desaturation, as well as a practical framework to simulate a fuel-efficient trajectory to a NEA, are all important components of the AOCS that require careful consideration and research. Currently, other deep-space CubeSat missions or mission designs rely on staging rockets for their interplanetary flight. This thesis has a more challenging mission starting condition, namely an SSGTO, and can therefore be considered novel in all these fields.

Thirdly, the research questions address several gaps in the current SOTA in space exploration, particularly with regard to the use of CubeSats for NEA exploration. The study of the SOTA of micro propulsion systems and their feasibility in NEA missions, as well as the identification of the optimal configuration for a propellant-optimal propulsion system, are important contributions to the field. Additionally, the practical framework for the preliminary mission design phase to simulate a fuel-efficient trajectory to a NEA is a novel approach that can potentially have implications for other space missions in their preliminary design phase.

Lastly, combining the answers found for the different research questions leads to a design for the AOCS. This design can then be a starting point for the standardization of these systems in future missions.

1.3. Thesis outline

the structure of the master thesis is as follows. In the introduction, the mission description is formulated which leads to the mission requirements. Then the satellite subsystems for an autonomous CubeSat NEA fly-by mission are selected in the satellite description necessary to answer the research questions in later chapters. In chapter 2 possible solutions for the interplanetary propulsion system and the reaction control propulsion system are discussed from the current SOTA. Then, in chapter 3, the astrodynamics model necessary to create a fuel-efficient trajectory design framework is formulated. Next, in chapter 4 a fuel-efficient low-thrust and high-thrust fly-by trajectory design framework is presented based on the astrodynamics model from the previous chapter. Following that, in chapter 5 the results for the possible solutions for the interplanetary propulsion systems and their fuel-efficient fly-by trajectories are presented and discussed with a focus on answering research question RQ1. Then, in chapter 6

the rotational dynamics model to simulate the attitude of the satellite for the different mission phases is formulated. In addition to that chapter, chapter 7 proposes a reaction control thruster design method, a satellite detumbling method, a reaction wheel desaturation method, and a motion tracking method built on top of the previously formulated rotational dynamics model. Next, in chapter 8 the results for the reaction control thruster design, satellite detumbling, reaction wheel desaturation, tracking of the optimal thrusting direction, and the asteroid are presented to answer research questions RQ2 and RQ3. Finally, in chapter 9 the conclusions and the recommendations are presented.

1.4. Mission description

Before a feasible design can be made, first the requirements for the satellite and the AOCS have to be formulated, and their verification methods have to be selected or developed. For this thesis, this is done by formulating a NEA fly-by mission goal and (secondary) objectives if present. Then the requirements to achieve the mission goal and objectives are formulated in unambiguous terms such that appropriate acceptance criteria can be made and verification methods can be defined later in the thesis. The system-specific AOCS requirements can also be formulated based on the higher-level spacecraft requirements and the constraints set for the mission. In addition, the AOCS is designed based on the mass, volume, power, and inertia of a satellite which partly comes from the selection of other systems. The mission description focuses on a NEA target selection that is possible using the current SOTA but remains reachable, the typical spacecraft requirements of a NEA fly-by mission, The AOCS-specific requirements that follow from the mission and the spacecraft requirements, the requirements for autonomy, and the radiation requirements.

1.4.1. Near-Earth asteroid target selection

The target asteroids are selected from a list of valuable NEAs that are suitable for autonomous navigation [5]. To showcase the capabilities of autonomous navigation, asteroids within a range of 0.5 to 0.7 astronomical units from the Sun are selected. This selection balances ambition with feasibility. In other words, the targets demonstrate what is possible using the current SOTA but remain reachable.

1.4.2. Spacecraft requirements

The assumed goal of the satellite mission is to fly by a NEA and make images at a distance of 10,000 km within five years after the satellite's deployment in an SSGTO in a low-cost project. The 10,000 km closest approach distance is chosen, because past missions such as PROCYON have the requirement of the closest approach distance in the range of 30 kilometers for a non-autonomous mission [6]. However, this is very ambitious for an autonomous satellite and it is more likely that an autonomous satellite will approach an asteroid in the range of a couple of thousand kilometers. Especially when the target is relatively small in size and has a low albedo, 10,000 km is a more reasonable closest fly-by constraint. Also, NEAScout has a target distance of 10,000 for the target search and approach mission phase which can be considered to be similar to the fly-by in this thesis.

The proposed solution to reach this goal is to use a miniature autonomous satellite that significantly reduces the mission cost by reducing the required volume, mass, and the mission's ground segment. Combining the mission goal and the proposed solution leads to the following mission requirements:

MR-SC-1: The satellite shall be able to fly by a near-Earth asteroid at a closest approach distance of 10,000 km within 5 years.

MR-SC-2: The satellite shall be deployed in a super synchronous geostationary transfer orbit (This

orbit has a perigee at 295 km and an apogee at 90,000 km).

MR-SC-3: The satellite shall be able to autonomously navigate and operate.

MR-SC-4: The satellite shall have a maximum volume of 6U.

MR-SC-5: The satellite shall have a maximum mass of 12 kg.

MR-SC-6: The satellite shall be able to send scientific data back to Earth.

MR-PL-1: The payload shall be able to take pictures of the near-Earth asteroid at a distance of 10,000 km.

1.4.3. Attitude and orbital control system requirements

Since there are no comparable previous missions to a NEA, no specific requirements could be found for an AOCS. Casini, Fodde, Monna, *et al.* [1] states that a fly-by exploration mission to a NEA starting from SSGTO can be divided into seven segments which are: orbit injection and de-spinning, Earth escape, deep-space cruise, NEA close encounter, scientific acquisition, data transmission, and final disposal. To fulfill MR-SC-1, the AOCS system shall be able to perform all these seven segments of the mission. This leads to the AOCS-specific requirements which are:

MR-AOCS-1: The attitude and orbital control system shall be able to maneuver the spacecraft to a distance of 10,000 km at the nearest point of approach to the near-Earth asteroid within 5 years.

MR-AOCS-2: The attitude and orbital control system shall be able to detumble the spacecraft after orbit injection.

MR-AOCS-3: The attitude and orbital control system shall be able to track the near-Earth asteroid at a distance of 10,000 km.

1.4.4. Autonomy requirements

The autonomy of a system can be seen as the condition of operating without the use of external system inputs. Currently, most satellites use a ground segment for navigation and operations such as flight path calculations or other advanced control maneuvers. A big problem arises when a system is autonomous and problems that are too computationally intensive for a typical computer processor to solve arise. For example, controlling multiple thrusters to desaturate reaction wheels in an optimal way or calculating the most optimal trajectory to an asteroid. The thesis will only focus on autonomy for the attitude control system (ACS) because autonomous orbital control and navigation is a noticeably big topic on its own. Therefore, the ACS for autonomous satellites should take into account that optimal control strategies which use a lot of computing power, such as model predictive control, cannot be used. To limit the computational load for attitude control calculations, the spacecraft shall therefore limit its control methods to reactive methods only. Predictive methods are then not considered. Also, the satellite should have systems that would in theory enable the spacecraft to navigate autonomously. A requirement for this navigation is taken from the M-ARGO mission. Their optical navigation systems can in theory reach a 3σ position error less than 1000 km and 1 m/s in velocity [7]. These will be the only extra requirements for the thesis design compared to ordinary satellites. From this the following requirements are formulated:

MR-AOCS-4: The spacecraft shall be able to autonomously navigate in deep space with a position error less than 1000 km (3σ) and a velocity error less than 3 m/s (3σ).

MR-AOCS-5: The spacecraft shall be able to autonomously acquire its attitude in any direction in deep space with an error of fewer than 10 arcseconds (3σ).

MR-AOCS-6: The spacecraft shall not use a predictive attitude control method.

1.4.5. Radiation requirements

For a space mission, there is always a radiation environment specification wherein all types of radiation are considered. This specification is then used for component selection, material selection, and shielding optimization. For radiation analysis, there are general models such as SPENVIS which can be used to characterize the radiation environment of a mission. For this thesis, however, a radiation environment specification and radiation analysis are considered outside of the scope. Yet a basic understanding is necessary to decide what components are potentially not feasible for a NEA mission if radiation tolerance is considered.

The radiation environment around Earth and in heliocentric orbit has many different sources. Throughout the Earth's magnetosphere and interplanetary space, energetically charged particles can be encountered. These particles can have energies in the range of several MeV and even above which could seriously harm the spacecraft and its components. Around Earth, there are radiation belts, also known as the Van Allen belts, which are formed by energetic electrons and ions that are magnetically trapped. These radiation belts extend from 100 to 65,000 km and consist of electrons with energies up to a few MeV and protons with energies up to several hundred MeV. Next to the radiation belts, solar energetic particles (SEPs) are also encountered in space and close to Earth. These particles are often seen in short-duration bursts and consist of protons, electrons, and heavy ions with energies ranging from tens of keV to GeV ranges. The Earth's magnetic field often provides shielding against these particles up to a certain degree. In deep space, however, these SEPs are more dominant. Further, there are galactic cosmic rays (GCRs) which are high-energy charged particles that enter the solar system from the outside. They are composed of protons, electrons, and fully ionized nuclei. Again, the Earth's magnetic field provides shielding against these particles, and thus GCRs are mostly dominant in deep space next to SEPs. Finally, Neutrons are ejected by the Sun. These particles are only important for missions close to the Sun because they decay rapidly in the interplanetary medium [8].

For a low thrust mission starting from an SSGTO to a NEA it is presumably the case that the most energetic particles are encountered during the Earth escape because the spacecraft will go through the Van Allen belt multiple times. The radiation environment is a serious hazard to electrical components, solar cells, and materials. These radiation effects can at least be categorized as Total Ionizing Dose (TID) and Single Event Effects (SEEs). The TID or ionization of the equipment can have many different effects such as electrical shorts, changes in material properties, and eventually the loss of a system. Single-event effects are often 'soft errors' such as bit-flips which could cause complete system lock-ups or 'hard errors' such as latch-ups which can even lead to the destruction of integrated circuits used on the spacecraft.

When talking about 'radiation resistant' equipment suppliers mostly mention the TID that a system can handle with a certain confidence. However, the Linear Energy Transfer (LIT) of a system, which is the amount of energy that an ionizing particle transfers to the material traversed per unit distance, can also be mentioned. A low LIT means that the effective TID a system accumulates in the same environment is far less compared to a system with a high LIT [9].

In all probability for a low thrust mission starting from an SSGTO to a NEA space-grade radiation tolerant systems are required of at least tens of kRads. While radiation is a critical consideration in satellite design, this master's thesis topic does not focus on it. Nevertheless, further research should

explore this important factor in future works. For this thesis, it is decided to assume that every system can be ordered as radiation hardened such that it can withstand the radiation environment of the mission. To still include that mass for a radiation shielding structure in the design, the satellite will have an aluminum radiation shield with a thickness of 5 mm. And finally, the component with a better radiation tolerance as listed by the supplier is favored over another comparable component that is less radiation hardened.

1.5. Satellite description

In order to answer the research questions, the satellite's subsystems other than the AOCS that in theory meet the requirements of a NEA fly-by mission are selected first to be able to form the conditions and constraints under which the AOCS has to operate in terms of power, volume, mass, and other comparable parameters. This section, therefore, focuses on the selection of the subsystems which are required for such a mission.

The subsystems that may comprise a NEA fly-by satellite mission include the payload system, the navigation system, the attitude and orbital control system, the communication system, the onboard data-handling system, the electrical power system, the thermal control system, and the satellite structure. For this thesis, the thermal control system is assumed to be a passive thermal control system that only uses paint, coatings, and/or louvers to regulate the temperature of the different parts of the satellite. Although thermal control is important and can significantly impact the power, volume, and mass budget of the satellite it is a topic on its own and not the focus of this thesis. Assumed is that the radiation shield and satellite structure can serve as a thermal control system at the same time because it can be seen as a thermal mass and its coating can regulate the temperature of the satellite.

1.5.1. Payload selection

To comply with requirement MR-PL-1 a camera must be selected such that the NEA can be observed from that distance.

MR-PL-1: The payload shall be able to take pictures of the near-Earth asteroid at a distance of 10,000 km.

This is important for the design of an AOCS because it contributes to the total mass and uses power and volume that then cannot be used by the AOCS. NEAScout, which is a rendezvous 6U CubeSat mission to a NEA still being developed by NASA's Marshall Space Flight Center and NASA's Jet Propulsion Laboratory, will have a camera that is able to observe an asteroid at a distance of 60,000 km. This camera is therefore selected since it meets the requirement MR-PL-1 [10]. This camera has a mass of 390 grams, a volume of $63 \times 63 \times 71$ mm, and uses < 3 W of power during operations.

1.5.2. Navigation system selection

The selection of a navigation system is again very important in the design of an AOCS because it adds mass to the spacecraft, and takes up power and volume that could have been used by the AOCS. Therefore a navigation system is selected that complies with MR-SC-3, MR-AOCS-4, and MR-AOCS-5.

MR-SC-3: The satellite shall be able to autonomously navigate and operate.

MR-AOCS-4: The spacecraft shall be able to autonomously navigate in deep space with a position error less than 1000 km (3σ) and a velocity error less than 3 m/s (3σ).

MR-AOCS-5: The spacecraft shall be able to autonomously acquire its attitude in any direction in deep space with an error of fewer than 30 arcseconds (3σ).

To navigate in Earth orbit and deep space autonomously without the use of a ground station or other satellites Turan, Speretta, and Gill [11] mentions four methods which are used for navigation: optical navigation, pulsar navigation, Sun/Earth sensor navigation, and magnetometer navigation. From these different navigation methods, one has to be selected together with the hardware necessary to perform autonomous navigation.

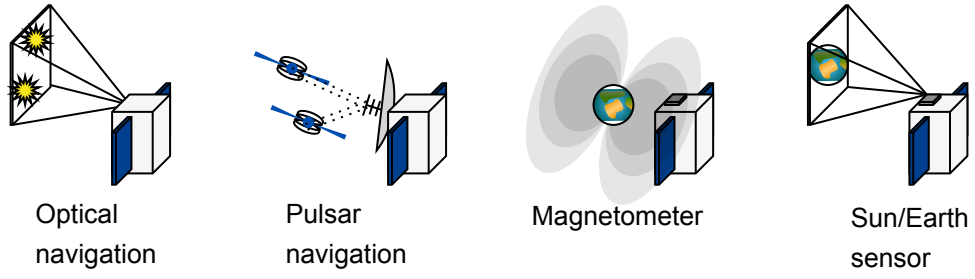

Figure 1.1: The following illustrations from left to right showcase possible methods for autonomous navigation in space. (1) Depicts a spacecraft equipped with optical sensors to observe and track star patterns to determine its position and orientation in space. (2) Depicts a spacecraft equipped with a pulsar detector that receives signals from distant pulsars to determine its position and velocity. (3) Depicts a spacecraft equipped with a magnetometer that detects variations in the magnetic field of nearby celestial bodies to determine its position and orientation. (4) Depicts a spacecraft equipped with sensors that detect the position and brightness of the sun and earth to determine its orientation and trajectory.

Optical navigation

Optical navigation refers to a number of methods that determine the spacecraft's state, relative position, and velocity in space using optical instruments. These methods can be categorized as star-based, celestial navigation, relative navigation, and terrain-relative navigation. Star-based optical navigation methods use stars for navigation. Celestial navigation uses celestial bodies such as the Sun, planets, or moons to estimate the state of the spacecraft. Relative navigation uses a target body for navigation. This is presumably not possible for NEA missions, because these asteroids can have a low albedo, a small size, and therefore a small apparent size. And finally, terrain-relative navigation uses the surface landmarks of a body to estimate the state of the spacecraft. Again, this would not be possible for a NEA mission when the spacecraft is during its deep space cruise toward the target. In principle, all these methods compute a body position in the camera reference frame and derive the target location in space from its location in the images. The main advantage of these methods is that they can be used in various mission phases. The downside is that the error is moderate to high depending on near bodies which can be used for navigation. As mentioned earlier, the M-ARGO missions navigation error using star-based and celestial navigation can be expected to be in the range of 1000 km and 1 m/s (3σ) for the position and velocity error of the spacecraft [7].

Pulsar navigation

Pulsar navigation uses periodic X-ray signals emitted from pulsars to estimate the spacecraft states, by estimating the time and direction-of-arrival of the pulses with a single instrument. The main advantage of this method is that due to the fast-spinning neutron stars, the onboard clocks can be stabilized. Furthermore, this method can reach a positional error of less than 0.1 km at 1AU with a timing of $10^{-7}s$ timing and a pulsar position error of $10^{-4}arcsec$ [12]. The downside of this method of autonomous navigation is that it requires a large antenna of at least 25 m in order to pick up the 100MHz to a

few GHz frequencies emitted by pulsars. Also, this method cannot be used for a rendezvous mission, because it also requires large integration times which means close proximity operations cannot be done.

Sun/Earth sensor navigation

Sun/Earth sensor navigation can be achieved by combining a Doppler measurement due to the relative motion from the spacecraft to the Sun, direction data from the spacecraft to the Sun, and direction data from the spacecraft to Earth. Yim, Crassidis, and Junkins [13] concludes with a simulation that autonomous navigation using a Sun and Earth sensor can estimate the position error of the spacecraft to within 3 km (3σ) under ideal conditions. The main advantage of this method is that it can be used during every mission phase with a relatively low position error. However, there are no known missions that use this navigation method, which means that the system has limited availability and the requirements for these systems are unknown.

Magnetometer navigation

Magnetometer navigation determines the attitude and orbital position of a spacecraft by using a well-defined magnetic field of a body in the proximity of the spacecraft such as the Earth. The advantage of this method of navigation is that a magnetometer is a widely used sensor and it has a low position error with respect to other methods. The downside, however, is that this method of navigation can only be used in characterized magnetic fields.

Feasibility & Hardware selection

Investigating the different possible options for autonomous navigation it is clear that for a deep-space mission using a small satellite, the magnetometer cannot be used, because there are no characterized magnetic fields in interplanetary space. Also, pulsar navigation cannot be used for small satellite missions due to the fact that a pulsar sensing antenna has to be 25 meters or more in size, which is not compatible with small satellite missions. That leaves an optical-based navigation method or Sun/Earth sensor solution as the only two feasible options for an autonomous navigation solution for the NEA fly-by mission. For this thesis, the optical-based navigation method is chosen because it has been selected for future deep-space missions such as M-ARGO or BIRDY-T, whereas the Sun/Earth sensor-based navigation has yet to be investigated further and selected on a mission.

Interplanetary optical-based navigation systems are limited available because most systems are still in their development phase. Only the system selected for the M-ARGO mission could be found in the literature. It is unknown what the characteristics are for the navigation system used in the BIRDY-T mission. Therefore, the camera selected for the M-ARGO mission was selected. As mentioned in Franzese, Topputo, Ankersen, *et al.* [7], the M-ARGO mission uses a VisNAV camera. The size of this camera is $13 \times 13 \times 8$ cm, has a total mass of 500 grams, and uses 2W of power [14].

1.5.3. Communication system selection

Without a communication system, data acquisition is possible but there will be no downlink. Even though an autonomous spacecraft should not require any communications to operate, the scientific data which is acquired has to be sent back to Earth, which is in line with the spacecraft requirement MR-SC-6. A proper selection of a communication system is vital for this thesis because it adds mass to the satellite and uses power and volume that could be used by the AOCS.

MR-SC-6: The satellite shall be able to send scientific data back to Earth.

Communication between a satellite and a ground station is often done by using radio frequency (RF) communication or laser communication because these are the most practical. There are other methods such as infrared communication, and visible light communication but these are less practical and not considered. Laser communication is also not considered, because these systems have yet-to-be-demonstrated performance. In theory, laser communication will be the better option due to its exceptional theoretical data rates compared to RF communication [15].

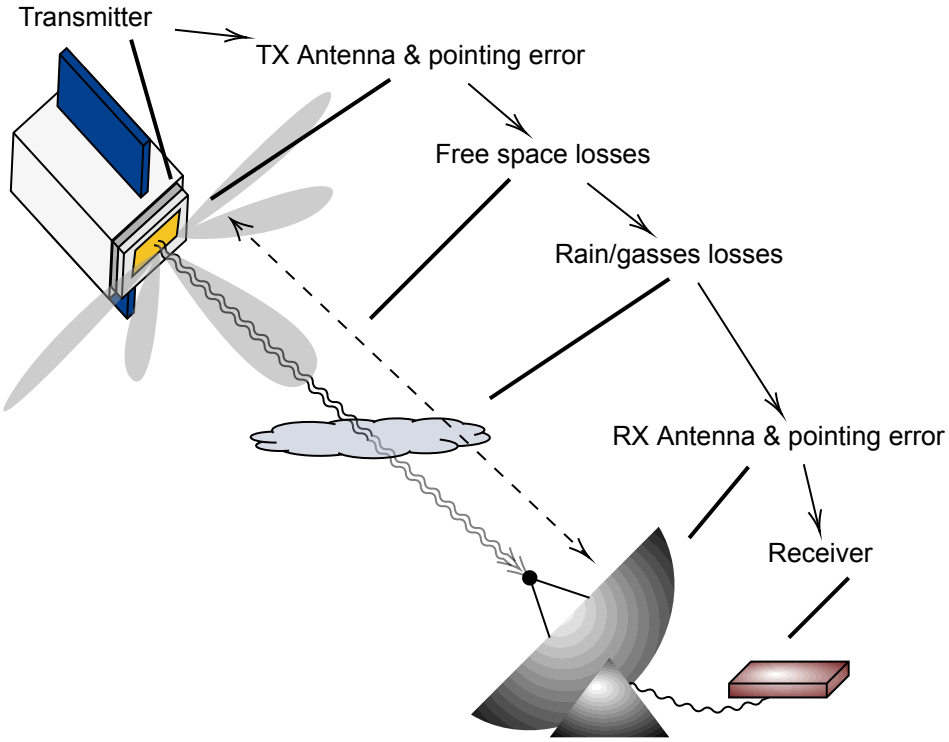

Figure 1.2: In this illustration, a satellite radio frequency communication system is depicted along with its standard communication losses. However, it is worth noting that the internal losses occurring in the transmitter and receiver are not depicted, yet they cannot be disregarded.

Deep space communication is mainly done by means of X-band-based systems, which are electromagnetic frequencies in the range from 8.0 to 12 GHz, or Ka-band-based systems which are in the range from 27 to 40 GHz. This is due to two major reasons: higher bandwidths are more readily available and higher carrier frequencies lead to higher data rates. Of these two bands, X-band systems are considered more applicable for deep-space CubeSat missions which communicate with a ground station. This is due to the fact that Ku-, K- and Ka-band systems have problems penetrating the Earth's atmosphere and these systems require a lower pointing error to properly function. Especially water droplets absorb a lot of the Ku- K- and Ka-band signals. The higher frequency bandwidths can work by increasing the transmission power and/or increasing the gain of the antenna which narrows the beam width. The downside of these systems is that a higher gain antenna increases the pointing error requirement for the link. And an even higher antenna gain is required for Ku- K- and Ka-bands if the weather and elevation angle is less ideal. With a similar gain and transmission power, X-band systems can generally reach higher data rates, because these systems have fewer problems penetrating the Earth's atmosphere and larger pointing errors lead to less signal power losses. Therefore, only X-band systems are considered [15].

Available options for antennas, transmitters, and transceivers are given in Table 1.1 and Table 1.2.

Table 1.1 provides a comprehensive overview of the various antennas, their design specifications, and features to assist in selecting the most suitable X-band communication antenna for the desired CubeSat mission. Table 1.2 provides detailed information on the design specifications and features of each radio, enabling a comprehensive comparison to help in choosing the most appropriate X-band communication radio for the desired CubeSat mission.

Table 1.1: The table presents a list of X-band communication antennas that are currently available for CubeSats [4]. These antennas are designed to provide high-gain, low-power communication solutions for CubeSat missions that require long-range and high data rate capabilities. Notice that data is missing because Endurosat does not provide size properties of their systems and AAC Clyde Space and Syrlinks do not give the half-power beamwidth in their specification sheets.

Manufacturer	**Model**	**Size (mm)**	**Mass (grams)**	**Gain (dBi)**	**Half-Power Beamwidth (deg)**	**Frequency range (MHz)**	**Reference**
Endurosat	X-band patch antenna	-	<3	6	74	8025-8400	[16]
Endurosat	X-band patch antenna 2×2	-	23.2	12	40	8025-8400	[16]
Endurosat	X-band patch antenna 4×4	-	53	16	18	8025-8400	[16]
Syrlinks	SPAN-X-T2	$10 \times 10 \times 7$	68	7.6	-	8025-8450	[4]
Syrlinks	SPAN-X-T3	$7.3 \times 7.3 \times 11$	65	11.5	-	8025-8450	[4]
AAC Clyde Space	XANT	$36 \times 36 \times 4.7$	9	7.75	-	8025-8450	[17]
AAC Clyde Space	XANT-PLUS	$58 \times 58 \times 4.7$	29	11.5	-	8025-8450	[17]

Note: Syrlinks does not provide specifications for the SPAN-X-T2 and T3, however NASA does provide this data.

Table 1.2: The table displays various X-band communication radios currently available for CubeSats [4]. These radios offer high data rates and long-range communication capabilities that are essential for successful CubeSat missions. Blue Canyon Technologies does not give mass specifications and Syrlinks does not provide data on power requirements in their datasheets.

Manufacturer	Model	Size (mm)	Mass (grams)	Power (W)	Tx Power (dBm)	Reference
Blue Canyon Technologies (BCT)	X-band Radio	$45 \times 43.5 \times 12.5$	-	1.8	30	[4]
Tethers Unlimited	SWIFT-XTX X Transmitter	$90 \times 98 \times 60$	300	4	33	[18]
General Dynamics	X-Band Small DeepSpace	$180 \times 170 \times 110$	3200	15.8	17.78	[19]
JPL/SDL	IRIS V2.1	$100 \times 100 \times 56$	1000	33.7	35.80	[20]
Innoflight, Inc.	SCR-106	$98 \times 82 \times 28$	290	2.5	33.98	[4]
EnduroSat	X-band Transmitter	$90 \times 96 \times 26$	270	2	33	[16]
IQ-Spacecom	XLINK-X	<0.2U	200	16	30	[21]
Syrlinks	X-band Transmit-terEWC27	$90 \times 96 \times 26$	225	-	33	[4]
AAC Clyde Space	PULSAR-DATA X-Band Transmitter	$96 \times 90 \times 11$	130	10	33.01	[22]

Note: Tethers Unlimited Swift-XTX and Innoflight Inc. SCR-106 do not have flight heritage.

Link budget and data rate

To properly select an X-band transmitter and antenna, the link budget has to be calculated and the system noise has to be estimated for the ground station receiver. A link has a positive signal-to-noise ratio (SNR) when the received power is more than the system noise power at the ground station. When a link has a positive SNR, data can in theory be transferred and recovered over a channel. The system's SNR is therefore a very important specification of a link. This ratio also closely relates to the amount of data that can be sent over a channel by the bandwidth and encoding and modulation used on the data stream. The SNR can be expressed as [23]:

$$SNR = P_{Rx} - N_0 - 10\log_{10}(B) \tag{1.1}$$

Where P_{Rx} is the received carrier power as calculated in Appendix A in dB and N_0 is the spectral noise density in dB Hz^{-1} and B the bandwidth in Hz.

To obtain the maximum symbol-rate f_s for a given minimum required energy per bit to noise power spectral density ratio E_b/N_0 in dB the following relation can be used [23]:

$$f_s = r \times 10^{\frac{1}{10}(P_{Rx,\text{dB}} - N_{0,\text{dB}} - E_b/N_0)} \tag{1.2}$$

where f_s is the symbol rate of the downlink in $b\ s^{-1}$, P_{Rx} is the received signal power in dB, N_0 is the noise spectral density in dB and E_b/N_0 is the energy per bit to noise power density ratio in dB.

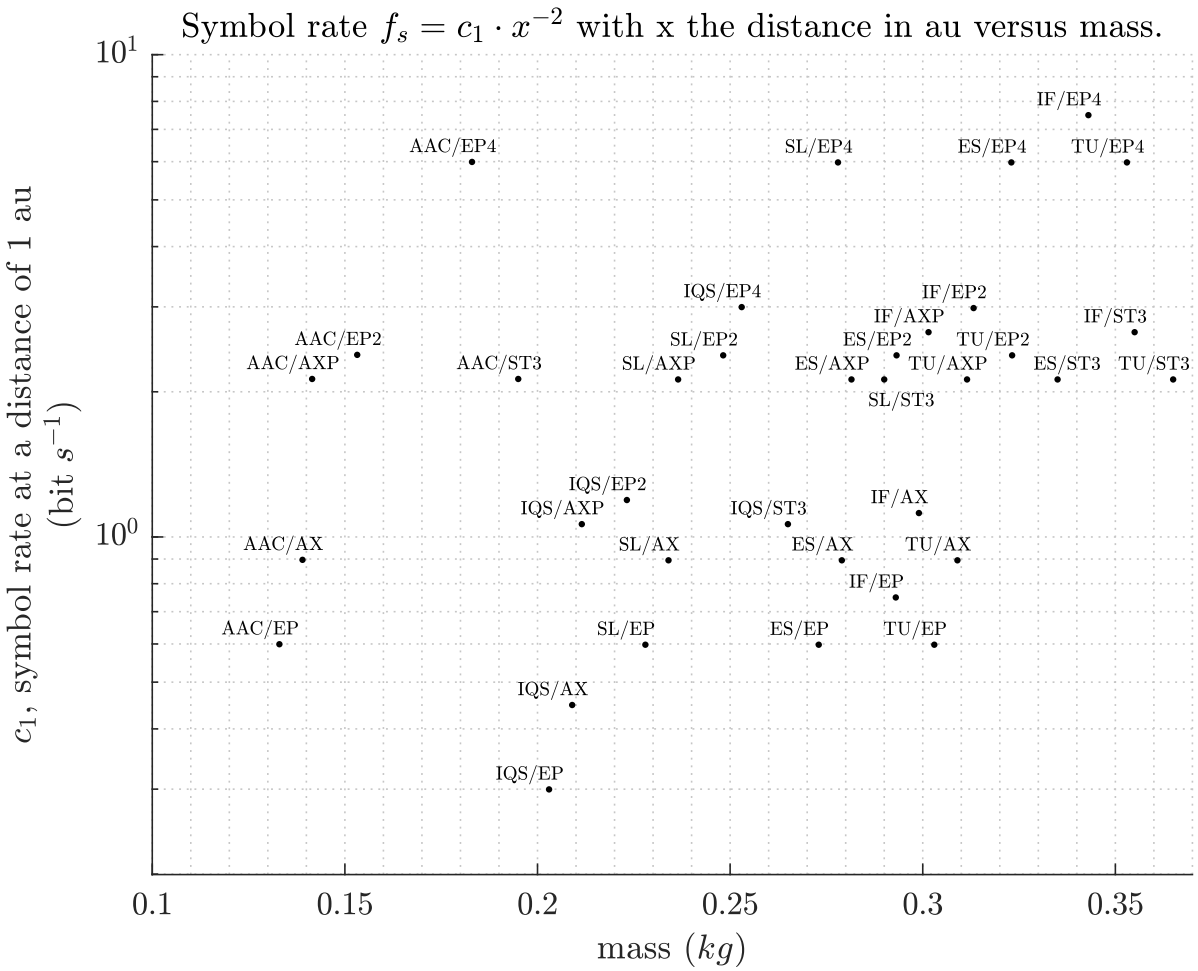

Figure 1.3: This figure depicts the symbol rate versus the total mass of the communication system as a function of the distance between the transmitting antenna and the receiving DSS-54 antenna located in Madrid for average clear weather conditions (CD=0.25) and an elevation angle of 90 degrees. The used equations can be found in Appendix A. The figure includes various transmitter and antenna names, which are combinations of the used transmitter and antenna. The symbol rate at a distance other than 1 au can be estimated using the formula $f_s = c_1 \cdot x^{-2}$, where x is the distance in astronomical units and c_1 is the symbol rate at a distance of 1 astronomical unit, as provided in the figure. The symbol rate is an important parameter that influences the data transfer rate in deep space missions. This figure provides valuable insights into the relationship between symbol rate, the total mass of the communication system, and distance, allowing for the selection and optimization of communication systems for deep space missions. Used abbreviations for the transmitters are TU=Tether Unlimited SWIFT-XTX, IF=Innoflight SCR-106, ES=EnduroSat X-band transmitter, IQS=IQ-Spacecom XLINK-X, SL= Syrlinks EWC27, AAC=AAC Clyde Space PULSAR-DATA. And used abbreviations for the antennas are EP=EnduroSat Patch, EP2=EnduroSat Patch 2×2, EP4=EnduroSat Patch 4×4, ST3=Syrlinks SPAN-X-T3, AX=AAC Clyde Space XANT and AXP=AAC Clyde Space XANT-PLUS.

Selected antenna and transmitter

To compare the different X-band transmitters and antennas a downlink to the DSS-54 in Madrid is simulated with an elevation of 90 degrees and average clear weather (CD=0.25). Further, a turbo code encoding with a symbol per bit rate of 1/6 and information block size of 8920 is used with a recommended minimum E_b/N_0 of -0.1 to have an allowable bit error rate. Additionally, the conversion loss in the satellite between the transmitter and transmitting antenna is assumed to be $2\,$dB, the conversion loss between the receiving DSN-antenna and the receiver is assumed to be $1\,$dB and extra data

conversion losses is assumed to be 0.6 dB. The resulting symbol rate can be seen in Figure 1.3. For comparison, the mass of the total system is also given. Syrlinks SPAN-X-T2 antenna is not considered, because the Syrlinks SPAN-X-T3 is a lighter, smaller, and more gain version of the T2, so only T3 is considered. Blue Canyon Technologies' X-band radio is excluded because its mass data could not be obtained. Further, JPL's IRIS V2.1 and General Dynamics' X-Band Small DeepSpace radios are also excluded, because these systems are considered too heavy for a NEA fly-by mission starting from SSGTO. For larger missions or CubeSat missions with a dedicated booster stage to enter heliocentric orbit, these systems could be considered.

From Figure 1.3 it can be seen that the AAC Clyde Space PULSAR-DATA transmitter combined with the EnduroSat Patch 4×4 antenna seems like the most feasible option in terms of symbol rate per mass. This combination gives the second-highest symbol rate but is more mass-efficient. In theory, it reaches a symbol rate of 6 bit/s at a distance of 1 au with a total mass of 0.183 kg. If a higher symbol rate is desired, then the Innoflight SCR-106 transmitter can be used instead of the AAC Clyde Space PULSAR-DATA transmitter. The downside of this combination is that it is the second heaviest option. For this mission, the AAC Clyde Space PULSAR-DATA transmitter combined with the EnduroSat Patch 4×4 antenna is chosen, because low mass seems more important. However, this could be different due to the required data size to be sent back to Earth. This should be further investigated in future research.

Additionally, if a pointing power loss of 3 dBi is considered the pointing error of the satellite must be less than 10 degrees for the EnduroSat Patch 4×4 antenna as can be seen in Appendix A and Figure A.5. This leads to an additional requirement for the AOCS:

MR-AOCS-7: The pointing error of the satellite antenna shall be less than 10 degrees during transmission.

1.5.4. Onboard data handling system selection

Most systems such as the payload, the communication system, or the AOCS come with internal processors that handle the data and do computations. However, for processes such as data processing, monitoring subsystems, storage, and autonomous operations an on-board data handling system is required. Again the selection of an onboard data handling system is required in this thesis because it contributes to the total mass of the satellite, takes up the volume, and consumes power. The mass is required in a trajectory calculation for the AOCS system, the inertia for attitude maneuvers, and the power and volume are required in the AOCS selection.

A trade-off on different onboard data handling systems will not be performed because it is considered outside of the scope. Only a competitive reference for the power, volume, and mass of these systems is required for this thesis. Therefore, the AAC Clyde Space CP400.85 (formerly known as Hyperion Technologies CP400.85) as selected in Casini, Fodde, Monna, *et al.* [1] is selected. This system has a mass of 7 grams, uses <1000 mW of peak power, 500 mW of nominal power, and has a size of $20 \times 50 \times 10$ mm. It further has a random access memory (RAM) storage of 512 MB, main storage of 512 MB, and a TID radiation tolerance of more than 25 krad [24].

1.5.5. Power system selection

For a CubeSat mission to a NEA, a power system should be able to provide enough power in the different mission phases to power a high specific impulse propulsion system, a deep space communication system, a payload, an attitude control system, the on-board data handling system and navigation and

attitude sensing equipment. It is assumed that the power system for these missions consists of solar panels and a battery system for moments when the solar panels are not in (direct) sunlight. Other options such as, but not limited to, nuclear power are considered to be outside of the thesis topic.

Solar panels

For a CubeSat, there exist many solar panel solutions to power the satellite. While very low-power CubeSats and SmallSats may only need body-mounted solar panels, a mission to a NEA will require more power from deployed solar arrays. An electrical power system engineer can decide to design a solar panel array from scratch using solar cells, however, this often leads to higher costs and a longer time schedule. COTS solar panel arrays are therefore selected and preferred for this mission.

Table 1.3: This table lists the solar panel arrays that are currently available for CubeSats and have a proven performance and flight heritage [4].

Manufacturer	Model	Type	Specific Power (W/kg)	Peak Power (W)
AAC Clyde Space	Photon	Body mount + deployed rigid	68.52 (body) / 29.84 (deployed)	9.25W / 3U Face
DHV Technolgies	Solar Panels for CubeSats Set	Deployed Rigid	67	0.272-60 (1P / 1U/ 3U/ 6U/ 12U)
MMA Design	Hawk	Deployed rigid	117-135	89-191
MMA Design	zHawk	Deployed rigid	95	36
Agencia Espacial Civil Ecuatoriana	DSA/1A	Deployed rigid	107	7.2
ISISPACE	Smallsat Solar Panels	Body mount + deployed rigid	46	2.3W/U
EnduroSat	1U Solar Panel	Deployed rigid	50	2.4
EnduroSat	1.5U Solar Panel	Deployed rigid	55	2.4
EnduroSat	3U Solar Panel/Array	Deployed rigid	66	8.4

The MMA Design Hawk generates the most power per mass of all available solar panels. Therefore, the MMA Design Hawk 38A-191 with a peak power of 191W at 1AU and an approximated mass of 1.415 kg is selected.

Battery system

Before a battery system can be selected, the time in the shadow of the Earth has to be approximated. The size and shape of the shadow and half-shadow regions are mainly functions of the planet size, Sun size, and distance between the two celestial bodies. From the definition of the shadow cone surfaces in Longo and Rickman [25] the time in shadow and half-shadow can be found for the SSGTO. In the worst case for the shadow, the SSGTO is in the same plane as the Earth's elliptical plane which is assumed for this thesis. Furthermore, the orientation of the SSGTO is chosen such that the orbit's perigee lies within the shadow because this leads to the shortest shadow time and is thus considered

more desirable. This leads to a maximum shadow time in both half-shadow and complete shadow of approximately 21.893 minutes.

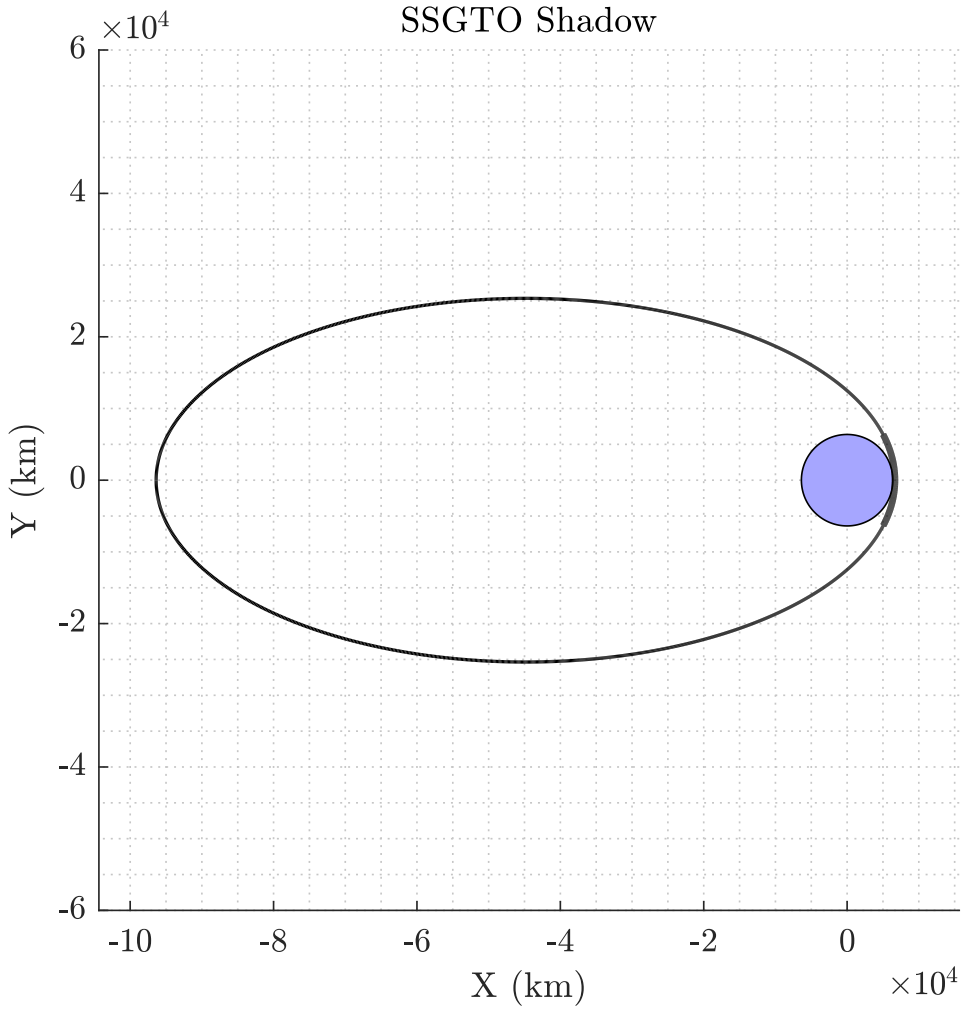

Figure 1.4: The shadow of a super synchronous geostationary transfer orbit. The figure shows the shadow of the orbit if the perigee lies within the shadow of the Earth (depicted by the blue circle) and the orbit is within the Earth's elliptical plane. This orbit (depicted by the black ellipse) has a perigee of 295 km above the Earth and an apogee of 90,000 km. This leads to a time in shadow (depicted by the thicker black line) including a half-shadow of 21.893 minutes calculated using the definition of the shadow cone surfaces from Longo and Rickman [25].

For the battery system, it is assumed that 80 Wh of energy is enough to power the propulsion system during this time in shadow. From the peak power of 191W produced by the MMA Design Hawk, 80Wh can power the satellite with equal power for 25 minutes before running out of electrical energy. This is more than the estimated maximum time in the Earth's shadow.

Next, from the peak power of 191W produced by the MMA Design Hawk, AAC Clyde Space's NANO-PLUS is selected with its lithium polymer battery pack OPTIMUS-80. This battery system has a combined mass of 0.818 kg and dimensions of $95.89 \times 90.17 \times 77.76$ mm [4].

1.5.6. Attitude determination and control system

The ADCS consists of attitude sensors, reaction wheels, and magnetorquers (optional). This is a vital part of the AOCS. The combination of reaction wheels, RCTs, and magnetorquers must be able

to detumble and track a reference orientation for every mission phase. This subsystem must meet requirements MR-SC-3, MR-AOCS-2, MR-AOCS-3, MR-AOCS-5, MR-AOCS-6, MR-AOCS-7.

MR-SC-3: The satellite shall be able to autonomously navigate and operate.

MR-AOCS-2: The attitude and orbital control system shall be able to detumble the spacecraft after orbit injection.

MR-AOCS-3: The attitude and orbital control system shall be able to track the near-Earth asteroid at a distance of 10,000 km.

MR-AOCS-5: The spacecraft shall be able to autonomously acquire its attitude in deep space with an error of fewer than 30 arcseconds (3σ).

MR-AOCS-6: The spacecraft shall not use a predictive attitude control method.

MR-AOCS-7: The pointing error of the satellite antenna shall be less than 10 degrees during transmission.

For comparable missions, the ADCS system is often 10 to 20% of the total mass of the satellite. In NASA [4] three ADCS can be identified that could potentially be used for the 6U CubeSat as can be seen in Table 1.4. Of the systems shown in the table, iADCS-400 is the most radiation resistant and has the largest reaction wheels. XACT-100 has relatively larger magnetorquers. Relatively large magnetorquers are not necessary for a satellite in SSGTO because the magnetic field strength is very high near the perigee. To be conservative, iADCS-400 is chosen because of the larger reaction wheels. The pointing error might be worse than in other systems but combined with the autonomous navigation system, this can be improved if necessary. The iADCS-400 has a total mass of 1.7 kg, dimensions of $95.4 \times 95.9 \times 67.3$ mm, and a maximum magnetic moment of 0.5 A m^2 in X/Y-direction and 0.4 A m^2 in the Z-direction. The iADCS-400 consists of three RW400 reaction wheels with a mass of 0.375 kg each, a peak power of 1.7 W, a maximum torque of 0.008 Nm, and a maximum rotational speed of 5000 rpm or 524 rad/s [26].

Table 1.4: This table presents the attitude determination and control systems that are available for 6U CubeSats [4].

Manufacturer	**Model**	**Mass (kg)**	**Actuators**	**Pointing Error**
Berlin Space Technologies / Hyperion Technologies	iADCS-400	1.7	3 reaction wheels, 3 magnetic torquers	<1°
Blue Canyon Technologies	XACT-100	1.813	3 reaction wheels, 3 magnetorquers	0.007°
CubeSpace	CubeADCS 3-Axis Large with Star Tracker	1.15	3 reaction wheels, 3 magnetorquers	<0.5°

Note: Hyperion Technologies is now a part of AAC Clyde Space.

1.5.7. Satellite structure

For a 6U CubeSat's primary structure, the following COTS options are available on the market: Endurosat 6U with a mass of 1 kg [16], ISISPACE 6U with a mass of 0.9 kg [27], GomSpace 6U with a mass of 1.060 kg [28], AAC Clyde Space Zaphod 6U with a mass of 0.674 kg [29] and Spacemind 6U with a mass of 0.754 kg [30]. From these options, AAC Clyde Space Zaphod 6U with a mass of 0.674 kg is selected because it is the option with the least mass.

These days CubeSats with proper radiation shielding are uncommon because typical CubeSat missions only last a few months to a year. This mission however to a NEA has to deal with a harsh radiation environment for up to 5 years. The LUMIO mission can be taken as an example of the shielding thickness. Although it is difficult to directly apply the shielding thickness for the LUMIO mission to a 6U CubeSat mission to a NEA as the radiation environment and the mission parameters differ significantly. However, based on the information provided in Menicucci, Cervone, Speretta, *et al.* [31], some general observations can be made.

The LUMIO mission is planned to operate in a lunar halo orbit, which is a highly elliptical orbit around the Moon, and will be exposed to the harsh radiation environment outside the protection of the Earth's magnetosphere. The preliminary radiation analysis in the paper estimated a TID of 11.7 $\pm$ 1.8 krad for the worst case of 18 months in lunar orbit assuming only 1.5 mm of shielding [31]. The degradation of electrical components caused by the TID of 11.7 krad is noticeable in most electronic components but for space-grade components, not the absolute limit.

A mission to a NEA will have a different radiation environment, depending on the asteroid's distance from the Sun. Additionally, the mission parameters such as the orbit and the duration of the mission will also affect the radiation exposure.

Given the uncertainty, it is difficult to give a definitive answer on the required shielding thickness for a 6U CubeSat on a mission to a NEA based on the LUMIO radiation analysis. It is unlikely that 1.5 mm of shielding will be sufficient to protect the critical COTS components from the radiation environment. Further analysis and testing will be required to fully estimate the potential risk and determine the appropriate shielding thickness.

For the radiation shielding, the side panels of the Zaphod 6U are assumed to be sufficient. However, the front, back, top, and bottom panels lack radiation shielding. It is assumed that the front and back panels of the Zaphod 6U structure are 2 mm thick aluminum (density $2.7\,\mathrm{g\,cm^{-2}}$) and a thickness of 5 mm aluminum shielding is considered sufficient. This assumption comes from the assumption that the LUMIO radiation shielding of 1.5 mm for 18 months can be scaled to 5 mm for 5 years. This adds an additional weight of 0.4878 kg for the front panel ($20 \times 30 \times 3$ cm), 0.4878 kg for the back panel, 0.271 kg for the top panel ($20 \times 10 \times 5$ cm), and 0.271 kg for the bottom panel. Together this means that a mass of 1.5176 kg is added to the satellite structure. However, it is worth noting that the statement is specific to the Zaphod 6U satellite, and the radiation shielding requirements and solutions may vary for other satellites depending on the mission and environment. Also, for future work, a better analysis of the radiation environment must be done.

1.5.8. Summary

To meet the requirements of the autonomous NEA CubeSat mission starting from SSGTO the following subsystems are selected.

Table 1.5: his table provides information on selected preliminary subsystems for the satellite, excluding the propulsion system. The table lists the manufacturer, model, mass, power, and volume of each subsystem. The subsystems include the primary structure, power system, communication system, navigation system, attitude determination and control system, onboard data handling system, payload system, and total mass, power, and volume budget.

Manufacturer	**Model**	**Mass (kg)**	**Power (W)**	**Volume (U or dm^3)**
Primary structure				
AAC Clyde Space	Zaphod 6U	0.674	-	7.705 (outside)
-	Radiation shielding	1.5176	-	(outside)
Power system (power available)				
AAC Clyde Space	NANO-PLUS + OPTIMUS-80	0.818	80Wh	0.672
MMA Design	Hawk 38A-191	1.415	191 at 1AU	0.72 (outside)
Communication system				
AAC Clyde Space	PULSAR-DATA	0.130	10	0.101
Endurosat	Patch 4×4 antenna	0.053	-	$\sim$0.0006
Navigation system				
VisNAV	Camera	0.500	2	1.352
Attitude determination and control system				
AAC Clyde Space	iADCS-400	1.700	5	0.6157
Onboard data handling system				
AAC Clyde Space	CP400.85	0.007	1	0.01
Payload system				
NEAScout	Camera	0.390	3	0.282
Total mass-, power- and volume budget				
-	-	7.2046	Max 20W and 191 W available at 1AU	3.0333 (6U total available)

In the different mission phases which are orbit injection and de-spinning, Earth escape, deep-space cruise, NEA close encounter, scientific acquisition, data transmission, and final disposal, the power budget can be different due to systems being offline.

2

Propulsion system

The selection of a suitable propulsion system is a crucial factor in the success of an interplanetary mission. In this chapter, research question RQ1.1 is addressed by presenting the state-of-the-art propulsion systems for an autonomous 6U CubeSat NEA fly-by mission.

RQ1.1: What state-of-the-art propulsion systems meet the requirements for a near-Earth asteroid fly-by mission?

The mission requires interplanetary travel from a super synchronous geostationary transfer orbit within 5 years. This requires careful consideration of various factors such as performance, reliability, cost, and technology readiness. A selection of the most likely systems to meet the requirements can then be combined with the framework of research question RQ1.2 to answer research question RQ1.1 and eventually answer research question RQ1.

The propulsion system should also be able to desaturate the reaction wheels present in the CubeSat. This can be either done by the same system used for the interplanetary cruise or a separate RCT system. This addresses research question RQ2.1 by presenting the state-of-the-art propulsion systems for the desaturation of reaction wheels for a 6U CubeSat.

RQ2.1: What state-of-the-art propulsion systems meet the requirements for the desaturation of reaction wheels for a CubeSat NEA fly-by mission?

The goal of this chapter is to identify feasible designs for the propulsion system that meet the requirements of the mission and ensure a successful outcome. In the next chapters, the selected designs are simulated such that an option that meets the requirements can be identified.

2.1. Types of propulsion systems

Before a feasible propulsion system for an interplanetary cruise towards a NEA and the propulsion system for desaturation of reaction wheels can be selected the SOTA for micro propulsion systems has to be investigated and evaluated to identify options that meet the requirements. This then answers the research question RQ1.1 and RQ2.1.

The SOTA for micro propulsion systems is a fast-evolving area. New manufacturers regularly join the market. And every year new systems are developed. To limit the scope of the SOTA systems available, only systems that are past their development phase and are still being produced are considered. Furthermore, propellant-less options such as solar sails or electrodynamic tethers are not considered. However, these options could be a valuable alternative for future work. In principle, a propulsion system generates linear momentum by expelling accelerated mass. This is done via thermal acceleration, which increases the enthalpy of the propellant by heating and converting the propellant into a high-velocity jet via a nozzle. A second method is electrostatic acceleration, which derives thrust from the direct acceleration of positively, charged propellant ions or colloids by an electric field. The last method used is electrodynamic acceleration, which accelerates plasma by crossing electric and magnetic fields that induce a Lorentz force.

[32, Chapter 4] gives a good overview of in-space propulsion technologies available for CubeSats. A small adaptation of their classification provides an overview of the different types of principles used to create a propulsion system which can be seen in Table 2.1.

Table 2.1: This table provides a summary of different types of propulsion technology along with their corresponding thrust range and specific impulse range. The information is based on references from NASA [4] and Tummala and Dutta [33]. The propulsion technologies are categorized into two main groups, namely, chemical propulsion technologies and electric propulsion technologies. The table lists various propulsion technologies under each group, such as cold/warm gas, mono-propellant, bi-propellant, solid motors, hybrids, electrothermal, electrospray, gridded ion, Hall effect, pulsed plasma and vacuum arc thrusters, and ambipolar, and their corresponding thrust and specific impulse range.

Technology	Thrust (N)	Specific impulse range (sec)
CHEMICAL PROPULSION TECHNOLOGIES		
Cold / Warm Gas	10 μN – 3 N	30 – 110
Mono-propellant	30 mN - 25 N	160 - 255
Bi-propellant	100 mN - 22 N	160 - 310
Solid Motors	0.3 – 260 N	180 – 280
Hybrids	1 – 10 N	215 – 300
ELECTRIC PROPULSION TECHNOLOGIES		
Electrothermal	2 – 100 mN	50 – 185
Electrospray	10 μN – 1 mN	250 – 5,000
Gridded Ion	0.1 – 15 mN	1,000 – 3,500
Hall Effect	1 – 60 mN	800 – 1,900
Pulsed Plasma and Vacuum Arc Thrusters	1 – 600 μN	500 – 2,400
Ambipolar	0.25 – 10 mN	500 – 1,400

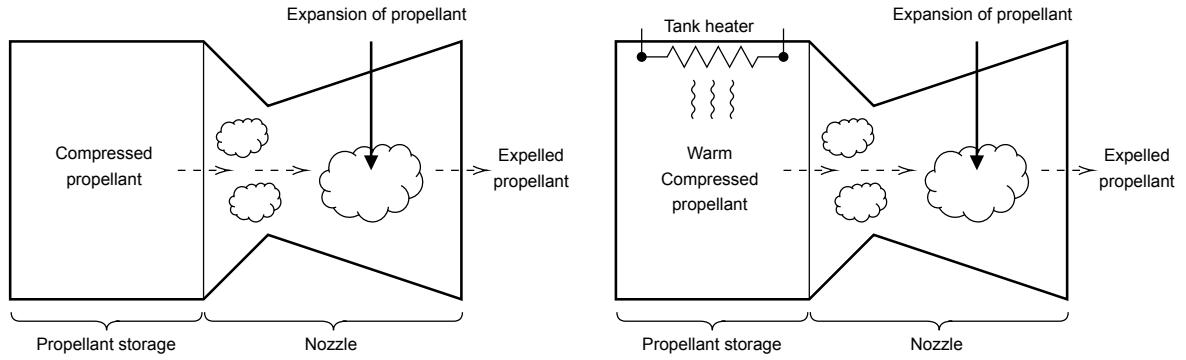

(a) Illustration of a cold gas propulsion system.

(b) Illustration of a warm gas propulsion system.

Figure 2.1: Figure 2.1a and Figure 2.1b show illustrations of cold and warm gas propulsion systems, respectively. Cold gas propulsion systems use an unheated propellant, while warm gas propulsion systems heat the propellant in the tank to achieve higher exhaust velocities. Both use a converging-diverging nozzle to generate thrust

2.1.1. Cold gas propulsion

Cold gas propulsion systems consist of basic components, including a nozzle, valve, propellant storage, and in some cases, a pressure regulator. The thrusters generate thrust through the acceleration of pressurized gas or sublimation of solid propellants, without the need for combustion or high temperatures. The low specific impulse and simple design of cold gas thrusters result in low power requirements and a reduced system mass and volume compared to other propulsion systems. However, the thrust decreases over time as the tank pressure decreases due to propellant consumption. Most systems use liquid and vapor pressure operating pressures, maintaining a constant tank pressure until all liquid propellant is exhausted [33].

2.1.2. Warm gas propulsion

Warm gas propulsion systems operate similarly to cold gas systems but with an added heating element that increases the temperature of the propellant. This results in a higher specific impulse, due to the higher exhaust velocity from the increased temperature. The equation for the limiting velocity (U_L) shows that it is proportional to the square root of the combustion temperature (T_c). The higher initial temperature of the propellant enables a higher limiting velocity and greater conversion of thermal energy into kinetic energy [33].

$$U_L = \sqrt{2 \cdot \frac{\gamma}{\gamma - 1} \cdot \frac{R_A}{M} \cdot T_c} \tag{2.1}$$

where: U_L is the limit exhaust velocity in $\mathrm{m\,s^{-1}}$, γ the specific heat ratio, $R_A = 8.314\,462\,618\,153\,24\,\mathrm{J\,K^{-1}\,mol^{-1}}$ the gas constant, M the molar mass in $\mathrm{kg\,mol^{-1}}$, and T_c the chamber temperature in K.

Table 2.2: This table highlights the advantages and disadvantages of cold and warm gas propulsion systems, which are commonly used due to their low cost, simplicity in design, and ability to achieve precise maneuvers. Non-toxic and inert propellants are typically used in these systems, reducing the risk of contamination to spacecraft surfaces. While they have long cycle lives, their low specific impulse limits their impulse capabilities, with warm gas systems offering only a slight improvement over cold gas systems. Furthermore, the use of pressurized gas can result in a decrease in the thrust profile over time, reducing the system's performance [32].

Technology	Advantage	Disadvantage
Cold/warm gas propulsion	• Precise maneuvers can be achieved due to their low minimum impulse bit. • Non-toxic, inert propellants are commonly used in these systems. • Power requirements are low, with warm gas systems requiring slightly more power to heat the propellant. • Cold/warm gas systems have a long cycle life. • The risk of contaminating spacecraft surfaces from propulsion plumes is reduced.	• They have low specific impulses, which limit their impulse capabilities. Warm gas systems have slightly higher specific impulses than cold gas systems. • If pressurized gas is used, the thrust profile decreases over time, resulting in decreasing performance.

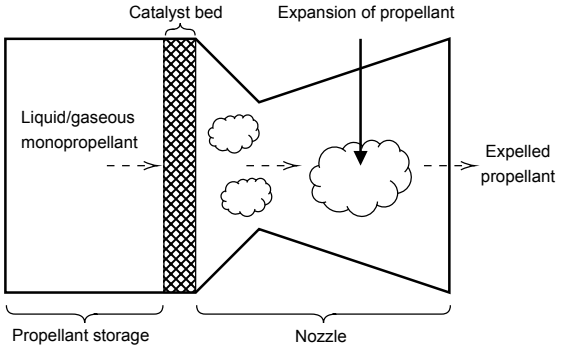

(a) This figure illustrates a mono-propellant propulsion system, which uses a single liquid propellant as both the fuel and the oxidizer. Often a catalyst bed is used to initiate the chemical reaction.

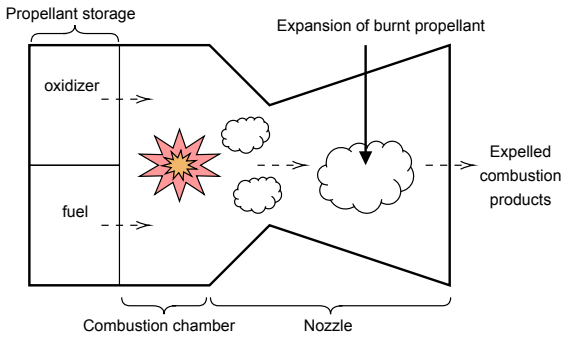

(b) This figure illustrates a bi-propellant propulsion system. The system consists of a fuel and an oxidizer, which are stored in separate tanks before being combined in a combustion chamber to produce hot gases that are expelled through a nozzle to generate thrust. The bi-propellant system typically provides higher thrust and specific impulse compared to mono-propellant systems.

Figure 2.2: This figure illustrates both mono- and bi-propellant propulsion systems, which are types of chemical propulsion technologies used in spacecraft. The figure on the left shows an illustration of a mono-propellant system, while the right half shows an illustration of a bi-propellant system. These systems differ in the type of propellant they use and can have different thrust and specific impulse ranges but are similar in the use of a convergent-divergent nozzle to create thrust from hot gas.

2.1.3. Mono-propellant propulsion

Mono-propellant thrusters rely on the exothermic chemical decomposition of a specific propellant to generate thrust. This process often involves the use of a catalyst bed that initiates the chemical reaction, resulting in the production of hot gas. This gas is then directed through a convergent-divergent nozzle creating thrust in a similar manner to how warm and cold gas systems function. The convergent-divergent nozzle accelerates the hot gas to supersonic velocities such that the divergent part of the nozzle accelerates the hot gas again. This method of propulsion is simple, efficient, and widely used in small spacecraft and satellites. Currently, the top mono-propellant systems still cannot compete with Bi-propellant systems in terms of specific impulse but mono-propellant systems make up for it by not producing as much heat as bi-propellant systems [32].

2.1.4. Bi-propellant propulsion

Bi-propellant systems utilize an exothermic chemical reaction or combustion of a fuel and oxidizer to generate thrust. These systems are composed of a variety of components, including a fuel, oxidizer, combustion chamber, igniter, convergent-divergent nozzle, and propellant storage systems. While bi-propellant systems are known to reach high operating temperatures, which can be a challenge for certain types of satellites, they offer a high specific impulse range that exceeds that of mono-propellant and cold/warm gas systems. This higher specific impulse is achieved through the use of higher chamber temperatures and/or pressures than those used in mono-propellant or cold/warm gas systems [32].

Table 2.3: Advantages and disadvantages of using bi-propellant systems in CubeSat propulsion [32]. The table summarizes the advantages, such as high thrust capability and reliable performance, and disadvantages, such as design complexity and challenges in thrust control, of using bi-propellant propulsion systems.

Technology	Advantage	Disadvantage
Bi-propellant propulsion	• Bi-propellant systems are relatively low mass and low volume for their high thrust capabilities. • The high thrust capability of bi-propellant systems means that more propellant can be used under optimal circumstances such as near the perigee. • Bi-propellant systems are reliable and widely used in spacecraft. • Bi-propellant systems have a higher specific impulse than other chemical micro propulsion systems. • Propulsion plumes are less likely to contaminate the spacecraft surfaces.	• Bi-propellant systems tend to be more intricate in design compared to mono-propellant systems. • Bi-propellant systems are not typically suited for precise maneuvers or low minimum impulse bits maneuvers. • The control of thrust in bi-propellant systems is more challenging than in mono-propellant systems. • Bi-propellant systems produce more heat than cold gas, warm gas, or mono-propellant systems because they make use of a composition process. This heat can pose a risk to sensitive spacecraft components, requiring careful thermal management or shorter burn times per burn cycle.

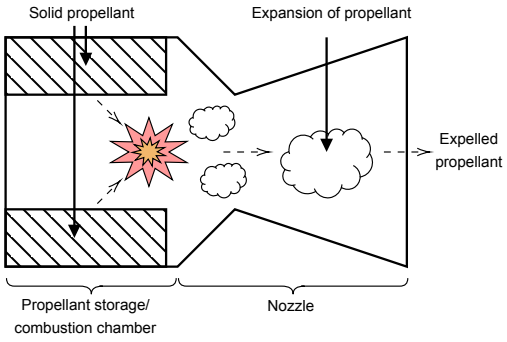

(a) Figure of a solid propellant propulsion system, including the solid propellant grain, nozzle, and combustion chamber.

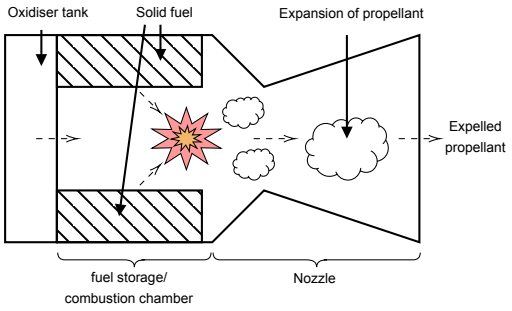

(b) Figure of a hybrid propellant propulsion system, including the oxidizer tank, fuel grain, combustion chamber, and nozzle.

Figure 2.3: Figures of solid and hybrid propulsion systems.

2.1.5. Solid motor propulsion

Solid propulsion systems, which consist of a pre-mixed oxidizer and fuel stored in the combustion chamber, offer a promising option for micro-propulsion systems designed for CubeSats. The compact size and simplicity of these systems make them an attractive option for smaller satellite platforms. With a relatively high specific thrust output compared to mono-propellant or cold/hot gas systems, solid propulsion systems can provide CubeSats with greater propulsion capabilities, enabling a wider range of mission options [32].

However, it's important to note that solid propulsion systems can only be started once, which limits their flexibility in mission planning. Additionally, the high operating temperature of these systems can pose a potential risk to CubeSat electronics, requiring careful thermal management. And finally, solid propulsion systems are not a viable option for precise or small maneuvers since these systems have high minimum impulse bits and a thrust offset cannot be mitigated by restarting the propulsion system.

2.1.6. Hybrid propulsion

Hybrid propulsion systems, which combine solid fuel grains with a gaseous oxidizer, offer a promising option for micro-propulsion systems designed for CubeSats. These systems are typically ignited by injecting the oxidizer into the combustion chamber, providing greater control over the engine compared to solid propulsion systems. By regulating the oxidizer flow, hybrid systems can be stopped and restarted, offering greater flexibility in mission planning than solid motor propulsion systems [32].

One of the key advantages of hybrid propulsion systems for CubeSats is their safety with respect to solid motors. Unlike solid propulsion systems, where the fuel and oxidizer are mixed together, hybrid systems store the fuel and oxidizer separately, making them safer to handle and store. This is particularly important for CubeSats, which often have limited space for safety measures.

However, it's important to note that the performance of hybrid propulsion systems, although higher than mono-propellant or cold-/warm gas systems, may not be as high as solid propulsion systems. Additionally, controlling the regression rate and slag buildup can be more challenging for hybrid systems.

Table 2.4: Advantages and disadvantages of using solid motor propulsion systems in CubeSat propulsion [32]. The table summarizes the advantages, such as high thrust capability and reliable performance, and disadvantages, such as design complexity and challenges in thrust control, of using solid motor propulsion systems.

Technology	Advantage	Disadvantage
Solid motor propulsion	• Solid propulsion systems offer short impulses of high delta-v, which are beneficial for certain mission scenarios. For example, firing at the perigee increases propellant efficiency. • The solid state of the propellant allows for high densities, making solid propulsion systems relatively low volume and compact. • Propulsion plumes from solid motors are less likely to contaminate spacecraft surfaces compared to other propulsion systems.	• Solid propulsion systems are typically non-restartable or have a limited number of restarts, which limits their flexibility in mission planning. • Solid propulsion systems often have high minimum impulse bits, making them unsuitable for small maneuvers. • The high operating temperatures of solid propulsion systems can pose a risk to sensitive spacecraft components, requiring careful thermal management. • Solid propulsion systems have a limited ability to finely control the thrust output of the engine, making them less suitable for precise maneuvers. • Solid propulsion systems present a safety risk due to the mixing of fuel and oxidizer, which can lead to potentially hazardous situations.

Table 2.5: Advantages and disadvantages of using hybrid propulsion systems in CubeSat propulsion [32]. The table summarizes the advantages, such as high thrust capability and reliable performance, and disadvantages, such as design complexity and challenges in thrust control, of using hybrid propulsion systems.

Technology	Advantage	Disadvantage
Hybrid propulsion	• Hybrid propulsion systems can be restarted by controlling the oxidizer flow, providing flexibility in mission planning. • Hybrid propulsion systems can be designed to have adjustable thrust levels, allowing for precise control during maneuvers. • Hybrid propulsion systems can provide short impulses of high delta-v. • Hybrid propulsion systems are safer to handle with respect to solid propulsion systems, which makes these systems similar in safety with respect to other systems. • Hybrid propulsion systems are relatively low volume and low mass for their high thrust capabilities because the solid state of the fuel allows high storage densities. • Hybrid propulsion systems have a high specific impulse compared to other chemical propulsion systems. • Propulsion plumes are less likely to contaminate the spacecraft surfaces.	• Hybrid propulsion systems can have issues with combustion instability and sloshing of the liquid oxidizer, resulting in reduced performance and potential failure. • The regression rate control tends to be a problem, so the thrust can be unpredictable. • The high operating temperatures of hybrid propulsion systems can pose a risk to sensitive spacecraft components, requiring careful thermal management.

2.1.7. Electrothermal propulsion

An Electrothermal propulsion system is a type of advanced hot gas propulsion system that utilizes electrical energy to heat the propellant inside the thruster, leading to a higher enthalpy and, therefore, a more significant increase in the kinetic energy of the propellant. The electric heating element is designed to operate at high temperatures and can be powered by various energy sources (NASA [32, p. 64-67]).

It is worth noting that electrothermal propulsion systems differ from warm/hot gas systems in that the heating element is located within the thruster head, rather than in the propellant tank or plenum tank. Therefore, if the propellant is only preheated in the tank or a plenum tank, it cannot be considered an electrothermal propulsion system.

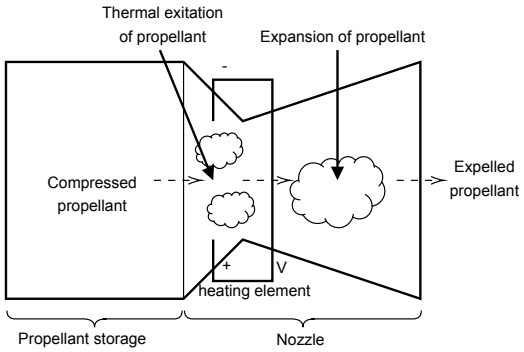

Figure 2.4: This figure illustrates the concept of an Electrothermal Resistojet Propulsion System, where electrical energy is converted into heat by a resistor. The resulting thermal energy is used to heat a propellant, creating a high-velocity exhaust that generates thrust.

Table 2.6: Advantages and disadvantages of electrothermal propulsion systems according to NASA [32]. The table lists the advantages of electrothermal propulsion such as neutral charge plume and disadvantages such as low power efficiency and thermal soak back.

Technology	Advantage	Disadvantage
Electrothermal propulsion	• Electrothermal propulsion systems are simple to operate. • Electrothermal propulsion systems are reliable, as they have fewer moving parts than other types of propulsion systems.	• Electrothermal propulsion systems require high-temperature materials, which can be challenging to find or produce, and can increase the system's mass. • Electrothermal propulsion systems introduce a non-negligible thermal load to the spacecraft that can pose a risk to sensitive spacecraft components, requiring careful thermal management. • Electrothermal electrode-less thrusters, which are becoming more popular due to their simplicity and reliability, may require a dedicated power subsystem to meet their specific power requirements. This then increases the system's mass.

2.1.8. Electrospray propulsion

Electrospray propulsion systems generate thrust by electrostatically extracting and accelerating ions or droplets from a low-vapor-pressure, electrically conductive, liquid propellant. (NASA [32, p. 67-70]) Generally, two types can be classified: Ionic-Liquid Electrosprays which use salts in the liquid phase, and Field Emission Electric Propulsion which uses low-melting-point metals. Electrospray propulsion systems can reach high specific impulses, but the system generally requires high voltage in the kilovolts range.

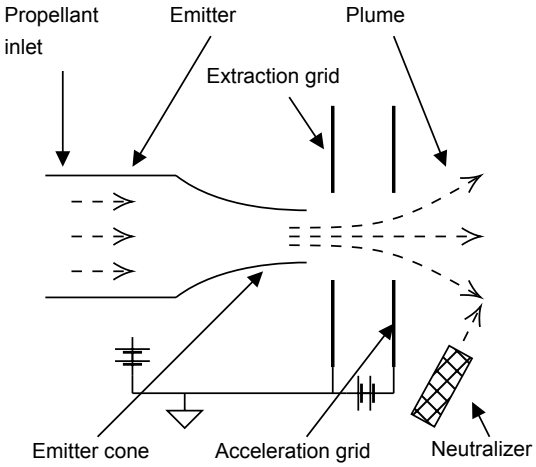

Figure 2.5: An illustration of an electrospray propulsion system in which the liquid propellant is electrically conductive and accelerated by extracting and accelerating ions or droplets through electrostatic forces from the low-vapor-pressure propellant.

Table 2.7: Comparison of advantages and disadvantages of electrospray propulsion systems for space applications [32].

Technology	Advantage	Disadvantage
Electrospray propulsion	• The magnitude of the thrust can be precisely controlled. • The minimum impulse bit of a single burst can be very low for these systems.	• Electrospray systems may contaminate other systems or surfaces on the spacecraft or even cause electrical shorting because the plumes are electrically charged. • Electrospray systems are sensitive to foreign objects. These objects could potentially form an electric bridge between the extraction and acceleration grid which could cause an electric short. • The system may have unexpected end-of-life behavior such as shorting. • The performance over time still has to be verified in a space or deep-space environment.

2.1.9. Gridded-ion propulsion

Gridded-ion propulsion systems ionize gaseous propellant via a plasma discharge, and the resultant ions are subsequently accelerated via electrostatic grids. The positively charged accelerated ions are then neutralized by a neutralizing cathode to prevent charge build-up of the spacecraft which can cause a static discharge (NASA [32, p. 70-73]). This technology can generally be classified into the following types according to the type of plasma discharge employed: Direct-Current Discharge and Radio-Frequency Discharge.

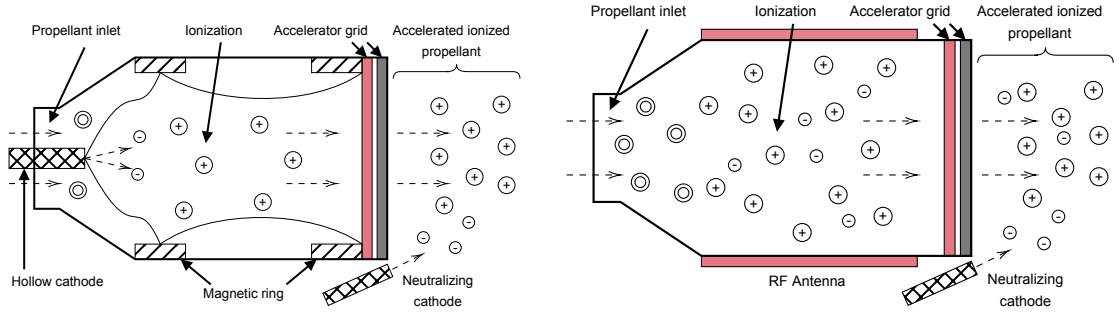

(a) An illustration of a direct-current discharge gridded-ion thruster.

(b) An illustration of a radio-frequency discharge gridded-ion thruster.

Figure 2.6: This figure shows two types of gridded-ion propulsion systems. The first type, depicted in (a), is a direct-current discharge gridded-ion thruster. In this system, the cathode and magnetic rings ionize the propellant, which is then accelerated by the positively- (red) and negatively charged (black) accelerator grids. The second type, shown in (b), is a radio-frequency discharge gridded-ion thruster. Here, the RF antenna ionizes the propellant, which is then accelerated by the positive (red) and negative (black) accelerator grids.

Table 2.8: This table summarizes the advantages and disadvantages of gridded-ion propulsion systems, as reported by NASA [32]. The table highlights that gridded-ion thrusters have a long history of successful use, making their performance predictions more reliable. However, these systems can contaminate other spacecraft components, are sensitive to foreign objects, can experience misalignments, and may interfere with electronic and communication systems.

Technology	Advantage	Disadvantage
Gridded-ion propulsion	• Gridded-ion thrusters have more flight heritage than other technologies which makes their performance predictions more reliable.	• Gridded-ion systems may contaminate other systems or surfaces on the spacecraft or even cause electrical shorting because the plumes are electrically charged. • Gridded-ion systems are sensitive to foreign objects. These objects could potentially form an electric bridge in the grid which could cause an electric short. • Miss alignment of the different components in the thruster could cause torque. • Gridded-ion systems could interfere with electronic systems and communication systems.

2.1.10. Hall-effect propulsion

Hall-effect propulsion systems are a form of ion propulsion, ionizing and electrostatically accelerating the propellant as can be seen in Figure 2.7. In Goebel and Katz [34] the Hall effect thrusters working principle is described as:

> *'The Hall effect thruster is a type of electrostatic thruster that utilizes a cross-field discharge described by the Hall effect to generate a plasma. An electric field established perpendicular to an applied magnetic field electrostatically accelerates the ions in the plasma to high exhaust velocities, while the transverse magnetic field inhibits electron motion that would tend to short out the electric field.'*

This basically means that the ions are accelerated due to the Hall effect using only magnetic rings instead of accelerator grids which are used in the gridded-ion thruster.

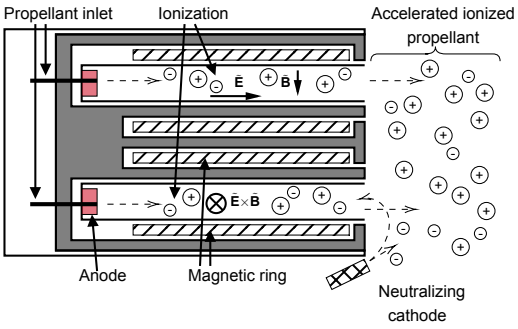

Figure 2.7: This figure shows an illustration of the cross-section of a Hall effect propulsion system. The system utilizes an anode and cathode to ionize the propellant, which is then accelerated by the Hall effect.

Table 2.9: This table displays the advantages and disadvantages of Hall effect propulsion systems as outlined by NASA [32]. Hall effect systems are power efficient and have a reliable flight heritage, but they may cause contamination and produce torque due to the internal magnetic field.

Technology	Advantage	Disadvantage
Hall effect propulsion	• Hall effect thrusters are the most flown systems and thus have the most flight heritage compared to other technologies which make their performance predictions more reliable. • Hall effect systems are power efficient which means that the electrical input power is more efficiently converted to jet power than other electrical propulsion systems.	• Hall effect systems may contaminate other systems or surfaces on the spacecraft or even cause electrical shorting because the plumes are electrically charged. • Hall effect thrusters naturally create a 'swirl' torque due to the interaction between the accelerated ions and the internal magnetic field of the thruster.

2.1.11. Pulsed plasma vacuum arc propulsion

In Goebel and Katz [34] the pulsed plasma propulsion system's working principle is defined as:

> *'A pulsed plasma thruster (PPT) is an electromagnetic thruster that utilizes a pulsed discharge to ionize a fraction of a solid propellant ablated into a plasma arc, and electromagnetic effects in the pulse to accelerate the ions to high exit velocity. The pulse repetition rate is used to determine the thrust level.'*

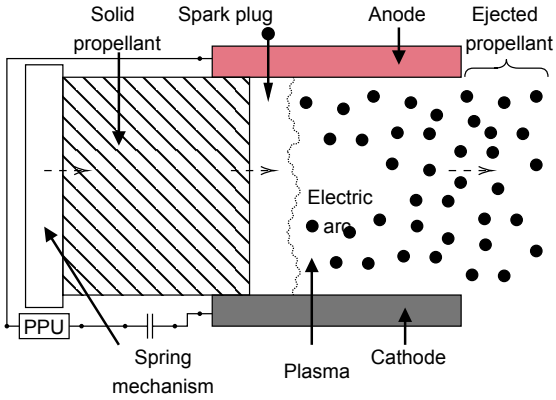

Figure 2.8: An illustration of a pulsed plasma propulsion system. Periodically an electric arc ablates a part of the solid propellant which reaches a plasma state. This plasma is then accelerated by an anode and cathode. A spring system pushes new propellant into the electric arc which repeats the sequence creating a pulsed plasma propulsion system.

The working principle of a pulsed plasma is similar to that of a vacuum arc thruster. The only key difference is that the pulsed plasma propulsion system uses an insulator as a propellant and the vacuum arc thruster uses a metal cathode as a propellant which it consumes.

Table 2.10: Advantages and disadvantages of pulsed plasma vacuum arc propulsion systems according to NASA [32]. The table highlights the advantages and disadvantages of the technology, including low power budget requirements, low impulse bits, simple and compact design as advantages, and low power efficiency and contamination of satellite surfaces as disadvantages.

Technology	Advantage	Disadvantage
Pulsed plasma vacuum arc propulsion	• Pulsed Plasma vacuum arc propulsion works in pulsed modes with capacitors, which means that systems with a tight power budget can use these propulsion systems. • These systems can reach very low minimum impulse bits. • The design of pulsed plasma vacuum arc thrusters can be simple and compact due to the solid propellant.	• Pulsed plasma vacuum arc systems have low power efficiencies which means that they generate a relatively high amount of waste heat that flows back into the satellite. • The propulsion plumes of pulsed plasma or vacuum arc systems contaminate the satellite's surfaces such as the solar panels or sensors.

2.1.12. Ambipolar propulsion

Ambipolar propulsion systems are based on the principle of ambipolar diffusion of a plasma formed by either radiofrequency excitation or DC breakdown. In an ambipolar thruster, a gas is effectively ionized to a plasma which then accelerates due to ambipolar diffusion to high speeds. In most systems, this plasma is further accelerated by a magnetic field commonly created by a magnetic nozzle. The benefit of this system over other systems is that the plasma is 'neutral' which means that the expelled propellant does not need a neutralizer to mitigate charging effects in the spacecraft (NASA [32, p. 79-80]).

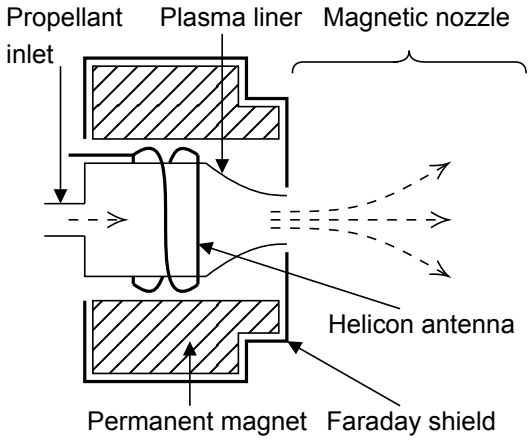

Figure 2.9: An illustration of an ambipolar thruster. The propellant is turned into plasma using either radio frequency excitation or DC breakdown. This plasma is then accelerated by a permanent magnet and magnetic nozzle.

Table 2.11: Advantages and disadvantages of ambipolar propulsion systems according to NASA [32]. The table lists the advantages of ambipolar propulsion such as neutral charge plume and disadvantages such as low power efficiency and thermal soak back.

Technology	Advantage	Disadvantage
Ambipolar propulsion	• The plume of these systems is neutral in charge which means there are no concerns for charge build-up in the spacecraft due to the propulsion system. • Hall effect systems are power efficient which means that the electrical input power is more efficiently converted to jet power than other electrical propulsion systems.	• Ambipolar systems have low power efficiencies. • Ambipolar systems have a relatively high thermal soak back, or waste heat flowing back into the spacecraft. • Propulsion plumes can contaminate the spacecraft surfaces, but less than other systems due to their neutral charge.

2.2. Interplanetary propulsion system

The requirements for the primary propulsion system for interplanetary travel as described in the introduction are:

MR-SC-1: The satellite shall be able to fly by a near-Earth asteroid at a closest approach distance of 10,000 km within 5 years.

MR-SC-2: The satellite shall be deployed in a super synchronous geostationary transfer orbit.

MR-SC-4: The satellite shall have a maximum volume of 6U.

MR-SC-5: The satellite shall have a maximum mass of 12 kg.

And the system-specific requirement for the AOCS also must be fulfilled using the primary propulsion system:

MR-AOCS-1: The attitude and orbital control system shall be able to maneuver the spacecraft to a distance of 10,000 km at the nearest point of approach to the near-Earth asteroid within 5 years.

Optional, the primary control system can be used to desaturate the reaction wheels of the CubeSat, but this can also be done using a secondary RCT propulsion system.

Next to the mission and system requirements, ESA [35] fills in the conditions under which the requirements MR-SC-1 and MR-AOCS-1 can be verified if with a simulation can be proven that under the following extra conditions the spacecraft can reach the target asteroid:

1. The equipment dry mass shall have a 5% mass margin.
2. The propulsion system dry mass shall have a 10% mass margin (because it requires adjustments). In the case of major modifications, the mass margin is 20%.
3. The spacecraft's total dry mass shall have a 20% mass margin (on top of the equipment/propulsion system mass margin).
4. The propellant storage shall have a minimum tank ullage volume of 10% (only applies to liquid or gas propellants).
5. A 2% propellant residual shall be added to the calculated required propellant.

This chapter only makes a pre-selection based on the performance characteristics of the different available propulsion systems. The actual verification of the requirements is done in other chapters.

In the past, missions to NEAs have utilized either low-thrust, high-specific impulse electric propulsion or high-thrust, chemical propulsion technologies to maneuver toward their targets. While high-specific impulse systems are fuel-efficient and can reach NEAs, their low-thrust nature means that they often require years to reach their destination. The propulsion system has to be fired over long periods of time to be effective. Since the mission duration is not unlimited these systems have to be used in sub-optimal regions to maneuver to the target asteroid in time. On the other hand, high-thrust systems that are not inherently fuel-efficient can fire more of their propellant at optimal positions, such as at perigee, resulting in a trajectory that requires less delta-V and thus requires less propellant.

To address these challenges, modern NEA missions aim to combine the benefits of both types of propulsion technologies. However, for CubeSats, the volume and propulsion system dry mass of two propulsion systems that both perform the interplanetary trajectory can not be justified with the decrease in mission duration. Therefore, for this thesis, dual propulsion systems are not considered for interplanetary travel.

2.2.1. High-specific impulse propulsion systems

The first propulsion system branch that is assessed is the low-thrust, high-specific impulse propulsion system branch. This branch consists of electrospray, gridded-ion, Hall effect, pulsed plasma & vacuum arc, and ambipolar propulsion systems. In order to answer research question RQ1.1, the selected propulsion system must meet the requirements of an interplanetary trajectory to a NEA. In an ideal scenario, the propulsion system should have a high specific impulse, high thrust, low power consumption, low mass, and small volume. A high specific impulse is necessary to maneuver to a distant target like a NEA, but sufficient thrust is required to maneuver to the destination within the 5-year constraint. The minimum amount of thrust and specific impulse required for the fly-by mission can only be determined through simulation for low-thrust systems.

As shown in Figure 2.10, there is a noticeable difference between the various propulsion types in terms of thrust and specific impulse. Ambipolar and Hall-effect systems tend to have a higher thrust, but a lower specific impulse. On the other hand, pulsed plasma vacuum arc and electrospray systems have a high specific impulse, but a lower thrust. Gridded-ion systems are more balanced, with a higher emphasis on a higher specific impulse and a lower thrust.

Next, The comparison of the required power for the maximum specific impulse at full thrust for different propulsion systems is shown in Figure 2.11. Ambipolar and Hall-effect systems are observed to have a higher electrical power requirement but relatively lower specific impulse compared to Pulsed plasma vacuum arc, electrospray, and gridded-ion systems. This observation can be explained in combination with the thrust-specific impulse comparison shown in Figure 2.10, where it is noted that ambipolar and Hall-effect systems generally have a higher thrust than other system types. Also, Figure 2.12 shows that Hall-effect systems offer more thrust per unit of power but fall short in terms of specific impulse. Electrospray, pulsed plasma vacuum arc, and gridded-ion systems can be considered for higher specific impulse ranges, but they come with a lower thrust-to-power ratio.

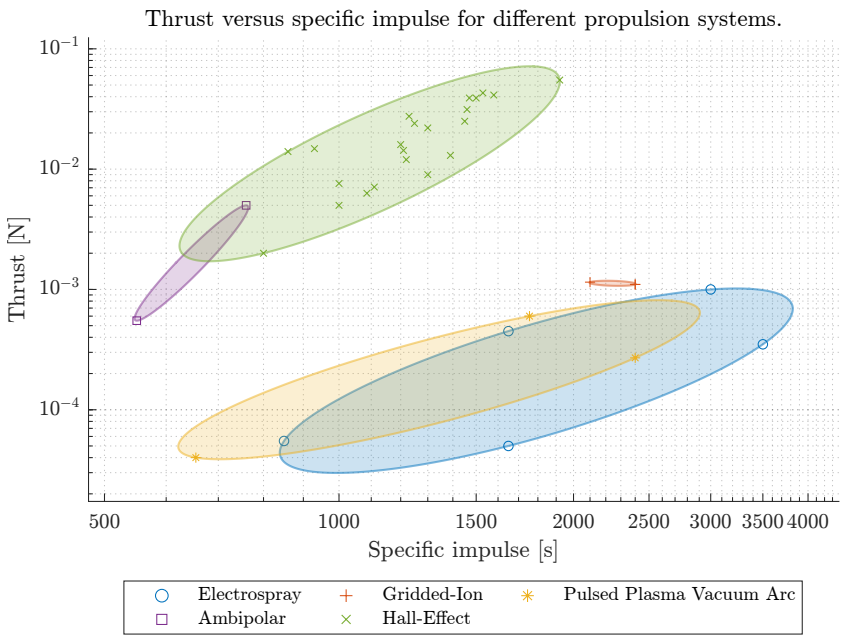

Figure 2.10: In this figure the relationship between specific impulse and maximum thrust for various types of propulsion systems is depicted [4]. This information is essential in selecting the appropriate propulsion system for interplanetary missions, where a balance between high specific impulse and sufficient thrust is necessary to reach the destination within the given constraints. Ambipolar and Hall-effect systems tend to have higher thrust, but a lower specific impulse. In contrast, pulsed plasma vacuum arc and electrospray systems have a high specific impulse, but a lower thrust. Gridded-ion systems are more balanced, with a higher emphasis on a higher specific impulse and a lower thrust.

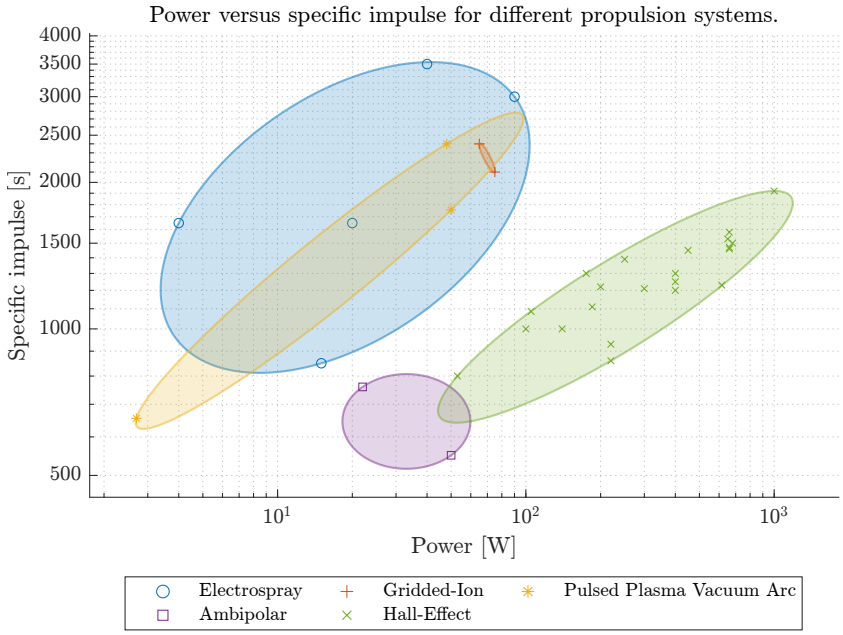

Figure 2.11: This figure presents a comparison of the required power for achieving maximum specific impulse at full thrust among various propulsion systems [4]. Ambipolar and Hall-effect systems require a higher electrical power input but offer relatively lower specific impulses when compared to Pulsed Plasma Vacuum Arc, Electrospray, and Gridded-ion systems. The higher power requirement of Ambipolar and Hall-effect systems is in agreement with their higher thrust values as seen in the thrust-specific impulse relation presented in Figure 2.10.

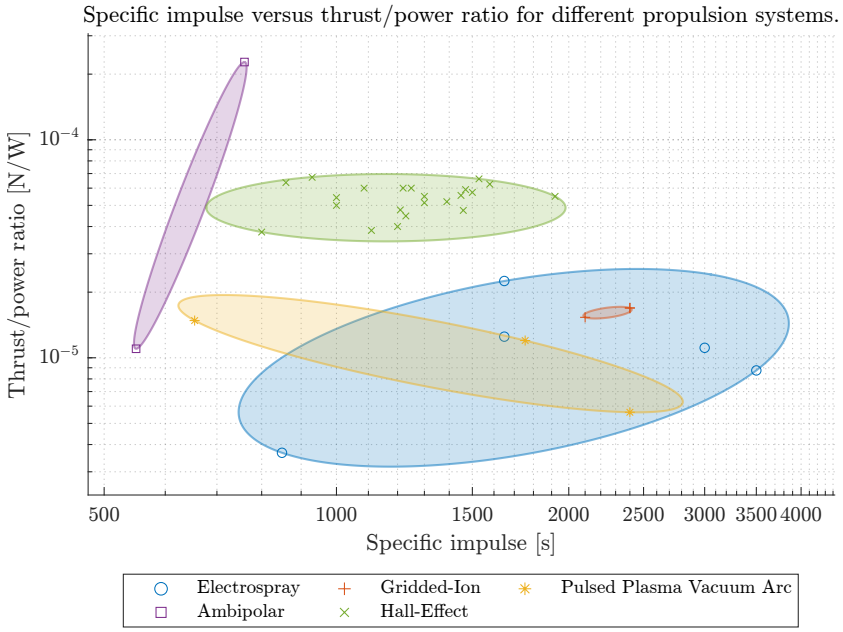

Figure 2.12: This figure shows the relation between the specific impulse versus the thrust-to-power ratio for different propulsion system types [4]. Hall-effect systems are observed to offer more thrust per unit of power but have a lower specific impulse compared to other systems. Electrospray, pulsed plasma vacuum arc, and gridded-ion systems are suitable for higher specific impulse ranges, but they come with a lower thrust-to-power ratio. These findings provide critical insights into the trade-offs involved in selecting an optimal propulsion system for a mission.

Evaluating every potential propulsion system with a simulation is a very time-consuming process and can be avoided by eliminating systems that are unlikely to meet the requirements of a fly-by mission to a NEA. To determine which systems are unsuitable, those with relatively low thrust and low specific impulse are excluded. Also, systems that have a relatively high thrust but a relatively low specific impulse will be excluded because they would either not be able to maneuver to the NEA or fly by the NEA within 5 years. Additionally, it is assumed that systems that require more power than is available on the satellite will have their maximum thrust reduced in proportion to the ratio of available power to the required power. This 'corrected thrust', $F_{T,corr}$, is expressed as:

$$F_{T,corr} = \begin{cases} F_T, & \text{if } 1 \leq \frac{P_{prop}}{P_{in}} \\ F_T \frac{P_{prop}}{P_{in}}, & \text{if } 1 > \frac{P_{prop}}{P_{in}} > 0 \\ 0, & \text{otherwise} \end{cases} \tag{2.2}$$

where F_T is the maximum thrust, P_{prop} the required propulsion system power, and P_{in} the available satellite power which is assumed to be 191 W. This then results in the specific impulse versus corrected thrust that can be seen in Figure 2.13.

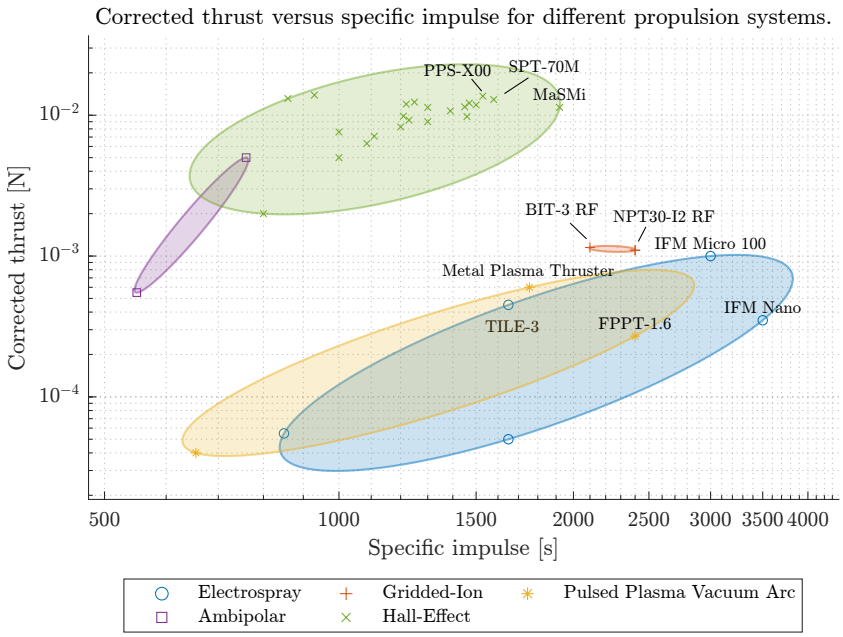

Figure 2.13: The figure shows the comparison of specific impulse versus the corrected thrust for different types of propulsion systems [4]. The potentially feasible propulsion systems in the upper right side of the figure are labeled while low thrust and/or low specific impulse systems are excluded. A low thrust system would result in a mission duration exceeding the maximum requirement, while a low specific impulse system would require an excessive amount of propellant mass to reach the target asteroid.

The nine low-thrust high-specific impulse propulsion systems in Table 2.12 were selected from Figure 2.13 to be simulated and evaluated for their suitability for a NEA fly-by mission. This selection was made because these systems fall in the upper-right area of the corrected thrust versus specific impulse graph, and only a limited number of systems were chosen to reduce the number of simulations. The systems within this range are believed to be most promising of reaching a NEA from SSGTO within 5 years. Accion Systems' TILE-3 was excluded due to its low specific impulse and very low thrust compared to other systems and it did not provide a competitive advantage in terms of system mass or volume.

Table 2.12: This table presents the characteristics of selected low-thrust primary propulsion systems for a near-Earth asteroid fly-by mission, including the manufacturer, model, type of propellant, thrust in mN, specific impulse in seconds (Isp), wet and dry mass in kg, volume in U, and power in W. The propulsion systems are categorized as electrospray (ES), gridded-ion (GI), pulsed plasma vacuum arc (PPVA), and Hall effect (HE) thrusters [4]. The densities of the propellants are not included in the table but as a reference, these are around $7\,\mathrm{kg\,L^{-1}}$ for liquid Indium (In), $5\,\mathrm{kg\,L^{-1}}$ for solid Iodine (I2), $10\,\mathrm{kg\,L^{-1}}$ for solid Molybdenum (Mo), $2\,\mathrm{kg\,L^{-1}}$ for solid Teflon (PTFE), and $3\,\mathrm{kg\,L^{-1}}$ for liquid Xenon (Xe).

Type	Mfr.	Model	Prop.	Thrust (mN)	Isp (s)	Wet mass (kg)	Dry mass (kg)	Volume (U)	Power (W)
ES	Enpulsion Austria	IFM Nano	In	0.350	3500	0.900	0.680	0.830	40
ES	Enpulsion Austria	IFM Micro 100	In	1	3000	3.90	2.6	2.234	90

The table continues on the next page.

Type	Mfr.	Model	Prop.	Thrust (mN)	Isp (s)	Wet mass (kg)	Dry mass (kg)	Volume (U)	Power (W)
GI	Busek USA	BIT-3 RF	I2	1.15	2100	2.78	1.28	1.616	75
GI	ThrustMe France	NPT30-I2 RF	I2	1.10	2400	1.70	1.297	1.00	65
PPVA	Alameda Applied Sciences Corp. USA	Metal Plasma Thruster	Mo	0.600	1756	0.850	0.618	0.700	50
PPVA	CU Aerospace USA	FPPT-1.6	PTFE Fiber	0.270	2400	2.80	1.921	1.60	48
HE	EDB Fakel Russia	SPT-70M	Xe	41.3	1580	NaN	2.0	1.453	660
HE	JPL USA	MaSMi	Xe	55	1920	NaN	3.40	1.70	1000
HE	Safran France	PPS-X00	Xe	43	1530	NaN	3.2	4.2	650

2.2.2. High-thrust propulsion systems

The second propulsion system branch that is assessed is the high-thrust propulsion system branch. This branch consists of cold/warm gas, mono-propellant, bi-propellant, solid motors, hybrid, and electrothermal propulsion systems. In order to answer research question RQ1.1, the selected propulsion system must meet the requirements of an interplanetary trajectory to a NEA. High-thrust propulsion systems are not directly linked to the efficient use of propellant since their specific impulse are often not as high as high-specific impulse propulsion systems. However, due to their high thrust, more propellant mass can be used near optimal regions such as the perigee of the SSGTO. This leads to a decrease in the delta-V requirement for these trajectories to first of all escape an orbit around the Earth and secondly fly by a NEA. The delta-V required for an excess escape velocity V_{∞_e} to fly by a NEA using an impulse shot can be expressed as [36]:

$$\Delta V_0 = \sqrt{V_{esc_0}^2 + V_{\infty_e}^2} - V_{c_0} \tag{2.3}$$

where V_{esc_0} is the escape velocity at a given orbital radius r_0 and V_{c_0} is the initial orbital velocity. For an elliptical starting orbit this equation can be rewritten to:

$$\Delta V_0 = \sqrt{\frac{2\mu}{r_0} + V_{\infty_e}^2} - \sqrt{\frac{2\mu}{r_0} - \frac{\mu}{a}} \tag{2.4}$$

Upon examining this equation, it becomes evident that the escape velocity and orbital velocity both increase proportionally with the square root of the inverse of the orbital radius ($\sqrt{\frac{1}{r_0}}$). As a result, a spacecraft starting at a lower altitude requires less initial velocity change (ΔV_0) to achieve the necessary escape velocity and orbital velocity than one starting at a higher altitude. A velocity change near the

perigee consequently results in greater orbital energy, eventually leading to a reduction in the required ΔV_0 to fly by a NEA.

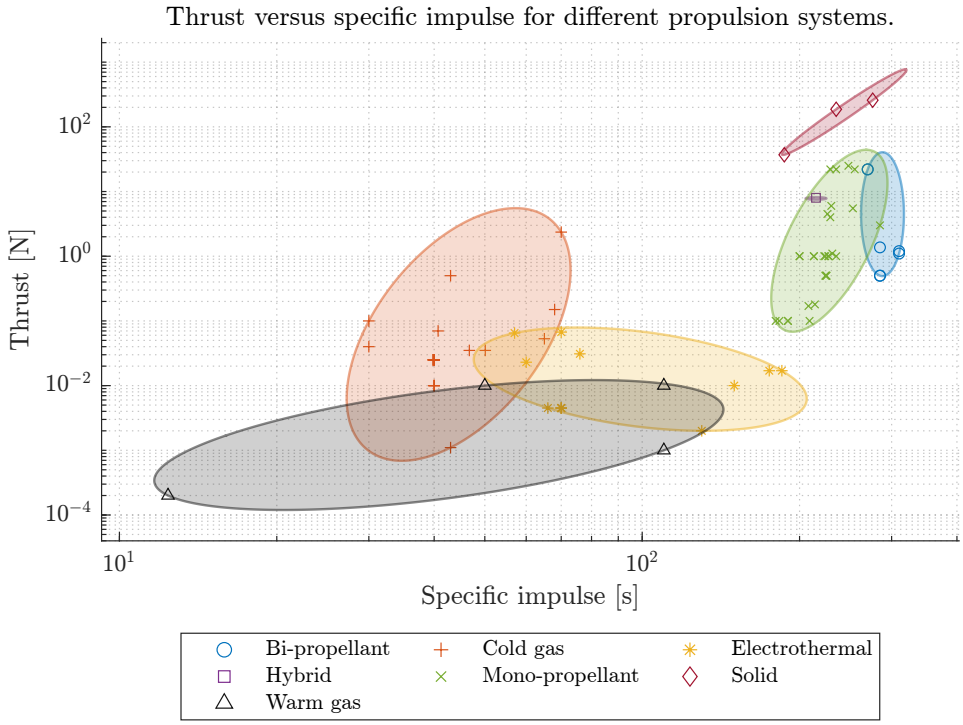

Figure 2.14: In this figure, the relationship between specific impulse and maximum thrust for various types of high-thrust propulsion systems is shown [4]. This information is essential in selecting the appropriate propulsion system for interplanetary missions, where a balance between high-thrust and sufficient specific impulse is necessary to maneuver the spacecraft to the target asteroid within the given constraints. It can be seen that solid propulsion systems have both a high thrust and high specific impulse with respect to the other high-thrust systems. Bi-propellant propulsion systems show thrust properties two magnitudes lower than solid propulsion systems but make up for it with the highest specific impulses of all the high-thrust systems.

From Figure 2.14 it can be seen that solid propulsion systems have both a high thrust and high specific impulse with respect to the other high-thrust systems. Bi-propellant propulsion systems show thrust properties two magnitudes lower than solid propulsion systems but make up for it with the highest specific impulses of all the high-thrust systems. Mono-propellant systems and hybrid propulsion systems match bi-propellant systems in terms of thrust and are in the same specific impulse region as solid propulsion systems. Cold/warm gas and electrothermal propulsion systems are not competitive in terms of specific impulse and thrust compared to the other high-thrust propulsion systems.

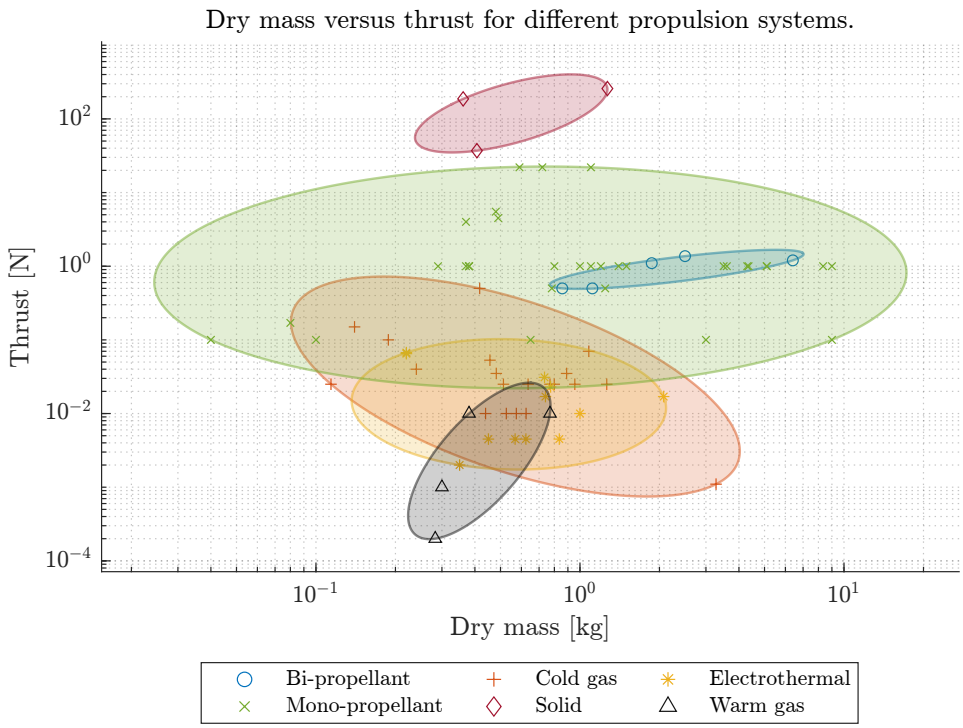

Figure 2.15: In this figure, the relationship between system dry mass and maximum thrust for various types of high-thrust propulsion systems is shown [4]. This information is essential in selecting the appropriate propulsion system for interplanetary missions because the system's dry mass leads to less propellant mass available for the fly-by maneuver while a higher thrust enables more efficient trajectories that require less delta-V. It can be seen that solid propulsion systems have both a high thrust and dry mass in the range of 1 kg. Mono-propellant propulsion systems have system dry mass ranging from less than 100 grams up to 10 kg. Some mono-propellant systems are however thruster head-only systems which naturally leads to a lower dry mass. Bi-propellant systems range from 1 to 10 kg.

From Figure 2.15 it can be seen that solid propulsion systems have both a high thrust and dry mass in the range of 1 kg. Mono-propellant propulsion systems have system dry mass ranging from less than 100 grams up to 10 kg. Some mono-propellant systems are however thruster head-only systems which naturally leads to a lower dry mass. Bi-propellant systems range from 1 to 10 kg.

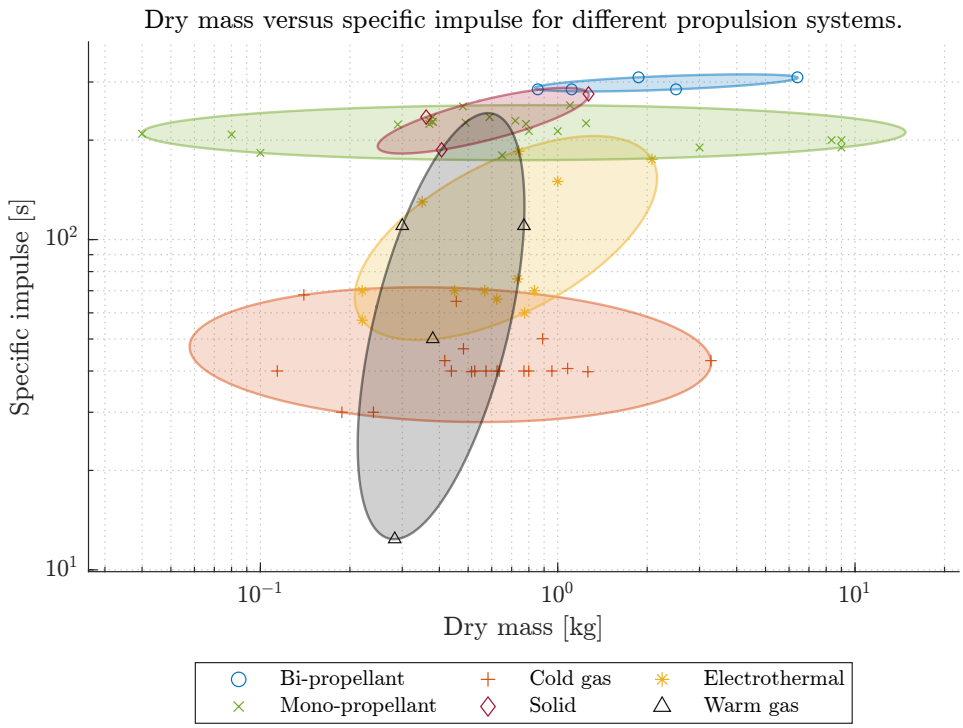

Figure 2.16: In this figure, the relationship between system dry mass and specific impulse for various types of high-thrust propulsion systems is shown [4]. This information is essential in selecting the appropriate propulsion system for interplanetary missions because the system's dry mass leads to less propellant mass available for the fly-by maneuver while specific impulse leads to less propellant mass consumption per delta-V. It can be seen that solid propulsion systems have both a high thrust and dry mass in the range of 1 kg. Mono-propellant propulsion systems have system dry mass ranging from less than 100 grams up to 10 kg. Some mono-propellant systems are however thruster head-only systems which naturally leads to a lower dry mass. Bi-propellant systems range from 1 to 10 kg. For mono- and bi-propellant systems it can be seen that a change in dry mass does not lead to a significant change in specific impulse. For solid propulsion systems, there is an increase in dry mass for higher specific impulse systems.

From Figure 2.16 it can be seen that for the current SOTA for solid propulsion systems, an increase in dry mass enables higher specific impulses. For mono- and bi-propellant systems a change in dry mass does not significantly impact the specific impulse.

Since Figure 2.15 and Figure 2.16 do not show significant changes in thrust and specific impulse for changes in dry mass high-thrust propulsion systems with a high specific impulse and high thrust are selected for the simulation because those properties lead to a lower required propellant mass. The system dry mass should at least be lower than 5 kg because from the mass budget in the introduction already 7.2 kg is reserved for other satellite systems. This leads to the high-thrust propulsion system selection given in Figure 2.17

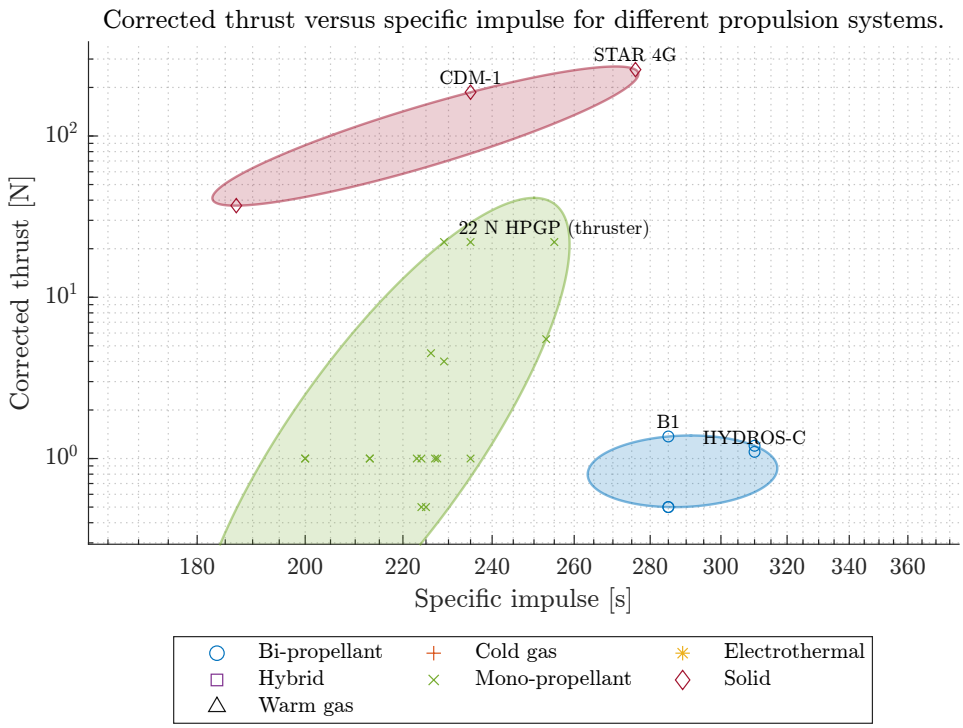

Figure 2.17: In this figure, the relationship between specific impulse and maximum thrust for various types of high-thrust propulsion systems and the selected systems are shown [4]. Systems with both relatively high thrust and high specific impulse are selected to be simulated which proves if they can maneuver the satellite to its target destination. The hybrid propulsion system is excluded because no dry mass properties are listed for Utah State University's Green Hybrid Rocket.

From Figure 2.17, TETHERS UNLIMITED HYDROS-C a water electrolysis propulsion system has the highest I_{sp} while having a relatively low dry mass of 2.2 kg and high thrust of 1.2 N. Another high-thrust chemical propulsion option is the Dawn Aerospace B1 module with 285 seconds I_{sp}, 2.5 kg dry mass, and 1.37 N of thrust. Of the mono-propellant propulsion systems, Bradford-ECAPS's 22 N HPGP thruster head has competitive thrust and specific impulse properties with a thrust of 22 N, a specific impulse of 255 seconds, and a dry mass of 1.1 kg. Finally, of the solid propulsion systems, DSSP's CDM-1 with a maximum thrust of 186.8 N, a specific impulse of 235 seconds, and a dry mass of 0.36 kg is selected, and Northrop Grumman's (Former Orbital ATK) STAR 4G with a maximum thrust of 258 N, specific impulse of 276 seconds, and a dry mass of 1.27 kg is selected.

These five chemical propulsion systems are selected to be simulated because of their high-thrust and relatively high specific impulse compared to other high-thrust systems. These systems might be able to maneuver to a NEA from SSGTO utilizing the efficiency gain that comes from using most of their propellant near the perigee.

Table 2.13: Selected high-thrust primary propulsion systems based on their specific impulse. The table includes information on the manufacturer, model, propellant type, thrust, specific impulse, wet mass, dry mass, volume, and power for the Tethers Unlimited HYDROS-C and Dawn Aerospace B1 propulsion systems [4]. Densities of the different propellants are around $1\,\mathrm{kg\,L^{-1}}$ for liquid water, $1.2\,\mathrm{kg\,L^{-1}}$ for liquid nitrous oxide (N2O), $1.7\,\mathrm{kg\,L^{-1}}$ for liquid propylene (C3H6), $1.81\,\mathrm{kg\,L^{-1}}$ for LMP-103S, up to $2.0\,\mathrm{kg\,L^{-1}}$ for AP/HTPB, and approximately $1.8\,\mathrm{kg\,L^{-1}}$ for TP-H-3399. (BiP = Bi-propellant propulsion, MP = Mono-propellant propulsion, S = Solid propulsion).

Type	Mfr.	Model	Prop.	Thrust (N)	Isp (s)	Wet mass (kg)	Dry mass (kg)	Volume (U)	Power (W)
BiP	Tethers Unlimited	HYDROS-C	Water	1.2	310	2.7	2.20	2.2724	25
BiP	Dawn Aerospace	B1	N2O and C3H6	1.37	285	4	2.5	4	12
MoP	Bradford-ECAPS	22 N HPGP	LMP-103S	22	255	1.1	1.1	0.13	50
S	DSSP	CDM-1	AP/ HTPB	186.8	235	0.46	0.36	0.15	5
S	Northrop Grumman	STAR 4G	TP-H-3399	258	276	1.49	1.27	1.38	N/A

Note: Northrop Grumman does not list the required power to ignite the STAR 4G solid engine therefore the power data is missing.

2.2.3. Interplanetary propulsion system selection

From the comparisons of the low-thrust high-specific impulse propulsion systems and high-thrust propulsion systems, a selection of systems that can potentially meet the requirements of a fly-by trajectory to a NEA is made. This selection reduces the number of simulations that have to be done to verify that a propulsion system meets the requirements. The following low-thrust propulsion systems are found to likely meet the requirements: Enpulsion's IFM Nano, Enpulsion's IFM Micro, Busek's BIT-3, ThrustMe's NPT30-I2 RF, CU Aerospace's FPPT-1.6, EDB Fakel's SPT-70M, JPL's MaSMi and Safran's PPS-X00. And the following high-thrust propulsion systems are found to likely meet the requirements: Tethers Unlimited's HYDROS-C, Dawn Aerospace's B1, Bradford-ECAPS's 22 N HPGP, DSSP's CDM-1, and Northrop Grumman's STAR 4. These systems are simulated using the framework described in chapter 3 and chapter 4 and their results can be seen in chapter 5. This then answers research question RQ1.1 in chapter 5.

2.3. Reaction control propulsion system

To desaturate the reaction wheels when no magnetic field is present the RCT system is used. There are a couple of options to generate a torque to counteract the momentum dumping of the reaction wheels which are: Thrust vectoring the main propulsion system such that the thrust misalignment with the satellite's center of mass creates a torque, actuating multiple main propulsion modules in a combination that the force imbalance in the center of mass leads to torque, and using a secondary propulsion system of multiple thrusters purely for attitude control. Thrust vectoring is discarded as an option because it is considered outside of the thesis scope, using multiple main thrusters is also discarded because there is not enough volume to fit enough main thrusters to also control the three axes of rotation. This leaves

the thesis with only one possible solution which is the use of a secondary propulsion system purely for the rotational actions.

In this section, a secondary propulsion system with the goal of desaturating the reaction wheels and performing attitude maneuvers with other together with reaction wheels is selected in this chapter.

In Table 2.1 the thrust and specific impulse ranges for different propulsion types are listed. From only these characteristics, it would be common sense to also go for electric propulsion systems for the secondary propulsion system because it has a high specific impulse in general. However, the dry mass and volume of these systems are often much larger than chemical propulsion systems. Next to the dry mass and volume of these systems, these systems are also much more complex and their thrusters cannot easily be placed at any position and in any orientation.

As mentioned in NASA [4], Solid propulsion systems are not suitable for CubeSat reaction control systems due to their inability to provide precise control of the satellite's attitude. Their use is limited by their one-time fire capability and lack of throttleability. The minimum impulse bit of these systems is also too high to use these propulsion systems for precise maneuvers. These systems are therefore not considered.

Hybrid propulsion systems, while offering a high thrust-to-weight ratio, are problematic due to the unpredictable burn pattern that makes precise attitude control challenging. These systems are therefore not considered [4].

Electrothermal propulsion systems, while having high performance, present design challenges for CubeSats. The tendency for significant thermal soak-back, along with the large volume and mass of the thruster heads, constrain orientation possibilities and placement on the CubeSat. These systems are therefore not considered [4].

In contrast, cold and warm gas systems present a simple and effective solution. These systems have low dry mass and volume, making precise orientation and placement possible. Their simplicity allows for ease of control and their thruster heads can be placed in various positions and orientations on the CubeSat [4].

For an RCT system, a bi- or mono-propellant system would be most suitable. Bi-propellant systems use a combination of two chemicals, such as hydrogen peroxide and hydrazine, which react to produce a high-speed exhaust plume. This type of system provides a high thrust-to-weight ratio and can be easily throttled. Mono-propellant systems use a single chemical, such as hydrazine, which is forced to react through a catalyst. Hydrazine catalyst reactions are exothermic and produce a high-temperature gas mixture of nitrogen, hydrogen, and ammonia. This type of system is simple, reliable, and has a low cost, but provides a lower thrust-to-weight ratio compared to bi-propellant systems. Like cold and warm gas systems, thruster heads are very simple and can be placed in various positions and orientations on the CubeSat [4].

Another alternative for CubeSat RCT systems is to utilize the same propellant as the primary propulsion system. This solution streamlines the overall system design and reduces the complexity of managing multiple propellant types. However, it can be argued that sharing one propellant tank for two propulsion systems comes with its own challenges. Additionally, it may also enhance reliability and safety, as a single propellant type reduces the potential for compatibility issues.

2.3.1. Comparison of propulsion systems

To answer RQ2.1 cold gas-, warm gas-, mono-propellant-, and bi-propellant propulsion systems are compared. An optimal desaturation system is low-mass, low-volume, low-power, and has a low mini-

mum impulse bit. Additionally, the thrusters must be compact and simple in design to allow for placement in various positions and orientations on the CubeSat. The preliminary search for an RCT system necessitates an evaluation of the propulsion system's volume to ensure it does not exceed 0.5U, leaving adequate space of approximately 2-2.5U for the interplanetary propulsion system. To limit the volume and minimize the total mass of the propulsion system, a systematic approach is employed, evaluating the propulsion system's volume and specific impulse as can be seen in Figure 2.18, together with the dry mass of the propulsion system as can be seen in Table 2.14. This methodology enables an informed decision regarding the propulsion system while information is limited.

From Figure 2.18 eleven propulsion systems that are below 0.5U in total volume can be identified. These are listed in Table 2.14. Inspecting the specific impulse, dry mass, and wet mass of the different propulsion systems it can be seen that the total impulse strongly influences the impulse per total mass. For example, despite possessing an outstanding specific impulse, the Nanoprop CGP3 suffers from a high dry mass compared to its wet mass. Nonetheless, for impulse values in the range of 50-150 Ns, the Nanoprop CGP3 still holds the greatest impulse-to-total mass ratio as can be seen in Figure 2.19. Above this threshold, the most mass-efficient system is the end-mounted standard MiPS 0.44U due to its superior total impulse-to-total mass ratio in the volume range of under 0.5U. Therefore, for the RCT system, GomSpace Nanoprop CGP3 and VACCO the end-mounted standard MiPS 0.44U are selected as possible options for the desaturation of the reaction wheels. Both these systems do not have the downside of using cold/hot gas propulsion which is that the thrust profile is decreasing over time because their propellants are stored as liquids. The pressure of the propellants comes from the vapor pressure of these propellants which means the pressure is not decreasing as long as there is still propellant in the liquid form available in the tank.

An alternative approach involves utilizing the interplanetary propulsion system's propellant for the desaturation of reaction wheels. However, for low-thrust interplanetary propulsion systems, this approach is not deemed to be competitive because multiple low-thrust propulsion systems would not fit in the current CubeSat configuration. Furthermore, RCTs utilizing the same propellant as low-thrust systems such as indium, iodine, and xenon warm gas are expected to have specific impulses ranging from 10 to 30 seconds (as demonstrated by the I2T5 Cold Iodine Thruster and the MEPSI Xenon cold gas thruster in CANX-2). Although such a system eliminates the need for an additional propellant storage tank, the low specific impulse diminishes its overall benefit. For high-thrust interplanetary propulsion systems, it could be beneficial to use the propellant for both desaturation and interplanetary travel. As a potential area for future research, it could be explored whether it is feasible to develop a standardized propulsion system for NEAs that can be accessed by high-thrust interplanetary propulsion systems that simultaneously serve to desaturate reaction wheels using the same propellant.

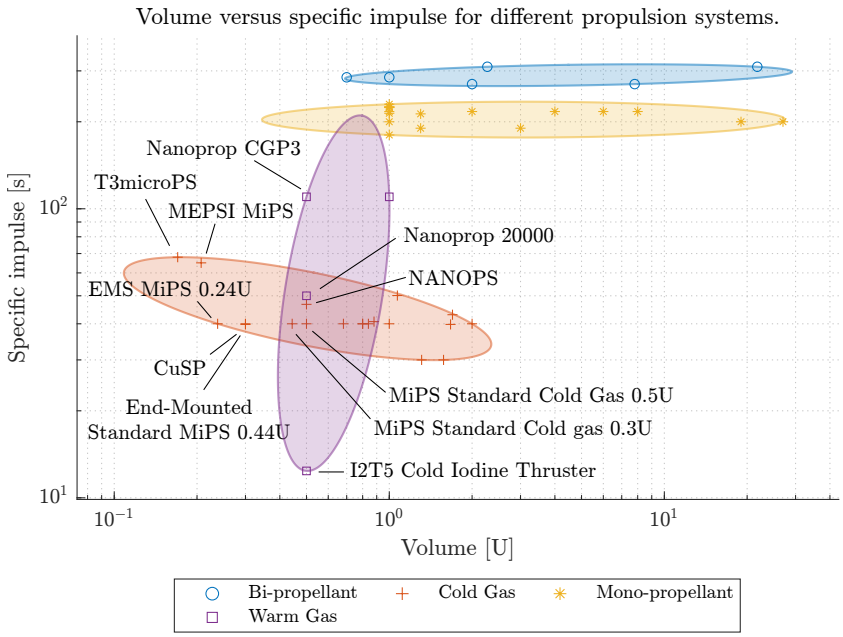

Figure 2.18: Relation between the volume and the specific impulse for various reaction control propulsion systems [4]. The figure shows that most mono- and bi-propellant systems have larger volumes than Cold- and Warm gas propulsion systems while offering similar or lower specific impulses. This information can aid in selecting the appropriate reaction control propulsion system for a given mission. Systems below a volume of 0.5U are labeled because these will fit on the 6U CubeSat.

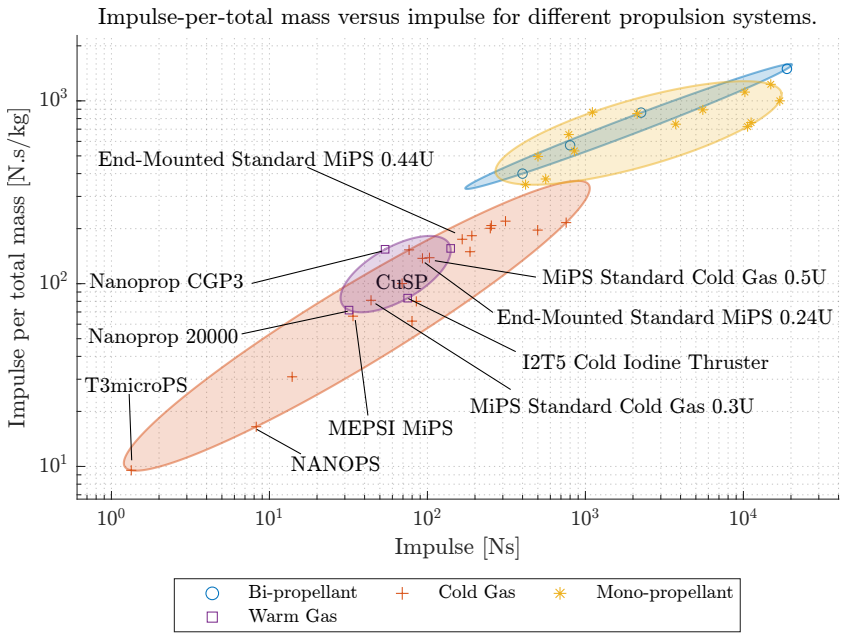

Figure 2.19: Total impulse per total mass versus total impulse for different reaction control propulsion systems [4]. This figure demonstrates that as the impulse of a system increases, the impulse-to-total mass ratio generally increases across all types of propulsion systems. This trend is due to the fact that the size and mass of system components typically do not increase in proportion to the increase in propellant mass. By analyzing this graph, one can gain insight into the relative performance of different propulsion systems and can determine which system might be the most appropriate for a given mission. Systems below a volume of 0.5U are labeled because these will fit on the 6U CubeSat. From these systems, Nanoprop CGP3 and the End-Mounted Standard MiPS 0.44U are most promising for their high impulse per total mass properties.

Table 2.14: This table presents a range of possible reaction control propulsion system solutions that could be employed for the described mission. The systems are classified by their type, manufacturer (Mfr.), model, propellant (Prop.), and various performance metrics such as thrust, minimum impulse bit (Impulse bit), specific impulse, mass, and volume (Size). The data in this table can be used to aid in the selection of an appropriate system based on the mission's specific requirements [4].

Type	Mfr.	Model	Prop.	Thrust (mN)	Impulse bit (mNs)	Isp (s)	Wet Mass (kg)	Dry Mass (kg)	Size (U)
Cold Gas	SFL	NANOPS	SF6	35	0.07	46.7	0.500	0.482	0.500
Cold Gas	VACCO	MiPS Standard Cold Gas 0.3U	R236fa	25	0.5	40	0.542	0.430	0.300
Cold Gas	VACCO	MiPS Standard Cold Gas 0.5U	R236fa	25	0.5	40	0.743	0.481	0.500
Cold Gas	VACCO	CuSP	R236fa	25	0.500	39.8	0.690	0.513	0.300
Cold Gas	VACCO	End-Mounted Standard MiPS 0.24U	R134A	10	0.05	40	0.676	0.439	0.238
Cold Gas	VACCO	End-Mounted Standard MiPS 0.44U	R134A	10	0.05	40	0.949	0.526	0.444
Cold Gas	VACCO	MEPSI MiPS	C4H10	53	1	65	0.509	0.456	0.207
Cold Gas	TNO, TU Delft, & UTwente	T3-microPS	N2 (solid)	150	0.03	68	0.140	0.138	0.170
Warm Gas	GomSpace	Nanoprop CGP3	C4H10	1	0.025	110	0.350	0.300	0.500
Warm Gas	GomSpace	Nanoprop 20000	C4H10	10	0.025	50	0.445	0.380	0.500
Warm Gas	ThrustMe	I2T5 Cold Iodine Thruster	I2 (solid)	0.2	NaN	12.388	0.900	0.283	0.500

3

Astrodynamics model

An astrodynamics model is necessary to simulate the trajectory from Earth to a NEA. This model is composed of several components including:

- Reference system: This essentially defines the spacecraft's position and velocity at a given moment in time, with respect to a fixed point or observer. The reference system provides a standardized set of coordinates that are necessary for accurately measuring the spacecraft's motion, orientation, and position in space.
- Kinematics: This describes the change of the spacecraft's position and velocity parameters independent of the forces acting on the spacecraft. This is an essential consideration when modeling the motion of a spacecraft because non-Cartesian kinematics can have non-zero higher-order derivatives, even in the absence of external forces.
- Dynamics: The dynamics account for all the forces acting on the spacecraft. This can be subdivided into the main forces such as the gravitational pull of the Earth, the Sun, and the thrust of the propulsion system, and perturbations such as the oblateness effects on the Earth's gravity, atmospheric drag, and solar radiation pressure.

This model is necessary because it provides a framework to simulate a fuel-efficient trajectory to a NEA. When combined with an optimal control method in chapter 4, the astrodynamics model answers the research question RQ1.2.

RQ1.2: What is a practical framework to simulate a fuel-efficient trajectory to a near-Earth asteroid within 5 years?

In chapter 4, the simulation is split up into two parts: The Earth escape trajectory and the interplanetary cruise to the NEA. This chapter focuses on the selection of the reference system, celestial bodies, and other perturbations for both these two segments separately.

3.1. Reference frame & time definition

To determine the position and velocity of the satellite at a certain moment in time a reference frame has to be defined. Together with the coordinate system and system for time measurement this then forms a reference system.

There exist many definitions of time which can be used. Because this thesis will be with NASA's SPICE Toolkit to retrieve the positions of celestial bodies, the time used will be epoch or seconds past J2000 (January 1, 2000 at 12:00, terrestrial time).

To define a reference frame the origin and the orientation of the fundamental planes or axes have to be defined. For a trajectory around the Earth, there are three frames that are used most often. These frames are topocentric, geocentric, or heliocentric. Other frames such as the galactic system frame or other planetary frames are not considered. The galactic system frame is oriented such that it aligns the primary axis with the approximate center of the milky way and the XY-plane aligned with the galactic plane. Since it is not interesting for this mission to define the satellite with respect to the galactic plane this reference frame is not considered. The same applies to planetary frames other than Earth. Including the position and velocity of the satellite with respect to another planet would overcomplicate the simulation needlessly, given that the mission does not involve a trajectory to another planet.

Topocentric frames are frames that use an observer on the Earth's surface as the origin of the reference frame. This frame is most used to define observed trajectories of satellites in Earth's orbit from the perspective of a ground station. Logically, this reference frame is unwieldy and counter-intuitive when it is used for Earth escape trajectory analysis because it is rotating and translating along a point on the surface of the Earth [36].

Reference geocentric frames are more often used to describe the motion of a rocket or satellite with respect to the Earth's surface. This frame is defined such that the z-axis is along the Earth's axis of rotation towards the north pole and the x-axis is in the Earth's equatorial plane crossing the Greenwich meridian. The advantage of this reference frame is that the position of a satellite or rocket can be directly linked to the Earth's surface. The disadvantage of this rotating frame is that other celestial bodies such as the Moon have to be redefined in this new rotating frame as well, which makes calculating trajectories to the Moon or interplanetary trajectories overly complicated. It is also possible to consider a non-rotating geocentric reference frame. This is often used to calculate trajectories for missions to the Moon [36].

Finally, a heliocentric reference frame can be used for interplanetary trajectories. This frame places a fixed Sun or the barycenter of our solar system at the origin of the reference frame. The x-axis is defined as the direction towards the First Point of Aries and the XY-plane is then oriented such that it is identical to the Earth's elliptical plane. This frame can therefore also be referred to as the non-rotating heliocentric ecliptic reference frame. The advantage of this reference frame in the barycenter is that it does not undergo significant accelerations and rotations. For more simplified models, the Sun-fixed reference frame can be used [36].

For the Earth escape trajectory the geocentric non-rotating reference frame will be used because, for the first part of the trajectory, the influence of the Sun and other celestial bodies is not taken into account to simplify the framework without significantly affecting the applicability of the results. For the interplanetary cruise towards the NEA, the ECLIPJ2000 reference frame will be used, which is defined as the non-rotating heliocentric frame with the XY-plane coinciding with the mean ecliptic of J2000 and the x-axis with the equinox of J2000. This frame can easily be used in combination with NASA's SPICE toolbox for celestial bodies and can be considered not accelerating and not-rotating.

3.2. Coordinate system & kinematics

The coordinate system can be described in many different representations. The choice of the coordinate system influences the ease of implementation, the convergence of optimizations, and computa-

tional efficiency. The most often used reference frames are cartesian state vector (CSV) representation, spherical coordinates (SC), cylindrical coordinates (PSV3), classical orbital elements (COE), and modified equinoctial elements (MEE). This section presents the different coordinate systems and their kinematics and discusses which is the best fit for the practical framework to simulate the interplanetary trajectory.

3.2.1. Cartesian state vector representation

To define the motion of an orbiting body in a three-dimensional space a CSV representation can be used. In this coordinate system representation a position vector $\vec{p}$ at a time t is described using Cartesian coordinates with respect to an origin. The position and velocity of an orbiting body can then be described using six Cartesian coordinates which result in $[x, y, z, \dot{x}, \dot{y}, \dot{z}]^\top$. The last three parameters in this state vector are the time derivatives of the position coordinates, which result in the velocity coordinates of the satellite.

An advantage of using Cartesian coordinates is that it leads to relatively simple mathematical expressions for the position, velocity, and acceleration of the satellite. The disadvantage of using Cartesian coordinates is that the parameters describing the satellite's trajectory change relatively fast over time with respect to other state representations. This leads to more numerical integration steps being required to calculate a trajectory under the same accuracy requirements as other state representations. Finally, interpreting Cartesian coordinates is not as straightforward as COE or MEE, and 2- or 3-dimensional visualization of the orbit is required.

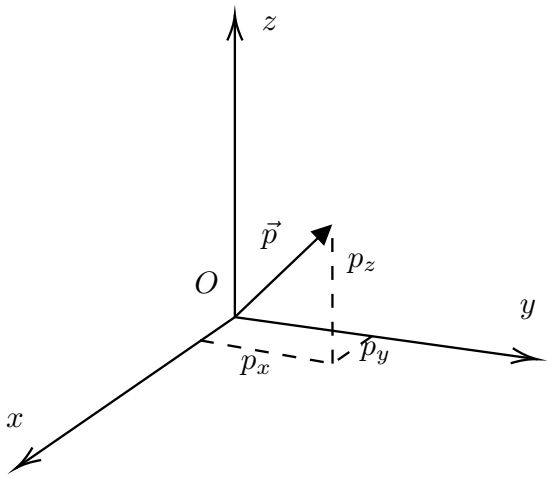

Figure 3.1: An illustration of the Cartesian state vector coordinate system representation. $\vec{p}$ is a position vector with coordinates $[p_x, p_y, p_z]^\top$ which denote the distance along the x-, y- and z-axis.

The derivatives of the state vector in Cartesian coordinates is straight forward. Let $\vec{p} = [x, y, z]^\top$, then the first- and second-time derivatives are:

$$\dot{\vec{p}} = [\dot{x}, \dot{y}, \dot{z}]^\top,$$
$$\ddot{\vec{p}} = [\ddot{x}, \ddot{y}, \ddot{z}]^\top$$

3.2.2. Spherical coordinates representation

To define the motion of an orbiting body in space also an SC representation can be used. This particular coordinate system replaces the Cartesian coordinates of a position with a point on a sphere described

by a radius, co-latitude, and longitude angle: $[r, \theta, \varphi]^\top$. To define a motion of an orbiting body, the time-derivative of the position can be taken which results in the six spherical coordinates that describe an object in motion in space: $[r, \theta, \varphi, \dot{r}, \dot{\theta}, \dot{\varphi}]^\top$. There also exist other ways to define the derivatives of the position vector for spherical coordinates. Often, velocity vectors are used instead of angular velocities which are defined as $v_\theta = \dot{\theta} r$ and $v_\varphi = \dot{\varphi} r$ and $\dot{r}$ is then $v_r = \dot{r}$.

An advantage of using SC is that this particular coordinate system is more stable than CSV when calculating a trajectory. Especially in the vicinity of a central body such as the Earth, the nature of the SC system reduces the complexity of the mathematical equations for the dynamics because the gravitational attraction of the central body only acts in the radial direction. In CSV this force would act in x,y, and z directions leading to a more complex definition of the dynamics. Furthermore, constraint definitions or heuristic laws based on the orbital angular position and distance to a central body are easier to define because these do not have to be calculated from the CSV representation but come directly from the SC.

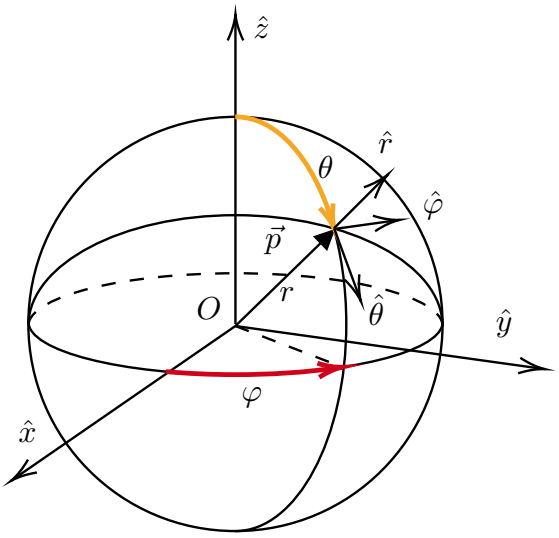

Figure 3.2: An illustration of the spherical coordinates system representation. A position vector $\vec{p}$ is described by the coordinates $[r, \theta, \varphi]^\top$ which denote the radius of the sphere, the co-latitude which is the inclination from the z-axis, and the longitude as measured from the positive Cartesian x-axis. Where $\hat{r}, \hat{\theta}$ and $\hat{\varphi}$ are the local orthogonal unit vectors in the direction of increasing r, θ, and φ.

The position vector $\vec{p}$ can be described using:

$$\vec{p} = r\ \hat{r} \tag{3.1}$$

where $\hat{r}$ is one of the $\hat{r}, \hat{\theta}$ and $\hat{\varphi}$ vectors which are local orthogonal unit vectors that are related to the Cartesian coordinates unit vectors $\hat{x}, \hat{y}$ and $\hat{z}$ by the following relations:

$$\hat{r} = \sin\theta \cos\varphi\ \hat{x} + \sin\theta \sin\varphi\ \hat{y} + \cos\theta\ \hat{z} \tag{3.2a}$$

$$\hat{\theta} = \cos\theta \cos\varphi\ \hat{x} + \cos\theta \sin\varphi\ \hat{y} - \sin\theta\ \hat{z} \tag{3.2b}$$

$$\hat{\varphi} = -\sin\varphi\ \hat{x} + \cos\varphi\ \hat{y} + 0\ \hat{z} \tag{3.2c}$$

To find the derivative of $\vec{p}$, first the first order time-derivatives of $\hat{r}, \hat{\theta}$ and $\hat{\varphi}$ are derived as follows from Equation 3.2a, Equation 3.2b and Equation 3.2c:

$$\dot{\hat{r}} = \dot{\theta}\,(\cos\theta \cos\varphi\ \hat{x} + \cos\theta \sin\varphi\ \hat{y} - \sin\theta\ \hat{z}) + \dot{\varphi}\,(-\sin\theta \sin\varphi\ \hat{x} + \sin\theta \cos\varphi\ \hat{y} + 0\ \hat{z}) \tag{3.3a}$$

$$\dot{\hat{\theta}} = \dot{\theta}\,(-\sin\theta\cos\varphi\;\hat{x} - \sin\theta\sin\varphi\;\hat{y} - \cos\theta\;\hat{z}) + \dot{\varphi}\,(-\cos\theta\sin\varphi\;\hat{x} + \cos\theta\cos\varphi\;\hat{y} + 0\;\hat{z}) \tag{3.3b}$$

$$\dot{\hat{\varphi}} = \dot{\varphi}\,(-\cos\varphi\;\hat{x} - \sin\varphi\;\hat{y} + 0\;\hat{z}) \tag{3.3c}$$

Substitution of the relations Equation 3.2a, Equation 3.2b, and Equation 3.2c inside Equation 3.3a, Equation 3.3b and Equation 3.3c gives the simplified first order time-derivatives of $\hat{r}$ and $\hat{\theta}$:

$$\dot{\hat{r}} = \dot{\theta}\;\hat{\theta} + \dot{\varphi}\sin\theta\;\hat{\varphi} \tag{3.4a}$$

$$\dot{\hat{\theta}} = -\dot{\theta}\;\hat{r} + \dot{\varphi}\cos\theta\;\hat{\varphi} \tag{3.4b}$$

And $\dot{\hat{\varphi}}$ can be simplified as follows using the same substitutions and the Pythagorean identity law $\cos^2\varphi + \sin^2\varphi = 1$:

$$\begin{aligned}
\dot{\hat{\varphi}} = &-\dot{\varphi}\left(\cos\varphi\left(\sin\theta\cos\varphi\;\hat{r} + \cos\theta\cos\varphi\;\hat{\theta} - \sin\varphi\;\hat{\varphi}\right) + \ldots\right.\\
&\left.\sin\varphi\left(\sin\theta\sin\varphi\;\hat{r} + \cos\theta\sin\varphi\;\hat{\theta} + \cos\varphi\;\hat{\varphi}\right)\right)\\
\dot{\hat{\varphi}} = &-\dot{\varphi}\sin\theta\left(\cos^2\varphi + \sin^2\varphi\right)\;\hat{r} - \dot{\varphi}\cos\theta\left(\cos^2\varphi + \sin^2\varphi\right)\;\hat{\theta}\\
\dot{\hat{\varphi}} = &-\dot{\varphi}\sin\theta\;\hat{r} - \dot{\varphi}\cos\theta\;\hat{\theta}
\end{aligned} \tag{3.5}$$

Now to find the first-order time-derivative of the position vector $\vec{p}$, which is the velocity vector the product rule can be used which results into:

$$\dot{\vec{p}} = \dot{r}\;\hat{r} + r\;\dot{\hat{r}} \tag{3.6}$$

Substitution of Equation 3.3a in the found expression results in:

$$\dot{\vec{p}} = \dot{r}\;\hat{r} + r\dot{\theta}\;\hat{\theta} + r\dot{\varphi}\sin\theta\;\hat{\varphi} \tag{3.7}$$

The second-order time-derivative of the position vector can be found by using the product rule as well which results in:

$$\ddot{\vec{p}} = \ddot{r}\;\hat{r} + \dot{r}\;\dot{\hat{r}} + \dot{r}\dot{\theta}\;\hat{\theta} + r\ddot{\theta}\;\hat{\theta} + r\dot{\theta}\;\dot{\hat{\theta}} + \dot{r}\dot{\varphi}\sin\theta\;\hat{\varphi} + r\ddot{\varphi}\sin\theta\;\hat{\varphi} + r\dot{\phi}\dot{\theta}\cos\theta\;\hat{\varphi} + r\dot{\varphi}\sin\theta\;\dot{\hat{\varphi}} \tag{3.8}$$

Substitution of Equation 3.4a, Equation 3.4b and Equation 3.5 in the found expression results in second-order time-derivative position vector equation:

$$\begin{aligned}
\ddot{\vec{p}} = &\ddot{r}\;\hat{r} + \dot{r}\left(\dot{\theta}\;\hat{\theta} + \dot{\varphi}\sin\theta\;\hat{\varphi}\right) + \dot{r}\dot{\theta}\;\hat{\theta} + r\ddot{\theta}\;\hat{\theta} + r\dot{\theta}\left(-\dot{\theta}\;\hat{r} + \dot{\varphi}\cos\theta\;\hat{\varphi}\right) + \ldots\\
&\dot{r}\dot{\varphi}\sin\theta\;\hat{\varphi} + r\ddot{\varphi}\sin\theta\;\hat{\varphi} + r\dot{\phi}\dot{\theta}\cos\theta\;\hat{\varphi} + r\dot{\varphi}\sin\theta\left(-\dot{\varphi}\sin\theta\;\hat{r} - \dot{\varphi}\cos\theta\;\hat{\theta}\right)
\end{aligned} \tag{3.9}$$

gathering together the accelerations in the different local directions $\hat{r}, \hat{\theta}$ and $\hat{\varphi}$ results in:

$$\begin{aligned}
\ddot{\vec{p}}\,\hat{r} &= \ddot{r} - r\dot{\theta}^2 - r\dot{\varphi}^2\sin^2\theta\\
\ddot{\vec{p}}\,\hat{\theta} &= r\ddot{\theta} + 2\dot{r}\dot{\theta} - r\dot{\varphi}^2\sin\theta\cos\theta\\
\ddot{\vec{p}}\,\hat{\varphi} &= 2\dot{r}\dot{\varphi}\sin\theta + 2r\dot{\theta}\dot{\varphi}\cos\theta + r\ddot{\varphi}\sin\theta
\end{aligned} \tag{3.10}$$

notice that $\ddot{\vec{p}}$ contains the accelerations coming from the dynamics of the system.

The velocity and acceleration expressions in SC representation from this section are also very important for the formulation of the attitude-tracking motion for the asteroid fly-by mission segment and optimal thrusting law direction in Earth orbit.

3.2.3. Cylindrical coordinates representation

For most NEA trajectories, the desired trajectory is not significantly tilted with respect to the Earth's ecliptic plane. This means that a cylindrical representation that uses a height instead of a co-latitude with respect to the z-axis is also acceptable. The states in the PSV3 coordinate system can be described very similarly to the SC representation as can be seen in Figure 3.3. The advantage over CSV is that for orbital motions, PSV3 is more stationary like SC. For example, a circular orbit without an inclination has a stationary radius and linear changing longitude angle φ, while CSV in x and y parameters oscillate. Therefore PSV3 can be considered to be more stable for orbits and orbital trajectories. For numerical integration, this means that a smaller numerical error can be achieved using fewer integration steps for the same integration scheme.

The downside however is that the kinematic derivatives are more complex than CSV. Especially for optimal control, this leads to more complex mathematical expressions.

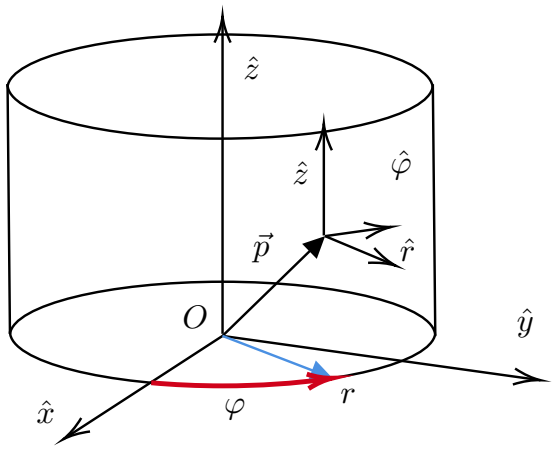

Figure 3.3: An illustration of the cylindrical coordinates system representation. A position vector $\vec{p}$ is described by the coordinates $[r, \varphi, z]^\top$ which denote the radius of the sphere, the longitude as measured from the positive Cartesian x-axis, and the height in the z-direction. Where $\hat{r}, \hat{\varphi}$ and $\hat{z}$ are the local orthogonal unit vectors in the direction of increasing r, φ and z.

As can be seen in Figure 3.3 a position in PSV3 can be described as:

$$\vec{p} = r\,\hat{r} + z\,\hat{z} \tag{3.11}$$

where:

$$\hat{r} = \cos\varphi\,\hat{x} + \sin\varphi\,\hat{y} + 0\,\hat{z} \tag{3.12a}$$

$$\hat{\varphi} = -\sin\varphi\,\hat{x} + \cos\varphi\,\hat{y} + 0\,\hat{z} \tag{3.12b}$$

$$\hat{z} = 0\,\hat{x} + 0\,\hat{y} + 1\,\hat{z} \tag{3.12c}$$

For the time-derivative of $\vec{p}$ $\dot{\hat{r}}$, $\dot{\hat{\varphi}}$ an $\dot{\hat{z}}$ are required and can be written as:

$$\dot{\hat{r}} = -\dot{\varphi}\sin\varphi\,\hat{x} + \dot{\varphi}\cos\varphi\,\hat{y} + 0\,\hat{z} = \dot{\varphi}\,\hat{\varphi} \tag{3.13a}$$

$$\dot{\hat{\varphi}} = -\dot{\varphi}\cos\varphi\,\hat{x} - \dot{\varphi}\sin\varphi\,\hat{y} + 0\,\hat{z} = -\dot{\varphi}\,\hat{r} \tag{3.13b}$$

$$\dot{\hat{z}} = 0 \tag{3.13c}$$

The first-order time-derivative or the velocity vector can then be described using the product rule and substitution of Equation 3.13a, Equation 3.13b and Equation 3.13c:

$$\begin{aligned} \dot{\vec{p}} &= \dot{r}\,\hat{r} + r\,\dot{\hat{r}} + \dot{z}\,\hat{z} + z\,\dot{\hat{z}} \\ \dot{\vec{p}} &= \dot{r}\,\hat{r} + r\dot{\varphi}\,\hat{\varphi} + \dot{z}\,\hat{z} \end{aligned} \tag{3.14}$$

The second-order time-derivative or the acceleration vector can then be described using the product rule of the first derivative and substitution of Equation 3.13a, Equation 3.13b and Equation 3.13c:

$$\begin{aligned}\ddot{\vec{p}} &= \ddot{r}\,\hat{r} + \dot{r}\,\dot{\hat{r}} + \dot{r}\dot{\varphi}\,\hat{\varphi} + r\ddot{\varphi}\,\hat{\varphi} + r\dot{\varphi}\,\dot{\hat{\varphi}} + \ddot{z}\,\hat{z} + \dot{z}\,\dot{\hat{z}} \\ \ddot{\vec{p}} &= \ddot{r}\,\hat{r} + 2\dot{r}\dot{\varphi}\,\hat{\varphi} + r\ddot{\varphi}\,\hat{\varphi} - r\dot{\varphi}^2\,\hat{r} + \ddot{z}\,\hat{z}\end{aligned} \tag{3.15}$$

gathering together the accelerations in the different local directions $\hat{r}, \hat{\varphi}$ and $\hat{z}$, and isolating $\ddot{r}$, $\ddot{\varphi}$ and $\ddot{z}$ results in:

$$\begin{aligned}\ddot{r} &= \ddot{\vec{p}}\,\hat{r} + r\dot{\varphi}^2 \\ \ddot{\varphi} &= \frac{\ddot{\vec{p}}\,\hat{\varphi}}{r} - \frac{2\dot{r}\dot{\varphi}}{r} \\ \ddot{z} &= \ddot{\vec{p}}\,\hat{z}\end{aligned} \tag{3.16}$$

3.2.4. Classical orbital elements

To describe trajectories to a NEA, classical orbital elements can also be used. Particularly interesting is this parameterization includes information on the shape of the orbit if it were to orbit around a body without perturbations. The advantage for COEs is that their parameters are exceptionally stable while applying numerical integration schemes on the trajectory of the satellite. This means that fewer integration steps are required to solve a trajectory with the same accuracy as for example CSV, SC, or PSV3. The disadvantage of COEs is that for some trajectories singularities may occur during the numerical integration. And that the mathematical expression necessary to solve for an optimal path to a NEA can be relatively complex. This can also slow down the computational time for a single integration step.

The definition of the parameters of a COE representation are taken from Wakker [36] as e the eccentricity of the elliptical orbit, a the semi-major axis of the orbit, i the inclination of the orbit with respect to the reference plane, Ω the longitude of the ascending node which is the angle at which the orbit passes upwards through the reference plane, ω the argument of periapsis which is the angle between the longitude of the ascending node and the periapsis of the orbit, and ν is the true anomaly which is the position of the satellite on the elliptical orbit at a time t.

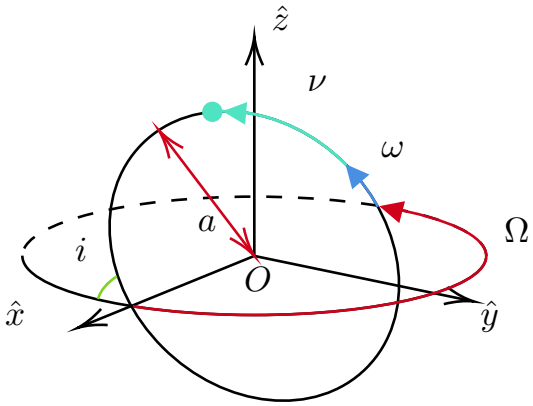

Figure 3.4: Classical orbital elements representation. a Is the semi-major axis of the orbit. i Is the inclination of the orbit with respect to the reference plane. Ω Is the longitude of the ascending node which is the angle at which the orbit passes upwards through the reference plane. ω Is the argument of periapsis which is the angle between the longitude of the ascending node and the periapsis of the orbit. And ν is the true anomaly which is the position of the satellite on the elliptical orbit at a time t. The eccentricity of the elliptical orbit is described using e which is not displayed in the figure.

3.2.5. Modified equinoctial elements

The main drawback of COEs with respect to MEEs is that singularities exist for circular orbits with $e = 0$ and orbit inclinations of 0° and 90°. Using MEEs these singularities do not exist anymore and only two parameters have singularities for inclinations of 180°, which can be solved by redefining the reference plane in these situations. Therefore MEEs are used more often for trajectory analysis or optimization. The relation between COE and MEE is defined as [36]:

$$\begin{aligned} p &= a\left(1-e^2\right) \\ f &= e\cos\left(\omega+\Omega\right) \\ g &= e\sin\left(\omega+\Omega\right) \\ h &= \tan\left(\frac{i}{2}\right)\cos\Omega \\ k &= \tan\left(\frac{i}{2}\right)\sin\Omega \\ L &= \Omega+\omega+\nu \end{aligned} \tag{3.17}$$

MEE has the same advantages as COE. but with singularities that can be handled. The disadvantage of MEE is that the mathematical expressions are relatively complex. The strength of MEE comes out best when calculating many revolution trajectories because five out of the six parameters are 'slow' changing.

3.2.6. Coordinate system conclusion

The choice of a coordinate system can lead to either simple or complex mathematical expressions. From the five different coordinate system options, CSV leads to the most simple mathematical expressions followed by PSV3, SC, COE and MEE.

For numerical integration MEE and COE are the most stable options which require fewer integration steps for the same numerical error. Of these options, COE has singularities for an orbit with an eccentricity of zero and orbit inclinations of 0° and 90° and MEE has a singularity for an orbital inclination of 180°. PSV3 and SC require more integration steps to reach the same numerical error, and CSV is the least stable option, which has fast-changing parameters when describing a (multi-revolution) trajectory.

The interplanetary cruise from Earth orbit to a NEA does not require coordinate systems that can easily handle many revolutions and require fewer integration steps such as COE, MEE, or to a lesser degree SC and PSV3. Therefore CSV is chosen for this part of the trajectory.

The Earth escape trajectory from SSGTO until the moment of Earth escape is however assumed to be a many-revolution problem for some low thrust systems. To have slightly more stability, SC is chosen for this particular trajectory.

3.3. Satellite state and dynamics

The state of the satellite can be defined by its position, velocity, and mass. In CSV this can be defined as:

$$\vec{\chi} = \left[x, y, z, \dot{x}, \dot{y}, \dot{z}, m\right]^\top \tag{3.18}$$

where x, y, and z is the Cartesian position of the satellite with respect to a reference frame, $\dot{x}$, $\dot{y}$, and $\dot{z}$ are the velocity of the satellite with respect to a reference frame and m is the mass of the satellite.

And in SC the state of the satellite can be defined as:

$$\vec{\chi} = \Big[r, \theta, \varphi, v_r, v_\theta, v_\varphi, m\Big]^\top \tag{3.19}$$

where r is the distance from the reference frame to the satellite as measured in the XY-plane, φ is the longitude of the satellite measured from the x-axis, and θ is the co-latitude of the satellite measured from the positive z-axis. v_r Is the velocity in the direction of the position vector r, v_φ is the velocity in the direction of the longitude angle φ and v_θ is the velocity in the direction of co-latitude angle θ.

For the Earth's escape trajectory, it is assumed that only a two-dimensional maneuver will be performed to escape the Earth's orbit. This means that the parameters for the state of the satellite for the Earth escape segment can be reduced such that only a two-dimensional polar coordinate system can be used or two-dimensional SC without a co-latitude angle θ. The new state vector which describes the position, velocity, and mass of the satellite at an instance t is then defined as:

$$\vec{\chi} = \Big[r, \varphi, v_r, v_\varphi, m\Big]^\top \tag{3.20}$$

3.3.1. Two-body problem

In Figure 3.5 a system of three bodies is given. When the gravitational attraction between the bodies i and j can be neglected with respect to the gravitational attraction between the bodies i and k, then the motion of the body i can be described as a two-body problem such that [36]:

$$\frac{\mathsf{d}^2\vec{r}_{k,i}}{\mathsf{d}t^2} = -G\frac{m_k + m_i}{\|\vec{r}_{k,i}\|^3}\vec{r}_{k,i} \tag{3.21}$$

When the motion of the body i is described with respect to the barycenter as the origin, the two-body problem equation can be written as:

$$\frac{\mathsf{d}^2\vec{r}_{O,i}}{\mathsf{d}t^2} = -G\frac{m_k + m_i}{\left(1 + \frac{m_i}{m_k}\right)^3\|\vec{r}_{O,i}\|^3}\vec{r}_{O,i} \tag{3.22}$$

where $r_{O,i} = \vec{r}_{B,k} - \vec{r}_{i,k}$, $\vec{r}_{B,k} = -\frac{m_i}{m_k}\vec{r}_{B,i}$ and $\vec{r}_{i,k} = -\left(1 + \frac{m_i}{m_k}\right)\vec{r}_{B,i}$.

Now let $\mu = Gm_k\left(1 + \frac{m_i}{m_k}\right)^{-2}$ be the gravitational parameter in $\mathrm{m}^3\,\mathrm{s}^{-2}$ which depends on the gravitational constant G and the masses of the bodies i and k, then the motion of the body i can be described as [36]:

$$\frac{\mathsf{d}^2\vec{r}_{O,i}}{\mathsf{d}t^2} = -\frac{\mu}{\|\vec{r}_{O,i}\|^3}\vec{r}_{O,i} \tag{3.23}$$

If $m_i << m_k$, then $\mu \approx Gm_k$ can be used, which is the standard gravitational parameter of a body k. For example, when i is a satellite and k is the Earth, then the mass of the satellite can be neglected such that the standard gravitational parameter of the Earth can be used to calculate the motion of the satellite.

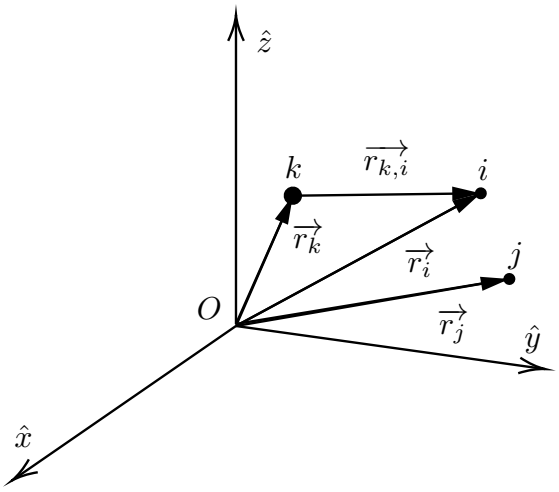

Figure 3.5: Figure of a three body system.

3.3.2. Perturbations

In an ideal situation, a trajectory around the Earth or Sun can be calculated with just the gravitational attraction forces. However, in reality, there are other forces such as perturbation effects of the oblation on the gravity of the Earth, aerodynamic drag in Earth orbit, other celestial bodies, solar radiation pressure, and even general relativistic effects [36, See Chapter 20]. Including the perturbation effects $\vec{a}_{p,i}$ in Equation 3.23, the general form of the equation of motion for a body i can be expressed as:

$$\frac{\mathrm{d}^2\vec{r}_{O,i}}{\mathrm{d}t^2} = -\frac{\mu}{\|\vec{r}_{O,i}\|^3}\vec{r}_{O,i} + \vec{a}_{p,i} \tag{3.24}$$

simplifying the notation to $\vec{r}_{O,i} = \vec{r}$, $\vec{a}_{p,i} = \vec{a}_p$ and $\frac{\mathrm{d}^2\vec{r}_{O,i}}{\mathrm{d}t^2} = \ddot{\vec{r}}$, the general form of the equation of motion for a body i can be expressed as:

$$\ddot{\vec{r}} = -\frac{\mu}{\|\vec{r}\|^3}\vec{r} + \vec{a}_p \tag{3.25}$$

Earth's gravitational force

The Earth's mass is not distributed in a perfect sphere. Under the assumption that the effect of a solid Earth, ocean, and pole tides can be neglected, the Earth can be expressed in Legendre polynomials such that the gravitation potential of a point outside the Earth may be written as [36, Chapter 20]:

$$\begin{aligned} U(r,\theta,\varphi) = -\frac{\mu}{r}\Bigg[1 - \sum_{n=2}^{\infty} J_n \left(\frac{R}{r}\right)^n P_n(\sin\theta) + \dots \\ \sum_{n=2}^{\infty}\sum_{m=1}^{n} J_{n,m}\left(\frac{R}{r}\right)^n P_{n,m}(\sin\theta)\left\{\cos m\left(\varphi - \varphi_{n,m}\right)\right\}\Bigg] \end{aligned} \tag{3.26}$$

where $P_{n,m}(\sin\theta)$ are Legendre polynomials of degree n and m of the function $\sin\theta$, $J_{n,m}$ and $\varphi_{n,m}$ are model parameters, r, θ, and φ are the spherical coordinates of the point that is considered, relative to the Earth's geocentric rotating reference frame, μ is the Earth's standard gravitational parameter, R is the mean equatorial Earth radius.

Wakker [36] concludes that in non-geostationary orbit cases, the effects of deviations in the shape and mass density distribution in the east-west direction will largely average out over periods longer than a day, and we may then neglect the effects of the $J_{n,m}$-terms for many applications. Also, the effect of J_2 or $J_{2,0}$, often referred to as the second-degree zonal harmonic coefficient, is about a thousand times

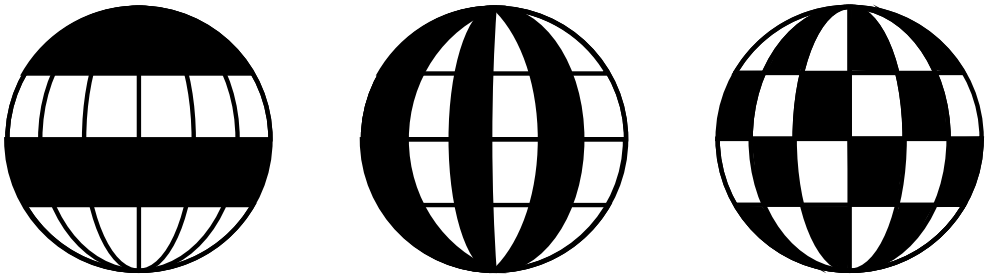

(a) Zonal harmonics ($n \neq 0, m = 0$). **(b)** Sectorial harmonics ($n = m \neq 0$). **(c)** Tesseral harmonics ($n \neq m \neq 0$).

Figure 3.6: This figure depicts the harmonic modes of Earth's mass distribution, where white regions indicate elevation above the mean spherical surface, and black regions indicate elevation below it.

larger than the other J_n- and $J_{n,m}$-coefficients. For first-order orbit computations of non-geostationary satellites only the J_2-term has to be included in the computations. Only considering this J_2-effect, the perturbing acceleration due to the non-spherical Earth's mass distribution can be expressed as [36]:

$$\vec{a}_{p,g} = -\vec{\nabla}\left[\frac{\mu}{r}J_2\left(\frac{R}{r}\right)^2\left(3sin^2\theta - 1\right)\right] \tag{3.27}$$

where J_2 =1082.6357×10^{-6} for associated constants μ =$398\,600.4415\,\text{km}^3\,\text{s}^{-2}$ and R =$6378.1363\,\text{km}$ [36].

Atmospheric drag

The acceleration of a satellite due to atmospheric drag can be expressed as [36]:

$$\vec{a}_{p,d} = -C_D\frac{1}{2}\rho\frac{A}{M}\|\vec{v}\|\vec{v} \tag{3.28}$$

where C_D is the satellite's drag coefficient, A is the satellite reference surface, M is the mass of the satellite and $\vec{v}$ is the velocity of the satellite with respect to the rotating Earth's atmosphere. A drag coefficient between $2-3$ is often used for computations. $C_D = 3$ is used in this thesis to be conservative. To obtain the densities at different altitudes, the mathematical representation of the 2001 United States Naval Research Laboratory Mass Spectrometer and Incoherent Scatter Radar Exosphere (NRLMSISE-00) of the MSIS model is used. Worst case values are used for the solar activity which is a solar flux F10.7cm average of 300, an F10.7cm daily of 300, and a magnetic index APH of 9.

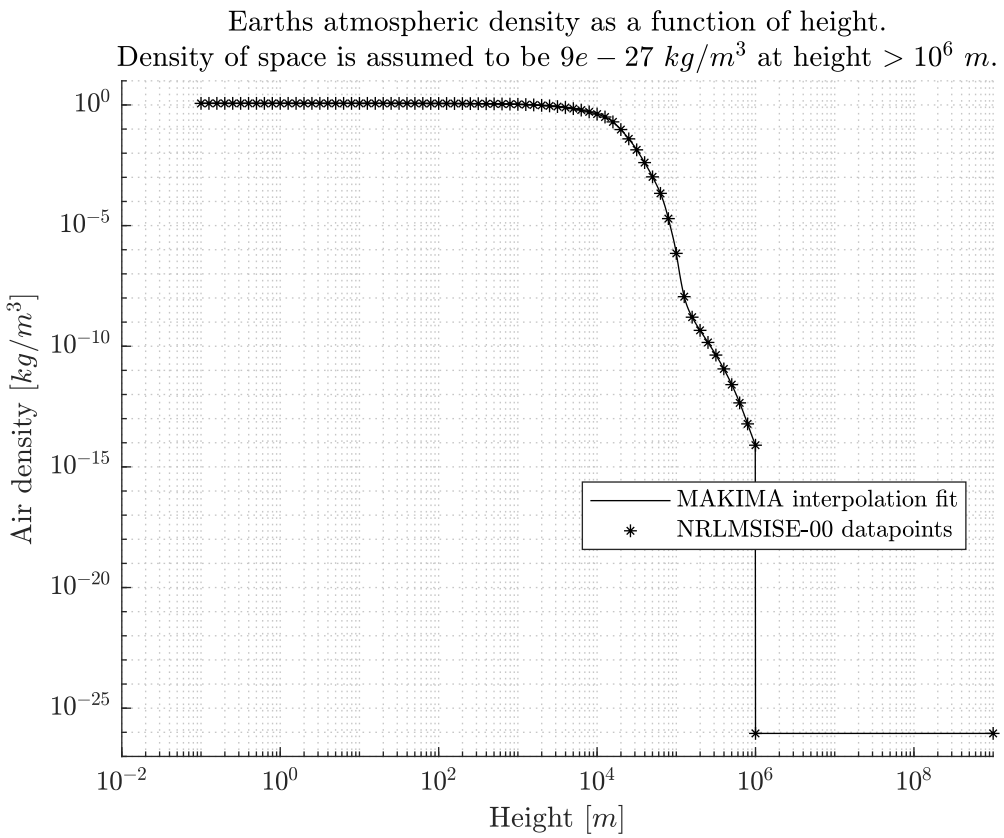

Figure 3.7: The figure shows the variation of air density with altitude above the Earth, as predicted by the NRLMSISE-00 model. The calculations were made for a magnetic index of 9, an average F10.7 solar flux of 300, and a daily F10.7 solar flux of 300. This figure contains valuable information for worst-case aerodynamic drag analysis for satellites.

Gravitational attraction of other celestial bodies

Other bodies such as the Sun or the Moon will also lead to perturbing forces. The perturbing acceleration caused by other celestial bodies expressed with respect to a non-rotating inertial reference frame can be expressed as [36]:

$$\vec{a}_{p,c} = G \sum_{j \neq i} \frac{m_i m_j}{\|\vec{r}_{ij}\|^3} \vec{r}_{ij} \tag{3.29}$$

where $\vec{r}_i$ is the position vector of the satellite, $\vec{r}_j$ is the position vector of a celestial body j, m_i is the mass of the satellite, m_j is the mass of the celestial body j and G is the gravitational constant.

Wakker [36] also gives an expression for the perturbing acceleration caused by other celestial bodies with respect to a non-rotating reference frame fixed at body k. This expression can be used for Earth-fixed frames. The perturbing acceleration caused by other celestial bodies can be expressed as:

$$[\vec{a}_{p,c}]_{\mathcal{K}} = -G \sum_{j \neq k,i} m_j \left(\frac{1}{\vec{r}_{ij}} - \frac{\vec{r}_i \cdot \vec{r}_j}{\|\vec{r}_j\|^3} \right) \tag{3.30}$$

where $[\ldots]_{\mathcal{K}}$ denotes that the perturbing acceleration $\vec{a}_{p,c}$ is with respect to the non-rotating reference frame fixed at body k and m_j is the mass of another celestial body.

Solar radiation pressure

A satellite in Earth's orbit will experience radiation force produced by incoming direct sunlight, reflected sunlight from Earth, and infrared radiation from Earth itself. Accurately modeling this force is complex, especially for satellites with complex shapes. Therefore an approximate expression for the perturbing

acceleration caused by radiation from the Sun is often used. This perturbing acceleration can then be expressed as [36]:

$$\vec{a}_{p,R} = -C_R \frac{WA}{m_i c} \hat{r}_{Si} \tag{3.31}$$

where C_R is the satellite's effective reflectivity, W is the energy flux of the incoming solar radiation, c is the speed of light, m_i is the mass of the satellite, and $\hat{r}_{Si}$ is the unit vector from the satellite to the Sun.

Electromagnetic force

In space, a satellite can become negatively or positively charged by the partly ionized Earth's atmosphere at higher altitudes, trapped high energy particles, and direct sunlight. An electrically charged satellite interacts with the Earth's magnetic field, which results in a Lorentz force. This force may be expressed as [36]:

$$\vec{F}_L = q\vec{v} \times \vec{B} \tag{3.32}$$

where F_L is the Lorentz force, q is the electric charge of the satellite, $\vec{v}$ is the satellite's velocity relative to the Earth's magnetic field, and $\vec{B}$ is the magnetic induction of the geomagnetic field.

Under normal conditions, electromagnetic forces produce very small orbit perturbations. Wakker [36, Chapter 20] shows that in these conditions with a potential of 100 Volts the perturbing acceleration is likely around 11 magnitudes weaker than the Earth's gravitational acceleration. This means that this perturbation does not have to be included in first-order orbital approximations.

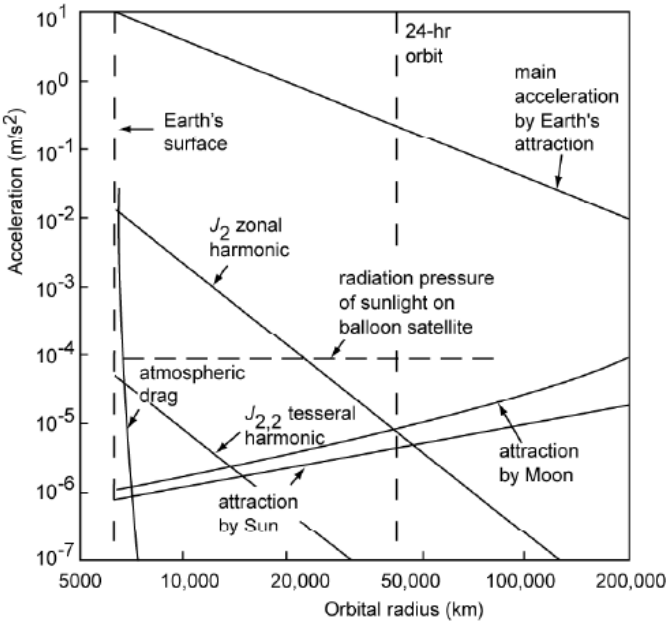

Figure 3.8: This sketch depicts the magnitude of perturbing forces as a function of the orbital radius in Earth orbit. This sketch, adapted from Wakker [36], provides valuable insight into the types and relative strengths of forces that affect satellite motion and is critical for the design and analysis of spacecraft propulsion systems. As can be seen, the J_2 zonal harmonic effects and aerodynamic drag accelerations are in the magnitude range of 1% of the main acceleration by the Earth's attraction.

Perturbation selection

Including all the perturbations in the trajectory simulation model for this thesis would not be practical if the goal is to be able to verify if a propulsion system is able to get the satellite from an SSGTO to a NEA. Therefore, for the Earth's escape trajectory, only perturbations with a magnitude of at least 1%

of the Earth's gravitational attraction are included. From Figure 3.8 it can be concluded that at lower altitudes atmospheric drag and the J_2 zonal harmonic effect are significant forces with respect to the main acceleration by the Earth's gravitational attraction. Therefore only these perturbations will be taken into account.

Optimizing an interplanetary fuel-efficient trajectory to a NEA is very complex even without perturbing forces after the Earth escape trajectory segment. Therefore, it has been decided to exclude all the perturbations for this segment of the trajectory. After the Earth escape trajectory segment, the satellite will start at the position of the Earth and the model will only include the gravitation attraction of the Sun.

3.3.3. Thrust

The thrust of the satellite can be modeled in many different forms. It can be modeled as a stationary variable force and direction which has a maximum thrust and constant specific impulse and required electrical power. In reality, the thrust, power, and specific impulse of the satellite change over time. Throttling the thrust in most cases influences the specific impulse. Over time while thrusting the tank pressure changes which the propulsion system's characteristics. The propulsion system degrades over time due to operations itself, the space environment, or other subsystems which negatively impacts performance. At different positions in space, the available power from the solar panels is different which can be taken into account. And finally, every propulsion system has a thrust profile that isn't perfectly controllable. For this thesis, it is assumed that the incoming power is not proportional to the distance from the Sun squared, but always identical to the power at a distance of 1 AU of the Sun, the thrust is perfectly controllable with a constant maximum thrust and specific impulse. This is assumed because it simplifies the fuel-efficient trajectory design. Furthermore, NEAs closer to the Sun are selected for their significance for autonomous navigation as mentioned in the introduction in chapter 1. Therefore, the actually received power is higher than the assumed power for mission segments closer to the NEA. This means that the assumption made in this thesis leads to a worse case than the real-life scenario. The thrust including the assumed received electrical power can then be expressed as:

$$F_{T,corr} = \begin{cases} F_T, & \text{if } 1 \leq \frac{P_{prop}}{P_e} \\ F_T \frac{P_{prop}}{P_e}, & \text{if } 1 > \frac{P_{prop}}{P_e} > 0 \\ 0, & \text{otherwise} \end{cases}$$
$$P_e = P_0 \tag{3.33}$$

With:

$$\left\{ \frac{\mathrm{d}I_{sp}}{\mathrm{d}t} = 0,\ \frac{\mathrm{d}P_0}{\mathrm{d}t} = 0 \right\}, \quad \forall t \in [t_0, t_f]$$

where P_e is the effective received power, P_0 is the power at the beginning of life and a distance of 1 AU from the Sun and F_T is the maximum thrust power for the propulsion system-rated power requirement P_{prop}.

3.4. Summary

This chapter describes the astrodynamics model required to simulate a fuel-efficient trajectory from Earth to a NEA. The astrodynamics model when combined with an optimal control method in chapter 4, answers the research question RQ1.2.

RQ1.2: What is a practical framework to simulate a fuel-efficient trajectory to a near-Earth asteroid

within 5 years?

The model consists of two components which are selected based on their complexity and accuracy which are the reference system and the dynamics.

3.4.1. Reference system definition

The reference system is necessary to determine the position and velocity of a spacecraft at a certain moment in time. The reference system is a combination of a time definition, a reference frame definition, and the definition of a coordinate system with its kinematics.

Time definition

The used time definition for the interplanetary trajectory will be in epochs or seconds past J2000 because it enables the use of NASA's SPICE toolbox that can be used to obtain the position of celestial bodies such as the Earth and the Sun for a particular time. For the Earth escape trajectory, seconds from the start of the trajectory will be used which is defined as a starting time of zero seconds.

Reference frame definition

The most commonly used reference frames in the context of a trajectory around the Earth are topocentric, geocentric, and heliocentric. For the interplanetary trajectory towards the NEA, the heliocentric 'ECLIPJ2000' reference frame will be used, which is a non-rotating heliocentric frame that can be easily used in combination with NASA's SPICE toolbox. For the Earth escape trajectory, the geocentric non-rotating reference frame will be used because it leads to the simplest kinematics of all the considered options.

Coordinate system definition

The coordinate system can be described in many different representations. The choice of the coordinate system influences the kinematic equations and therefore influences the ease of implementation, the convergence of optimizations, and the computational efficiency.

Out of the five options given in this chapter, CSV provides the simplest mathematical expressions but has the least stability for multi-revolution calculations. MEE and COE are the most stable options for numerical integration, with COE having singularities for certain orbital parameters. PSV3 and SC are intermediate in terms of stability but require more integration steps.

For the interplanetary trajectory, CSV is preferred as the assumed few-revolution nature of the problem doesn't require a more stable system. The kinematic equations for the CSV that follow from the first- and second-time derivatives of the position vector $\vec{p} = [x, y, z]^\top$ in CSV are:

$$\dot{\vec{p}} = [\dot{x}, \dot{y}, \dot{z}]^\top,$$
$$\ddot{\vec{p}} = [\ddot{x}, \ddot{y}, \ddot{z}]^\top$$

For the Earth escape trajectory, SC is chosen because it is expected to be a many-revolution problem for low-thrust systems. The kinematic equations for the SC come from the first- and second-time derivatives of the position vector $\vec{p} = \begin{bmatrix} r & \theta & \varphi \end{bmatrix}^\top$ in SC coordinates:

$$\dot{\vec{p}}\,\hat{r} = \dot{r}$$
$$\dot{\vec{p}}\,\hat{\theta} = r\dot{\theta}$$
$$\dot{\vec{p}}\,\hat{\varphi} = r\dot{\varphi}\sin\theta$$

and

$$\ddot{\vec{p}}\,\hat{r} = \ddot{r} - r\dot{\theta}^2 - r\dot{\varphi}^2 \sin^2\theta$$
$$\ddot{\vec{p}}\,\hat{\theta} = r\ddot{\theta} + 2\dot{r}\dot{\theta} - r\dot{\varphi}^2 \sin\theta\cos\theta$$
$$\ddot{\vec{p}}\,\hat{\varphi} = 2\dot{r}\dot{\varphi}\sin\theta + 2r\dot{\theta}\dot{\varphi}\cos\theta + r\ddot{\varphi}\sin\theta$$

3.4.2. Perturbation definition

The choice of perturbations to include in the trajectory simulation model is an important factor in determining its practicality. In order to verify if a propulsion system can get a satellite from SSGTO to a NEA, only perturbations with a magnitude of at least 1% of the Earth's gravitational attraction are included in the Earth escape trajectory. These perturbations are atmospheric drag and the J_2 zonal harmonic effect. This is done because the trajectory does not have to be more accurate. Only an approximation of the required time to escape an Earth orbit and the required propellant to perform this trajectory is sufficient. Including more perturbations will make the model more complex without significantly impacting the applicability of the results. For the interplanetary trajectory astrodynamics model, all the perturbations are excluded because an interplanetary fuel-efficient trajectory to a NEA is already very challenging to solve. Adding more perturbations can make the model unsolvable without the use of a computing cluster and does not significantly impact the applicability of the results. Therefore, the model only includes the gravitational attraction of the Sun. Also, the starting position of the spacecraft is assumed to be equal to the center of mass of the Earth. In the astrodynamics model for the interplanetary trajectory also the Earth's gravitational attraction is excluded because, in a heliocentric orbit, the Earth's gravitational attraction is considered a perturbing force unless the spacecraft is close enough to the Earth that the Earth's gravitational attraction force exceeds the Sun's gravitational attraction force.

3.4.3. Thrust definition

The thrust of a satellite is a multi-faceted phenomenon that requires consideration of various factors including time-varying thrust, power, specific impulse, degradation of the propulsion system, variations in solar panel power, and the uncertainty of the propulsion system's thrust profile. However, for the purposes of this thesis, a simplified approach is adopted that assumes constant maximum thrust, specific impulse, and received power, with the effective received power being proportional to the available power from the solar panels. Next to this, the available power from the solar panels is assumed to be identical to the power at a distance of 1 AU from the Sun. This is done because the fuel-efficient trajectory design is already very challenging to solve for a simplified thrust model. Furthermore, NEAs closer to the Sun are selected for their significance for autonomous navigation as mentioned in the introduction in chapter 1. Therefore, the actually received power is higher than the assumed power for mission segments closer to the NEA. This means that the assumption made in this thesis leads to a worse case than the real-life scenario.

4

Design of a fuel-efficient fly-by trajectory to a near-Earth Asteroid

In order to prove the feasibility of a selected propulsion system for a fly-by mission to a NEA, it is necessary to simulate a fuel-efficient low-thrust trajectory and high-thrust trajectory for the mission. For a high-thrust trajectory, the fuel-efficient interplanetary trajectory problem is written as a minimum initial velocity trajectory problem. The high-thrust fly-by trajectory is considered a simplified version of the low-thrust trajectory because it does not consider optimal control during the interplanetary trajectory. Therefore, this chapter focuses more on the low-thrust trajectory problem.

Many numerical approaches for solving low-thrust trajectory optimization problems have already been proposed and surveyed in Morante, Rivo, and Soler [37]. However, few of these solutions take into consideration the practicality aspect, which is critical when making accurate and prompt decisions based on simulations. This thesis aims to fill this gap by proposing a framework that not only solves the problem of low-thrust trajectory optimization for propellant-optimal NEA fly-by missions but also provides quick and usable results for preliminary decision-making, particularly for CubeSats using COTS systems.

As previously noted, the optimization of a low-thrust trajectory to a NEA is a challenging task. This mathematical problem can be categorized as an Optimal Control Problem (OCP), where the goal is to find the optimal control path from one state to another. The complexity of this problem arises from the high non-linearity and non-convexity of the low-thrust trajectory problem. To address this challenge, this thesis outlines the design of a practical framework for simulating fuel-efficient low-thrust trajectories to a NEA. In order to solve the research question RQ1.2 this chapter builds on top of the astrodynamics model as described in chapter 3.

RQ1.2: What is a practical framework to simulate a fuel-efficient trajectory to a near-Earth asteroid within 5 years?

Before the framework can be implemented, several decisions must be made beforehand regarding the optimal control solution approach, OCP parameterization method, and solver strategy to be used.

4.1. Fuel-efficient low-thrust optimal control problem

A fuel-efficient low-thrust fly-by trajectory is a well-known problem in the aerospace industry. In the mathematical community, this problem is called an OCP and can be solved using many different methods. A standard OCP can be expressed as:

$$\begin{aligned} &\min_{u(t)} \mathcal{J} = \Phi\left(\vec{\chi}, t\right)\big|_{t=t_f} + \int_{t_0}^{t_f} \mathcal{L}\left(\vec{\chi}, \vec{u}\left(t\right), t\right)\mathrm{d}t \\ &\text{Subject to:} \\ &\{\vec{u} : t \mid \vec{u} \in \mathcal{U}\}, \quad \forall t \in [t_0, t_f] \\ &\dot{\vec{\chi}} = f\left(\vec{\chi}, \vec{u}, t\right) \end{aligned} \tag{4.1}$$

where $\mathcal{J}$ is the performance parameter to minimize, Φ is the terminal cost function, and $\mathcal{L}$ is the path cost function, $\vec{\chi}$ is the state vector and f is the state derivative function. $\mathcal{J}$ is called a Bolza problem unless $\Phi = 0$, in that case, it is called a Lagrange problem or if $\int_{t_0}^{t_f} \mathcal{L}\left(\vec{\chi}, \vec{u}\left(t\right), t\right)\mathrm{d}t = 0$, then it is called a Mayer problem.

For the particular case of a satellite in a heliocentric CSV reference system [36], the state vector $\vec{\chi}$ (including the spacecraft's mass) and state derivative function f can be expressed as:

$$\vec{\chi} = \begin{bmatrix} \vec{r}\left(t\right) \\ \vec{v}\left(t\right) \\ m\left(t\right) \end{bmatrix}, \quad \dot{\vec{\chi}} \equiv f\left(\vec{\chi}, \vec{u}, t\right) = \begin{bmatrix} \frac{T_{\max}(t)\vec{u}(t)}{m(t)} + \sum_{i=1}^{n} \frac{\mu_i(\vec{r}(t)-\vec{r}_i(t))}{\|\vec{r}(t)-\vec{r}_i(t)\|^3} + \vec{a}_p\left(t\right) \\ \vec{v}\left(t\right) \\ -\frac{T_{\max}\|\vec{u}(t)\|}{I_{sp}(t)g_0} \end{bmatrix} \tag{4.2}$$

where $\vec{r}$ is the position vector of the spacecraft, $\vec{v}$ is equal to $\dot{\vec{r}}$ or the velocity vector of the spacecraft, m is the mass of the spacecraft, μ_i is the standard gravitational parameter of a celestial body of a system with n bodies, $\vec{r}_i$ is the position vector of a celestial body, $\vec{a}_p$ are the accelerations due to perturbations, μ_i is the standard gravitational parameter of a body, T_{max} is the thrust of the spacecraft, I_{sp} is the gravimetric propellant specific impulse, and g_0 is the standard gravitational acceleration. In this case, the control vector $\vec{u}$ that controls the throttle and direction of the propulsion system can be expressed as:

$$\{\vec{u} : t \mid \vec{u} \in \mathbb{R}^3 \quad \wedge \quad 0 \leq \|\vec{u}\| \leq 1\}, \quad \forall t \in [t_0, t_f] \tag{4.3}$$

4.1.1. Optimal control solution approach

Approaches for solving the OCP for a satellite in a heliocentric CSV reference system are (Numerical) indirect methods, (Numerical) direct methods, and analytic methods [37], [38].

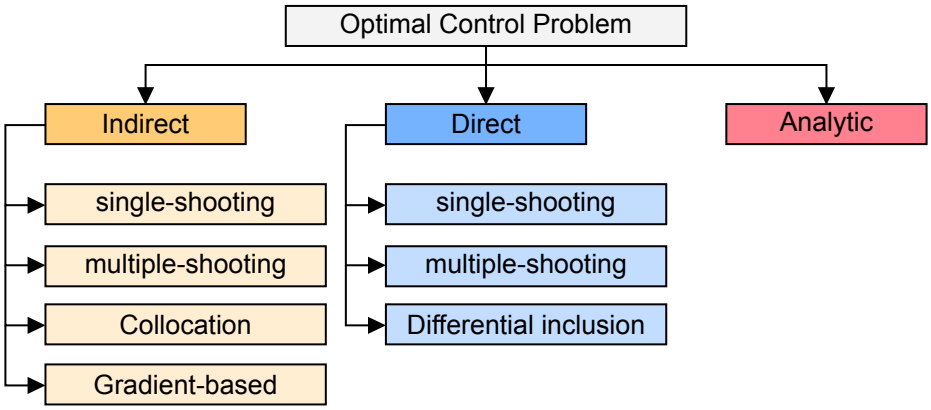

Figure 4.1: Most common optimal control problem solution branches for the low thrust trajectory problem.

Analytic methods do not pose valid solutions, because these solutions require extensive heuristic laws or assumptions to simplify the problem which leads to significantly less accurate results. There have been efforts to solve simple low-thrust trajectory cases analytically. For instance, by fixing the thrust direction or simplifying the boundary conditions. These methods can be convenient for rapid evaluations of low-thrust trajectories or as an initial guess for numerical approaches, but cannot proof if a propulsion system can maneuver to a NEA from SSGTO.

Indirect approach

The indirect approach tries to solve the OCP by implementing a set of rules which describe the behavior of the control input as a function of the state of the system and other parameters such that optimality is guaranteed at every interval. This often changes the OCP to a Two-point boundary value problem (TPBVP) which is optimal if the boundary conditions are met. An example of this is the calculus of variations-based parameterization method and the Lyapunov control parameterization techniques which indirectly solve the OCP instead of optimizing the objective function itself directly.

Indirect approaches can be solved by single-shooting, multiple-shooting, collocation, and gradient-based methods. Of these methods, single-shooting is the most commonly used approach to solve indirect approaches. The other methods although less popular due to their more complex nature, did provide similar successful results [37].

Previous single-shooting methods either solve interplanetary Sun-centered trajectories or planet-centered trajectories such as simple escapes or capture maneuvers. New methods that could go beyond planet-centered trajectories have been developed with MEEs or COEs to overcome this problem, but solving it even on a supercomputer can take hours to days. This limitation can be overcome by using heuristic laws and a patched approach that separates the interplanetary trajectory and the simple escape trajectory [37].

Direct approach

The direct approach tries to solve the OCP by directly rewriting the problem into a nonlinear programming (NLP) problem which directly optimizes the objective function. For example, the optimal control function $\vec{u}(t)$ is then a weighted sum of known functions such as a Fourier series or Taylor series. Then the objective function is evaluated by integration over the domain $[t_0, t_f]$. The weights are then optimized such that the objective function is minimized. Again the direct method can be done by either single-shooting, which uses an optimal control function for the complete trajectory, multiple-shooting, which splits the trajectory in segments which are patched together and optimized separately and differ-

ential inclusion. Differential inclusion tries to find a path that is optimal and satisfies the equations of motions to within a desired accuracy and all required controls to create the path are permissible [37].

OCP solving approach selection

To solve the OCP Chai, Savvaris, Tsourdos, *et al.* [38] and Morante, Rivo, and Soler [37] mention three categories of approaches which are: Indirect optimization, direct optimization and an analytic solution.

As mentioned in Morante, Rivo, and Soler [37], an analytic solution cannot be used, because the problem definition of an asteroid fly-by mission is too complex to deal with analytically directly.

A direct optimization approach tries to find a $u(t)$ that directly minimizes the objective function $\mathcal{J}$. This approach in general does converge better to a 'solution', but it does not guarantee that a global optimum is found unless the problem is complicated by adding more design parameters. The solution for direct optimization approaches for fuel-efficient trajectories results in an objective function that contains a non-zero value for the final mass of the spacecraft unless the propellant mass is also a design parameter that complicates the problem.

Finally, the last approach is an indirect approach which indirectly optimizes the integral performance term $\int_{t_0}^{t_f} \mathcal{L}(\chi, u, t)\mathrm{d}t$. The idea is to find the equations for $u(t)$ that guarantee optimal performance at every instance. This then introduces extra constraints which guarantee optimality when met. When an indirect optimization finds a solution this can be assumed to be a global optimum. This makes it ideal for comparison because it eliminates the factor that one system converged to a sub-optimal solution. Therefore an indirect optimization approach is selected.

4.1.2. Optimal control paramerization

In the problem definition, a list of different state representations is mentioned, however, this does not fully summarize all the variables such as how the control input and direction are formed. Morante, Rivo, and Soler [37] describes six main groups of techniques used to parameterize and synthesize the control function:

Blended Control (BC)

BC calculates the optimal control magnitude and the optimal steering direction based on the position of the satellite such that it maximizes or minimizes the variation of a set of orbital elements. BC is used in problems that do not have a final position constraint but are constrained to a final target orbit instead.

Calculus of Variations (COV)

COV is a way to indirectly optimize a performance function. Which can transform a performance function into a set of rules and costates which describe the control over time for a given initial condition. Given the following performance index $\mathcal{J}$ with states $\vec{\chi} = [\chi_1, \ldots, \chi_n]^\top$, co-states $\vec{\Lambda} = [\lambda_{\chi_1}, \ldots, \lambda_{\chi_n}]^\top$ and control $\vec{u}$:

$$\mathcal{J} = \psi(\vec{\chi}, t)\big|_{t=t_f} + \int_{t_0}^{t_f} \left\{ \mathcal{L}(\vec{\chi}, \vec{u}, t) + \vec{\Lambda}^\top \left(f(\vec{\chi}, \vec{u}, t) - \dot{\vec{\chi}} \right) \right\} \mathrm{d}t \tag{4.4}$$

Using a COV-based approach, the performance can be maximized (or minimized) by introducing a virtual control $\delta\vec{u}$ which produces $\delta\vec{\chi}$ and $\delta\mathcal{J}$. An optimum can then be found for $\vec{\Lambda}$ and $\dot{\vec{\Lambda}}$ which make $\delta\mathcal{J} = 0$. Introducing the Hamiltonian $\mathcal{H}\left(\vec{\chi}, \vec{u}, t, \vec{\Lambda}\right) = \mathcal{L}(\vec{\chi}, \vec{u}, t) + \vec{\Lambda}^\top f(\vec{\chi}, \vec{u}, t)$ and $\delta\vec{u}$ with t_0 and t_f

fixed gives the following relation for optimal control:

$$\delta\mathcal{J} \equiv \left[\left(\frac{\partial\psi}{\partial\vec{\chi}} - \vec{\Lambda}^\top\right)\delta\vec{\chi}\right]_{t=t_f} + \left[\vec{\Lambda}^\top\delta\vec{\chi}\right]_{t=t_0} + \int_{t_0}^{t_f}\left\{\left(\frac{\partial\mathcal{H}}{\partial\vec{\chi}} + \vec{\Lambda}^\top\right)\delta\vec{\chi} + \left(\frac{\partial\mathcal{H}}{\partial\vec{u}}\delta\vec{u}\right)\right\}\mathrm{d}t = 0 \tag{4.5}$$

Solving for $\delta\mathcal{J} = 0$ leads to optimality conditions at the boundaries and differential equations of the Lagrange multipliers that guarantee optimality. During the numerical optimization process, the objective function is often never used during iterations, because it is indirectly optimized using the COV method.

Lyapunov Control (LC)
LC defines a Lyapunov function $V\left(\Delta s(t), W_s\right)$ where $\Delta s(t) = s(t) - s_f$ with s_f the target state. For the OCP, the static controls $W_s \in \mathbb{R}^{n_s}$ are the solution that must be found using an optimization strategy. For stability, the Lyapunov function always must fulfill the condition:

$$\dot{V}\left(W_s\right) = \nabla_s V\left(\Delta s\left(t\right), W_s\right) \cdot f\left(s, u\right) \tag{4.6}$$

Morante, Rivo, and Soler [37] suggests that the thrust steering law is obtained by minimizing the variation of $\dot{V}$ with respect to the control law (i.e., making it as negative as possible) as follows:

$$u^*\left(s, t\right) = \arg\min_u \nabla_s V\left(\Delta s\left(t\right), W_s\right) \cdot f\left(s, u\right) \tag{4.7}$$

The downside of this control strategy is that it requires a state $\vec{\chi}$ parameterization that enables the controller to steer towards the desired final state. If this is not the case, the controller will most likely move toward the desired target in a very inefficient way. Another downside is that there is no way to know beforehand how long it takes to reach the target, which means that also the required time of flight must be found.

Shape-based Approaches (SB)
SB defines the trajectory as a combination of predefined functions. Then the control input at any point in time is found by taking the difference between the trajectory required force for the motion and the actual forces acting on the satellite. The control input of the solution can exceed the maximum available thrust and be outside of the constraint bounds. This should therefore be part of the problem.

Neuro controller (NC) NC uses artificial intelligence to calculate the optimal magnitude and steering direction at any state for a given final state. The downside of this approach is that it requires many iterations or training data to be viable and training for a particular scenario does not guarantee that the NC will be optimal for another scenario. Another downside is that the NC does not guarantee that a global optimum is reached.

Finite Fourier Series (FFS) FFS assumes that the thrust and steering history can be represented by a Fourier series such that:

$$u^*\left(a_k, b_k t\right) = \sum_{k=0} a_k\left(t\right)\cos\left(\frac{2\pi k\theta}{\Delta\theta}\right) + b_k\left(t\right)\cos\left(\frac{2\pi k\theta}{\Delta\theta}\right) \tag{4.8}$$

For this method, θ can be linked to the true anomaly of the orbit and a_k and b_k are the coefficients that need to be solved. Increasing the number of coefficients may increase the accuracy of the representation, however, it will also increase the complexity of the problem which has to be solved. Again, another downside is that there is no way to know beforehand how long it takes to reach the target, which means

that also the required time of flight must be found. Finally, it is known that bang-bang control which switches the thruster on and off at defined intervals is likely the most fuel-efficient way of trajectory control. The proof of this claim can be seen in the derivation of equation 4.26, which indirectly optimizes a fuel-efficient OCP. FFS has a rough time doing this particular control scheme since the propellant-optimal control scheme is a square wave signal which is by definition a discontinuous signal in the time domain. A square wave manifests itself as a wide range of harmonics in the frequency domain. An FFS will cause the Gibbs phenomenon when trying to approach a true square wave signal.

4.1.3. Numerical optimization method

As stated in Morante, Rivo, and Soler [37], the low-thrust trajectory problem can either be solved using a direct or an indirect approach. This problem can then be parameterized using one of the six main parameterization groups as described in Section 4.1.2. After the parameterization selection, the problem can then be rewritten in a numerical optimization problem which is solved by either a single-shooting-, multiple-shooting-, collocation-, gradient-based-, or differential inclusion method. As previously mentioned in the introduction of this chapter, the design space of a low-thrust trajectory optimization problem is often of a highly non-linear and non-convex nature. This should be taken into account when selecting the right numerical optimization method to solve the numerical optimization problem. In general, an optimization method tries to minimize or maximize a function that can consist of one or more objectives. To solve a numerical optimization problem there exist two main optimization method groups: local optimization methods and global optimization methods. The main distinction between local- and global optimization methods is that global optimization methods try to find a minimum over a given design space as opposed to local optimization methods try to find a local minimum given an initial guess.

Local optimization methods evaluate Hessians, gradients, or function values to converge to a minimum starting from an initial design point. Global optimization methods do not always mathematically move towards a minimum but can converge to somewhere near the global minimum of an OCP. Global optimization methods can be further subdivided into deterministic methods that shrink the design space to the global minimum, stochastic methods that try to find a global minimum for a process that involves randomness in the objective or constraints, and heuristic methods that search the design space using an intelligent strategy such as evolutionary algorithms or swarm-based algorithms.

Papers such as Jiang, Baoyin, and Li [39] demonstrate that a hybrid approach that combines both a global optimization strategy and a local optimization method can be used to solve the low thrust trajectory problem or find a solution that is acceptable. This conclusion cannot be taken for granted because the paper does have a flaw in forming the objective. The paper uses an indirect optimization approach which guarantees an optimal solution if the boundary equality constraints are met. However, Jiang, Baoyin, and Li [39] creates an objective function for the numerical optimization which is the Cartesian vector norm of the equality constraints combined with the used propellant at the end of the trajectory. This contradicts the mathematical definition of COV-based indirect optimization. This definition states that the problem of Bolza, which tries to minimize the performance parameter $\mathcal{J}$, becomes a pure boundary value problem when it is indirectly optimized. The hybrid approach proposed by Jiang, Baoyin, and Li [39] is valid because it employs a global optimization method to obtain an initial estimate that is sufficiently close to the global minimum, followed by a local optimization method to converge to that minimum. For this reason, this approach has also been chosen for the framework presented in this thesis.

For the hybrid numerical optimization approach, a particle swarm optimization method is selected as the global optimization method because it is an effective way to generate a suitable initial guess for the

local optimization algorithm. Particle swarm optimization is an artificial intelligence method that uses a population-based approach to search for optimal solutions in a large search space. This method can quickly and efficiently identify promising areas of the search space, providing a good starting point for the local optimization algorithm. For the local optimization method, the Levenberg-Marquardt algorithm is chosen because it is a well-established and widely used local optimization method that is known for its ability to efficiently converge to a global minimum. By combining the particle swarm optimization method with the Levenberg-Marquardt algorithm, the overall optimization process can be both efficient and effective, leading to better convergence.

4.2. Earth escape trajectory

Indirect optimization of a low-thrust trajectory from an SSGTO to a NEA using a COV-based method in the CSV representation is not feasible. According to Jiang, Baoyin, and Li [39], the sensitivity of the initial guess for the optimal Lagrangian multipliers of the COV-based method can make optimization of a trajectory with many revolutions infeasible. Without a suitable initial guess, the numerical iterative optimizer will not converge and a solution cannot be found. In Kluever [40], a similar issue is addressed for an optimal Earth-Moon rendezvous trajectory using a COV-based indirect approach. Kluever suggests dividing the trajectory into segments that can be optimized separately to improve solvability. However, the Earth escape itself can be considered a many-revolution low-thrust trajectory problem, which cannot be optimized using an indirect COV-based method. As a result, this segment must be simulated using heuristic laws, which provide an estimate of the amount of propellant required to escape Earth and the corresponding time but are not optimal.

4.2.1. Reference system and dynamics

For the Earth escape trajectory a non-rotating geocentric reference frame in the center of the Earth is chosen with the x-axis towards the First Point of Aries, the XY-plane oriented identically to the equatorial plane, and the z-axis in the direction of the Earth's north pole. The time is not defined with respect to a particular date, but in seconds from the satellite's decoupling and detumbling or the start of the Earth escape trajectory segment. After an interplanetary heliocentric trajectory has been found to the NEA, this Earth escape trajectory segment time can then be attached to the start of the interplanetary heliocentric trajectory to find a specific time interval for the complete mission.

The coordinate system of the Earth escape trajectory segment is chosen to be SC. However, since the Earth escape trajectory is assumed to be aligned with the Earth's elliptical plane, SC reduces to polar coordinates which results in the simplified state vector of the satellite:

$$\vec{\chi} = \left[r, \varphi, \dot{r}, \dot{\varphi}, m\right]^\top \tag{4.9}$$

The dynamics of the satellite in polar coordinates can be found by eliminating the inclination terms from the SC representation dynamics:

$$\begin{aligned} \ddot{r} =& a_r + r\dot{\varphi}^2 \\ \ddot{\varphi} =& \frac{a_\varphi}{r} - \frac{2\dot{r}\dot{\varphi}}{r} \\ \dot{m} =& -u\frac{T_{max}}{I_{sp}g_0} \end{aligned} \tag{4.10}$$

where a_r and a_φ are accelerations working on the satellite in the direction of r and φ.

Including the gravitational attraction of the Earth, the worst case J_2 effect at the equatorial plane

and the aerodynamic drag a_r can be expressed as:

$$a_r = -\frac{\mu}{r^2} - 2\left[\frac{\mu}{r} J_2 \left(\frac{R}{r}\right)^2\right] - C_D \frac{1}{2}\rho \frac{A}{m}\dot{r}\|\dot{r}\| + u\frac{T_{max}}{m}\cos(\alpha) \tag{4.11}$$

and a_φ is expressed as:

$$a_\varphi = -C_D \frac{1}{2}\rho \frac{A}{m} r\dot{\varphi}\|\dot{\varphi}\| + u\frac{T_{max}}{rm}\sin(\alpha) \tag{4.12}$$

where α is the optimal thrust direction, u is the optimal thrust throttle and T_{max} is the maximum thrust force. Notice that only for the J_2 effect it is assumed that the orbit is in the equatorial plane because it leads to a worst-case scenario. This is of course not the case but this assumption enables the simplification of the three-dimensional SC to two-dimensional polar coordinates while resulting in the worst-case system requirements.

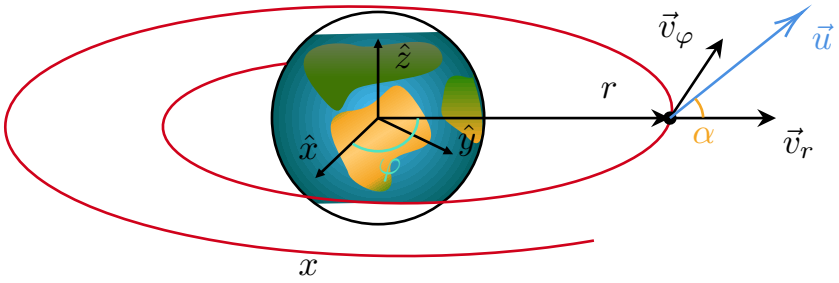

Figure 4.2: The figure illustrates a polar visualization of an Earth escape trajectory, showcasing the optimal thrusting direction (α) and thrust vector ($\vec{u}$) for the spacecraft. The illustrated trajectory depicts the efficient path taken by the spacecraft to leave Earth's gravitational pull, with the optimal thrust direction and vector ensuring maximum efficiency and propellant conservation.

4.2.2. Heuristic thrusting law

It is assumed that the thrust is continuous and maximum because it would otherwise take too long to escape an Earth orbit. Some propulsion systems would not be able to continuously thrust due to overheating itself or other systems. Also, some systems can only operate in intervals. For this thesis, however, it is assumed that all propulsion systems can be operated continuously to be able to compare each system If it is assumed that thrust influences orbital energy the most when thrusting parallel to the velocity direction of the spacecraft, then the least propellant is needed when thrusting in this direction independent of the shape of the orbit. This assumption follows from the specific orbital energy equation [36]:

$$\varepsilon = \tfrac{1}{2}\vec{v}\cdot\vec{v} - \frac{\mu}{\|\vec{r}\|} \tag{4.13}$$

Taking the first-time derivative of this relation gives:

$$\dot{\varepsilon} = \vec{v}\cdot\dot{\vec{v}} - \frac{\mu\vec{r}\cdot\dot{\vec{r}}}{\|\vec{r}\|^3} \equiv \vec{v}\cdot\dot{\vec{v}} - \frac{\mu\vec{r}\cdot\vec{v}}{\|\vec{r}\|^3} \tag{4.14}$$

Then the change of the specific energy which occurs by any acceleration is maximum when $\vec{v}$ is maximum and the acceleration vector is in the direction of $\vec{v}$ such that the optimal escape thrust strategy is:

$$\vec{u}^* = \frac{\vec{v}}{\|\vec{v}\|} \tag{4.15}$$

This means that continuous thrusting in the direction of the velocity vector is the most fuel-efficient way to escape an Earth orbit. Combined with the assumption that continuous maximum thrusting is optimal,

the optimal thrusting law can then be expressed as:

$$\{\alpha^* = \mathsf{atan2}\left(r\dot{\varphi}, \dot{r}\right),\ u^* = 1\}, \quad \forall t \in [t_0, t_f] \tag{4.16}$$

where atan2 is defined as:

$$\mathsf{atan2}\left(y, x\right) = \begin{cases} \mathsf{arctan}\left(\frac{y}{x}\right); & x > 0 \\ \mathsf{arctan}\left(\frac{y}{x}\right) + \pi; & x < 0,\ y \geq 0 \\ \mathsf{arctan}\left(\frac{y}{x}\right) - \pi; & x < 0,\ y < 0 \\ +\frac{\pi}{2}; & x = 0,\ y > 0 \\ -\frac{\pi}{2}; & x = 0,\ y < 0 \\ \mathsf{undefined}; & x = 0,\ y = 0 \end{cases} \tag{4.17}$$

4.3. Near-Earth asteroid fly-by trajectory

In Jiang, Baoyin, and Li [39] an indirect single-shooting COV-based hybrid approach for an interplanetary rendezvous trajectory is solved for both fuel- and energy-optimal design objectives. Bertrand and Epenoy [41] addresses the fuel-efficient design objective as a more complex problem using Pontryagin's maximum principle because in short, the optimal control solution should lead to a discontinuous bang-bang control. However, COV requires the resulting control function to be continuous and differentiable. This problem is then solved in Bertrand and Epenoy [41] by introducing the perturbed performance index which combines the fuel- and energy-optimal objective in a single objective. If the fuel-efficient performance index $\mathcal{J}_f$ and energy index $\mathcal{J}_e$ can be expressed as:

$$\mathcal{J}_f = \frac{T_{max}}{I_{sp} g_0} \int_{t_0}^{t_f} \{\|\vec{u}\|\} \mathsf{d}t \tag{4.18a}$$

$$\mathcal{J}_e = \frac{T_{max}}{I_{sp} g_0} \int_{t_0}^{t_f} \left\{\|\vec{u}\|^2\right\} \mathsf{d}t \tag{4.18b}$$

Then the perturbed performance index can be expressed as:

$$\mathcal{J} = \frac{T_{max}}{I_{sp} g_0} \int_{t_0}^{t_f} \{\|\vec{u}\| - \varepsilon \|\vec{u}\| \left[1 - \|\vec{u}\|\right]\} \mathsf{d}t \tag{4.19}$$

where ε is the fuel-to-energy-optimality-ratio with $\{0 \leq \varepsilon \leq 1\}$.

Bertrand and Epenoy [41] states that this particular performance index would be able to produce a solution if present. However, if the control law must adhere to $0 \leq \|\vec{u}\| \leq 1$. The paper proposes the use of a logarithmic penalty. The idea behind using a logarithmic penalty is to force the control magnitude to be within the range of zero to one without causing discontinuities. The new perturbed fuel-efficient performance index can then be expressed as:

$$\mathcal{J} = \frac{T_{max}}{I_{sp} g_0} \int_{t_0}^{t_f} \{\|\vec{u}\| - \varepsilon \left[(-\|\vec{u}\|) \ln\left(\|\vec{u}\|\right) - (1 - \|\vec{u}\|) \ln\left(1 - \|\vec{u}\|\right)\right]\} \mathsf{d}t \tag{4.20}$$

4.3.1. Reference system and dynamics

For the interplanetary trajectory to the NEA, a non-rotating heliocentric (barycentric) reference frame (ECLIPJ2000) is used with the x-axis pointing towards the First Point of Aries, the XY-plane oriented identically to the Earth's elliptical plane and the z-axis in the direction of the positive revolution direction of the Earth's orbit around the Sun. The time is defined in epochs or seconds past J2000 (January 1, 2000, at 12:00, terrestrial time).

Since only CEO and MEE will have significant improvements in terms of numerical integration stability, but also a significantly more complex dynamics and control definition, CSV is used to describe the motion of the satellite in the reference frame. The state of the satellite can then be defined by its position, velocity, and mass in CSV:

$$\vec{\chi}(t) = \left[x(t), y(t), z(t), \dot{x}(t), \dot{y}(t), \dot{z}(t), m(t)\right]^\top \tag{4.21}$$

Introducing $\vec{r}(t) = \left[x(t), y(t), z(t)\right]^\top$ and $\vec{v}(t) = \left[\dot{x}(t), \dot{y}(t), \dot{z}(t)\right]^\top$ simplifies $\vec{\chi}$ to:

$$\vec{\chi}(t) = \left[\vec{r}(t), \vec{v}(t), m(t)\right]^\top \tag{4.22}$$

Assuming only the gravitational pulling of the Sun and the thrust of the propulsion system play a significant role in the acceleration of the satellite the dynamics can be expressed as:

$$\dot{\vec{\chi}}\left(\vec{\chi}(t), \vec{u}(t), t\right) = \begin{bmatrix} \vec{v}(t) \\ \frac{\mu_\odot(\vec{r}(t)-\vec{r}_\odot(t))}{\|\vec{r}(t)-\vec{r}_\odot(t)\|^3} + \frac{T_{\max}}{m(t)}\vec{u}(t) \\ -\frac{T_{\max}\|\vec{u}(t)\|}{I_{sp}g_0} \end{bmatrix} \tag{4.23}$$

where

4.3.2. Optimal control law

To find the optimal control law the Hamiltonian as defined in the COV method has to be defined. With the performance index defined as $\mathcal{J} = \frac{T_{max}}{I_{sp}g_0}\int_{t_0}^{t_f}\{y(\vec{\chi}(t), \vec{u}(t), t)\}\mathrm{d}t$ the Hamiltonian can be expressed as:

$$\mathcal{H}\left(\vec{\chi}, \vec{u}, \vec{\Lambda}, t\right) = \frac{T_{\max}}{I_{sp}g_0}\left[y(\vec{\chi}, \vec{u}, t)\right] + \vec{\lambda}_r^\top\vec{v} + \vec{\lambda}_v^\top\left(\frac{T_{\max}}{m}\vec{u} + \vec{a}_p\right) - \lambda_m\frac{T_{\max}}{I_{sp}g_0}\|\vec{u}\| \tag{4.24}$$

From the COV optimality condition a control function is optimal if $\mathcal{H}\left(\vec{\chi}^*, \vec{u}^*, \vec{\Lambda}^*, t\right) \leq \mathcal{H}\left(\vec{\chi}^*, \vec{u}, \vec{\Lambda}^*, t\right)$. The optimal control function $\vec{u}^*$ can then be expressed as:

$$\vec{u}^* = \arg\min_{\vec{u}} \frac{T_{\max}}{I_{sp}g_0}y(\vec{\chi}, \vec{u}, t) + \vec{\lambda}_v^\top\frac{T_{\max}}{m}\vec{u} - \lambda_m\frac{T_{\max}}{I_{sp}g_0}\|\vec{u}\| \tag{4.25}$$

where $y(\vec{\chi}, \vec{u}, t)$ is the integral performance function.

Fuel-efficient control law

If the fuel-efficient integral performance function is used such that $y(\vec{\chi}, \vec{u}, t) = \|\vec{u}\|$ and the control is constrained by $0 \leq \|u\| \leq 1$, then the optimal control law can be expressed as [41]:

$$\vec{u}^* = -\beta_f(t)\frac{\vec{\lambda}_v}{\left\|\vec{\lambda}_v\right\|} \tag{4.26}$$

where $\beta_f(t)$ is defined as:

$$\beta_f(t) = \begin{cases} 1; & SF\left(\vec{\chi}, \vec{\Lambda}, t\right) < 0 \\ 0; & SF\left(\vec{\chi}, \vec{\Lambda}, t\right) > 0 \\ 0; & SF\left(\vec{\chi}, \vec{\Lambda}, t\right) = 0 \end{cases} \tag{4.27a}$$

$$SF\left(\vec{\chi}, \vec{\Lambda}, t\right) = 1 - \|\lambda_v\| \frac{I_{sp} g_0}{m} - \lambda_m \tag{4.27b}$$

where β_f is a scalar thrust throttle function that depends on the switching function $SF\left(\vec{\chi}, \vec{\Lambda}, t\right)$. It can be seen that this leads to a bang-bang control law, which is discontinuous.

Energy-efficient control law

If the energy-efficient integral performance function is used such that $y(\vec{\chi}, \vec{u}, t) = \|\vec{u}\|^2$ and the control is constrained by $0 \leq \|u\| \leq 1$, then the optimal control law can be written as [41]:

$$\vec{u}^* = \arg\min_{\vec{u}} \frac{T_{\max}}{I_{sp} g_0} \|\vec{u}\|^2 + \vec{\lambda}_v^\top \frac{T_{\max}}{m} \vec{u} - \lambda_m \frac{T_{\max}}{I_{sp} g_0} \|\vec{u}\| \tag{4.28}$$

which can be solved using the COV optimality condition:

$$\frac{\partial \mathcal{H}}{\partial \vec{u}} = 0 \tag{4.29}$$

Combining Equation 4.28 and Equation 4.29 leads to:

$$2\vec{u} \frac{T_{\max}}{I_{sp} g_0} + \vec{\lambda}_v \frac{T_{\max}}{m} - \lambda_m \frac{T_{\max}}{I_{sp} g_0} \frac{\vec{u}}{\|\vec{u}\|} = 0 \tag{4.30}$$

Using the same form as the propellant-optimal or fuel-efficient case gives:

$$\vec{u}^* = -\beta_e(t) \frac{\vec{\lambda}_v}{\left\|\vec{\lambda}_v\right\|} \tag{4.31}$$

This leads to:

$$\begin{aligned} -2\beta_e \frac{\vec{\lambda}_v}{\left\|\vec{\lambda}_v\right\|} \frac{T_{\max}}{I_{sp} g_0} + \left\|\vec{\lambda}_v\right\| \frac{\vec{\lambda}_v}{\left\|\vec{\lambda}_v\right\|} \frac{T_{\max}}{m} + \lambda_m \frac{T_{\max}}{I_{sp} g_0} \frac{\vec{\lambda}_v}{\left\|\vec{\lambda}_v\right\|} = 0 \\ \frac{\vec{\lambda}_v}{\left\|\vec{\lambda}_v\right\|} \left(\left\|\vec{\lambda}_v\right\| \frac{I_{sp} g_0}{m} + \lambda_m - 2\beta_e \right) = 0 \end{aligned} \tag{4.32}$$

where β_e is a scalar thrust throttle function that depends on the switching function $SF\left(\vec{\chi}, \vec{\Lambda}, t\right)$. Solving for β_e when $\frac{\vec{\lambda}_v}{\|\vec{\lambda}_v\|} \neq 0$ and constraining the control to $0 \leq \|u\| \leq 1$ results in an expression for β_e as a function of the switching function $SF\left(\vec{\chi}, \vec{\Lambda}, t\right)$:

$$\beta_e(t) = \begin{cases} 1; & SF\left(\vec{\chi}, \vec{\Lambda}, t\right) > 1 \\ 0; & SF\left(\vec{\chi}, \vec{\Lambda}, t\right) < 0 \\ SF\left(\vec{\chi}, \vec{\Lambda}, t\right); & 0 \leq SF\left(\vec{\chi}, \vec{\Lambda}, t\right) \leq 1 \end{cases} \tag{4.33a}$$

$$SF\left(\vec{\chi}, \vec{\Lambda}, t\right) = \frac{\left\|\vec{\lambda}_v\right\| \frac{I_{sp} g_0}{m} + \lambda_m}{2} \tag{4.33b}$$

Perturbed fuel-efficient control law

If the perturbed fuel-efficient integral performance function is used such that $y\left(\vec{\chi},\vec{u},t\right)=\ldots$ $\|\vec{u}\|-\varepsilon\left[(-\|\vec{u}\|)\ln\left(\|\vec{u}\|\right)-(1-\|\vec{u}\|)\ln\left(1-\|\vec{u}\|\right)\right]$ and the control is constrained by $0\leq\|u\|\leq 1$, then the optimal control law can be found by [41]:

$$\begin{aligned}\vec{u}^{*}=\arg\min_{\vec{u}}\frac{T_{\max}}{I_{sp}g_0}&\left\{\|\vec{u}\|-\varepsilon\left[(-\|\vec{u}\|)\ln\left(\|\vec{u}\|\right)-(1-\|\vec{u}\|)\ln\left(1-\|\vec{u}\|\right)\right]\right\}+\ldots\\&\vec{\lambda}_v\frac{T_{\max}}{m}\vec{u}-\lambda_m\frac{T_{\max}}{I_{sp}g_0}\|\vec{u}\|\end{aligned}\tag{4.34}$$

which can be solved using the COV optimality condition:

$$\frac{\partial\mathcal{H}}{\partial\vec{u}}=0\tag{4.35}$$

Combining Equation 4.34 and Equation 4.35 leads to:

$$\frac{T_{\max}}{I_{sp}g_0}\frac{\vec{u}}{\|\vec{u}\|}\left\{1-\varepsilon\ln\left(\frac{1-\|\vec{u}\|}{\|\vec{u}\|}\right)-\lambda_m\frac{T_{\max}}{I_{sp}g_0}\right\}+\vec{\lambda}_v\frac{T_{\max}}{m}=0\tag{4.36}$$

Substituting the optimal control direction $\vec{u}^{*}=-\beta\left(t\right)\frac{\vec{\lambda}_v}{\|\vec{\lambda}_v\|}$ in the found expression the optimal thrust throttle function β can be expressed as:

$$\begin{aligned}\frac{\vec{\lambda}_v}{\left\|\vec{\lambda}_v\right\|}\left\{1-\varepsilon\ln\left(\frac{1-\beta}{\beta}\right)-\lambda_m-\left\|\vec{\lambda}_v\right\|\frac{I_{sp}g_0}{m}\right\}&=0\\\ln\left(\frac{1-\beta}{\beta}\right)&=\frac{1-\lambda_m-\left\|\vec{\lambda}_v\right\|\frac{I_{sp}g_0}{m}}{\varepsilon}\\\beta&=\frac{1}{1+e^{\frac{1-SF\left(\vec{\chi},\vec{\Lambda},t\right)}{\varepsilon}}}\end{aligned}\tag{4.37}$$

where $SF\left(\vec{\chi},\vec{\Lambda},t\right)$ is the switching function:

$$SF\left(\vec{\chi},\vec{\Lambda},t\right)=\left\|\vec{\lambda}_v\right\|\frac{I_{sp}g_0}{m}+\lambda_m\tag{4.38}$$

4.3.3. Boundary conditions

For a fly-by trajectory to a NEA, the satellite and the target asteroid meet at a certain time t_f. In this particular case, the time of flight is also unknown. To solve this using a COV-based method, consider the following dynamical system for a fly-by trajectory to a NEA:

$$\dot{\vec{\chi}}\left(t\right)=f\left(\vec{\chi}\left(t\right),\vec{u}\left(t\right),t\right)\ ;\quad\vec{\chi}\left(t_0\right)\text{ given},\quad t_0\leq t\leq t_f\tag{4.39}$$

where $\vec{\chi}\left(t\right)$ is the state vector of the satellite with dimension n and $\vec{u}\left(t\right)$ the control vector with dimension m. Now consider the perturbed fuel-efficient performance index including equality constraints as:

$$\mathcal{J}=\psi\left(\vec{\chi}_{t_f},t_f\right)+\frac{T_{max}}{I_{sp}g_0}\int_{t_0}^{t_f}y\left(\vec{\chi}\left(t\right),\vec{u}\left(t\right),t\right)\mathrm{d}t\tag{4.40}$$

where $y\left(\vec{\chi}\left(t\right),\vec{u}\left(t\right),t\right)=\|\vec{u}\left(t\right)\|-\varepsilon\left[(-\|\vec{u}\left(t\right)\|)\ln\left(\|\vec{u}\left(t\right)\|\right)-(1-\|\vec{u}\left(t\right)\|)\ln\left(1-\|\vec{u}\left(t\right)\|\right)\right]$ is the perturbed fuel-efficient integral performance index and $\psi\left(\vec{\chi}_{t_f},t_f\right)$ is a terminal constraint function at the terminal time t_f when the satellite must fly by the NEA. ϕ for a fly-by trajectory can be expressed as:

$$\vec{\psi}\left(\vec{\chi}_{t_f},t_f\right)\equiv\vec{r}\left(t_f\right)-\vec{r}_{obj}\left(t_f\right)=0\tag{4.41}$$

where $\vec{r}$ is the position of the satellite and $\vec{r}_{obj}$ is the position of the NEA. Since it is a vector that contains equality constraint functions, the norm has to be taken when adding to the performance index, because the performance index cannot contain terms in the range of $[\infty, \infty]$, but only $[0, \infty]$.

The objective is to minimize $\mathcal{J}$ using $\vec{u}(t)$. Adjoining the differential equations of Equation 4.39 to $\mathcal{J}$ with the Lagrangian multipliers $\Lambda(t) = [\lambda_1, \ldots, \lambda_n]$ results in:

$$\mathcal{J} = \psi\left(\vec{\chi}_{t_f}, t_f\right) + \frac{T_{max}}{I_{sp} g_0} \int_{t_0}^{t_f} \left[y\left(\vec{\chi}(t), \vec{u}(t), t\right) + \Lambda^\top(t) \left\{ f\left(\vec{\chi}(t), \vec{u}(t), t\right) - \dot{\vec{\chi}}(t) \right\} \right] \mathrm{d}t \tag{4.42}$$

For convenience the Hamiltonian $\mathcal{H}$ in defined as:

$$\mathcal{H}\left(\vec{\chi}(t), \Lambda(t), \vec{u}(t), t\right) = y\left(\vec{\chi}(t), \vec{u}(t), t\right) + \Lambda^\top(t) f\left(\vec{\chi}(t), \vec{u}(t), t\right) \tag{4.43}$$

$\mathcal{J}$ can thus be expressed as:

$$\mathcal{J} = \psi\left(\vec{\chi}_{t_f}, t_f\right) + \frac{T_{max}}{I_{sp} g_0} \int_{t_0}^{t_f} \left[\mathcal{H}\left(\vec{\chi}(t), \Lambda(t), \vec{u}(t), t\right) - \Lambda^\top(t) \dot{\vec{\chi}}(t) \right] \mathrm{d}t \tag{4.44}$$

Integration by parts of the last term in the integral results in:

$$\begin{aligned} \mathcal{J} = \psi\left(\vec{\chi}_{t_f}, t_f\right) + \frac{T_{max}}{I_{sp} g_0} \int_{t_0}^{t_f} \left[\mathcal{H}\left(\vec{\chi}(t), \Lambda(t), \vec{u}(t), t\right) - \dot{\Lambda}^\top(t) \vec{\chi}(t) \right] \mathrm{d}t + \ldots \\ \Lambda^\top(t_0) \vec{\chi}(t_0) - \Lambda^\top(t_f) \vec{\chi}(t_f) \end{aligned} \tag{4.45}$$

To minimize (or maximize) $\mathcal{J}$, the variation of $u(t)$ or δu can be considered which results in $\delta\mathcal{J}$. For fixed t_0 and t_f, $\delta\mathcal{J}$ can be expressed as:

$$\delta\mathcal{J} = \left[\left(\frac{\partial\psi}{\partial\vec{\chi}} - \Lambda^\top(t) \right) \delta\vec{\chi} \right]_{t=t_f} + \left[\Lambda^\top(t) \delta\vec{\chi} \right]_{t=t_0} + \frac{T_{max}}{I_{sp} g_0} \int_{t_0}^{t_f} \left[\left(\frac{\partial\mathcal{H}}{\partial\vec{\chi}} - \dot{\Lambda}^\top(t) \right) \delta\vec{\chi} + \frac{\partial\mathcal{H}}{\partial\vec{u}} \delta\vec{u} \right] \mathrm{d}t \tag{4.46}$$

Now Λ, $\dot{\Lambda}$, and the control must be chosen such that every term of the equation cancels out and $\delta\mathcal{J} = 0$. This results in the following optimality conditions [42]:

$$\dot{\Lambda} = -\frac{\partial\mathcal{H}}{\partial\vec{\chi}} \tag{4.47a}$$

$$\frac{\partial\mathcal{H}}{\partial\vec{u}} = 0 \tag{4.47b}$$

$$\Lambda_j(t_f) = \begin{cases} \text{free} ; & \delta\chi_j = 0 \\ \frac{\partial\psi}{\partial\chi_j}\big|_{t=t_f} ; & \delta\chi_j \neq 0 \end{cases} \tag{4.47c}$$

And if $\vec{\chi}(t_0)$ is known or $[\delta\vec{\chi}]_{t=t_0} = 0$ then $\Lambda(t_0)$ is free.

From the found optimality conditions it can be seen that Λ is of the same dimension as $\vec{\chi}$. For simplicity the dimensions in Λ are defined as co-variables to their true state counterparts such that Λ can be expressed as:

$$\Lambda = \begin{bmatrix} \vec{\lambda}_r \\ \vec{\lambda}_v \\ \lambda_m \end{bmatrix} \tag{4.48}$$

Combining the performance index, the Hamiltonian definition, and the dynamics of the spacecraft the Hamiltonian can be expressed as:

$$\mathcal{H}\left(x,u,t,\Lambda\right)=\frac{T_{max}}{I_{sp}\cdot g_0}\left\{\vec{u}\left(t\right)-\varepsilon\left[\left(-\vec{u}\left(t\right)\right)\ln\left(\vec{u}\left(t\right)\right)-\left(1-\vec{u}\left(t\right)\right)\ln\left(1-\vec{u}\left(t\right)\right)\right]\right\}+\ldots$$
$$\Lambda^{\top}\begin{bmatrix}\vec{v}\left(t\right)\\ \frac{\mu_{\odot}\left(\vec{r}(t)-\vec{r}_{\odot}(t)\right)}{\left\|\vec{r}(t)-\vec{r}_{\odot}(t)\right\|^{3}}+\frac{T_{\max}}{m(t)}\vec{u}\left(t\right)\\ -\frac{T_{\max}\left\|\vec{u}(t)\right\|}{I_{sp}g_0}\end{bmatrix} \tag{4.49}$$

The optimal thrust direction and magnitude are already found in equation 4.37 and 4.38 such that the optimal thrust magnitude can be written as:

$$u^{*}=\beta=\frac{1}{1+e^{\frac{1-SF(\vec{\chi},\Lambda)}{\varepsilon}}} \tag{4.50a}$$

$$SF\left(\vec{\chi},\Lambda\right)=\left\|\vec{\lambda}_v\right\|\frac{I_{sp}g_0}{m}+\lambda_m \tag{4.50b}$$

and the optimal steering law can be defined as:

$$\vec{\alpha}=-\frac{\vec{\lambda}_v}{\left\|\vec{\lambda}_v\right\|} \tag{4.51}$$

Now that the optimal control magnitude and direction are found in terms of the state and the Lagrange multipliers, the derivatives of the Lagrange multipliers must be found which can be integrated over time next to the state variables to find the optimal control for the full trajectory. The derivatives of the Lagrange multipliers can be $\dot{\Lambda}=-\frac{\partial\mathcal{H}}{\partial\vec{\chi}}$ expressed as:

$$\dot{\vec{\lambda}}_r=-\sum_{i=1}^{n}\left[\frac{\mu_i\vec{\lambda}_v}{\left\|\vec{r}-\vec{r}_i\right\|^{3}}-\frac{3\mu_i[\vec{r}-\vec{r}_i]^{\top}\vec{\lambda}_v}{\left\|\vec{r}-\vec{r}_i\right\|^{5}}\left(\vec{r}-\vec{r}_i\right)\right] \tag{4.52a}$$

$$\dot{\vec{\lambda}}_v=-\vec{\lambda}_r \tag{4.52b}$$

$$\dot{\lambda_m}=-\left\|\vec{\lambda}_v\right\|\frac{T_{max}}{m^{2}}u \tag{4.52c}$$

And finally, the boundary conditions for the states and co-states can be expressed as:

$$\vec{\psi}\left(\vec{\chi}_{t_f},t_f\right)\equiv\vec{r}\left(t_f\right)-\vec{r}_{obj}\left(t_f\right)=0 \tag{4.53a}$$

$$\vec{\lambda_r}\left(t_f\right)=\text{free} \tag{4.53b}$$

$$\vec{\lambda_v}\left(t_f\right)=\left.\frac{\psi}{\partial\vec{v}}\right|_{t=t_f}\equiv 0 \tag{4.53c}$$

$$\lambda_m\left(t_f\right)=\left.\frac{\psi}{\partial m}\right|_{t=t_f}\equiv 0 \tag{4.53d}$$

One particularly interesting aspect of the co-state equations, optimal thrust function, and boundary constraints is that they are all scaled by one or more co-states. What this means is that the co-state derivatives, optimal thrust function, and boundary constraints only depend on the ratios of the co-states and not their absolute values. This knowledge can be used when optimizing for the initial co-states because the space in which the initial co-states exist can be constrained to a unit hyper-sphere which drastically reduces the design space for the numerical optimization. Jiang, Baoyin, and Li [39] also found this relation for a rendezvous mission and uses this method of design space reduction for a Mars rendezvous mission using a COV-based fuel-efficient low thrust trajectory design.

4.4. High-thrust fly-by trajectory

The interplanetary trajectory fly-by trajectory to the target asteroid in high-thrust propulsion systems can be modeled as a two-point boundary value problem with design parameters: the total time of flight and the initial velocity with respect to Earth. The solution to this two-point boundary value problem can be the characteristic energy objective at the need of the Earth escape trajectory which incorporates the principles of the Oberth effect. The Oberth effect considers that a spacecraft's velocity influences the efficiency of its propulsion system. It concludes that a higher velocity results in a greater energy gain from a fixed amount of propellant. A high-thrust system can use more of its propellant close or near the perigee when the satellite's relative velocity with respect to Earth is maximum, thereby making the most of the Oberth effect.

The boundary value problem for the interplanetary trajectory to the target asteroid has the following boundary conditions that should be met:

$$\vec{r}(t_f) - \vec{r}_{obj}(t_f) = 0 \tag{4.54}$$

subject to the objective:

$$\min_{\vec{\xi}} \mathcal{J} = V_{\infty_e} \tag{4.55}$$

And the design parameters for this problem are:

$$\vec{\xi} = \begin{bmatrix} \Delta t, & v_{\infty_e}, & \theta_v, & \phi_v, \end{bmatrix}^\top \tag{4.56}$$

where the initial velocity relative to Earth is defined as:

$$\vec{v}_{rel,\oplus}(t_f - \Delta t) = \begin{bmatrix} v_{\infty_e} \sin\theta_v \cos\phi_v \\ v_{\infty_e} \sin\theta_v \sin\phi_v \\ v_{\infty_e} \cos\theta_v \end{bmatrix} \tag{4.57}$$

Since the problem is a non-convex, non-linear problem, an initial guess can be made by using particle swarm optimization. This requires the objective to be a scalar value consisting of both objectives and constraints. A way to solve this is to rewrite the objective in the following form:

$$\min_{\vec{\xi}} \mathcal{J}_{pso} = \|\vec{r}(t_f) - \vec{r}_{obj}(t_f)\| (1 + v_{\infty_e}) \tag{4.58}$$

$(1 + v_{\infty_e})$ is chosen such that the particle swarm optimization can never directly minimize the objective function by setting v_{∞_e} to zero. And by using $\|\vec{r}(t_f) - \vec{r}_{obj}(t_f)\|$ the optimizer is forced to minimize the distance between the target asteroid and the satellite. Since it is almost impossible to get $\|\vec{r}(t_f) - \vec{r}_{obj}(t_f)\| = 0$, this can be used directly in the objective.

4.4.1. Earth escape velocity

When the minimum v_{∞_e} is found, the Earth escape trajectory to reach the characteristic energy $C_3 = v_{\infty_e}^2$ can be solved using the optimal Earth escape trajectory using heuristic laws starting from perigee. The characteristic energy of the satellite around Earth is equal to two times the specific orbital energy if a two-body problem is assumed. This leads to the following condition to stop the integration of the Earth escape trajectory segment simulation:

$$C_3 \leq \|\vec{v}\|^2 - \frac{2\mu}{r} \tag{4.59}$$

where μ is the standard gravitational parameter of Earth, r is the distance from the Earth's center of mass, and v is the velocity of the satellite relative to Earth. Solving this simulation results in the required propellant mass and combined with the interplanetary trajectory the total time of flight to reach the target asteroid [36].

4.4.2. Heuristic thrusting law

For low-thrust systems, it is assumed that the thrust is continuous and maximum because it would otherwise take too long to escape an Earth orbit. However, for high-thrust propulsion systems, the thrust does not have to be continuous over the complete Earth escape trajectory segment. Thrust influences orbital energy the most when thrusting parallel to the velocity direction of the spacecraft, then the least propellant is needed when thrusting in this direction independent of the shape of the orbit which results in Equation 4.15. Additionally, if a high-thrust system uses more of its propellant near the perigee when the satellite's relative velocity with respect to Earth is maximum, it also is more propellant-efficient. Assuming that the orbital angular position of the perigee does not change, the thrust can be throttled on and off in the direction of the velocity as defined in Equation 4.15 when it enters the angular region near the perigee and does not escape an Earth orbit yet such that the heuristic thrusting law for high-thrust systems can be expressed as:

$$\vec{u}^* = \begin{cases} \frac{\vec{v}}{\|\vec{v}\|}\,; & \|\theta' - \theta_p\| \leq \theta_r \\ \frac{\vec{v}}{\|\vec{v}\|}\,; & \|\vec{v}\|^2 - \frac{2\mu}{r} > 0 \\ 0\,; & \|\theta' - \theta_p\| > \theta_r \end{cases} \tag{4.60}$$

where θ' is the θ wrapped to $[\pi, -\pi]$ defined by $\theta' = ((\theta + \pi) \bmod (2\pi)) - \pi$, θ_p is the perigee position angle, and θ_r is the angular region near the perigee where the propulsion system is turned on. One exception is that systems such as most solid propulsion systems that can only be fired once are fired continuously starting from the perigee.

Selecting the right thrusting region with θ_r is an optimization problem on its own because it leads to longer escape trajectory durations for smaller θ_r and less efficient escape trajectories for larger θ_r. Therefore, a grid search can be performed until the smallest θ_r is found that has an escape trajectory duration of a year or shorter. A longer escape trajectory duration will exceed expected escape trajectory durations for low-thrust systems.

4.5. Summary

This chapter presents two strategies for establishing a practical framework for assessing the feasibility of both low-thrust and high-thrust propulsion systems. These approaches are aimed at addressing research question RQ1.2, which seeks to determine a practical method for simulating a fuel-efficient trajectory to a near-Earth asteroid within 5 years.

RQ1.2: What is a practical framework to simulate a fuel-efficient trajectory to a near-Earth asteroid within 5 years?

To answer research question RQ1.2, the chapter first proposes a COV-based single-shooting indirect method to optimize low-thrust fly-by trajectories to NEAs. This approach combines particle swarm optimization and Levenberg-Marquardt optimization techniques to determine the fuel-efficient trajectory.

In addition, the chapter outlines a second approach for high-thrust trajectories that involves a single-shooting two-point boundary value problem. This strategy minimizes the required initial escape velocity from Earth and the closest approach distance to the target asteroid, making it suitable for high-thrust systems.

Both methods use an Earth escape trajectory that begins at the perigee of the SSGTO, utilizing a full-throttle heuristic thrusting law that is always fired in the direction of the satellite's orbital velocity. The high-thrust system can turn off when it is not near the perigee to increase its propellant efficiency.

5

Interplanetary propulsion system simulation result

To answer research questions RQ1 and RQ1.1 the selected propulsion systems in chapter 2 were simulated using the practical fuel-efficient NEA fly-by trajectory framework that is a combination of the astrodynamic model described in chapter 3 and the trajectory designs for both low- and high-thrust propulsion systems described in chapter 4. The research questions are answered by demonstrating the capabilities of the most promising selected interplanetary SOTA propulsion systems and by validating to what degree the requirements for an interplanetary propulsion system are met for the selected targets. Additionally, the ESA margin philosophy for science assessment studies is used to properly validate the requirements for a selected interplanetary propulsion system.

RQ1: What is a feasible design for a propulsion system for interplanetary travel to perform an autonomous 6U satellite near-Earth asteroid fly-by mission starting from a super synchronous geostationary transfer orbit within 5 years?

RQ1.1: What state-of-the-art propulsion systems meet the requirements for a near-Earth asteroid fly-by mission?

This chapter presents the simulation setup for low-thrust propulsion system trajectories, high-thrust propulsion system trajectories, and the selected interplanetary propulsion system trajectory, their results and answers to research question RQ1.1, and a discussion. The chapter is concluded with an answer to research question RQ1.

5.1. Low-thrust trajectory simulation

To simulate the different propulsion systems a satellite with a mass of 12 kg and a maximum power of 191 W was chosen. This was done because the total mass of the system is in line with the maximum mass expected for a 6U satellite according to MR-SC-5. The total satellite mass was set fixed because the low thrust trajectory simulation as presented in chapter 4 could not deal with a variable mass as a design parameter. In reality, a more efficient propulsion system with a low dry mass and lower required propellant mass would result in a lighter satellite.

5.1.1. Selected targets

The target asteroids were selected from a list of valuable NEAs that are suitable for autonomous navigation [5]. To showcase the capabilities of autonomous navigation, four asteroids were chosen within a range of 0.5 to 0.7 astronomical units from the Sun. This selection balances ambition with feasibility. In other words, the targets demonstrate what is possible using the current SOTA.

Table 5.1: This table displays the key characteristics of four selected asteroids in the ECLIPJ2000 reference frame. The target asteroids were selected from a list of valuable NEAs that are suitable for autonomous navigation [5]. These asteroids were chosen based on their suitability for autonomous navigation and their proximity to the Sun, with distances ranging from 0.5 to 0.7 astronomical units. The table includes the X, Y, and Z coordinates of each asteroid, as well as the closest approach date for each target.

Asteroid Name	X (km)	Y (km)	Z (km)	Approach Date
2020QN1	-35,230,206.15609	108,960,648.73900	-13,641.65745	Jan 04, 2030
163693	22,339,498.14313	-87,769,735.19835	-298,590.82726	Oct 08, 2032
2017WV13	-21,509,416.34269	-76,608,898.69482	163,636.88090	Oct 02, 2032
2012BX34	46,204,831.99749	-59,012,656.47270	328,202.71421	Aug 02, 2031

5.1.2. Optimization setup

To find the solution to the low-thrust trajectory optimization problem a PSO is used. A swarm size of $7 \times 2,000 = 14,000$ was chosen which is 2000 times the number of design parameters. This number was chosen because lower swarm sizes tend to converge to sub-optimal local minima or no solutions at all and higher numbers exceeded the available 16GB RAM memory. The social-adjustment weight and self-adjustment weight were set to 1.49 and the inertia range of the particles was set to 0.4 to 0.9 as was proven to work in Jiang, Baoyin, and Li [39]. The maximum stall iterations were set to 20 and the maximum number of total iterations was set to 200 to decrease the total optimization time for problems that converge faster than others to a local minimum and to stop the optimization if a better guess could not be found. Finally, to make each iteration less computationally expensive, the integration's absolute tolerances were set to 10^{-3} which translates to an error tolerance of about 5,000,000 km. This error was assumed to be sufficient for an initial guess. After the initial guess using the PSO was obtained, the Levenberg-Marquardt local optimization method was used to converge to a local minimum close to the global optimum. For the Jacobian in the Levenberg-Marquardt optimization, a forward finite difference scheme was used. Since the simulation framework is very sensitive to changes integration absolute tolerances of 10^{-13} were used for the local optimizer which translates to an error tolerance of about 50 km. By trial, higher error tolerances were found to not converge. The lowest tolerance possible for the ode solver was 10^{-14} which nears the minimum error tolerance possible for ode solvers using double precision numbers. For the PSO, Matlab's 'particleswarm' function was used, and for the local optimization, Matlab's 'fsolve' function was used. This was done because the parallel processing of function evaluations in Matlab is already implemented which drastically speeds up the simulations.

5.1.3. Position of Earth

The position of the Earth in the ECLIPJ2000 reference frame was obtained by using MICE, the Matlab implementation of SPICE, an ancillary information system provided by NASA that provides scientists and engineers the capability to include space geometry, and event data into mission design, science

observation planning, and science data analysis software.

5.1.4. Initial position of the satellite

The initial orbit is an SSGTO around Earth with a perigee of 295 km and an apogee of 90,000 km. To maximize the use of the Oberth effect, the satellite begins its Earth escape segment at perigee. The simulation ends when the satellite successfully escapes Earth, as indicated by a characteristic energy of zero. The final mass of the satellite at Earth escape is used as the starting point for the interplanetary trajectory. The initial position and velocity of the satellite are set to match the Earth's center of mass in the ECLIPJ2000 reference frame. The interplanetary trajectory simulation does not consider the presence of celestial bodies other than the Sun and the target asteroid.

5.1.5. Low-thrust propulsion systems results

The optimal fly-by trajectory for the selected NEAs was simulated for each propulsion system. Their simulated trajectories can be seen in Appendix E. In Figure 5.1 the results are presented such that the total mission duration or time of flight and the total propulsion system mass for the different trajectories to the selected targets are given for the different propulsion systems.

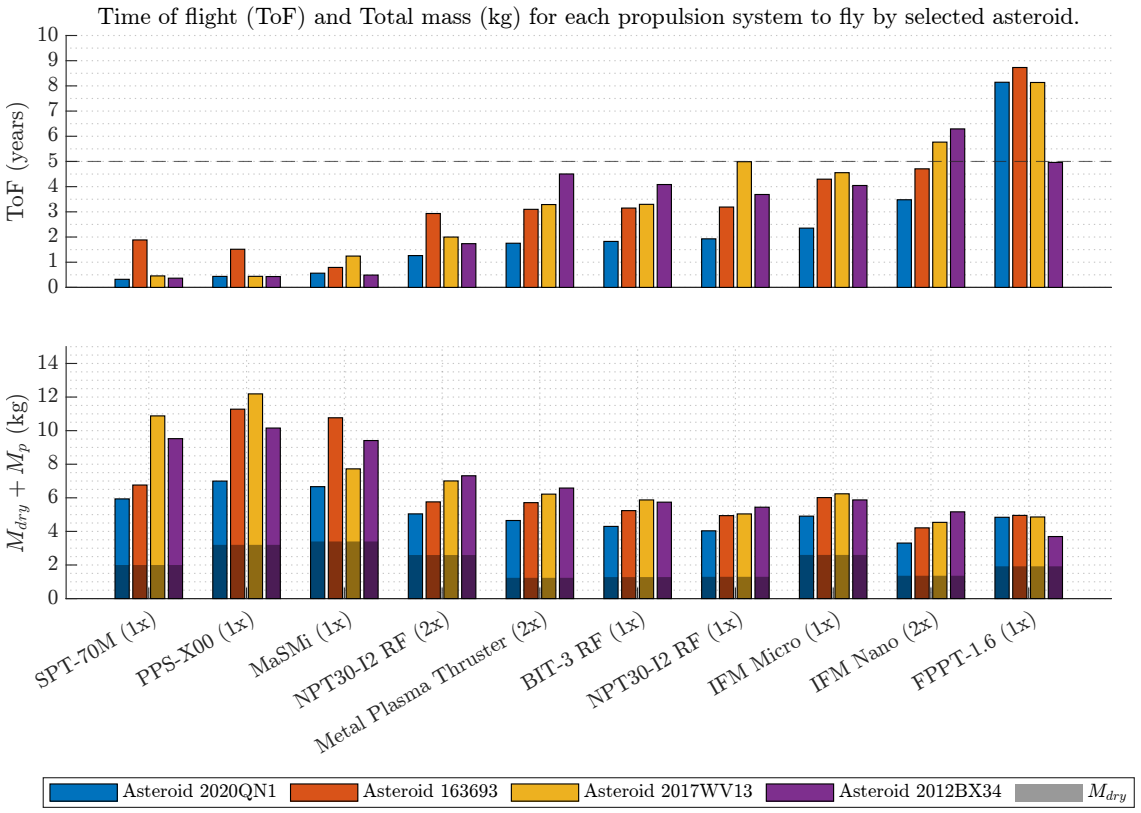

Figure 5.1: This figure presents a summary of the selected low-thrust propulsion systems' time of flight and total mass required to fly by the selected target asteroids using a 12 kg satellite. The dashed line at 5 years indicates the maximum mission duration requirement. The figure indicates that IFM Nano and FPPT-1.6 cannot be used for some of the selected targets because they exceed the maximum mission duration. Additionally, PPS-X00, SPT-70M, and MaSMi require more than half of the total mass in propellant and propulsion system dry mass for all targets. This information enables the selection of the most efficient propulsion systems for each mission.

Table 5.2: Low-thrust system results for the most challenging fly-by mission to Asteroid 2012BX34. ToF=Time of Flight or total mission duration.

System	Start Date	ToF (days)	Prop. mass (kg)	Dry mass (kg)	Volume (U)	Distance (km)
PPS-X00 (1x)	Feb 25 06:12:08 2031	157.7416	6.9547	3.2000	6.518	3.160×10^{-6}
SPT-70M (1x)	Mar 21 05:25:37 2031	133.7739	7.5232	2.0000	3.953	1.720×10^{-6}
MaSMi (1x)	Feb 04 01:57:41 2031	178.9183	6.0105	3.4000	3.170	1.975×10^{3}
NPT30-I2 RF (2x)	Nov 05 17:23:49 2029	634.2751	4.7191	2.5940	2.783	9.478×10^{-7}
Metal Plasma Thruster (2x)	Jan 30 08:22:46 2027	1644.7	5.3459	1.2360	1.888	3.111×10^{4}
BIT-3 RF (1x)	Jul 02 06:45:27 2027	1491.7	4.4616	1.2800	2.208	6.568×10^{-5}
IFM Micro (1x)	Jul 16 06:10:43 2027	1477.7	3.2745	2.6000	2.516	7.979×10^{6}
IFM Nano (2x)	Apr 16 20:38:12 2025	2291.0	3.8050	1.3600	2.141	6.217×10^{5}
FPPT-1.6 (1x)	Aug 15 14:20:10 2026	1812.4	1.7732	1.9210	2.047	6.804×10^{7}
NPT30-I2 RF (1x)	Nov 23 18:07:04 2027	1347.20	4.1446	1.297	1.748	2.012×10^{-5}

Based on the Figure 5.1 and Table 5.2 the research question RQ1.1 can be answered for the selected low-thrust systems from chapter 2.

RQ1.1: What state-of-the-art propulsion systems meet the requirements for a near-Earth asteroid fly-by mission?

It can be concluded from Figure 5.1 that the IFM Nano and FPPT-1.6 systems are not suitable for a standard fly-by mission to a NEA due to their exceeding the maximum mission duration of 5 years for some targets.

Additionally, the PPS-X00, SPT-70M, and MaSMi systems are also not viable options as they demand an excessive total propulsion system mass for a 12 kg 6U CubeSat as can be seen in Figure 5.1. In most cases, over half of the CubeSat's mass would have to be allocated to the interplanetary propulsion system, which exceeds the current mass budget constraints.

Finally, it can be determined from Figure 5.1 that the NPT30-I2 RF (1x), Metal Plasma Thruster, BIT-3 RF, and IFM Micro are the most optimal systems for a fly-by mission to a NEA based on their compliance with the 5-year maximum mission duration and least required propulsion system mass. These systems have total propulsion system masses ranging from 4 to 6 kilograms, making them

suitable for a 12 kg 6U CubeSat. However, for specific targets such as asteroids 2020QN1 and 163693, the IFM Nano system would be the preferred choice based on the total mass. It can be concluded that without the ESA mass margins, these systems are able to meet the requirements.

Based on the results the propulsion systems with the least time of flight are SPT-70M for asteroid 2020QN1 with 117.3 days, MaSMi for asteroid 163693 with 117.3 days, PPS-X00 for asteroid 2017WV13 with 117.3 days, and SPT-70M for asteroid 2012BX34 with 117.3 days. The propulsion system with the least amount of propellant used and within 10,000 km distance of the NEA for asteroid 2020QN1 is the IFM Nano with 1.9456 kg propellant mass and 1.36 kg dry mass. For asteroid 163693 it is the NPT30-I2 RF (1x) 3.6424 kg propellant mass and 1.297 kg dry mass. For asteroid 2017WV13 it is the IFM Nano with a propellant mass of 3.1786 kg and a dry mass of 1.36 kg. For asteroid 2012BX34 it is the NPT30-I2 RF (1x) with a propellant mass of 4.1446 kg and a dry mass of 1.297 kg. The results can be seen in more detail in Appendix E.

Investigating the volume of the different low-thrust propulsion systems then IFM Nano, NPT30-I2 RF, and Metal Plasma Thruster have volumes without extra propellant and customized propellant storage of less than 1U. Next, BIT-3 RF, FPPT-1.6, SPT-70M, and MaSMi all have volumes without extra propellant and customized propellant storage of less than 2U. IFM Micro 100 (2.234U) and PPS-X00 (4.2U) exceed a volume of 2U. Based on the COTS available PPS-X00's volume this system is not compatible with the 6U CubeSat. The estimated required volume which combines the specifications of the propulsion systems combined with the required propellant volume can be seen in Table 5.2. From this table, it can be seen that from the low-thrust systems that come close to 10,000 km from the target asteroid NPT30-I2 RF (1x) (1.748U), Metal Plasma Thruster (2x) (1.888U), and BIT-3 RF (1x) (2.208U), NPT30-I2 RF (1x) requires the least volume. IFM Micro (1x) and IFM Nano (2x) are also options that can be considered but these require more volume in general and the IFM Nano has a mission duration exceeding 5 years for some targets.

Considering all the results, the ThrustMe NPT30-I2 RF (1x) gridded-ion thruster is the system with the smallest total mass and volume for the majority of targets and the closest approach distance of under 10,000 km within a 5-year period (requirement MR-SC-1). From the results, it can also be concluded that the solar panels' area and thus the mass of the solar panels can be reduced for the most challenging mission to Asteroid 2012BX34 because less power is required than expected. In the case of the NPT30-I2, only 65W is required for the interplanetary propulsion system, so the MMA Design Hawk 38A-191 deployable solar panels can be replaced by the MMA Design Hawk 38A-95 deployable solar panels for the detailed satellite design.

5.2. High-thrust trajectory simulation

To simulate the different high-thrust propulsion systems a satellite similar to the low-thrust case with an initial mass of 12 kg and a maximum power of 191 W was chosen. This was done because the total mass of the system is in line with the maximum mass expected for a 6U satellite according to MR-SC-5. The total initial satellite mass was set fixed because the low thrust trajectory simulation as presented in chapter 4 could not deal with a variable mass as a design parameter. Therefore, the initial satellite mass was also fixed for the high-thrust trajectory simulation. In reality, a more propellant-efficient propulsion system with a low dry mass and lower required propellant mass would result in a lighter satellite.

5.2.1. Selected targets

The target asteroids are identical to the selected targets for the low-thrust trajectory. See Section 5.1.1.

5.2.2. Optimization setup

To find the solution to the high-thrust trajectory optimization problem a PSO is used to find the global optimum. A swarm size of $4 \times 2,000 = 8,000$ was chosen which is 2000 times the number of design parameters for the high-thrust trajectory. From trial and error, this swarm size was found to converge in most cases. Higher swarm sizes exceed the available RAM memory limit of 16GB of the used computer for this thesis. The social-adjustment weight and self-adjustment weight were set to 1.49 and the inertia range of the particles was set to 0.4 to 0.9 similar to the values used in Jiang, Baoyin, and Li [39]. The maximum stall iterations were set to 20 and the maximum number of total iterations was set to 200. From trial and error, this number of stall iterations and iterations was found to be sufficient to converge and stop the optimization if no likely proper initial guess could be found. Finally, to make each iteration less computationally expensive, the integration absolute tolerances were set to 10^{-3} similar to that of the low-thrust trajectory case which means the PSO uses an error tolerance in the range of 5,000,000 km. For the particle swarm optimization, v_∞ was bound between 0 and 20 $\mathrm{km\,s^{-1}}$ to decrease the design space and increase convergence speed.

After the initial guess using the particle swarm was obtained, the Levenberg-Marquardt local optimization method was used to converge to a local minimum close to the global optimum. For the Jacobian in the Levenberg-Marquardt optimization, a forward finite difference scheme was used. Since the simulation framework is very sensitive to changes integration absolute tolerances of 10^{-13} were used for the local optimizer similar to the low-thrust trajectory optimization. For the particle swarm, Matlab's 'particleswarm' function was used, and for the local optimization, Matlab's 'fsolve' function was used. This was done because the parallel processing of function evaluations in Matlab is already implemented which drastically speeds up the simulations.

5.2.3. Position of Earth

The position of Earth in the ECLIPJ2000 reference frame was obtained by using MICE, the Matlab implementation of SPICE, an ancillary information system provided by NASA that provides scientists and engineers the capability to include space geometry, and event data into mission design, science observation planning, and science data analysis software.

5.2.4. Initial position of the satellite

The initial orbit is an SSGTO around Earth with a perigee of 295 km and an apogee of 90,000 km. To maximize the propellant efficiency, the satellite starts its Earth escape segment at the perigee, and the region near the perigee when the propulsion system is thrusting is found by a grid search starting from an angular region θ_r of 1 degree from the perigee until the escape segment duration is shorter than a year.

The simulation ends when the satellite successfully escapes Earth and has the required characteristic energy to obtain a v_∞ required to reach the target asteroid. The final mass of the satellite at Earth escape is also the final mass at the end of the interplanetary fly-by trajectory. The initial position and velocity of the satellite are set to match the Earth's center of mass in the ECLIPJ2000 reference frame with the added found v_∞ in the optimal direction. The interplanetary trajectory simulation does not consider the presence of celestial bodies other than the Sun and the target asteroid.

5.2.5. High-thrust propulsion systems results

The optimal fly-by trajectories for the selected NEAs were simulated for each high-thrust propulsion system.

Table 5.3: This table displays the minimum required velocity at infinity from Earth to fly by the selected near-Earth asteroid targets.

Asteroid Name	v_{∞_e} (km/s)
2020QN1	3.4077
163693	4.1384
2017WV13	5.3016
2012BX34	6.3429

To give an idea of the required ΔV to achieve the velocities relative to Earth as found in Table 5.3 required to fly by the target NEAs an impulse shot from perigee is calculated using Equation 2.4:

$$\Delta V = \sqrt{\frac{2\mu}{r_0} + v_{\infty_e}^2} - \sqrt{\frac{2\mu}{r_0} - \frac{\mu}{a}}$$

In Figure 5.2 the results are presented such that the total mission duration or time of flight and the total propulsion system mass for the different trajectories to the selected targets are given for the different high-thrust propulsion systems including the theoretical total mass using an impulse shot approximation. From the theoretical ΔV for an impulsive shot from perigee a total mass estimate is made using Tsiolkovsky's law rewritten for the used propellant mass [36]:

$$M_{prop} = M_0 \left(1 - e^{\frac{-\Delta V}{I_{sp} g_0}}\right) \tag{5.1}$$

where M_0 is the initial mass of the satellite of 12 kg for this simulation and M_{prop} the required propellant calculated for the impulsive shot Earth escape trajectory of Equation 2.4.

Based on the Figure 5.2 the research question RQ1.1 can be answered for the selected high-thrust systems from chapter 2.

RQ1.1: What state-of-the-art propulsion systems meet the requirements for a near-Earth asteroid fly-by mission?

From Figure 5.2 it can be seen that HYDROS-C and B1 will likely not meet the requirements for a near-Earth asteroid fly-by mission because they require too much total mass to maneuver to the NEA targets. Further, it can be seen that overall the CDM-1 (x1) requires the least total mass to maneuver to the target asteroids. It requires between 4.1 kg for asteroid 2020QN1 and 7.5 kg for asteroid 2012BX34 of the 12 kg satellite to be dedicated to the interplanetary propulsion system. Since the satellite will likely have a total dry mass excluding the propulsion system and mass margins of around 5 kg CDM-1 will be able to fly by a near-Earth asteroid within 5 years on a 6U CubeSat for most target asteroids. High-thrust propulsion systems are therefore considered to be feasible for a selection of the NEA targets. STAR 4G and 22N HPGP show similar results in terms of the total mass. In terms of volume, these systems will require approximately 2U to 3U for asteroid 2020QN1 and up to approximately 3U to 4U for asteroid 2012BX34 based on the propellant densities of$1.81\,\mathrm{kg\,L^{-1}}$ for LMP-103S, $2.0\,\mathrm{kg\,L^{-1}}$ for AP/HTPB, and approximately $1.8\,\mathrm{kg\,L^{-1}}$ for TP-H-3399.

Apart from the performance of all five systems, it can clearly be seen that an impulsive shot approximation starts to divert from the high-thrust trajectory model at a specific thrust of $1.8\,\mathrm{N\,kg^{-1}}$ for the

22N HPGP propulsion system on the simulated 12 kg satellite. The performance of the impulse shot approximation can be approached by reducing the thrust region near the perigee and increasing the Earth escape trajectory segment duration.

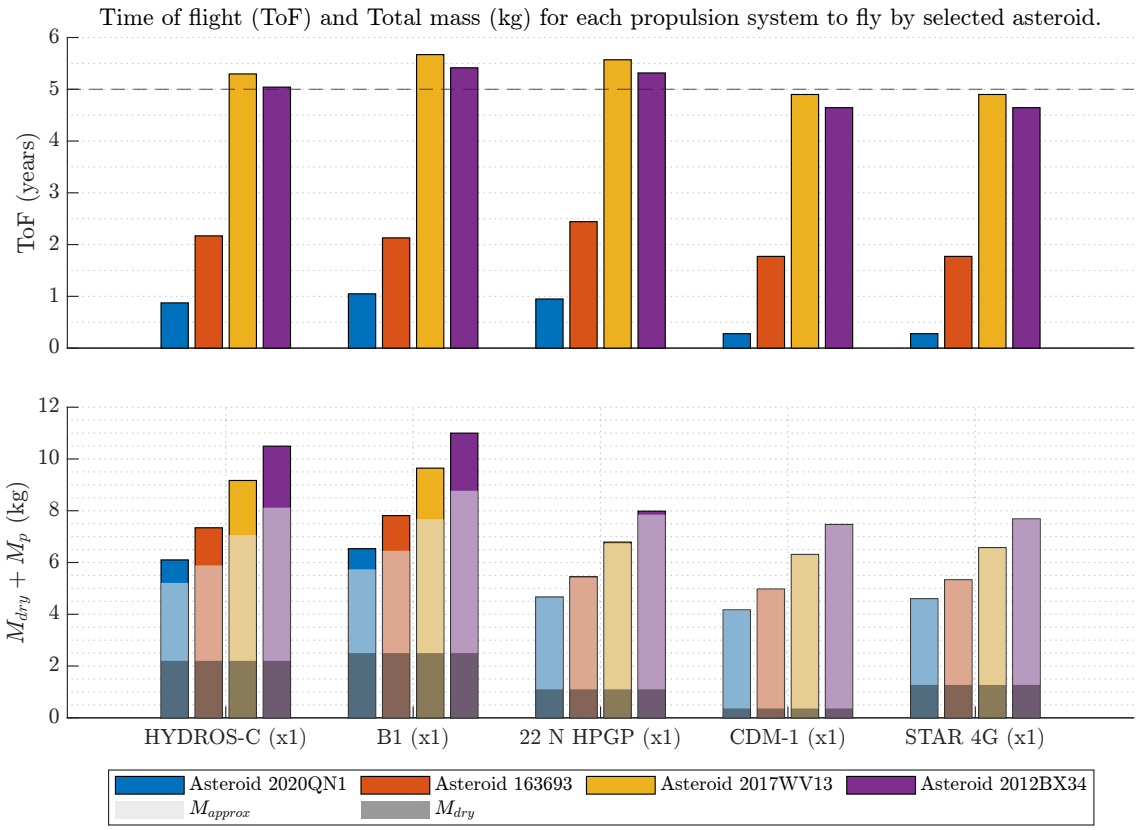

Figure 5.2: This figure shows the time of flight and total mass of high-thrust propulsion systems required to fly by selected target asteroids using a 12 kg satellite including theoretical total mass using an impulsive shot approximation. The dashed line at 5 years marks the maximum mission duration requirement. The M_{approx} (white) is the approximated total mass using an impulse shot approximation from perigee. The graph shows that 22 N HPGP, CDM-1, and STAR 4G propulsion systems are most compatible with the mission compared to the other high-thrust systems. However, these systems still require at least 7.5 kg of the 12 kg satellite to be dedicated to the interplanetary propulsion system for the most ambitious target 2012BX34. Since the satellite's total dry mass, excluding the propulsion system and mass margins, is likely to be around 5 kg HYDROS-C and B1 will not meet the requirements for a near-Earth asteroid fly-by mission. This information shows that 22 N HPGP, CDM-1, and STAR 4G are currently feasible for some NEA targets in terms of the total mass. 22 N HPGP, CDM-1, and STAR 4G give almost identical results for their escape trajectories with respect to the approximated mass using an impulse shot assumption. This can be explained due to their high thrust with respect to HYDROS-C and B1 that give significant other values than the impulse shot approximation.

5.3. Discussion low-thrust versus high-thrust

One major advantage of using high-thrust systems is the shorter mission duration. A shorter mission duration leads to a lower radiation shielding requirement. In the most ideal case, no radiation shield is required. Considering that the current assumed 5-mm aluminum radiation shield has a total mass of 1.518 kg a relatively low mission duration could save this much dry mass.

Considering all the results for both low-thrust and high-thrust systems it can be seen that there is a significant difference in mission duration for the asteroids 2020QN1. High-thrust systems require 3 to 4 months for asteroid 2020QN1 to fly by the target asteroid and approximately 4.1 kg of propulsion system mass. High-specific impulse, low-thrust systems such as SPT-70M, PPS-X00, and MaSMi show

similar mission duration results, about 5 to 6 months, for these targets but require 6 to 7 kg. Low-thrust propulsion systems with even higher specific impulses but lower thrust such as NPT30-I2 (1x) and IFM Nano (2x) require 2 to 4 years to fly by this target and they require 3.5 to 4 kg of total system mass. Therefore, high-thrust systems for less ambitious targets such as asteroid 2020QN1, are as good as high-specific impulse, low-thrust systems with a relatively high thrust if a reduction in the radiation shield thickness is taken into account. However, due to their low propellant storage densities, high-thrust systems need more propellant storage volume which leads to higher system volumes. To conclude, for asteroid 2020QN1, high-thrust propulsion systems can potentially be a lower total mass option than low-thrust systems but low-thrust propulsion systems require less propulsion system volume.

Next, considering the results for both high- and low-thrust systems for the other more ambitious target asteroids it can be seen that high-thrust systems require more than 7.5 kg for the most ambitious target. Mission durations for these systems are below 2 years up to 5 years for asteroids 2017WV13 and 2012BX34. The low-thrust propulsion systems perform better in terms of total propulsion system mass for the more ambitious targets.

Lastly, considering the propellant storage volume, the selected high-thrust propulsion systems require large propellant storage volumes. Therefore, these systems cannot be used on a 6U CubeSat. This means that approximately 2U to 3U of the satellite is required for only propellant storage which is too much considering all the other systems. Low-thrust, high-specific electric propulsion systems often come with solid propellants that can store up to double or triple the amount of propellant compared to high-thrust systems in the same volume.

To conclude, low-thrust, high-specific impulse systems outperform every other propulsion system in terms of mass, and volume for the most ambitious targets 163693, 2017WV13, and 2012BX34. Even when considering the mission duration and the extra required radiation shielding mass, these systems are still equal to or better than other systems. In the case of asteroid 2020QN1, high-thrust propulsion systems can be the better option in terms of total mass if a radiation shielding mass reduction is taken into account, and in terms of mission duration high-thrust takes significantly shorter to fly by the asteroid 2020QN1. However, low-thrust, high-specific impulse systems still outperform high-thrust systems in terms of total volume.

5.4. Selected interplanetary propulsion system detailed results

From the results of the different propulsion systems on a 12 kg satellite, the NPT30-I2 RF propulsion was selected. To conclude RQ1, a more detailed design of the satellite and interplanetary propulsion system was formulated. This design was then simulated for a fly-by mission to the asteroid 2012BX34 which is considered the most challenging target NEA of the selected targets. In this section, the design is verified for the requirements MR-SC-1, MR-SC-2, MR-SC-4, MR-SC-5, and MR-AOCS-1.

MR-SC-1: The satellite shall be able to fly-by a near-Earth asteroid at a closest approach distance of 10,000 km within 5 years.

MR-SC-2: The satellite shall be deployed in a super synchronous geostationary transfer orbit.

MR-SC-4: The satellite shall have a maximum volume of 6U.

MR-SC-5: The satellite shall have a maximum mass of 12 kg.

MR-AOCS-1: The attitude and orbital control system shall be able to bring the spacecraft to the near-Earth asteroid at the closest approach distance of 10,000 km within 5 years.

Additionally, the following requirements must be met for the detailed simulation according to ESA [35]:

1. The equipment dry mass shall have a 5% mass margin.
2. The propulsion system dry mass shall have a 10% mass margin (because it requires adjustments).
3. The spacecraft's total dry mass shall have a 20% mass margin (on top of the equipment/propulsion system mass margin).
4. The propellant storage shall have a minimum tank ullage volume of 10% (only applies to liquid or gas propellants).
5. A 2% propellant residual shall be added to the calculated required propellant.

Table 5.4: This table presents the detailed characteristics of a CubeSat propulsion system, including the selected interplanetary propulsion system. The table provides information on the type, manufacturer, model, propellant (Prop.), propellant density, thrust, specific impulse (Isp), dry mass, volume, and power of the propulsion system.

Type	Mfr.	Model	Prop.	Prop. density (g/cm^3)	Thrust (mN)	Isp (s)	Dry mass (kg)	Volume (U)	Power (W)
Gridded-ion	ThrustMe France	NPT30-I2 RF	I2	4.930	1.10	2400	1.297	1	65

Including the NPT30-I2 RF the total dry mass for the satellite can be approximated. A detailed design of the CubeSat can be seen in Table 5.5. The simulated mission on the 12 kg satellite for the NPT30-I2in Table 5.2 shows that approximately 4.2 kg of propellant mass was required to fly by the NEA. This means that 35% of the 12 kg satellite's total mass of the satellite has to be dedicated to the propellant mass. The detailed CubeSat design shows that including mass margins the satellite has a total dry mass of 8.97882 kg, which is 6.544 kg for equipment and 1.597 kg for the propulsion system dry mass. Assuming a similar mass percentage of propellant is required of 35% percent including 2% extra propellant margin for the residual propellant requirement a total satellite mass of $\frac{8.978\,82\,\text{kg}}{100\%-37\%} \approx 14.3\,\text{kg}$. Note that the simulated total mass is not constrained to the total mass requirement MR-SC-5 of the actual CubeSat design so the assumption of 14.3 kg total mass can be made. MR-SC-5 is excluding mass margins.

Table 5.5: This table summarizes the selected subsystems for the satellite and their characteristics, including the attitude and orbital control system. The table provides details on the manufacturer, model, mass, power, and volume of each subsystem. The subsystems include a primary structure, power system, communication system, navigation system, attitude determination and control system, onboard data handling system, payload system, and propulsion system. The table also presents the total dry mass, power, and volume budget excluding the mass margin, as well as the total dry mass including equipment level mass margins and spacecraft mass margin of 20% as provided by the ESA mass margin philosophy [35] and the secondary propellant for the reaction control thrusters.

Manufacturer	Model	Mass (kg)	Power (W)	Volume (U or dm^3)
Primary structure excl. 5% mass margin				
AAC Clyde Space	Zaphod 6U	0.674	-	7.705 (outside)

The table continues on the next page.

Manufacturer	Model	Mass (kg)	Power (W)	Volume (U or dm^3)
-	Radiation shielding	1.5176	-	(outside)
Power system (power available) ecxl. 5% mass margin				
AAC Clyde Space	NANO-PLUS + OPTIMUS-80	0.818	80Wh	0.672
MMA Design	Hawk 38A-95	0.754	95 at 1AU	0.36 (outside)
Communication system ecxl. 5% mass margin				
AAC Clyde Space	PULSAR-DATA	0.130	10	0.101
Endurosat	Patch 4×4 antenna	0.053	-	$\sim$0.0006
Navigation system ecxl. 5% mass margin				
VisNAV	Camera	0.500	2	1.352
Attitude determination and control system ecxl. 5% mass margin				
AAC Clyde Space	iADCS-400	1.700	5	0.6157
Onboard data handling system ecxl. 5% mass margin				
AAC Clyde Space	CP400.85	0.007	1	0.01
Payload system ecxl. 5% mass margin				
NEAScout	Camera	0.390	3	0.282
Propulsion System ecxl. 10% dry mass margin				
ThrustMe	NPT30-I2	1.297	65	1
ThrustMe	Iodine propellant	$\sim$4.8	-	0.8519
GomSpace	NanoProp CGP3	0.300	2	0.5
GomSpace	Butane propellant	0.050	-	-
Total dry mass-, power- and volume budget excl. mass margin				
-	-	6.544 (equipment) and 1.597 (propulsion system)	95 W	4.5333 excl. propellant
Total dry mass including equipment level mass margins				
6.871 kg (equipment) and 1.7567 kg (propulsion system)				
Total dry mass including spacecraft mass margin of 20% and secondary propellant mass				
8.97882 kg + 0.050 kg Butane				

5.4.1. Simulation results

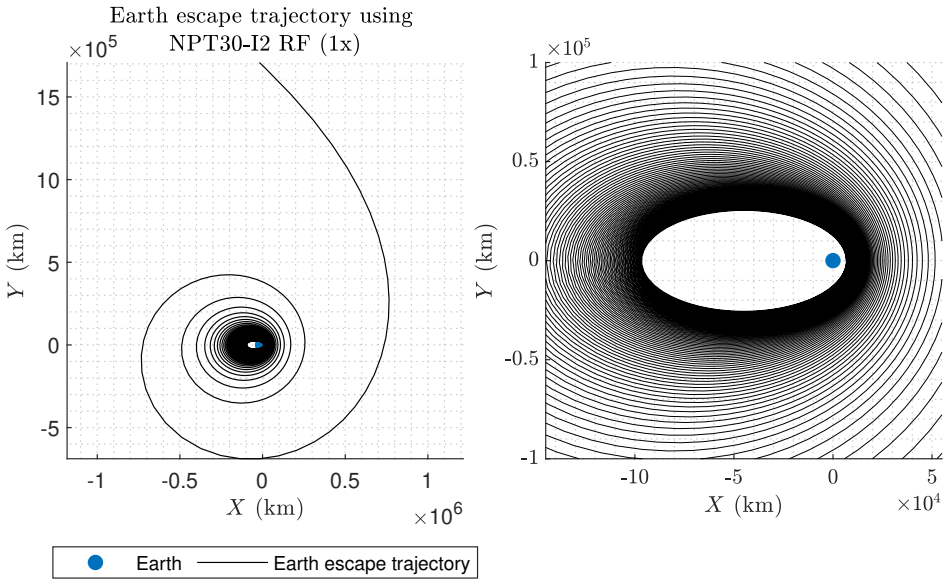

Figure 5.3: The figure depicts the simulated Earth escape trajectory of the NPT30-I2 RF (1x) propulsion system on the detailed satellite design. The left-side figure displays the complete trajectory, while the right-side figure provides a zoomed-in view. The simulation results showcase the effectiveness of the selected propulsion system in enabling the satellite to successfully escape Earth's gravity.

Table 5.6: Results of simulated Earth escape trajectory using the NPT30-I2 RF (1x) propulsion system on a 14.3 kg satellite. The table shows the starting and ending dates of the trajectory, its duration, starting and final masses, the amount of propellant used, and the specific orbital energy after the trajectory.

Variable	Result
Start of Earth escape trajectory	Dec 03 01:31:01.813337818 2026
End of Earth escape trajectory	Dec 19 23:18:25.303776000 2027
Earth escape trajectory duration (years)	1.04562834491868
Starting mass (kg)	14.3
Final mass (kg)	12.7578267536360
Used propellant (kg)	1.542173246364
Specific orbital energy after trajectory (km^2/s^2)	0

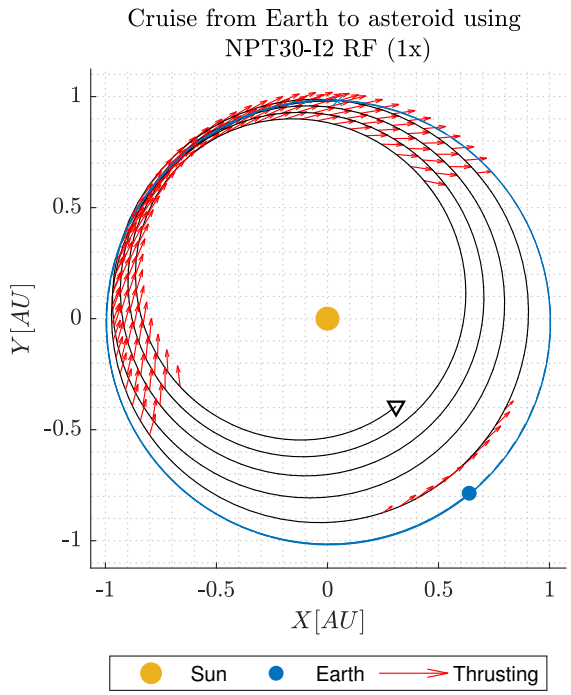

Figure 5.4: The figure presenters the simulated fuel-efficient interplanetary cruise trajectory to Asteroid 2012BX34 using the NPT30-I2 RF (1x) on a detailed 14.3 kg satellite. The trajectory shows a successful fly-by of the asteroid. The blue cross marks the starting point of the trajectory, while the blue dot indicates the final position of the Earth. The Earth's orbit is shown for reference but is not included in the orbital dynamics. The optimal thrusting control, represented by a bang-bang control, is illustrated as a vector in the optimal thrusting direction when the propulsion system is firing at maximum thrust. The trajectory sections without thrusting vectors correspond to intervals when the propulsion system is turned off.

Table 5.7: Optimal fuel-efficient solution for the interplanetary trajectory from Earth to the asteroid 2012BX34 on a 14.3 kg satellite using the NPT30-I2 RF (1x) propulsion system. This table presents the design parameters that resulted in the fuel-efficient trajectory found. The trajectory duration is 3.61685421000812 years, and the boundary condition norms converged below 10^{-12}. The λ parameters are the Lagrange multipliers that enforce the boundary conditions. These design parameters were optimized to obtain the most fuel-efficient trajectory.

Design parameter	Solution
Trajectory duration (years)	3.61685421000812
λ_x	0.462877025807
λ_y	0.772078949646
λ_z	0.041211954016
λ_{v_x}	-0.197544221686
λ_{v_y}	-0.059163681404
λ_{v_z}	0.005437968421
λ_m	0.381296337671

Table 5.8: Fuel-efficient interplanetary trajectory results from Earth to the asteroid 2012BX34 using the NPT30-I2 RF (1x) propulsion system. This table summarizes the key results of the optimized trajectory, including the start and fly-by dates, trajectory duration, starting and final masses, propellant usage, and closest approach distance. These results demonstrate the effectiveness of the NPT30-I2 RF for interplanetary near-Earth asteroid 6U CubeSat missions.

Variable	Result
Start of trajectory	Dec 19 23:18:25.303776000 2027
Asteroid fly-by date	Aug 02 00:00:00.000000000 2031
Trajectory duration (years)	3.61685421000812
Starting mass after Earth escape (kg)	12.757826753636
Final mass after fly-by (kg)	9.546859755875
Used propellant for trajectory (kg)	3.210966997762
The total propellant used incl. Earth escape (kg)	4.753140244125
Residual propellant (kg)	0.518039755875
Closest approach distance (km)	$4.492631264208 \times 10^{-6}$

From the results, it can be verified with the simulation that the CubeSat theoretically can fly by a NEA within 10,000 km and a mission duration of fewer than 5 years. The residual propellant of 9.828% is excessive. Therefore a new total propellant is calculated from the used propellant for the trajectory including Earth escape $\frac{4.753140244125\ kg}{98\%} = 4.850\ kg$. This takes into account the required residual propellant of 2%. This reduces the propellant mass from 5.271 kg to only 4.850 kg. The total satellite's volume is less than 6U which means the volume requirement is met. However, the total wet mass without the dry mass margins and total spacecraft dry mass margin is 13.041 kg which is more than the 12 kg requirement. Since the 12 kg requirement for a 6U CubeSat is more of a guideline for CubeSat missions which depends on the dispenser, larger masses may occasionally be evaluated by a designer on a mission-specific basis. This however will require a reconsideration of some COTS CubeSat deployment mechanisms. Thus, this interplanetary propulsion system design is considered feasible although MR-SC-5 is not met.

To conclude a total of 4.850 kg solid iodine propellant with a volume of 0.983U is required which brings the total mass and volume excluding margins of the CubeSat to 5.527U and 13.041 kg.

5.5. Summary

High-thrust propulsion systems do not gain enough propellant efficiency by using most of their propellant near the perigee to be competitive for ambitious NEA targets. Low-thrust propulsion systems that have a high specific impulse are the better option from the simulation results. From the low-thrust propulsion system results, the ThrustMe NPT30-I2 RF gridded ion propulsion system was found to be the most mass efficient of the systems that met the requirements. This system was simulated on a detailed satellite design including ESA standard mass margins to properly validate the requirements as presented in the introduction and be able to answer research question RQ1.

RQ1: What is a feasible design for a propulsion system for interplanetary travel to perform an autonomous 6U satellite near-Earth asteroid fly-by mission starting from a super synchronous geostationary transfer orbit within 5 years?

From the detailed satellite trajectory simulation an answer to research question RQ1 was found. From

the results, an adaptation of the ThrustMe NPT30-I2 RF gridded ion propulsion system including 4.810 kg of solid iodine propellant was found to be a feasible design for a propulsion system for interplanetary travel to perform an autonomous 6U satellite fly-by mission to an ambitious near-Earth asteroid target such as asteroid 2012BX34 starting from a super synchronous geostationary transfer orbit within 5 years. This interplanetary propulsion system met the mission requirements as presented in the introduction and met the additional ESA margin philosophy. Other less ambitious targets such as asteroid 2020QN1, asteroid 163693, and asteroid 2017WV13 are also possible mission targets with even less required propellant mass. For asteroid 2020QN1, DSSP's CDM-1 can also be considered as an alternative with comparable total propulsion system mass but a significantly lower total mission duration of less than half a year instead of 2 years for the NPT30-I2. However, NPT30-I2 has a lower total volume.

6

Rotational Dynamics Model

To answer research questions 2, 3, and in particular 3.1 it is necessary to simulate the rotational dynamics of the satellite. This requires a rotational dynamics model that combines a reference system, the angular kinematics, and the rotational dynamics of a satellite including perturbing torques acting on the satellite.

RQ2: What is a feasible design for a propulsion system to desaturate reaction wheels for an autonomous 6U satellite near-Earth asteroid fly-by mission starting from a super synchronous geostationary transfer orbit for 5 years?

RQ3: What is a feasible design for an attitude control system including a control algorithm for an autonomous 6U satellite near-Earth asteroid fly-by mission starting from a super synchronous geostationary transfer orbit?

RQ3.1: What is a practical framework to simulate the attitude of a CubeSat?

The thesis aims to develop an AOCS design for an autonomous 6U CubeSat NEA fly-by mission, and therefore, only rigid body dynamics are assumed. More complex rotational dynamics, such as flexible body dynamics or non-linear flexible body dynamics, are deemed too complicated for this thesis' purpose. The decision to limit the analysis to rigid body dynamics for the design of the AOCS for an autonomous 6U CubeSat NEA fly-by mission is due to the consideration that the increase in complexity with more complex rotational dynamics is not required. This is because rigid body dynamics are considered to be accurate enough to verify the requirements of the goal of this thesis, and the gain in accuracy from more complex models is not significant enough to justify the added complexity. Therefore, to keep the analysis as simple as possible, only rigid body dynamics are assumed in the design process.

6.1. Reference frame & time definition

To determine the orientation of the satellite at a certain moment in time a reference frame and time definition are required. There exist many definitions of time, but since the position of the satellite with respect to another celestial object is not a requirement, time does not have to be defined in a specific

way and can be defined as seconds from the start of a mission segment such as detachment from the satellite's piggyback ride.

The reference frame for the rotational dynamics model can either be non-rotating, rotating with respect to a celestial body, or rotating at an orbit's angular velocity. In the case of a rotating reference frame, the own rotation of the reference frame has to be taken into account in the dynamic and kinematic equations of the satellite which could complicate the matter. Therefore for this thesis, a non-rotating reference frame is used.

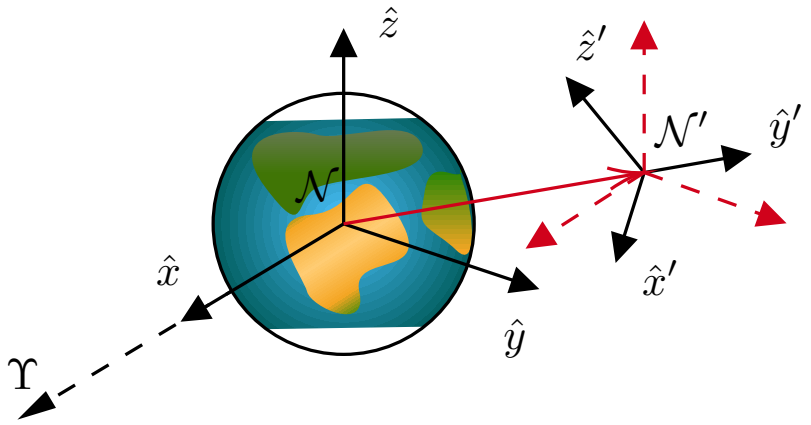

Figure 6.1: Illustration of a non-rotating geocentric reference frame $\mathcal{N}$. Υ points to the first point of Aries and $\mathcal{N}'$ is a rotated reference frame with respect to the non-rotating geocentric reference frame $\mathcal{N}$.

6.2. Rotational coordinates and kinematics

The rotational coordinates of the satellite describe the orientation of the satellite with respect to a reference frame. This choice of parameterization of the rotation between one frame to another frame or object influences how many parameters are required to define this rotation, the complexity of the mathematical expressions, and the limitations of the model. After a parameterization for the rotation between two frames has been chosen, the rotational kinematics can be specified. These are required to define the laws of motion and how eventually a torque affects the orientation of the satellite. This section briefly describes the different parameterizations and their corresponding kinematic equations. Then a discussion is done on which parameterization is the most suitable for the model.

The most common representations for rotations between one frame to another are the direction cosine matrix parameters, Euler angles, quaternions, Rodrigues Parameters (RP), and modified Rodrigues parameters (MRP).

6.2.1. Direction cosine matrix

Consider a reference frame $\mathcal{N}$ with a right-hand set of three orthogonal unit vectors $[\hat{n}_1, \hat{n}_2, \hat{n}_3]$ and a reference frame $\mathcal{B}$ with another right-hand set of three orthogonal unit vectors $[\hat{b}_1, \hat{b}_2, \hat{b}_3]$, The unit vectors of $\mathcal{B}$ can then be described as:

$$[\hat{n}_1, \hat{n}_2, \hat{n}_3]^\top = C_{\mathcal{B}}^{\mathcal{N}} [\hat{b}_1, \hat{b}_2, \hat{b}_3]^\top \tag{6.1}$$

Where $C_{\mathcal{B}}^{\mathcal{N}}$ is the direction cosine matrix. Since the direction cosine matrix is an orthonormal matrix which means $CC^\top = C^\top C = \mathbb{I}$, the inverse is equal to the transpose of the direction cosine matrix which rotates $\mathcal{N}$ to $\mathcal{B}$ such that: $C_{\mathcal{N}}^{\mathcal{B}} = \left[C_{\mathcal{B}}^{\mathcal{N}}\right]^{-1} = \left[C_{\mathcal{B}}^{\mathcal{N}}\right]^T$. In the component form the direction cosine

matrix can be written as:

$$C = \begin{bmatrix} c_{11} & c_{12} & c_{13} \\ c_{21} & c_{22} & c_{23} \\ c_{31} & c_{32} & c_{33} \end{bmatrix} \tag{6.2}$$

This means that a rotation from a reference frame to another frame can be fully expressed in the 9 components that make up the direction cosine matrix.

Next to the orientation definition, the direction cosine matrix can also be time-variant, thus the change in orientation also can be defined using a direction cosine. The kinematic differential equation for the direction cosine matrix can be expressed as:

$$\dot{C}_{\mathcal{B}}^{\mathcal{N}} = -\,\Omega_{\mathcal{N}\mathcal{B}}^{\mathcal{B}}\, C_{\mathcal{B}}^{\mathcal{N}} \tag{6.3}$$

where Ω is the skew symmetric matrix defined as:

$$\Omega_{\mathcal{N}\mathcal{B}}^{\mathcal{B}} = \begin{bmatrix} 0 & -\omega_3 & \omega_2 \\ \omega_3 & 0 & -\omega_1 \\ -\omega_2 & \omega_1 & 0 \end{bmatrix} \tag{6.4}$$

This relation is known as the kinematic differential equation for the direction cosine matrix $C_{\mathcal{B}}^{\mathcal{N}}$. The derivation of this equation can be found in Section B.1. Rearranging equation (B.7) such that ω as a function of the direction cosine matrix is found results in:

$$\omega_1 = \dot{c}_{21}c_{31} + \dot{c}_{22}c_{32} + \dot{c}_{23}c_{33} \tag{6.5a}$$

$$\omega_2 = \dot{c}_{31}c_{31} + \dot{c}_{32}c_{12} + \dot{c}_{33}c_{13} \tag{6.5b}$$

$$\omega_3 = \dot{c}_{11}c_{21} + \dot{c}_{12}c_{22} + \dot{c}_{13}c_{23} \tag{6.5c}$$

The advantage of using direction cosines over other representations is that its form is simple and linear. The clear disadvantage of this representation is that there are 9 state variables required to define the orientation and another 3 state variables to define the angular velocities of a frame. This slows down calculations of the state of the orientation of the satellite. Since this thesis will also define reaction wheels, the frames of the reaction wheels also need to be defined which makes the disadvantage even greater than other representations.

6.2.2. Euler angles

Another way to define rotations is the use of Euler angles. The direction cosine matrix can be expressed as a composition of three elementary rotations around three different axes using Euler angles. This is represented mathematically as $C_{\mathcal{B}}^{\mathcal{N}} = C_1(\theta_1)\, C_2(\theta_2)\, C_3(\theta_3)$, where C_n denotes the cosine matrix for a rotation around the nth basis vector. An example for C_1, C_2, and C_3 can be:

$$C_1(\theta_1) = \begin{bmatrix} 1 & 0 & 0 \\ 0 & \cos(\theta_1) & \sin(\theta_1) \\ 0 & -\sin(\theta_1) & \cos(\theta_1) \end{bmatrix} \tag{6.6a}$$

$$C_2(\theta_2) = \begin{bmatrix} \cos(\theta_2) & 0 & -\sin(\theta_2) \\ 0 & 1 & 0 \\ \sin(\theta_2) & 0 & \cos(\theta_2) \end{bmatrix} \tag{6.6b}$$

$$C_3(\theta_3) = \begin{bmatrix} \cos(\theta_3) & \sin(\theta_3) & 0 \\ -\sin(\theta_3) & \cos(\theta_3) & 0 \\ 0 & 0 & 1 \end{bmatrix} \tag{6.6c}$$

Now again an important part of the representation is the change of the Euler angles over time. To find the change of the Euler angles over time the relation between the change in Euler angles and the local angular velocities can be used which is:

$$\vec{\omega}^{\mathcal{B}}_{\mathcal{NB}} = C_1(\theta_1)\, C_2(\theta_2)\, \dot{\vec{\theta}}_3 + C_1(\theta_1)\, \dot{\vec{\theta}}_2 + \dot{\vec{\theta}}_1 \tag{6.7}$$

where

$$\dot{\vec{\theta}}_1 = \begin{bmatrix} \dot{\theta}_1 & 0 & 0 \end{bmatrix}^\top \tag{6.8a}$$

$$\dot{\vec{\theta}}_2 = \begin{bmatrix} 0 & \dot{\theta}_2 & 0 \end{bmatrix}^\top \tag{6.8b}$$

$$\dot{\vec{\theta}}_3 = \begin{bmatrix} 0 & 0 & \dot{\theta}_3 \end{bmatrix}^\top \tag{6.8c}$$

To find the changes in Euler angles the inverse must be taken such that the changes in Euler angles are expressed in terms of their current state and angular velocity vector $\vec{\omega}^{\mathcal{B}}_{\mathcal{NB}}$. The changes of Euler angles have difficulties for angles of $\left[-\frac{\pi}{2}, \quad \frac{\pi}{2}\right]$, because the inverse that maps $\vec{\omega}^{\mathcal{B}}_{\mathcal{NB}}$ to the changes in Euler angles contains an $\frac{1}{\cos(\theta)}$-term that will cause a singularity.

The downside of Euler angles is clearly this singularity. Unless a small angle approximation is used, it is not possible to use Euler angles for applications like satellites in orbit. The advantage of Euler angles is that they only require 3 states for the orientation and 3 for the angular velocities which reduce the required number of calculations per integration step.

6.2.3. Euler's eigenaxis rotations or fixed axis rotations

A rotation of one reference frame $\mathcal{N}$ to another reference frame $\mathcal{B}$ can also be described using a fixed axis and an angle. This theory states:

> *Euler's eigenaxis rotation theorem states that by rotating a rigid body about an axis that is fixed to the body and stationary in an inertial reference frame, the rigid body attitude can be changed from any given orientation to any other orientation. Such an axis of rotation, whose orientation relative to both an inertial reference frame and the body remains unchanged throughout the motion, is called the Euler axis or eigenaxis* [43].

Let $\vec{e} = [\hat{e}_1, \hat{e}_2, \hat{e}_3]^\top$ described in frame $\mathcal{N}$ be the unit eigenaxis and θ the angle of rotation then the direction cosine matrix C can be found using:

$$C^{\mathcal{N}}_{\mathcal{B}} = \begin{bmatrix} c\theta + \hat{e}_1^2(1-c\theta) & \hat{e}_1\hat{e}_2(1-c\theta) + \hat{e}_3 s\theta & \hat{e}_1\hat{e}_3(1-c\theta) - \hat{e}_2 s\theta \\ \hat{e}_2\hat{e}_1(1-c\theta) - \hat{e}_3 s\theta & c\theta + \hat{e}_2^2(1-c\theta) & \hat{e}_2\hat{e}_3(1-c\theta) + \hat{e}_1 s\theta \\ \hat{e}_3\hat{e}_1(1-c\theta) + \hat{e}_2 s\theta & \hat{e}_3\hat{e}_2(1-c\theta) - \hat{e}_1 s\theta & c\theta + \hat{e}_3^2(1-c\theta) \end{bmatrix} \tag{6.9}$$

where: $c\theta = cos(\theta)$ and $s\theta = sin(\theta)$. Also, $\hat{e}_1^2 + \hat{e}_2^2 + \hat{e}_3^2 = 1$. The change of the axis of rotation and the angle of rotation can be calculated separately, but this theory can only handle fixed axis rotations. Ideally, this representation can be used to describe rigid bodies that do not change their axis of rotation with respect to another rigid body such as a reaction wheel with respect to the rest of the satellite it is mounted on.

6.2.4. Quaternions

In the last section Euler's eigenaxis rotations were only able to describe rotations that were around a fixed axis. Quaternions extend this theory further to any rotation. Let $\vec{e} = \begin{bmatrix} \hat{e}_1 & \hat{e}_2 & \hat{e}_3 \end{bmatrix}^\top$ be a unit vector along an eigenaxis and θ a rotation around that unit vector then the rotation quaternions are defined as [43]:

$$q_i = \hat{e}_i \sin\left(\frac{\theta}{2}\right), \quad q_4 = \cos\left(\frac{\theta}{2}\right), \quad (i = 1, 2, 3) \tag{6.10}$$

Since $\vec{e}$ is a unit vector:

$$\begin{aligned} \left(\sum_{i=1,2,3} q_i^2\right) + q_4^2 &= \left(\sum_{i=1,2,3} e_i^2\right) \sin^2\left(\frac{\theta}{2}\right) + \cos^2\left(\frac{\theta}{2}\right) \\ \left(\sum_{i=1,2,3} q_i^2\right) + q_4^2 &= \sin^2\left(\frac{\theta}{2}\right) + \cos^2\left(\frac{\theta}{2}\right) = 1 \end{aligned}$$

From this the following relation is found:

$$q_1^2 + q_2^2 + q_3^2 + q_4^2 = 1 \tag{6.11}$$

The direction cosine matrix for a rotation from a reference frame $\mathcal{B}$ to a reference frame $\mathcal{N}$ can then be written in quaternions as [43]:

$$C_{\mathcal{B}}^{\mathcal{N}} = \begin{bmatrix} 1 - 2\left(q_2^2 + q_3^2\right) & 2\left(q_1 q_2 + q_3 q_4\right) & 2\left(q_1 q_3 - q_2 q_4\right) \\ 2\left(q_2 q_1 - q_3 q_4\right) & 1 - 2\left(q_1^2 + q_3^2\right) & 2\left(q_2 q_3 + q_1 q_4\right) \\ 2\left(q_3 q_1 + q_2 q_4\right) & 2\left(q_3 q_2 - q_1 q_4\right) & 1 - 2\left(q_1^2 + q_2^2\right) \end{bmatrix} \tag{6.12}$$

The direction cosine matrix can also be written in terms of $\vec{q}$, q_4, and the skew matrix Q which are defined as:

$$\vec{q} = \begin{bmatrix} q_1 \\ q_2 \\ q_3 \end{bmatrix}, \quad Q = \begin{bmatrix} 0 & -q_3 & q_2 \\ q_3 & 0 & -q_1 \\ -q_2 & q_1 & 0 \end{bmatrix} \tag{6.13}$$

Then the direction cosine matrix in quaternions found earlier can be expressed as:

$$C_{\mathcal{B}}^{\mathcal{N}} = \left(q_4^2 - \vec{q}^\top \vec{q}\right) \mathbb{I}_{3\times 3} + 2\vec{q}\vec{q}^\top - 2q_4 Q \tag{6.14}$$

The kinematic differential equations can be expressed as:

$$\dot{\vec{q}} = \tfrac{1}{2}\left(q_4 \vec{\omega} - \vec{\omega} \times \vec{q}\right) \tag{6.15a}$$

$$\dot{q}_4 = -\tfrac{1}{2} \vec{\omega}^\top \vec{q} \tag{6.15b}$$

where $\vec{q} = \begin{bmatrix} q_1 & q_2 & q_3 \end{bmatrix}^\top$, $\vec{\omega} = \begin{bmatrix} \omega_1 & \omega_2 & \omega_3 \end{bmatrix}^\top$ and $\omega \times \vec{q}$ comes from:

$$\vec{\omega} \times \vec{q} = \begin{bmatrix} 0 & -\omega_3 & \omega_2 \\ \omega_3 & 0 & -\omega_1 \\ -\omega_2 & \omega_1 & 0 \end{bmatrix} \begin{bmatrix} q_1 \\ q_2 \\ q_3 \end{bmatrix} \tag{6.16}$$

The derivation of the kinematics of the quaternions can be seen in Section B.2.

The advantage of using quaternions over other representations such as Euler angles or direction cosine is that it does not have singularities and only uses 4 orientation parameters and 3 angular velocity parameters to describe a motion that is less than the direction cosine representation.

6.2.5. Rodrigues parameters

RPs are parameters that try to reduce the number of required variables that specify the rotation from one frame to another. Rewriting the definition of the quaternions results in the RPs [43]:

$$\vec{g} = \begin{bmatrix} g_1 \\ g_2 \\ g_3 \end{bmatrix} = \begin{bmatrix} q_1/q_4 \\ q_2/q_4 \\ q_3/q_4 \end{bmatrix} = \vec{e}\tan\left(\tfrac{\theta}{2}\right) \tag{6.17}$$

This reduces the number of parameters to 3 instead of 4 quaternions. These are called the RPs. However, it can be seen that the definition now involves a tangent function that has real poles where the function is not defined at $k\pi + \frac{\pi}{2}$, with $k \in \mathbb{Z}$. This means that RPs can only define motions in the domain of $-\frac{\pi}{2} < \theta < \frac{\pi}{2}$. This is one of the reasons RPs are not used very often.

For the derivation of the kinematic differential equation of the RPs the time derivative of the definition of the RPs can be used:

$$\dot{\vec{g}} = \frac{\mathrm{d}}{\mathrm{d}t}\left\{\frac{\vec{q}}{q_4}\right\}$$

Which results in:

$$\dot{\vec{g}} = \frac{\dot{\vec{q}}}{q_4} - \frac{\dot{\vec{q}}}{q_4^2}\dot{q}_4 \tag{6.18}$$

Substitution of Equation 6.15 in the found expression results in:

$$\dot{\vec{g}} = \tfrac{1}{2}\left[\vec{\omega} + \tfrac{1}{q_4}Q\left(\vec{q}\right)\vec{q} + \tfrac{1}{q_4^2}\vec{q}\vec{q}^{\top}\vec{\omega}\right] \tag{6.19}$$

The definition of the RPs can also be rewritten to quaternions as a function of the RPs:

$$\vec{q} = \frac{\vec{g}}{\sqrt{1 + \vec{g}\vec{g}^{\top}}} \tag{6.20a}$$

$$q_4 = \frac{1}{\sqrt{1 + \vec{g}\vec{g}^{\top}}} \tag{6.20b}$$

Substitution of these equations inside of the found expression in Equation 6.19 results in [43]:

$$\dot{\vec{g}} = \tfrac{1}{2}\left[\mathbb{I}_{3\times 3} + Q\left(\vec{g}\right) + \vec{g}\vec{g}^{\top}\right]\vec{\omega} \tag{6.21}$$

where:

$$Q\left(\vec{g}\right) = \begin{bmatrix} 0 & -g_3 & g_2 \\ g_3 & 0 & -g_1 \\ -g_2 & g_1 & 0 \end{bmatrix}$$

As stated in this section, RPs require fewer parameters to represent a rotation. The disadvantage of this representation is that singularities are present due to the reduction.

6.2.6. Modified Rodrigues parameters

To solve the singularity problem that occurs when using RPs to try to express rotations of 90 degrees, MRPs were introduced in terms of quaternions as [44]:

$$\vec{\psi} = \frac{\vec{q}}{1 + q_4} \tag{6.22}$$

rewriting the quaternions in terms of MRPs then gives:

$$\vec{q} = \frac{2\vec{\psi}}{1 + \vec{\psi}^{\top}\vec{\psi}}, \quad q_4 = \frac{1 - \vec{\psi}^{\top}\vec{\psi}}{1 + \vec{\psi}^{\top}\vec{\psi}} \tag{6.23}$$

Combining Equation 6.14 and Equation 6.23 gives the direction cosine matrix for a rotation from a reference frame $\mathcal{B}$ to a reference frame $\mathcal{N}$ in MRPs:

$$C_{\mathcal{B}}^{\mathcal{N}} = \mathbb{I}_{3\times 3} - 4\frac{1-\vec{\psi}^{\top}\vec{\psi}}{\left(1+\vec{\psi}^{\top}\vec{\psi}\right)^{2}}Q\left(\vec{\psi}\right) + 8\frac{1}{\left(1+\vec{\psi}^{\top}\vec{\psi}\right)^{2}}Q^{2}\left(\vec{\psi}\right) \tag{6.24}$$

with $Q\left(\vec{\psi}\right)$ the MRPs skew matrix:

$$Q\left(\vec{\psi}\right) = \begin{bmatrix} 0 & -\psi_3 & \psi_2 \\ \psi_3 & 0 & -\psi_1 \\ -\psi_2 & \psi_1 & 0 \end{bmatrix} \tag{6.25}$$

To find the rotation from one MRP vector to another the composition rule for the MRPs can be applied which reads [44]:

$$\vec{\psi}_3 = \frac{\left(1-\left\|\vec{\psi}_1\right\|^2\right)\vec{\psi}_2 + \left(1-\left\|\vec{\psi}_2\right\|^2\right)\vec{\psi}_1 - 2\vec{\psi}_2\times\vec{\psi}_1}{1+\left\|\vec{\psi}_2\right\|^2\left\|\vec{\psi}_1\right\|^2 - 2\vec{\psi}_2\cdot\vec{\psi}_1} \tag{6.26}$$

where $\vec{\psi}_3$ represents the rotation from a rotated frame 1 defined using $\vec{\psi}_1$ to a rotated frame 2 defined using $\vec{\psi}_2$.

In a similar way as the RPs also the kinematics in MRPs can be found using the definition and time derivative:

$$\dot{\vec{\psi}} = \frac{\mathrm{d}}{\mathrm{d}t}\left\{\frac{\vec{q}}{1+q_4}\right\}$$

$$\dot{\vec{\psi}} = \frac{1}{1+q_4}\dot{\vec{q}} - \frac{\vec{q}}{\left(1+q_4\right)^2}\dot{q}_4 \tag{6.27}$$

Substitution of equation (6.15) results in:

$$\dot{\vec{\psi}} = \tfrac{1}{2}\left[\frac{1}{1+q_4}q_4\vec{\omega} + \frac{1}{1+q_4}Q\vec{q} + \frac{1}{\left(1+q_4\right)^2}\vec{q}\vec{q}^{\top}\vec{\omega}\right] \tag{6.28}$$

The definition of the MRPs can also be rewritten to quaternions as a function of the MRPs:

$$\vec{q} = \frac{2\vec{\psi}}{1+\vec{\psi}^{\top}\vec{\psi}} \tag{6.29a}$$

$$q_4 = \frac{1-\vec{\psi}^{\top}\vec{\psi}}{1+\vec{\psi}^{\top}\vec{\psi}} \tag{6.29b}$$

Substitution of these equations inside of the found equation (6.28) results in:

$$\dot{\vec{\psi}} = \tfrac{1}{2}\left[\mathbb{I}_{3\times 3} + Q\left(\vec{\psi}\right) + \vec{\psi}\vec{\psi}^{\top} - \tfrac{1}{2}\left(1+\vec{\psi}^{\top}\vec{\psi}\right)\mathbb{I}_{3\times 3}\right]\vec{\omega} \tag{6.30}$$

where:

$$Q\left(\vec{\psi}\right) = \begin{bmatrix} 0 & -\psi_3 & \psi_2 \\ \psi_3 & 0 & -\psi_1 \\ -\psi_2 & \psi_1 & 0 \end{bmatrix}$$

Often $\dot{\vec{\psi}}$ is expressed as:

$$\dot{\vec{\psi}} = G\left(\vec{\psi}\right)\vec{\omega} \tag{6.31}$$

where

$$G\left(\vec{\psi}\right) = \tfrac{1}{2}\left[\mathbb{I}_{3\times 3} + Q\left(\vec{\psi}\right) + \vec{\psi}\vec{\psi}^{\top} - \tfrac{1}{2}\left(1+\vec{\psi}^{\top}\vec{\psi}\right)\mathbb{I}_{3\times 3}\right] \tag{6.32}$$

Tracking of a frame

The tracking of a reference frame or the error between two rotational motions depends on the selected parameterization. For one-dimensional problems which are uncoupled from other dimensions, it is very straightforward. For example, let $\delta x = x - x_r$ be the error of the system x with respect to a reference state x_r then the derivative of the error is simply $\delta \dot{x} = \dot{x} - \dot{x}_r$. However, for angular rotations, this is not as straightforward. To find the rotation from one rotated frame $\mathcal{C}$ to another rotated frame $\mathcal{D}$ the direction cosines can be used such that the rotation from $\mathcal{C} \to \mathcal{D}$ can be found by rotating $\mathcal{C}$ back to the Newtonian inertial reference frame $\mathcal{N}$ or $\mathcal{C} \to \mathcal{N}$ and then rotate from $\mathcal{N} \to \mathcal{D}$. For further reference, this means that:

$$C_{\mathcal{C}}^{\mathcal{D}} \equiv C_{\mathcal{N}}^{\mathcal{D}} C_{\mathcal{C}}^{\mathcal{N}} \tag{6.33}$$

Or

$$C_{\mathcal{C}}^{\mathcal{D}} \equiv \left[C_{\mathcal{D}}^{\mathcal{N}}\right]^{\top} C_{\mathcal{C}}^{\mathcal{N}} \tag{6.34}$$

Using Equation 6.26 the difference $\delta\vec{\psi}$ between the current reference frame $\vec{\phi}$ and the desired reference frame $\vec{\phi}_r$ in MRPs can be expressed as:

$$\delta\vec{\psi} = \frac{\left(1 - \left\|-\vec{\psi}_r\right\|^2\right)\vec{\psi} + \left(1 - \left\|\vec{\psi}\right\|^2\right) - \vec{\psi}_r - 2\vec{\psi} \times -\vec{\psi}_r}{1 + \left\|\vec{\psi}\right\|^2 \left\|-\vec{\psi}_r\right\|^2 - 2\vec{\psi} \cdot -\vec{\psi}_r} \tag{6.35}$$

where $\vec{\psi}$ is the true state of the rigid body and $\vec{\psi}_r$ is the desired reference state. Notice that $\vec{\psi}_r$ has negative signs in front of it because the rotation from the body to the inertial reference frame to the desired reference frame has to be found, which is a composition of the true rotation and the inverse of the rotation of the desired reference frame.

To find a similar expression for $\delta\dot{\vec{\psi}}$ recall Equation 6.31 from the rigid body kinematics such that $\delta\dot{\vec{\psi}}$ can be expressed as:

$$\delta\dot{\vec{\psi}} = G\left(\delta\vec{\psi}\right)\delta\vec{\omega} \tag{6.36}$$

where

$$G\left(\delta\vec{\psi}\right) = \tfrac{1}{2}\left[\mathbb{I}_{3\times 3} + Q\left(\delta\vec{\psi}\right) + \delta\vec{\psi}\delta\vec{\psi}^{\top} - \tfrac{1}{2}\left(1 + \delta\vec{\psi}^{\top}\delta\vec{\psi}\right)\mathbb{I}_{3\times 3}\right]$$

and where

$$Q\left(\delta\vec{\psi}\right) = \begin{bmatrix} 0 & -\delta\psi_3 & \delta\psi_2 \\ \delta\psi_3 & 0 & -\delta\psi_1 \\ -\delta\psi_2 & \delta\psi_1 & 0 \end{bmatrix}$$

To find $\delta\vec{\omega}$, the angular rotations in the reference frame have to be rotated to the rigid body frame such that $\delta\vec{\omega}$ can be expressed as:

$$\delta\vec{\omega} = \vec{\omega} - [\vec{\omega}_r]_{\mathcal{B}} \tag{6.37}$$

or

$$\delta\vec{\omega} = \vec{\omega} - C_{\mathcal{R}}^{\mathcal{B}}\left(\delta\vec{\psi}\right)\vec{\omega}_r \tag{6.38}$$

Using Equation B.7 and taking the time derivative of $\delta\vec{\omega}$, $\delta\dot{\vec{\omega}}$ can be found (see Section B.3 for the full derivation):

$$\delta\dot{\vec{\omega}} = \dot{\vec{\omega}} - C_{\mathcal{R}}^{\mathcal{B}}\left(\delta\vec{\psi}\right)\left[\dot{\vec{\omega}}_r\right]_{\mathcal{R}} + \omega \times C_{\mathcal{R}}^{\mathcal{B}}\left(\delta\vec{\psi}\right)[\vec{\omega}_r]_{\mathcal{R}} \tag{6.39}$$

Strengths and weaknesses

The advantage of using MRPs is that they are a compact and efficient representation. It is less prone to numerical errors than other representations such as Euler angles or quaternions and can be used for fast and accurate attitude estimation, tracking, and control. The disadvantage of using MRPs is that they are not easy to understand. Additionally, they are not as intuitive as other rotation representations, like Euler angles, which makes them more difficult to work with. Furthermore, they still have singularities when $q_4 = -1$. To overcome this singularity switching to the shadow component is a common practice. This is explained in more detail in Section B.3.

6.2.7. Rotational coordinate selection

Euler angles are a very good parameterization for small rotations and when simplicity is desired. These parameters are also more intuitive than other parameters. However, the downside is that Euler angles have singularities for angles which are $k\pi + \frac{\pi}{2}$. A better representation that is able to handle every rotation would be the use of the direction cosine. The downside of the representation is that 9 parameters are used for a single rotation. Quaternions can be used to reduce the number of parameters to 4 parameters while still being able to handle every rotation. This reduces the required calculations. Rodrigues parameters are a way to decrease the number of parameters even further down to 3. However, this presentation constrains the domain of rotations to $-\frac{\pi}{2} < 0 < \frac{\pi}{2}$. Modified Rodrigues parameters are similar to Rodrigues parameters, but these parameters are able to handle every rotation. These parameters are therefore considered to be the best representation for the satellite because they decrease the required calculations to solve the kinematics which is helpful when doing autonomous calculations.

6.3. Rigid body dynamics

In Wie [43] the effect of external torques on the attitude of a system is described by the angular momentum theory for rigid bodies. consider a Newtonian reference frame $\mathcal{N}$ with a rigid body placed at a distance R_c as can be seen in Figure 6.2. The equations of motion of a rigid body about an arbitrary point in space $\mathcal{O}$ can then be expressed as:

$$\int \vec{r} \times \ddot{\vec{R}} \, \mathrm{d}m = M_{\mathcal{O}} \tag{6.40}$$

where $\vec{r}$ is the position vector of a infinitesimal mass element dm relative to point $\mathcal{O}$. $\vec{R}$ is the position vector of dm from the inertial origin of $\mathcal{N}$, $\ddot{\vec{R}}$ is the inertial acceleration of dm, and $\vec{M}_{\mathcal{O}}$ is the total external torque about point $\mathcal{O}$.

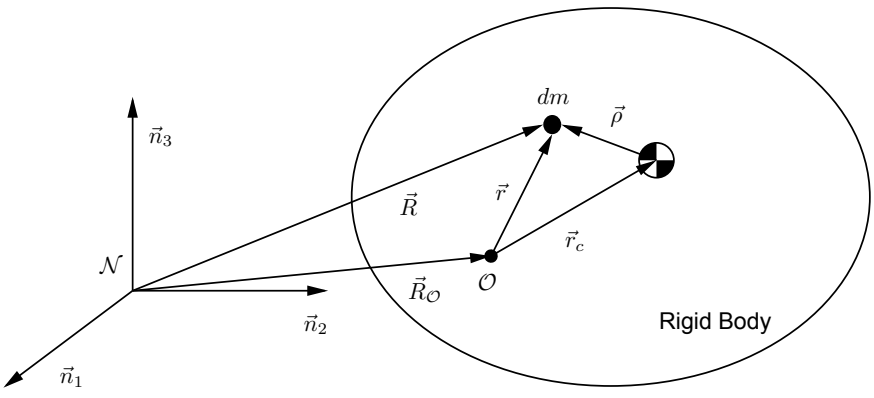

Figure 6.2: Rigid body in motion relative to a frame $\mathcal{N}$.

If $\vec{r}_c$ is the position vector from the center of mass to the point $\mathcal{O}$ and $\vec{\rho}$ is the position vector of $\mathrm{d}m$ to the center of mass, then:

$$\int \vec{r}\mathrm{d}m = m\vec{r}_c \tag{6.41}$$

$$\int \vec{\rho}\mathrm{d}m = 0 \tag{6.42}$$

Since $\vec{R} = \vec{R}_{\mathcal{O}} + \vec{r}$ Equation 6.40 can be rewritten as:

$$\dot{\vec{h}}_{\mathcal{O}} + m\vec{r}_c \times \ddot{\vec{R}}_{\mathcal{O}} = \vec{M}_{\mathcal{O}} \tag{6.43}$$

where $\vec{h}_{\mathcal{O}}$ is called the relative angular momentum about $\mathcal{O}$, which is defined as:

$$\vec{h}_{\mathcal{O}} = \int \vec{r} \times \dot{\vec{r}}\mathrm{d}m \tag{6.44}$$

The absolute angular momentum vector about $\mathcal{O}$ is defined as:

$$\vec{H}_{\mathcal{O}} = \int \vec{r} \times \dot{\vec{R}}\mathrm{d}m \tag{6.45}$$

Combining Equation 6.40 and Equation 6.45 the following equation can be obtained:

$$\dot{\vec{H}}_{\mathcal{O}} + m\ddot{\vec{R}}_{\mathcal{O}} \times \dot{\vec{r}}_c = \vec{M}_{\mathcal{O}} \tag{6.46}$$

Note that the relative and absolute angular momentum are the same if $\mathcal{O}$ is exactly at the center of mass. Therefore the satellite's reference point is taken at the center of mass which means $\vec{r}_c = [0, 0, 0]^\top$ or $\dot{\vec{H}}_{\mathcal{O}} = \vec{M}_{\mathcal{O}}$.

6.3.1. Inertia

Consider a rigid body with a body-fixed reference frame $\mathcal{B}$ with its origin at the center of mass of the rigid body as can be seen in Figure 6.3. Let $\vec{\omega} = \vec{\omega}^{\mathcal{B}}_{\mathcal{N}\mathcal{B}}$ be the angular velocity vector of the rigid body with respect to the inertial reference frame $\mathcal{N}$. The angular momentum vector $\vec{H}$ of the rigid body about the center of mass is then defined as [43]:

$$\vec{H} = \int \vec{\rho} \times \dot{\vec{R}}\,\mathrm{d}m = \int \vec{\rho} \times \dot{\vec{\rho}}\,\mathrm{d}m = \int \vec{\rho} \times (\vec{\omega} \times \vec{\rho})\,\mathrm{d}m \tag{6.47}$$

as $\vec{R} = \vec{R}_c + \vec{\rho}$, $\int \vec{\rho}\,\mathrm{d}m = 0$, $\dot{\vec{R}} \equiv \left\{\frac{\mathrm{d}\vec{R}}{\mathrm{d}t}\right\}_{\mathcal{N}}$, and

$$\dot{\vec{\rho}} \equiv \left\{\frac{\mathrm{d}\vec{\rho}}{\mathrm{d}t}\right\}_{\mathcal{N}} = \left\{\frac{\mathrm{d}\vec{\rho}}{\mathrm{d}t}\right\}_{\mathcal{B}} + \vec{\omega}^{\mathcal{B}}_{\mathcal{N}\mathcal{B}} \times \vec{\rho} \tag{6.48}$$

Note that $\{\mathrm{d}\vec{\rho}/\mathrm{d}t\}_B = 0$ for a rigid body.

Let $\vec{\rho}$ and $\vec{\omega}$ be expressed as:

$$\vec{\rho} = \rho_1\vec{b}_1 + \rho_2\vec{b}_2 + \rho_3\vec{b}_3 \tag{6.49a}$$

$$\vec{\omega} = \omega_1\vec{b}_1 + \omega_2\vec{b}_2 + \omega_3\vec{b}_3 \tag{6.49b}$$

Where $\{\vec{b}_1, \vec{b}_2, \vec{b}_3\}$ is a set of three orthogonal unit vectors, called basis vectors, of a body-fixed reference frame $\mathcal{B}$. Combining with Equation 6.47 the angular momentum vector can be written as:

$$\begin{aligned}\vec{H} = &\left(J_{11}\omega_1 + J_{12}\omega_2 + J_{13}\omega_3\right)\vec{b}_1 + \left(J_{21}\omega_1 + J_{22}\omega_2 + J_{23}\omega_3\right)\vec{b}_2 \\ &+ \left(J_{31}\omega_1 + J_{32}\omega_2 + J_{33}\omega_3\right)\vec{b}_3\end{aligned} \tag{6.50}$$

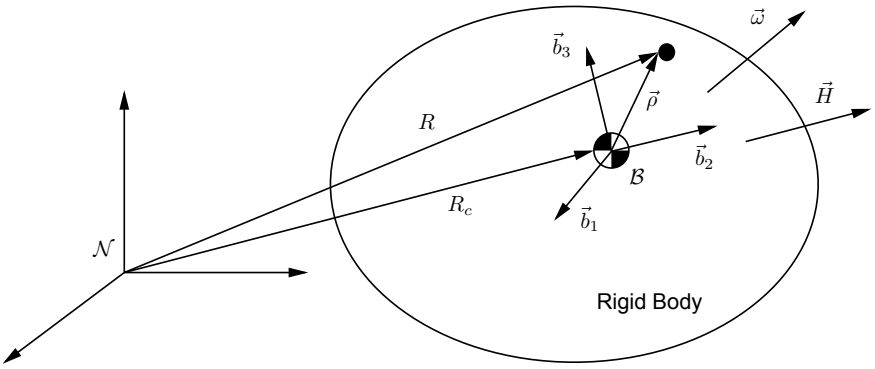

Figure 6.3: Rigid body with a body-fixed reference frame $\mathcal{B}$ with its origin at the center of mass. $\vec{\rho}$ denotes the position vector of a infinitesimal mass element $\mathrm{d}m$ from the center of mass, $\vec{R}_c$ is the position vector of the center of mass from an inertial origin of $\mathcal{N}$, and $\vec{R}$ is the position vector of $\mathrm{d}m$ from an inertial origin of $\mathcal{N}$

Where J_{11}, J_{22} and J_{33} are often referred to the moments of inertia which can be defined as:

$$J_{11} = \int \left(\rho_2^2 + \rho_3^2\right) \mathrm{d}m \tag{6.51a}$$

$$J_{22} = \int \left(\rho_1^2 + \rho_3^2\right) \mathrm{d}m \tag{6.51b}$$

$$J_{33} = \int \left(\rho_1^2 + \rho_2^2\right) \mathrm{d}m \tag{6.51c}$$

And J_{ij} where $(i \neq j)$ are often referred to as the products of inertia defined as:

$$J_{12} = J_{21} = -\int (\rho_1 \rho_2) \, \mathrm{d}m \tag{6.52a}$$

$$J_{13} = J_{31} = -\int (\rho_1 \rho_3) \, \mathrm{d}m \tag{6.52b}$$

$$J_{23} = J_{32} = -\int (\rho_2 \rho_3) \, \mathrm{d}m \tag{6.52c}$$

Expressing $\vec{H}$ as:

$$\vec{H} = H_1 \vec{b}_1 + H_2 \vec{b}_2 + H_3 \vec{b}_3 \tag{6.53}$$

Equation 6.50 can also be written in matrix form as:

$$\vec{H} = J\vec{\omega} \tag{6.54}$$

or

$$\begin{bmatrix} H_1 \\ H_2 \\ H_3 \end{bmatrix} = \begin{bmatrix} J_{11} & J_{12} & J_{13} \\ J_{21} & J_{22} & J_{23} \\ J_{31} & J_{32} & J_{33} \end{bmatrix} \begin{bmatrix} \omega_1 \\ \omega_2 \\ \omega_3 \end{bmatrix} \tag{6.55}$$

Where J is called the inertia matrix.

In the special case that the rigid body consists of multiple fixed bodies, the parallel axis theorem can be used to find the combined inertia of the system. The general form of the well-known parallel axis theorem states that:

$$J_2 = J_1 + m\left(\left(\vec{\rho}^{\top}\vec{\rho}\right)\mathbb{I}_{3\times 3} - \vec{\rho}\vec{\rho}^{\top}\right) \tag{6.56}$$

This states that the inertia of a body J_2 around a point removed from its center of mass can be expressed as the body's own inertia in its center of mass J_1 combined with its mass times the displacement of the point in question from the body's center of mass $\vec{\rho}$ squared.

Using Equation 6.56, the inertia tensor of a rigid body consisting of N multiple bodies around its center of mass denoted with the subscript i can then be expressed as:

$$J = \sum_{i=1}^{N} \left\{ J_i + m_i \left(\left(\vec{\rho}_i^{\top} \vec{\rho}_i \right) \mathbb{I}_{3\times 3} - \vec{\rho}_i \vec{\rho}_i^{\top} \right) \right\} \tag{6.57}$$

6.3.2. Euler's Rotational Equations of Motion

As discussed in Section 6.3, the angular momentum equation of a rigid body about its center of mass is can be expressed as:

$$\vec{M}_{\mathcal{O}} = \dot{\vec{H}}_{\mathcal{O}} \tag{6.58}$$

Where $\vec{M}_{\mathcal{O}}$ is the total torque acting on the rigid body and $\dot{\vec{H}}_{\mathcal{O}}$ is the time-derivative of the angular momentum vector about the center of mass. For simplicity, in this subsection the subscript $\mathcal{O}$ is dropped such that $\vec{M}_{\mathcal{O}} \equiv \vec{M}$ and $\dot{\vec{H}}_{\mathcal{O}} \equiv \dot{\vec{H}}$. $\dot{\vec{H}}$ can also be expressed as:

$$\dot{\vec{H}} \equiv \left\{ \frac{\mathrm{d}\vec{H}}{\mathrm{d}t} \right\}_{\mathcal{N}} = \left\{ \frac{\mathrm{d}\vec{H}}{\mathrm{d}t} \right\}_{\mathcal{B}} + \vec{\omega}_{\mathcal{N}\mathcal{B}}^{\mathcal{B}} \times \vec{H} \tag{6.59}$$

This expression can be read as the change in angular momentum of the rigid body in the Newtonian inertial reference frame $\mathcal{N}$ is equal to the change in angular momentum of the rigid body in its own body frame $\mathcal{B}$ plus the effect of the rotation of the $\mathcal{B}$ itself. This means that the rigid body rotational dynamics around its center of mass can be written as:

$$\vec{M} = \left\{ \frac{\mathrm{d}\vec{H}}{\mathrm{d}t} \right\}_{\mathcal{B}} + \vec{\omega}_{\mathcal{N}\mathcal{B}}^{\mathcal{B}} \times \vec{H} \tag{6.60}$$

For convenience let $\vec{\omega} \equiv \vec{\omega}_{\mathcal{N}\mathcal{B}}^{\mathcal{B}}$ and from Equation 6.54 $\vec{H} = J\vec{\omega}$ so the rotational equation of motion can be written as [43]:

$$\begin{aligned} \vec{M} &= \left\{ \frac{\mathrm{d}}{\mathrm{d}t} \left(J\vec{\omega} \right) \right\}_{\mathcal{B}} + \vec{\omega} \times J\vec{\omega} \\ \vec{M} &= \left\{ \frac{\mathrm{d}J}{\mathrm{d}t} \right\}_{\mathcal{B}} \vec{\omega} + J \left\{ \frac{\mathrm{d}\vec{\omega}}{\mathrm{d}t} \right\}_{\mathcal{B}} + \vec{\omega} \times J\vec{\omega} \end{aligned} \tag{6.61}$$

Assuming the rigid bodies Inertia in the $\mathcal{B}$ does not change over time then $\left\{ \frac{\mathrm{d}J}{\mathrm{d}t} \right\}_{\mathcal{B}} = 0$ and rewriting $\left\{ \frac{\mathrm{d}\vec{\omega}}{\mathrm{d}t} \right\}_{\mathcal{B}} = \left\{ \frac{\mathrm{d}\vec{\omega}}{\mathrm{d}t} \right\}_{\mathcal{N}} = \dot{\vec{\omega}}$ the rotational equation of motion becomes:

$$\vec{M} = J\dot{\vec{\omega}} + \vec{\omega} \times J\vec{\omega} \tag{6.62}$$

Introducing the skew matrix:

$$\Omega = \begin{bmatrix} 0 & -\omega_3 & \omega_2 \\ \omega_3 & 0 & -\omega_1 \\ -\omega_2 & \omega_1 & 0 \end{bmatrix} \tag{6.63}$$

Then the rotational equation of motion can be written as:

$$\vec{M} = J\dot{\vec{\omega}} + \Omega J\vec{\omega} \tag{6.64}$$

$\dot{\vec{\omega}}$ can now be isolated:

$$\dot{\vec{\omega}} = J^{-1} \left[\vec{M} - \Omega J\vec{\omega} \right] \tag{6.65}$$

6.3.3. Rigid body dynamics including reaction wheels

Now consider a rigid body including internal rotating reaction wheels which can move freely in a fixed orientation with respect to the rigid body. Then using Equation 6.57 the inertia of the rigid body including reaction wheels can be expressed as:

$$J_s = J_{\mathcal{B}} + \sum_{i=1}^{N} \left\{ W_i J_{w,i} W_i^\top + m_{w,i} \left(\left(\vec{\rho}_{w,i}^\top \vec{\rho}_{w,i} \right) \mathbb{I}_{3\times 3} - \vec{\rho}_{w,i} \vec{\rho}_{w,i}^\top \right) \right\} \tag{6.66}$$

where J_s is the inertial tensor of the total satellite, $J_{\mathcal{B}}$ the inertial tensor of the satellite without the reaction wheels W_i is a rotation matrix that rotates the inertia tensor $J_{w,i}$ of the reaction wheel in its own frame to the satellite body frame, $m_{w,i}$ is the mass of the reaction wheel, $\vec{\rho}_{w,i}$ is the displacement vector from the center of mass of the satellite to the reaction wheel's center of mass and N is the number of reaction wheels.

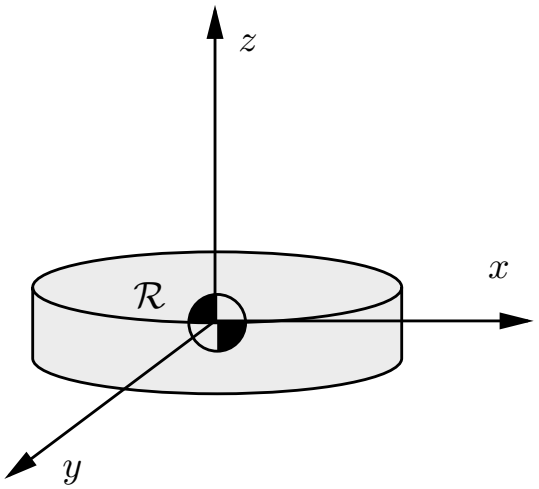

Figure 6.4: Visualisation of a reaction wheel as a disk in its own frame $\mathcal{R}$.

Assuming that the reaction wheel is ideal and has no inconsistencies, the reaction wheel can be described as a disk as can be seen in Figure 6.4 with inertia expressed as:

$$J_{w,i} = \begin{bmatrix} J_{xx} & 0 & 0 \\ 0 & J_{yy} & 0 \\ 0 & 0 & J_{zz} \end{bmatrix} \tag{6.67}$$

where $J_{xx} = J_{yy}$ and J_{zz} is the moment of inertia around the rotation axis.

With the new information about the inertia of the complete system and the knowledge that the reaction wheels can only spin along a fixed axis in the body frame, the total angular momentum of the satellite can then be expressed as:

$$H = J_s \vec{\omega} + \sum_{i=1}^{N} \left\{ W_i J_{w,i} \vec{\omega}_{w,i} \right\} \tag{6.68}$$

Using Equation 6.64 the rotational equations of motion for the satellite with a single reaction wheel can be expressed as:

$$M = J_s \dot{\vec{\omega}} + W_i J_{w,i} \dot{\vec{\omega}}_{w,i} + \Omega \left(J_s \vec{\omega} + W_i J_{w,i} \vec{\omega}_{w,i} \right) \tag{6.69}$$

where $\vec{\omega}_{w,i} = \begin{bmatrix} 0 & 0 & \omega_{w,i} \end{bmatrix}^\top$ and $\dot{\vec{\omega}}_{w,i} = \begin{bmatrix} 0 & 0 & \dot{\omega}_{w,i} \end{bmatrix}^\top$ because rotations around other axes than the local z-axis of the reaction wheel are fixed.

Since the reaction wheel axis of rotation is fixed and the $\vec{\omega}_{w,i}$ contains zeros in the local x and y direction the found expression for the rotational equations of motion can be simplified to:

$$M = J_s\dot{\vec{\omega}} + W_{z,i}J_{zz,i}\dot{\omega}_{w,i} + \Omega\left(J_s\vec{\omega} + W_{z,i}J_{zz,i}\omega_{w,i}\right) \tag{6.70}$$

where

$$W_{z,i} = \begin{bmatrix} 0 & 0 & c_{13} \\ 0 & 0 & c_{23} \\ 0 & 0 & c_{33} \end{bmatrix} \tag{6.71}$$

Further substitution of $J_{zz,i}\dot{\omega}_{w,i} = T_i$ and $J_{zz,i}\omega_{w,i} = h_i$ leads to the decoupled expression for the satellite's change in angular velocity:

$$M = J_s\dot{\vec{\omega}} + W_{z,i}T_i + \Omega\left(J_s\vec{\omega} + W_{z,i}h_i\right) \tag{6.72}$$

and the change in angular velocity of each reaction wheel can be expressed as:

$$\dot{h}_i = T_i \tag{6.73}$$

For three reaction wheels, this expression can be rewritten to:

$$M = J_s\dot{\vec{\omega}} + W_{z,w}\vec{T} + \Omega\left(J_s\vec{\omega} + W_{z,w}\vec{h}\right) \tag{6.74}$$

$$\dot{\vec{h}} = \vec{T} \tag{6.75}$$

or

$$M = J_s\dot{\vec{\omega}} + W_{z,w}\vec{T} + \Omega\left(J_s\vec{\omega} + W_{z,w}J_W\vec{\omega}_w\right) \tag{6.76}$$

$$\dot{\vec{\omega}}_w = J_{Wz}^{-1}\vec{T} \tag{6.77}$$

where $\vec{T} = \begin{bmatrix} T_1 & T_2 & T_3 \end{bmatrix}^\top$, $W_{z,w} = \begin{bmatrix} c_{13,1} & c_{13,2} & c_{13,3} \\ c_{23,1} & c_{23,2} & c_{23,3} \\ c_{33,1} & c_{33,2} & c_{33,3} \end{bmatrix}$, and $\vec{h} = \begin{bmatrix} h_1 & h_2 & h_3 \end{bmatrix}^\top$

6.3.4. Rigid body dynamics including magnetorquers

Attitude control systems on satellites are systems that keep the satellite pointed in a specific direction, usually by using reaction wheels, thrusters, and magnetorquers. Magnetorquers work by interacting with the Earth's magnetic field to generate a torque that can be used to rotate the satellite. This torque occurs because the Earth's magnetic field interacts with any conductive material in its vicinity. When electric current flows through a conductor in a magnetic field, it experiences a force perpendicular to both the current and the magnetic field (known as Lorentz force). By appropriately orienting magnets and electrical conductors on a satellite, this force can be used to generate torque and rotate the satellite. The magnetic torque generated by a single magnetic torquer can be expressed as:

$$T_m = \vec{\mu}_m \times \vec{B} \tag{6.78}$$

where μ_m is the magnetic dipole or magnetic moment of the magnetorquer and $\vec{B}$ is the Earth's magnetic field vector. Including the magnetic torque in Equation 6.64 results in the equations of motion of the satellite's attitude including a magnetic torquer:

$$T_m = J\dot{\vec{\omega}} + \Omega J\vec{\omega} \tag{6.79}$$

An advantage of using magnetic torquers for attitude control is that they do not require any propellant, which reduces both cost and complexity for small satellites. Additionally, since there are no moving parts involved in their operation, they tend to be more reliable than other types of attitude control systems.

Since the satellite must operate in Earth orbit first before it goes into a trajectory to the NEA, it can be beneficial to use magnetic torquers to detumble the satellite and desaturate the reaction wheels. The decision on using magnetorquers or leaving them out to save mass is made based on the simulation results for the different possible attitude control configurations for the different mission segments in chapter 8.

Centered dipole model

In order to find the magnetic torque generated by a single torquer the Earth's magnetic field has to be defined. Navabi and Barati [45] states that the centered dipole model can be used which is a simplified magnetic model of the Earth's magnetic field which aligns a dipole magnetic field with the Earth's axis of rotation. The magnetic field at each point in Earth's orbit can then be described in spherical coordinates using [45]:

$$\vec{B}\left(r,\varphi,\theta\right)=\begin{bmatrix}2\left(\frac{R}{r}\right)g^{1,0}\cos\varphi\\ 2\left(\frac{R}{r}\right)g^{1,0}\sin\theta\\ 0\end{bmatrix} \tag{6.80}$$

where the Gaussian coefficient for the magnetic field model $g^{1,0}=-29\,432\,\text{nT}$ and $R=6378.1363\,\text{km}$ is the radius of the Earth.

6.3.5. Rigid body dynamics including reaction control thrusters

RCTs are a type of spacecraft propulsion system that allows for the change of an object's orientation in space. This is necessary for tasks such as station-keeping, rendezvous, and docking, proximity operations (maneuvering around other objects), desaturation of reaction wheels, or attitude correction maneuvers to maintain the correct pointing direction of scientific instruments. In this particular case, the main task of the RCTs is the desaturation of reaction wheels.

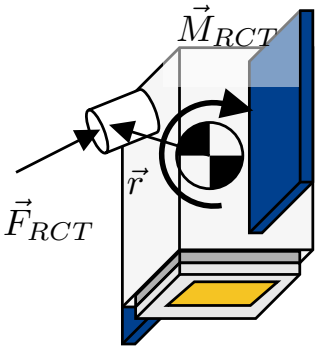

Figure 6.5: This figure depicts the visualization of a reaction control thruster illustrating the force vector $\vec{F}_{RCT}$, generated torque $\vec{M}_{RCT}$, and distance vector $\vec{r}$ from the center of mass of the satellite to the thrust vector. Reaction control thrusters are used for attitude control, adjustments in the orientation of a satellite in space, and desaturation of reaction wheels.

RTCs often come in thruster pairs to be able to generate pure torques if required. However, it is also possible to generate net translation forces. The forces and torques generated by a single RTC can be expressed as:

$$\begin{bmatrix}\vec{F}_{RCT}\\ \vec{M}_{RCT}\end{bmatrix}=\begin{bmatrix}\mathbb{I}_{3\times3}\\ \vec{r}_{\times}\end{bmatrix}\vec{F}_{RCT} \tag{6.81}$$

where $\vec{F}_{RCT}$ is the force vector generated by the RTC, $\vec{r}_\times = \begin{bmatrix} 0 & -r_z & r_y \\ r_z & 0 & -r_x \\ r_y & r_x & 0 \end{bmatrix}$ is the skew-symmetric matrix of the distance vector from the center of mass of the satellite to the thrust vector and $\vec{M}_{RCT}$ is the generated torque. In the rotational rigid body dynamics, the torque generated by the RCT results in the following rigid body dynamics expression:

$$M_{RCT} = J\dot{\vec{\omega}} + \Omega J\vec{\omega} \tag{6.82}$$

6.4. Summary

In this chapter, the rotational dynamics in a non-rotating reference frame are described in MRPs. MRPs are selected because they reduce the number of parameters required to describe a rotation to only three parameters whereas quaternions have four and direction cosine rotations even have 9 parameters to describe a single rotation. Euler angles and Rodrigues parameters also require three parameters to describe a single rotation. The downside of using Euler or Rodrigues parameters is that they have singularities for some angles whereas direction cosine rotations and quaternions do not have singularities for any rotation. MRPs also have singularities but these can be mitigated by switching to the shadow component of the MRPs that describes the same rotation but in the opposite direction when the norm of the MRP or shadow MRP exceeds 1. MRPs ($\vec{\psi}$) are defined in terms of quaternions ($\vec{q} = [q_1, q_2, q_3]^\top$ and q_4):

$$\vec{\psi} = \frac{\vec{q}}{1 + q_4}$$

The MRP shadow component can be obtained using:

$$\vec{\psi}_s = -\frac{\vec{\psi}}{\|\vec{\psi}\|^2}$$

The direction cosine matrix for a rotation from a reference frame $\mathcal{B}$ to a reference frame $\mathcal{N}$ in MRPs is expressed as:

$$C_{\mathcal{B}}^{\mathcal{N}} = \mathbb{I}_{3\times 3} - 4\frac{1 - \vec{\psi}^\top\vec{\psi}}{\left(1 + \vec{\psi}^\top\vec{\psi}\right)^2} Q\left(\vec{\psi}\right) + 8\frac{1}{\left(1 + \vec{\psi}^\top\vec{\psi}\right)^2} Q^2\left(\vec{\psi}\right)$$

where:

$$Q\left(\vec{\psi}\right) = \begin{bmatrix} 0 & -\psi_3 & \psi_2 \\ \psi_3 & 0 & -\psi_1 \\ -\psi_2 & \psi_1 & 0 \end{bmatrix}$$

The kinematics of MRPs can be expressed as:

$$\dot{\vec{\psi}} = \tfrac{1}{2}\left[\mathbb{I}_{3\times 3} + Q\left(\vec{\psi}\right) + \vec{\psi}\vec{\psi}^\top - \tfrac{1}{2}\left(1 + \vec{\psi}^\top\vec{\psi}\right)\mathbb{I}_{3\times 3}\right]\vec{\omega}$$

The choice of the reference frame, rotational parameterization, and MRP kinematics can further be used in combination with the rigid body dynamics to simulate the attitude of the satellite for different scenarios that demonstrate the feasibility of the RCT system and ADCS. In other words, it forms a basis to answer research questions 2, 3, and 3.1 in chapter 7 and chapter 8.

6.4.1. Rigid body dynamics

The rigid body dynamics for a satellite containing reaction wheels (Equation 6.76, Equation 6.77), magnetorquers (Equation 6.79), and RCTs (Equation 6.82) can be written as:

$$\dot{\vec{\omega}} = J_s^{-1}\left[-W_{z,w}\vec{T} + \vec{M}_{rct} - \left(C_{\mathcal{N}}^{\mathcal{B}}\,\vec{B}_{\mathcal{N}}\right) \times \vec{\mu}_m - \vec{\omega} \times J_s\vec{\omega} - \vec{\omega} \times W_{z,w}J_W\vec{\omega}_w\right] \tag{6.83a}$$

$$\dot{\vec{\omega}}_w = J_{Wz}^{-1}\vec{T} \tag{6.83b}$$

Adaptations for these rigid body dynamics can be used in chapter 7 to answer research questions 2, 3, and 3.1.

7

Design of the attitude control system

In this chapter, the kinematics and dynamics laws explained in chapter 6 are applied in combination with different control designs to simulate the different mission phases that require attitude control. The goal of this chapter is to primarily answer RQ2 by formulating a feasible configuration for a propulsion system to desaturate the reaction wheels present in the ADCS. Additionally, the goal of this chapter is to answer RQ3 by formulating a feasible design of the complete ADCS including the RCT system and control algorithms to detumble the satellite, track the asteroid, and track an optimal Earth escape thrusting direction.

RQ2: What is a feasible design for a propulsion system to desaturate reaction wheels for an autonomous 6U satellite near-Earth asteroid fly-by mission starting from a super synchronous geostationary transfer orbit for 5 years?

RQ3: What is a feasible design for an attitude control system including a control algorithm for an autonomous 6U satellite near-Earth asteroid fly-by mission starting from a super synchronous geostationary transfer orbit?

To answer research question RQ2, the answer to research question RQ2.1 given in chapter 2, which is the selection of the COTS propulsion system that would meet the requirements, must be combined with the answer to RQ2.2. After the answer to RQ2 is found and a feasible propulsion system for desaturation is formulated, RQ3 can be answered by simulating the different mission scenarios (desaturation, detumbling, asteroid tracking, and orientation correction maneuver) using the attitude simulation framework of chapter 6 for developed ACS designs including control algorithms.

Next in this chapter, the control laws to desaturate the reaction wheels in MRPs are found using a linear quadratic regulator (LQR) method which uses a mathematical algorithm to minimize a cost function that consists of the angular momenta of the reaction wheels and a term that takes into account the magnitude of the control action itself. This control action which should be minimal is of course the thrust because this will minimize the required amount of propellant.

7.1. Reaction control thruster system design

In this section, the number of RCTs, their position, and the direction required to desaturate the reaction wheels are investigated and a method to answer this research question is formulated.

RQ2.2: What number of thrusters, their position, and direction are required to perform momentum dumping maneuvers?

To desaturate the reaction wheels when no magnetic field is present the RCT system is used. There are a couple of options to generate a torque to counteract the momentum dumping of the reaction wheels that lead to reaction wheel desaturation which are: Thrust vectoring the main propulsion system such that the thrust misalignment with the satellite's center of mass creates a torque, actuating multiple main propulsion modules in a combination that the force imbalance in the center of mass leads to torque, and using a secondary propulsion system of multiple thrusters purely for attitude control. It is generally not possible to control every axis of rotation using thrust vectoring of a single thruster. While thrust vectoring can provide some control over the orientation of an object in space, additional thrusters or other attitude control systems are typically required to maintain precise control over all three axes of rotation separately. Therefore, thrust vectoring is not considered an option. Using multiple main thrusters is also discarded because there is not enough volume to fit enough interplanetary propulsion system thrusters to also control the three axes of rotation. This leaves the thesis with only one possible solution which is the use of a secondary propulsion system with fixed thrusters purely for rotational actions.

For low-thrust trajectories, only the three axes of rotation have to be controlled, because orbital corrections can be done by steering the satellite and thus the main thruster in such a way that the trajectory of the spacecraft can be corrected. In Biggs and Fournier [46] attitude control is done using only four fixed thrusters. The paper addresses the minimum number of thrusters to directly control every rotation axis is four thrusters. It is possible to control every rotation axis with only three fixed thrusters but this requires the satellite to change its orientation over time to fully control each axis of rotation. A configuration with only three RCTs is tested in the results.

Next to the number of thrusters, the position and orientation have to be found. This leads to an optimization problem that can be solved. This thesis proposes the use of a super-ellipsoid parameterization combined with a performance index to be minimized which is the sum of the logarithmic of multiple objectives and penalties to optimize the position, orientation, and thrust allocation for the different rotation axis controls.

7.1.1. Thrusters configuration optimization problem

It is desired that a thruster configuration maximizes the produced angular acceleration (or torques if desired) in both positive and negative directions for every rotational axis and minimizes the generated angular acceleration in other axes. This minimizes the required amount of propellant for desaturation maneuvers and simplifies the allocation of the thrusters for the desired angular acceleration. This then leads to a set of six objectives to maximize and twelve penalties to minimize which can be expressed as:

$$\begin{aligned} \mathcal{L}_1 &= \max\left(\frac{M_x}{I_{xx}},\, 0\right) \qquad \mathcal{L}_2 = \max\left(\frac{-M_x}{I_{xx}},\, 0\right) \\ \mathcal{L}_3 &= \max\left(\frac{M_y}{I_{yy}},\, 0\right) \qquad \mathcal{L}_4 = \max\left(\frac{-M_y}{I_{yy}},\, 0\right) \\ \mathcal{L}_5 &= \max\left(\frac{M_z}{I_{zz}},\, 0\right) \qquad \mathcal{L}_6 = \max\left(\frac{-M_z}{I_{zz}},\, 0\right) \end{aligned} \tag{7.1}$$

where $\mathcal{L}_i$ is an objective for the case i, M_e is the torque around the axis $e \in [x,\ y,\ z]$ and I_{ee} is the moment of inertia around the axis e. Then the penalties $\mathcal{P}_{i,k}$ per case are expressed as:

$$\begin{aligned} \mathcal{P}_{1,1} = \mathcal{P}_{2,1} &= \left|\frac{M_y}{I_{yy}}\right| \qquad \mathcal{P}_{1,2} = \mathcal{P}_{2,2} = \left|\frac{M_z}{I_{zz}}\right| \\ \mathcal{P}_{3,1} = \mathcal{P}_{4,1} &= \left|\frac{M_x}{I_{xx}}\right| \qquad \mathcal{P}_{3,2} = \mathcal{P}_{4,2} = \left|\frac{M_z}{I_{zz}}\right| \\ \mathcal{P}_{5,1} = \mathcal{P}_{6,1} &= \left|\frac{M_x}{I_{xx}}\right| \qquad \mathcal{P}_{5,2} = \mathcal{P}_{6,2} = \left|\frac{M_y}{I_{yy}}\right| \end{aligned} \tag{7.2}$$

The penalties for some cases are similar because the objective of these cases is to maximize the angular acceleration about the same axis of rotation in either the positive or negative direction.

To combine the multiple objectives together such that each angular acceleration is maximized in both the positive and negative direction for each axis a logarithmic addition strategy is used. The reason for a logarithmic addition strategy is that maximizing a single or a selection of objectives leads to a worse performance metric than maximizing all objectives equally similar to the sum of roots of the objectives for values larger than one. Logarithmic addition is preferred over the sum of roots because the objectives may not necessarily be in the range of one to infinity; they can be below one as well.

So from this reasoning, a sum of the logarithms of the objectives will result in a design that optimizes all axes of rotations instead of a selection of the axes because optimizing a selection of the axes will lead to a worse performance index. The penalties are added in a similar way such that the performance index to minimize can be expressed as:

$$\min_{\vec{\xi}_{act}} \mathcal{J} = \sum_{i=1}^{6}\sum_{k=1}^{2}\left\{\log_{10}\left(\nu\mathcal{P}_{i,k}\right)\right\} - \sum_{i=1}^{6}\left\{\log_{10}\left(\mathcal{L}_i\right)\right\} \tag{7.3}$$

where $\vec{\xi}_{act}$ is the vector containing the design parameters for the thruster placement, orientation, and allocation for the six angular acceleration cases of the thrusters, and ν is a penalty scaling factor that prioritizes the minimalization of the penalties over the maximization of the torques. To solve this minimization problem, only a direct optimization method can be used because the problem is a multiple-input-single-output (MISO) problem without any integration action required. This means that the problem can be solved by either a global optimization scheme, a gradient-based optimization scheme, or a hybrid optimization consisting of both global and gradient-based methods. It can already be seen that the minimization problem contains max () functions in $\mathcal{L}_i$ which means that the performance index function can be discontinuous over its design space. Therefore, gradient-based methods cannot be used in these special regions. Hence global optimization is used as an initial guess. For global optimization, a PSO method is selected because it can handle the non-linear and non-convex nature of the optimization problem. The solution of the PSO method can then be used as an initial guess for a gradient-based optimization method to find a true local minimum. Depending on the initial guess, this can be the true global minimum however, there is no way to verify this unless a complete grid search is performed instead of the PSO method.

Parameterization

To parameterize the location and the orientation of the thrusters on the surface of the satellite it is assumed that the satellite can be described by a super-ellipsoid shape. In Barr [47] the general inside-outside function of a super-ellipsoid is given as:

$$g\left(x,\ y,\ z\right) = \left(\left(\frac{x}{A}\right)^r + \left(\frac{y}{B}\right)^r\right)^{r/t} + \left(\frac{z}{C}\right)^t \tag{7.4}$$

where r and z describe the squareness of the super-ellipsoid in the xy-plane and z-direction respectively, A, B, C are scaling factors that stretch out the super-ellipsoid into the x, y, z axes. This means that a 6U CubeSat with dimensions $0.2 \times 0.1 \times 0.3$ m can be described with the parameters $A = \frac{0.2}{2}$, $B = \frac{0.1}{2}$, $C = \frac{0.3}{2}$ and the squareness is assumed to be $r = t = 8$. Setting $g\,(x,\ y,\ z) = 1$ then leads to the super-ellipsoid surface function. In Figure 7.1 the CubeSat's surface model to place the RCTs can be seen.

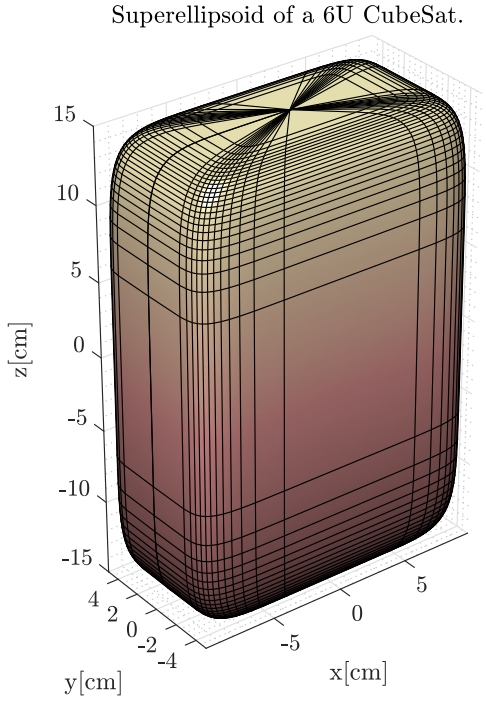

Figure 7.1: The figure shows a continuous 3-D approximation of the surface of a 6U CubeSat using a super-ellipsoid. This shape parametrization is useful in the optimization of reaction control thruster placement as it provides a smooth and continuous surface that can be easily represented mathematically and optimized using optimization algorithms. The edge lines on the surface of the satellite represent the angular coordinates that have a higher spatial resolution in the areas with greater curvature, allowing for a more precise representation of the satellite's shape in these areas. The shape is made by solving for the super-ellipsoid surface function $\left(\left(\frac{x}{A}\right)^r + \left(\frac{y}{B}\right)^r\right)^{r/t} + \left(\frac{z}{C}\right)^t = 1$ with the following parameters: $A = \frac{0.2}{2}$, $B = \frac{0.1}{2}$, $C = \frac{0.3}{2}$ and $r = t = 8$. The edge lines on the surface of the satellite represent the angular coordinates that have a higher spatial resolution in the areas with greater curvature.

Barr [47] also shows that the super-ellipsoid can be expressed in angular coordinates which have a better spatial resolution in areas with a greater curvature as can be seen in Figure 7.1. The surface coordinates expressed in angular coordinates can be expressed as:

$$\begin{aligned} x &= A\,\mathrm{sgn}\,(\cos v)\,\|\cos v\|^{\frac{2}{t}}\,\mathrm{sgn}\,(\cos w)\,\|\cos w\|^{\frac{2}{r}} \\ y &= B\,\mathrm{sgn}\,(\cos v)\,\|\cos v\|^{\frac{2}{t}}\,\mathrm{sgn}\,(\sin w)\,\|\sin w\|^{\frac{2}{r}} \\ z &= C\,\mathrm{sgn}\,(\sin v)\,\|\sin v\|^{\frac{2}{t}} \end{aligned} \tag{7.5}$$

where $-\frac{\pi}{2} \geq v \geq \frac{\pi}{2}$ and $-\pi \geq w \geq \pi$ The vector normal to the surface can also easily be obtained from the partial derivatives of the surface equation $g = 1$. The partial derivatives of g can be expressed in

the angular surface parameters by the following expressions [47]:

$$\begin{aligned} n_x &\equiv \frac{\partial g}{\partial x} = \frac{1}{A}\cos(v)^{2-\frac{2}{t}}\cos(w)^{2-\frac{2}{r}} \\ n_y &\equiv \frac{\partial g}{\partial y} = \frac{1}{B}\cos(v)^{2-\frac{2}{t}}\sin(w)^{2-\frac{2}{r}} \\ n_z &\equiv \frac{\partial g}{\partial z} = \frac{1}{C}\sin(v)^{2-\frac{2}{t}} \end{aligned} \tag{7.6}$$

Now that the location of the thruster can be defined by v and w and the normal vector to the surface of the satellite is known for any location, the direction of the thruster has to be parameterized. A way to do this is by rewriting the normal vector to a unit direction vector and then transforming this vector in spherical coordinates. This transformation can be expressed as:

$$\begin{aligned} \phi &= \arccos z \\ \theta &= \operatorname{sgn}(y)\arccos\left(\frac{x}{\sqrt{x^2+y^2}}\right) \end{aligned} \tag{7.7}$$

Now that the thruster direction can be written as a function of the normal unit vector such that its parameters only change the local direction with respect to the normal of the satellite's surface, the thruster direction in Cartesian coordinates can be written as:

$$\begin{aligned} x &= \sin(\phi+\phi_d)\cos(\theta+\theta_d) \\ y &= \sin(\phi+\phi_d)\sin(\theta+\theta_d) \\ z &= \cos(\phi+\phi_d) \end{aligned} \tag{7.8}$$

where θ_d and ϕ_d are direction parameters that describe the thruster orientation with respect to the local normal vector on the surface of the satellite.

The final parameters u_n to describe a thruster are the percentages of thrust used for the six different angular accelerations in the different axes of rotation. For example, assuming the case of four RCTs, firing thrusters 2 and 3 and partly thruster 1, while thruster 4 is not thrusting produces a pure negative angular acceleration around the y-axis of the satellite. The complete vector of 40 design parameters for four thrusters can thus be expressed as (For three RCTs 30 design parameters are required):

$$\begin{aligned} \vec{\xi}_{act} = \big[&v_1,\ w_1,\ \theta_{d,1},\ \phi_{d,1},\ u_{1,1},\ u_{2,1},\ u_{3,1},\ u_{4,1},\ u_{5,1},\ u_{6,1}, \\ &v_2,\ w_2,\ \theta_{d,2},\ \phi_{d,2},\ u_{1,2},\ u_{2,2},\ u_{3,2},\ u_{4,2},\ u_{5,2},\ u_{6,2}, \\ &v_3,\ w_3,\ \theta_{d,3},\ \phi_{d,3},\ u_{1,3},\ u_{2,3},\ u_{3,3},\ u_{4,3},\ u_{5,3},\ u_{6,3}, \\ &v_4,\ w_4,\ \theta_{d,4},\ \phi_{d,4},\ u_{1,4},\ u_{2,4},\ u_{3,4},\ u_{4,4},\ u_{5,4},\ u_{6,4}\big] \end{aligned} \tag{7.9}$$

7.1.2. Control mapping

Using the found solution for the parameters for the optimization problem a desired control torque must be mapped to the corresponding thruster actuation. The allocation matrix that maps the desired accelerations around each axis of rotation in both positive and negative directions to unit thrust actions can be expressed as:

$$A_u = \begin{bmatrix} u_{1,1} & \cdots & u_{1,4} \\ \vdots & \ddots & \vdots \\ u_{6,1} & \cdots & u_{6,4} \end{bmatrix} \tag{7.10}$$

A required control torque $\vec{M}_{RCT,control}$ can then be mapped to the approximated thrusting actions using the following expression:

$$\begin{bmatrix} u_{RCT,1} \\ u_{RCT,2} \\ u_{RCT,3} \\ u_{RCT,4} \end{bmatrix} = A_u^{\top} F_{RCT,max}^{-1} \begin{bmatrix} \max\left(J_s^{-1}\vec{M}_{RCT,control}, 0\right) \\ \max\left(-J_s^{-1}\vec{M}_{RCT,control}, 0\right) \end{bmatrix} \tag{7.11}$$

Then the true torque that the RCTs combined provide can be calculated using:

$$M_{RCT,true} = \sum_{n=1}^{4} \left\{ u_{RCT,i}\, p_{RCT,i} \times \vec{F}_{RCT,i,max} \right\} \tag{7.12}$$

7.2. Satellite detumbling

In order to comply with requirement MR-AOCS-2, the ADCS must be able to detumble the satellite.

MR-AOCS-2: The attitude and orbital control system shall be able to detumble the spacecraft after orbit injection.

The starting condition after separation or orbit injection is a complex multi-faced problem on its own. Therefore, the requirement for detumbling of the LUMIO 12U CubeSat Lunar orbiter is taken as the detumbling requirement for this thesis. This requirement states that the ADCS complies with the requirement for detumbling if it can detumble the satellite with tip-off rates of up to 30 deg/s or 0.524 rad s^{-1} on each axis [48].

To detumble the satellite, four methods can be used. The first one involves the use of only reaction wheels, the second involves the use of reaction wheels and RTCs, the third involves the use of reaction wheels and magnetic torquers, and the last one involves only RTCs.

A combination of the second and third options can also be used. However, if magnetorquers are present on the satellite, RCTs do not have to be used which saves mass. The saved mass is investigated in the results in chapter 8. This leads to the systems engineering question: Does using magnetorquers result in a lower total mass requirement for the ACS, or does eliminating them result in a smaller ACS mass?

A method using only RCTs is not considered because it is considered to be very similar to a combination of reaction wheels and RTCs. The distinction is that it provides less torque to detumble the satellite and leaves the reaction wheels with some residual spin. This residual spin has to be reduced after the detumbling maneuver. The benefit of using a combination of RCTs and reaction wheels is that detumbling can be done faster than RCTs only.

7.2.1. Detumbling using only reaction wheels

For detumbling, without the use of RCTs or magnetorquers, it is important that the reaction wheels do not saturate and exceed their angular velocity limits. Therefore, an optimal control strategy would be most beneficial. Considering that a fast-rotating satellite leads to a non-linear control problem, non-linear optimal control strategies should be used. Focusing purely on performance, (nonlinear) model predictive control, finite-horizon COV-based control, Linear Quadratic Regulator (LQR), and Linear Quadratic Gaussian Regulator (LQGR) are often used methods. Model predictive control and finite-horizon COV-based control cannot be used because these options are a type of predictive control that is considered too computationally demanding. LQR and LQGR are then the only two options left.

LQGR is not used in this thesis because it is an extension of LQR when sensor noise and unknown disturbances are taken into account, however, these are not considered for this thesis. Therefore, an LQR method is used to control the attitude of the satellite during the detumbling phase. Before an LQR can be used, the kinematics and dynamics of the system must be linearized for the controller.

Linearized kinematic and dynamic equations

As stated in Equation 6.31 and Equation 6.32 the kinematics of a satellite in MRPs can be expressed as:

$$\dot{\vec{\psi}} = G\left(\vec{\psi}\right)\vec{\omega}$$

where:

$$G\left(\vec{\psi}\right) = \tfrac{1}{2}\left[\mathbb{I}_{3\times3} + Q\left(\vec{\psi}\right) + \vec{\psi}\vec{\psi}^{\top} - \tfrac{1}{2}\left(1 + \vec{\psi}^{\top}\vec{\psi}\right)\mathbb{I}_{3\times3}\right]$$

and

$$Q\left(\vec{\psi}\right) = \begin{bmatrix} 0 & -\psi_3 & \psi_2 \\ \psi_3 & 0 & -\psi_1 \\ -\psi_2 & \psi_1 & 0 \end{bmatrix}$$

And the dynamics of a satellite with three reaction wheels can be expressed as a combination of Equation 6.72 and Equation 6.82:

$$0 = J_s\dot{\vec{\omega}} + \sum_{i=1}^{3}\{W_{z,i}T_i\} + \vec{\omega}\times J_s\vec{\omega} + \vec{\omega}\times\sum_{i=1}^{3}\{W_{z,i}h_i\} \tag{7.13}$$

and the change in angular velocity of each reaction wheel as stated in Equation 6.73 for three reaction wheels can be expressed as:

$$\dot{\vec{h}} = \vec{T} \tag{7.14}$$

or

$$J_{Wz}\dot{\vec{\omega}}_w = \vec{T} \tag{7.15}$$

where $\vec{\omega}_w$ is a vector containing all the angular velocities of the reaction wheels around their own fixed axis, J_{wz} is a matrix containing only the reaction wheel moments of inertia around their fixed rotation axis which can be expressed as:

$$J_{wz} = \begin{bmatrix} J_{zz,1} & 0 & 0 \\ 0 & J_{zz,2} & 0 \\ 0 & 0 & J_{zz,3} \end{bmatrix} \tag{7.16}$$

where $J_{zz,1}$, $J_{zz,2}$ and $J_{zz,3}$ are the moments of inertia around the rotation axis of the reaction wheels.

To be able to linearize the system of differential equations which fully describe the dynamics and kinematics of the satellite with reaction wheels first, the system of equations should be rewritten to the form $\dot{\vec{\chi}} = f\left(\vec{\chi},\ \vec{u}\right)$ where $\vec{\chi} = \begin{bmatrix}\vec{\omega} & \vec{\omega}_w & \vec{\psi}\end{bmatrix}^{\top}$ and $\vec{u} = \begin{bmatrix}\vec{T}\end{bmatrix}$ where $\vec{T}$ are the torques generated by changing the angular velocity of the reaction wheels. Then from top to bottom $\dot{\vec{\chi}}$ can be written as:

$$\dot{\vec{\omega}} = J_s^{-1}\left[-W_{z,w}\vec{T} - \vec{\omega}\times J_s\vec{\omega} - \vec{\omega}\times W_{z,w}J_W\vec{\omega}_w\right] \tag{7.17a}$$

$$\dot{\vec{\omega}}_w = J_{Wz}^{-1}\vec{T} \tag{7.17b}$$

$$\dot{\vec{\psi}} = G\left(\vec{\psi}\right)\vec{\omega} \tag{7.17c}$$

To use an LQR the equations of rotational motion, $\dot{\vec{\chi}} = f\left(\vec{\chi},\ \vec{u}\right)$, have to be linearized every time the controller evaluates what the control should be over the next interval. Using MATLAB's symbolic

toolbox the partial derivatives of the system can be found such that for the current time the linearized system of equations can be written as:

$$\dot{\vec{\chi}} = A\vec{\chi} + B\vec{u} \tag{7.18}$$

where

$$\begin{aligned} A &= \left.\frac{\partial f}{\partial \vec{\chi}}\right|_{\vec{\chi}_a, \vec{u}=0} \\ B &= \left.\frac{\partial f}{\partial \vec{u}}\right|_{\vec{\chi}_a, \vec{u}=0} \end{aligned} \tag{7.19}$$

This can then be discretized to the form $\vec{\chi}_{k+1} = A_k\vec{\chi}_k + B_k\vec{u}_k$ using:

$$\begin{aligned} A_k &= \mathbb{I}_{9\times 9} + \Delta t A \\ B_k &= \Delta t B \end{aligned} \tag{7.20}$$

Better discretization methods exist but these have the downside of being more computationally demanding. Therefore a zero-order hold estimation is used that is less computationally demanding.

Linear quadratic regulator

Let $\vec{\chi}_{k+1} = A_k\vec{\chi}_k + B_k\vec{u}_k$ be a discrete-time linear system. Where $\vec{\chi}_k$ is expressed as: $\vec{\chi}_k = \begin{bmatrix} \delta\vec{\omega} & \vec{\omega}_w & \delta\vec{\psi} \end{bmatrix}^\top$. Since only detumbling of the satellite is required $\delta\vec{\omega} = \vec{\omega}$ and $\delta\vec{\psi} = 0$. Then the cost function of the system which should be minimized can be expressed in the following way [49]:

$$L = \sum_0^\infty \left\{ \vec{\chi}_k^\top Q \vec{\chi}_k + \vec{u}_k^\top R \vec{u}_k + \vec{\chi}_k^\top N \vec{u}_k \right\} \tag{7.21}$$

From Bryson's rule, Q is a matrix that contains on the diagonal the square of the maximum acceptable value of error in the states, in this case, the maximum acceptable value of $\delta\omega$ and ω_w are set to $0.524\,\mathrm{rad\,s^{-1}}$ which is the maximum expected tip-off rate of the satellite from MR-AOCS-2. Next, the maximum acceptable value of $\delta\psi$ is set to one because it is the maximum rotation error norm possible due to switching to the shadow component. R is a matrix that contains the square of the maximum acceptable value of error in the control states and N is a matrix that contains the maximum acceptable value of error cross-terms between the states and the control states. For this thesis, N is set to zero because cross-relations between the states and the control states are required. Then the optimal feedback control law that minimizes this cost function can be expressed as [49]:

$$\vec{u}_k = K_k\vec{\chi}_k \tag{7.22}$$

where K is expressed as:

$$K = -\left(B^\top S B + R\right)^{-1}\left(B^\top S A + N^\top\right) \tag{7.23}$$

and where S is found by solving the discrete-time algebraic Riccati equation:

$$A^\top S A - S - \left(A^\top S B + N\right)\left(B^\top S B + R\right)^{-1}\left(B^\top S A + N^\top\right) + Q = 0 \tag{7.24}$$

This can be easily done by MATLAB's implicit discrete-time algebraic Riccati equations solver called 'idare'.

7.2.2. Detumbling using reaction wheels and reaction control thrusters

For detumbling, with the use of RCTs and reaction wheels, it is again important that the reaction wheels do not saturate and exceed their angular velocity limits. Therefore, an optimal control strategy would be most beneficial. Hence, an LQR method is used to control the attitude of the satellite during the detumbling phase. Before an LQR can be used for a system with both RCTs and reaction wheels, the kinematics and dynamics of the system must be linearized for the controller. The design of the LQR is identical to the satellite without RCTs as can be seen in Section 7.2.1. The only clear difference is the linearized kinematic and dynamic equations.

Linearized kinematic and dynamic equations

As stated in Equation 6.31 and Equation 6.32 the kinematics of a satellite can be expressed in MRPs. The dynamics of a satellite including RCTs and three reaction wheels can be expressed as a combination of Equation 6.72 and Equation 6.82:

$$\vec{M}_{rct} = J_s\dot{\vec{\omega}} + \sum_{i=1}^{3}\{W_{z,i}T_i\} + \vec{\omega}\times J_s\vec{\omega} + \vec{\omega}\times\sum_{i=1}^{3}\{W_{z,i}h_i\} \tag{7.25}$$

To be able to linearize the system of differential equations which fully describe the dynamics and kinematics of the satellite with RCTs and reaction wheels first, the system of equations should be rewritten to the form $\dot{\vec{\chi}} = f(\vec{\chi},\, \vec{u})$ where $\vec{\chi} = \begin{bmatrix}\vec{\omega} & \vec{\omega}_w & \vec{\psi}\end{bmatrix}^\top$ and $\vec{u} = \begin{bmatrix}\vec{T} & \vec{M}_{rct}\end{bmatrix}^\top$ where $\vec{T}$ are the torques generated by changing the angular velocity of the reaction wheels and $\vec{M}_{rct}$ the desired torquers generated by the RCTs. To use an LQR the equations of rotational motion, $\dot{\vec{\chi}} = f(\vec{\chi},\, \vec{u})$, have to be linearized every time the controller evaluates what the control should be over the next interval. Using MATLAB's symbolic toolbox the partial derivatives of the system can be found such that for the current time the linearized system of equations can be found.

7.2.3. Detumbling using reaction wheels and magnetorquers

Detumbling the satellite using both reaction wheels and magnetorquers is more complex than using RCTs and reaction wheels. Magnetorquers only work in the plane perpendicular to the Earth's magnetic field vector. The purpose of using magnetorquers next to reaction wheels is to make sure the reaction wheels do not saturate and desaturate the wheels after detumbling. The simplest way to do this is to generate torque with the magnetorquers while at the same time compensating with the reaction wheels such that the angular momenta of the reaction wheels decrease. For a simplified optimal control system, an LQR method cannot be used because, at a certain point in time, the magnetorquers can only generate torque in the perpendicular plane to the Earth's magnetic field vector. This means that for a specific state, one of the reaction wheels can be oriented in the same orientation as the Earth's magnetic field vector, which means that an LQR system will not be able to minimize the angular velocity of that particular reaction wheel. This makes the discrete-time algebraic Riccati equation for that particular case unsolvable which leads to no control solution at all.

To solve this problem, the magnetic torquers can be used to decrease the angular velocity of the reaction wheels using a proportional controller combined with an LQR system for the reaction wheel control action to track a desired reference frame motion. Again the LQR method is used for performance like the case of reaction wheels combined with RCTs because it focuses more on performance than stability.

Linearized kinematics and dynamic equations

As stated in Equation 6.31 and Equation 6.32 the kinematics of a satellite can be expressed in MRPs. And the dynamics of a satellite including three magnetorquers and three reaction wheels can be expressed as a combination of Equation 6.79 and Equation 6.72:

$$\vec{T}_m = J_s\dot{\vec{\omega}} + \sum_{i=1}^{3}\{W_{z,i}T_i\} + \vec{\omega}\times J_s\vec{\omega} + \vec{\omega}\times\sum_{i=1}^{3}\{W_{z,i}h_i\} \tag{7.26}$$

where $\vec{T}_m$ is expressed as:

$$\vec{T}_m = \vec{\mu}_m \times \vec{B} \equiv -\vec{B}\times\vec{\mu}_m \tag{7.27}$$

where $\vec{\mu}_m$ is the magnetic dipole vector expressed in the body reference frame of all the magnetorquers combined and $\vec{B}$ is the Earth's magnetic field vector in the body frame described by Equation 6.80. This expression can be written to a form that contains $\vec{B}_{\mathcal{N}}$ in the inertial reference frame as:

$$\vec{T}_m = -\left(C_{\mathcal{N}}^{\mathcal{B}}\,\vec{B}_{\mathcal{N}}\right)\times\vec{\mu}_m \tag{7.28}$$

Such that the dynamics of the system can be written as:

$$-\left(C_{\mathcal{N}}^{\mathcal{B}}\,\vec{B}_{\mathcal{N}}\right)\times\vec{\mu}_m = J_s\dot{\vec{\omega}} + \sum_{i=1}^{3}\{W_{z,i}T_i\} + \vec{\omega}\times J_s\vec{\omega} + \vec{\omega}\times\sum_{i=1}^{3}\{W_{z,i}h_i\} \tag{7.29}$$

To be able to linearize the system of differential equations which fully describe the dynamics and kinematics of the satellite with magnetorquers and reaction wheels first, the system of equations should be rewritten to the form $\dot{\vec{\chi}} = f(\vec{\chi},\,\vec{u})$ where $\vec{\chi} = \begin{bmatrix}\vec{\omega} & \vec{\psi}\end{bmatrix}^\top$ and $\vec{u} = \begin{bmatrix}\vec{T} & \vec{\mu}_m\end{bmatrix}^\top$ where $\vec{T}$ are the torques generated by changing the angular velocity of the reaction wheels. Notice that for the linearized equations of motion, $\vec{\omega}_w$ is excluded in the state vector because it will not be directly controlled by the reaction wheel control torques. Using MATLAB's symbolic toolbox the partial derivatives of the system can then be found such that for the current time the linearized system of equations can be found.

Linear quadratic regulator and proportional controller

For detumbling and desaturation the control action for the magnetic torquers is calculated using a simple proportional control scheme that can be expressed as:

$$\begin{aligned}\vec{\mu}_m = -\vec{k}_p\left(\frac{C_{\mathcal{N}}^{\mathcal{B}}\,\vec{B}_{\mathcal{N}}}{\|\vec{B}_{\mathcal{N}}\|}\right)\times\left(W_{z,w}J_W\vec{\omega}_w + \delta\vec{\omega}\times J_s\delta\vec{\omega}\right)\\ -\vec{\mu}_{m,max} \geq \vec{\mu}_m \geq \vec{\mu}_{m,max}\end{aligned} \tag{7.30}$$

where $\vec{k}_p$ is a proportional control gain vector which is a positive semi-definite matrix and $\left(\frac{C_{\mathcal{N}}^{\mathcal{B}}\,\vec{B}_{\mathcal{N}}}{\|\vec{B}_{\mathcal{N}}\|}\right)_\times$ is required to cancel out the irrelevant control action for the magnetic torquers that results in zero torque. k_p is assumed to be:

$$\vec{k}_p = \text{diag}\left(\mu_{m,max,1},\quad \ldots,\quad \mu_{m,max,n}\right)\oslash\left(\tfrac{1}{2}W_{z,w}J_W\vec{\omega}_{w,max}\right) \tag{7.31}$$

Next, let $\vec{\chi}_{k+1} = A_k\vec{\chi}_k + B_k\vec{u}_k$ be a discrete-time linear system. Where $\vec{\chi}_k = \begin{bmatrix}\delta\vec{\omega} & \delta\vec{\psi}\end{bmatrix}^\top$ and $\vec{u}_k$ contains only the reaction wheel torques and the magnetic torquer values are considered constants at every interval. Since only detumbling of the satellite is required $\delta\vec{\omega} = \vec{\omega}$ and $\delta\vec{\psi} = 0$. The design of the LQR is identical to the satellite without RCTs and magnetic torquers as can be seen in Section 7.2.1.

7.2.4. Reference motion

To simulate the detumbling of the satellite using reaction wheels thrusters, magnetorquers, or a combination of the three. The reference orbit has to be defined for the magnetic torquers. Since an SSGTO is selected, this will be the reference orbit. As mentioned in chapter 1 this orbit is characterized by a perigee of 295 km and an apogee of 90,000 km above the surface of the Earth with an assumed radius of 6378.1363 km. Assumed is that the orbit is an elliptical orbit without perturbations and the Earth is a point mass. The gravitational constant of this point mass is then considered to be $\mu = 398\,600.4415\,\text{km}^3\,\text{s}^{-2}$. This leads to the following dynamics in the orbital plane in polar coordinates:

$$a_r = -\frac{\mu}{r^2} \tag{7.32}$$

and a_φ is expressed as:

$$a_\varphi = 0 \tag{7.33}$$

And the kinematics of the orbital coordinates in polar coordinates can be expressed as:

$$\begin{aligned} \ddot{r} &= a_r + r\dot{\varphi}^2 \\ \ddot{\varphi} &= \frac{a_\varphi}{r} - \frac{2\dot{r}\dot{\varphi}}{r} \end{aligned} \tag{7.34}$$

To transform a trajectory given in polar coordinates to a frame that points in the direction of the orbital velocity, which is the optimal thrusting direction found in chapter 4, the trajectory must be converted to CSV. From the position vector with respect to the geocentric non-rotating frame this results in:

$$\vec{p} = r\ \hat{r}$$

And for the velocity vector:

$$\dot{\vec{p}} = \dot{r}\ \hat{r} + r\dot{\varphi}\ \hat{\varphi}$$

where:

$$\hat{r} = \begin{bmatrix} \cos\varphi & \sin\varphi & 0 \end{bmatrix}^\top$$

$$\hat{\varphi} = \begin{bmatrix} -\sin\varphi & \cos\varphi & 0 \end{bmatrix}^\top$$

and finally for the acceleration vector:

$$\ddot{\vec{p}} = \ddot{r}\ \hat{r} + 2\dot{r}\dot{\varphi}\ \hat{\varphi} + r\ddot{\varphi}\ \hat{\varphi} - r\dot{\varphi}^2\ \hat{r}$$

Then the three axes that make up the frame in the direction of the orbital velocity can be found as:

$$\begin{aligned} \hat{b}_x &= \frac{\dot{\vec{p}}}{\|\dot{\vec{p}}\|} \\ \hat{b}_z &= \hat{z} \\ \hat{b}_y &= \hat{b}_z \times \hat{b}_x \end{aligned} \tag{7.36}$$

This can then be transformed into an MRP representation by first converting the direction cosine matrix

for this orientation to quaternions:

$$\begin{aligned} q_w &= \tfrac{1}{2}\sqrt{2+2\left(\hat{b}_x\cdot\hat{x}+\hat{b}_y\cdot\hat{y}\right)} \\ q_x &= \frac{\left(\hat{b}_y\cdot\hat{z}-\hat{b}_x\cdot\hat{y}\right)}{\sqrt{2+2\left(\hat{b}_x\cdot\hat{x}+\hat{b}_y\cdot\hat{y}\right)}} \\ q_y &= \frac{\left(\hat{b}_x\cdot\hat{z}-\hat{b}_y\cdot\hat{x}\right)}{\sqrt{2+2\left(\hat{b}_x\cdot\hat{x}+\hat{b}_y\cdot\hat{y}\right)}} \\ q_z &= \tfrac{1}{2}\sqrt{2+2\left(\hat{b}_x\cdot\hat{x}-\hat{b}_y\cdot\hat{y}\right)} \end{aligned} \tag{7.37}$$

The MRP can then be found using:

$$\vec{\psi} = \frac{\begin{bmatrix} q_x & q_y & q_z \end{bmatrix}^\top}{1+q_w}$$

Finally, the angular velocity vector of this reference motion can be obtained from the orbital angular velocity and the change in orientation from the orbital velocity vector with respect to the position vector $\vec{p}$ which follows from the chain rule. So the angular velocity can be expressed as:

$$\vec{\omega} = \begin{bmatrix} 0 & 0 & \dot{\varphi} \end{bmatrix}^\top + \ddot{\vec{p}} \times \frac{\dot{\vec{p}}}{\|\dot{\vec{p}}\|} \tag{7.38}$$

7.3. Desaturation of reaction wheels

In order to desaturate the reaction wheels when there no properly defined and/or significant magnetic field is present during the trajectory to the NEA the selected propulsion system for reaction wheel desaturation must be simulated. Identical control algorithms can be used for the detumbling case. The RCT system designed in this chapter combined with the propulsion system selected in chapter 2 simulated in the rotational dynamics model described in chapter 6 is considered successful if the reaction wheels can be desaturated. This simulation starts from an identical motion as the LVLH frame defined in the detumbling case while all the reaction wheels are saturated in the positive rotational direction. The second case will have a similar starting condition, but the reaction wheels are saturated in the negative rotational direction. This is necessary because the RCTs system can only produce a thrust in the directions of the placed RCTs. This means that it is likely that torque actions about the same axis of rotation but in the opposite direction can give different results.

7.3.1. Desaturation in Earth orbit using magnetorquers

In Earth orbit when a magnetic field is present, the decision can be made to use magnetorquers to desaturate the reaction wheels. In order to do this, the satellite must track a different reference frame. One way to do this is to orient the satellite such that the angular momentum vector of the reaction wheels combined is perpendicular to the magnetic field vector of the Earth. This enables the magnetorquers to optimally desaturate the reaction wheels. From the results for detumbling, it can be decided if the extra required propellant for detumbling and desaturation in orbit is worth more than the additional mass of magnetorquers on the satellite.

7.4. Tracking the optimal thrusting direction in Earth orbit

During the tracking of a reference frame, control stability is more important than performance because during phases such as tracking celestial bodies or the NEA during fly-by, pointing accuracy and stability are the most important performance parameters. For a non-linear system such as the satellite, controllers that consider linearity cannot guarantee stability unless non-linear analysis methods are used. Therefore a direct Lyapunov control (LC) method is used to track a reference frame during normal operations. For this case study, only reaction wheels are used to track the optimal thrusting direction in Earth orbit as described in the detumbling case study.

7.4.1. Lyapunov stability

Consider a general non-linear dynamical system in its closed-loop form:

$$\dot{\chi} = f(\chi, u, t) \tag{7.39}$$

where u is an autonomous feedback control given as:

$$u = g(\chi) \tag{7.40}$$

To define the stability of the dynamical system an equilibrium state and reference motion have to be defined. A state vector point χ_e is said to be an equilibrium state (or equilibrium point) of a dynamical system described by $\dot{\chi} = f(\chi, t)$ at time t_0 if [50]:

$$f(\chi_e, t) = 0, \quad \forall t > t_0 \tag{7.41}$$

This means that once the system reaches this state, it will remain in this state. These equilibrium states can be seen as stability points. For example, a pendulum is considered to be at its equilibrium point if it is hanging straight down at rest, or inverted. The inverted is of course considered to be an unstable equilibrium point, while the pendulum hanging down is a stable equilibrium point. A stable equilibrium state is a state that a system naturally moves towards and an unstable equilibrium state is a state that the system moves away from when a small disturbance is applied.

If the system should follow a certain path or motion, then this is denoted as the nominal reference motion $\chi(t)$. To describe the proximity of one state to another the notion of the neighborhood is defined as: For a given $\delta > 0$, a state vector $\chi(t)$ is defined to be in the neighborhood $B_\delta(\chi_r(t))$ of the state $\chi_r(t)$ if [50]:

$$\|\chi(t) - \chi_r(t)\| < \delta \quad \Rightarrow \quad \chi(t) \in B_\delta(\chi_r(t)) \tag{7.42}$$

This definition is defined using the Euclidean vector norm definition which can be seen as a hyperdimensional sphere around the reference state which is the neighborhood around that state.

Finally, a state $\chi(t)$ is said to be Lagrange stable (or bounded) relative to $x_r(t)$ if there exists a $\delta > 0$ such that [50]:

$$\chi(t) \in B_\delta(\chi_r(t)), \quad \forall t > t_0 \tag{7.43}$$

While Lagrange stability is a way to define the stability of a system, it only gives information about the system being bounded and not about to what degree the reference motion is being tracked. In order to do this Lyapunov stability can be used to further specify the stability of the system.

In 1892 Aleksandr Mikhailovich Lyapunov published his doctoral thesis *"The general problem of the stability of motion."*. The theory Lyapunov came up with in 1892 is to this day still considered a powerful tool to analyze the stability of non-linear systems.

Lyapunov stated that a motion $\chi(t)$ is Lyapunov stable relative to $\chi_r(t)$ if for each $\varepsilon > 0$ there exists a $\delta(\varepsilon) > 0$ such that [50]:

$$\chi(t_0) \in B_\delta(\chi_r(t_0)) \Rightarrow \chi(t) \in B_\varepsilon(\chi_r(t_0)), \quad \forall t > t_0 \tag{7.44}$$

This means that that a state vector within the neighborhood B_ε of the $\chi_r(t)$, then there exists a corresponding initial neighborhood $B_\delta(\chi_r(t_0))$ from which all $\chi(t)$ must originate. If $\chi(t)$ is not stable, then the system is not stable. Just Lyapunov stability alone does not guarantee convergence. For this, a stronger stability criterion is required which is asymptotical stability. This means that eventually, the difference between $\chi(t)$ and $\chi_r(t)$ will approach zero over time. So the motion $\chi(t)$ is asymptotically stable relative to $\chi_r(t)$ if $\chi(t)$ is Lyapunov stable there exists a $\delta > 0$ such that [50]:

$$\chi(t_0) \in B_\delta(\chi_r(t_0)) \Rightarrow \lim_{t\to\infty} \chi(t) = \chi_r(t) \tag{7.45}$$

Asymptotic stability does guarantee convergence over time, but it does not state at which rate this occurs. Exponential stability is an even stronger stability statement that states: A motion $\chi(t)$ is said to be exponentially stable relative to $\chi_r(t)$ if $\chi(t)$ is asymptotically stable and there exists a $\delta > 0$ and corresponding $\alpha(\delta) > 0$ and $\lambda(\delta) > 0$ such that [50]:

$$\chi(t_0) \in B_\delta(\chi_r(t_0)) \Rightarrow \|\chi(t) - \chi_r(t)\| \leq \alpha e^{\lambda t} \|\chi(t_0) - \chi_r(t_0)\| \tag{7.46}$$

If a system is exponentially stable, then it will always converge to a reference state at the found decay rate or faster. This means that a system's response is more dependable as well.

Every stability criterion mentioned in this subsection is a local stability statement except for the Lagrange stability defined earlier. For Lyapunov's stability criteria, it is necessary that the state is within a certain neighborhood B_δ of the reference or desired state. However, if the state of the system can take any value and the required neighborhood for stability makes up the whole dimension space of $\chi(t_0)$, then the system is also said to be globally stable or stable at large. So, a motion $\chi(t_0)$ is said to be globally stable (asymptotically stable or exponentially stable) relative to $\chi_r(t_0)$ if $\chi(t_0)$ is stable (asymptotically stable or exponentially stable) for *any* initial state vector $\chi(t_0)$ [50].

7.4.2. Lyapunov's direct method controller

Proving stability for non-linear systems without using linear approximations is very difficult. Therefore Lyapunov introduced an energy-like Lyapunov function that can be used to study the stability of a system. The benefit of this function is that the non-linear differential equations do not have to be solved to claim stability. The idea of the Lyapunov function is that it is a canyon-like function in which a ball is released, goes through the valley, overshoots, and moves down again oscillating between each wall. As long as the ball is not able to move over any of the walls, there is no way that the ball will leave the canyon, thus the system is stable. If friction is present, this motion will dampen out and eventually reach its equilibrium point at the bottom of the canyon. This can be seen as an asymptotically stable system.

To create a function that looks like this the concept of positive definite functions is very important: A scalar continuous function $V(\chi)$ is said to be a locally positive definite function about χ_r if:

$$\chi = \chi_r \quad \Rightarrow \quad V(\chi) = 0 \tag{7.47}$$

and there exists a $\delta > 0$ such that:

$$\forall \chi \in B_\delta(\chi_r) \quad \Rightarrow \quad V(\chi) > 0 \tag{7.48}$$

If this is true for all χ, then this function is said to be globally positive definite. In the case of a positive semi-definite function, there exist points of χ which also give $V(\chi) = 0$ next to $V(\chi) > 0$ for $\chi \neq \chi_r$. Negative definite functions can be defined using the definition of a positive definite function so that if $-V(\chi)$ is positive definite, then $V(\chi)$ is a negative definite function.

If a function is only semi-definite, then there exist local minima in which the system can settle. This means that the system will move toward a point that is not χ_r.

A matrix is said to be positive (semi) definite if for every state of x:

$$\chi^\top K \chi \begin{cases} > 0 \Rightarrow & \text{Positive definite} \\ \geq 0 \Rightarrow & \text{Positive semi definite} \end{cases} \tag{7.49}$$

And a matrix is said to be negative (semi) definite if for every state of x:

$$\chi^\top K \chi \begin{cases} < 0 \Rightarrow & \text{Negative definite} \\ \leq 0 \Rightarrow & \text{Negative semi definite} \end{cases} \tag{7.50}$$

To prove the stability of a dynamical system, it is important to find the special positive definite functions which are called Lyapunov functions. The definition of a Lyapunov function for a dynamical system $\dot{\chi} = f(\chi)$ is a scalar function $V(\chi)$ if it is continuous and there exists a $\delta > 0$ such that for any $\chi \in B_\delta(\chi_r)$:

- $V(\chi)$ is a positive definite function about χ_r;
- $V(\chi)$ has continuous derivatives;
- $\dot{V}(\chi)$ is negative semi definite.

Since $V(\chi)$ is a function of χ alone, but χ is a function of time, $V(\chi)$ is also indirectly a function of time. $\dot{V}(\chi)$ can be found by using the chain-rule:

$$\dot{V}(\chi) = \frac{\partial V^\top}{\partial \chi} \frac{\partial \chi}{\partial t} = \frac{\partial V^\top}{\partial \chi} f(\chi) \tag{7.51}$$

where $\frac{\partial \chi}{\partial t}$ comes from the equations of motion $\dot{\chi} = f(\chi)$. The Lyapunov function is important because it will prove that a dynamical system is stable if one exists. However, if a Lyapunov function cannot be found, it cannot be concluded that the system is unstable. In this case, additional stability theories have to be sought.

For a dynamical system to be classified as asymptotically stable about χ_r using Lyapunov functions, the following conditions have to be met:

- the system is stable about $\chi_r(t)$;
- $\dot{V}(\chi)$ is negative definite about $\chi_r(t)$.

And for the dynamical system to be classified as exponentially stable about χ_r additional conditions have to be met. If there exists a Lyapunov function and the dynamical system is at least asymptotically stable. Then the system is exponentially stable if there exist scalar constants $c_1 > c_2 > 0$ and $\lambda > 0$, $k > 0$ such that:

$$\dot{V} \leq -\lambda V \tag{7.52}$$

and

$$c_1 \|\chi\|^k \leq V(x) \leq c_2 \|\chi\|^k \tag{7.53}$$

If the time derivative of the Lyapunov function does not give enough insight into the stability of the dynamical system, then higher-order derivatives can be explored which will prove asymptotic stability if the first non-zero odd derivative gives a negative definite function.

For the case of a satellite with reaction wheels Tsiotras [51] proposes a Lyapunov function which does not lead to a non-linear behavior of the attitude control feedback law which would follow from a conventional Lyapunov function using MRPs. The natural logarithm term has a desirable derivative instead of taking purely $\left(1+\delta\vec{\psi}^{\top}\delta\vec{\psi}\right)$:

$$V\left(\delta\vec{\psi},\delta\vec{\omega}\right)=\tfrac{1}{2}\delta\vec{\omega}^{\top}K_1\delta\vec{\omega}+2K_3\ln\left(1+\delta\vec{\psi}^{\top}\delta\vec{\psi}\right) \tag{7.54}$$

where K_1 is considered to be a positive definite gyroscopic acceleration feedback gain matrix and K_3 is a positive definite angular feedback gain matrix.

The first time derivative of the found Lyapunov function then becomes:

$$\dot{V}\left(\delta\vec{\psi},\delta\vec{\omega}\right)=\delta\dot{\vec{\omega}}^{\top}K_1\delta\vec{\omega}+\frac{4K_3}{1+\delta\vec{\psi}^{\top}\delta\vec{\psi}}\delta\vec{\psi}^{\top}\delta\dot{\vec{\psi}} \tag{7.55}$$

Which can be rewritten to:

$$\dot{V}\left(\delta\vec{\psi},\delta\vec{\omega}\right)=\delta\dot{\vec{\omega}}^{\top}K_1\delta\vec{\omega}+\frac{4K_3}{1+\delta\vec{\psi}^{\top}\delta\vec{\psi}}\delta\vec{\psi}^{\top}G\left(\delta\vec{\psi}\right)\delta\vec{\omega} \tag{7.56}$$

Combining with the earlier found expression $\vec{\psi}^{\top}G\left(\vec{\psi}\right)=\frac{1}{4}\vec{\psi}^{\top}\left(1+\vec{\psi}^{\top}\vec{\psi}\right)$ gives:

$$\dot{V}\left(\delta\vec{\psi},\delta\vec{\omega}\right)=\delta\dot{\vec{\omega}}^{\top}K_1\delta\vec{\omega}+\delta\vec{\psi}^{\top}K_3\delta\vec{\omega} \tag{7.57}$$

As previously discussed, a stable Lyapunov function requires $\dot{V}\left(\delta\vec{\psi},\delta\vec{\omega}\right)$ to be negative semi-definite. Therefore a good proposal is to find a control input such that: $\dot{V}\left(\delta\vec{\psi},\delta\vec{\omega}\right)=-\delta\vec{\omega}^{\top}K_2\delta\vec{\omega}$, where K_2 is a positive definite angular velocity feedback gain matrix or in other words the magnitude at which V is moving towards zero depending on the angular velocity error $\delta\vec{\omega}$ and K_2. This then leads to the stability constraint:

$$-\delta\vec{\omega}^{\top}K_2\delta\vec{\omega}=\delta\dot{\vec{\omega}}^{\top}K_1\delta\vec{\omega}+\delta\vec{\psi}^{\top}K_3\delta\vec{\omega} \tag{7.58}$$

Notice that $\vec{a}^{\top}A\vec{b}=\vec{b}^{\top}A\vec{a}$ such that the stability constraints can be rewritten to:

$$0=\delta\vec{\omega}^{\top}\left[K_1\delta\dot{\vec{\omega}}+K_3\delta\psi+K_2\delta\vec{\omega}\right] \tag{7.59}$$

Combining with Equation 6.39 and ignoring the $\delta\vec{\omega}^{\top}$-term gives:

$$0=K_1\dot{\vec{\omega}}-K_1\,C_{\mathcal{R}}^{\mathcal{B}}\,\dot{\vec{\omega}}_r+K_1\vec{\omega}\times C_{\mathcal{R}}^{\mathcal{B}}\,\vec{\omega}_r+K_3\delta\psi+K_2\delta\vec{\omega} \tag{7.60}$$

Substitution of the dynamics including reaction wheels in the rigid body dynamics for reaction wheels gives:

$$0=-K_1J_s^{-1}\vec{u}-K_1J_s^{-1}\left[\vec{\omega}\times J\vec{\omega}\right]-K_1J_s^{-1}\vec{\omega}\times\vec{h}_w-K_1\,C_{\mathcal{R}}^{\mathcal{B}}\,\dot{\vec{\omega}}_r+K_1\vec{\omega}\times C_{\mathcal{R}}^{\mathcal{B}}\,\vec{\omega}_r+K_3\delta\psi+K_2\delta\vec{\omega} \tag{7.61}$$

where $\vec{h}_w=W_{z,w}J_W\vec{\omega}_w$ and $\vec{u}=W_{z,w}\vec{T}$.

Rewriting in terms of the required control vector $\vec{u}$ gives:

$$\vec{u}=-\vec{\omega}\times J_s\vec{\omega}-\vec{\omega}\times\vec{h}_w-J_s{K_1}^{-1}\,C_{\mathcal{R}}^{\mathcal{B}}\,\dot{\vec{\omega}}_r+J_s{K_1}^{-1}\vec{\omega}\times C_{\mathcal{R}}^{\mathcal{B}}\,\vec{\omega}_r+J_s{K_1}^{-1}K_3\delta\psi+J_s{K_1}^{-1}K_2\delta\vec{\omega} \tag{7.62}$$

Redefining the feedback gain matrices $K_1=J_s{K_1}^{-1}$, $K_2=J_s{K_1}^{-1}K_2$ and $K_3=J_s{K_1}^{-1}K_3$ gives:

$$\vec{u}=-\vec{\omega}\times J_s\vec{\omega}-\vec{\omega}\times\vec{h}_w-K_1\left(C_{\mathcal{R}}^{\mathcal{B}}\,\dot{\vec{\omega}}_r-\vec{\omega}\times C_{\mathcal{R}}^{\mathcal{B}}\,\vec{\omega}_r\right)+K_2\delta\vec{\omega}+K_3\delta\psi \tag{7.63}$$

or when the control is defined as $\vec{u}=\vec{T}$ then:

$$\vec{u}=-W_{z,w}^{-1}\vec{\omega}\times J_s\vec{\omega}-W_{z,w}^{-1}\vec{\omega}\times\vec{h}_w-W_{z,w}^{-1}K_1\left(C_{\mathcal{R}}^{\mathcal{B}}\,\dot{\vec{\omega}}_r-\vec{\omega}\times C_{\mathcal{R}}^{\mathcal{B}}\,\vec{\omega}_r\right)+W_{z,w}^{-1}K_2\delta\vec{\omega}+W_{z,w}^{-1}K_3\delta\psi \tag{7.64}$$

In the special case that $\dot{\omega}_{r,n}=0$, $\omega_{r,n}=0$ and $\psi_{r,n}=0$ for $n=1,2,3$ then the required control for stability becomes:

$$\vec{u}=-\vec{\omega}\times J_s\vec{\omega}-\vec{\omega}\times\vec{h}_w+K_2\vec{\omega}+K_3\psi \tag{7.65}$$

7.5. Tracking the near-Earth asteroid

To comply with requirement MR-AOCS-3 a simulation must be made to verify that the satellite can track a NEA at a closest approach distance of 10,000 km.

MR-AOCS-3: The attitude and orbital control system shall be able to track the near-Earth asteroid at a distance of 10,000 km.

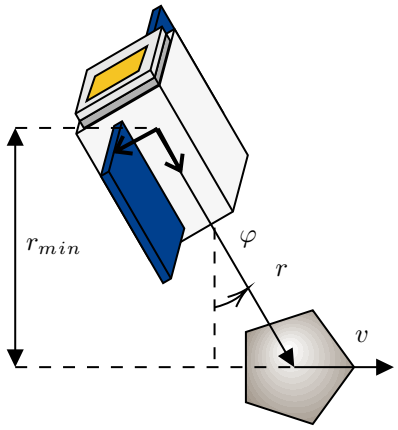

Figure 7.2: This figure illustrates the fly-by observation angle between a satellite and an asteroid as a function of the relative distance and relative velocity

If it is assumed that $\frac{\mathrm{d}v}{\mathrm{d}t} = 0$ and for convenience let $r = r_{min}$ then:

$$\varphi = \tan^{-1}\left(\frac{r}{vt}\right) \tag{7.66}$$

For the required minimum angular acceleration that has to be achieved with the reaction wheels, the maximum angular acceleration for the closest approach mission segment must be found, which can be found by $\ddot{\varphi}_{max} = \ddot{\varphi}\left(t : \dddot{\varphi}\left(t\right) = 0\right)$. The time derivatives of φ can be written as:

$$\begin{aligned}
\dot{\varphi} &= -\tfrac{rv}{v^2t^2+r^2} \\
\ddot{\varphi} &= \tfrac{2rtv^3}{(v^2t^2+r^2)^2} \\
\dddot{\varphi} &= \tfrac{2v^3\left(r^3-3rt^2v^2\right)}{(r^2+t^2v^2)^3}
\end{aligned} \tag{7.67}$$

Solving $\dddot{\varphi} = 0$ gives:

$$\dddot{\varphi} = \tfrac{2v^3\left(r^3-3rt^2v^2\right)}{(r^2+t^2v^2)^3} = 0$$

$$r^3 - 3rt^2v^2 = 0$$

$$t_{max} = \pm\tfrac{r}{\sqrt{3}v}$$

Substitution of the positive t_{max} inside $\ddot{\varphi}$ gives:

$$\ddot{\varphi}\left(\frac{r}{\sqrt{3}v}\right) = \frac{2r\left(\frac{r}{\sqrt{3}v}\right)v^3}{\left(v^2\left(\frac{r}{\sqrt{3}v}\right)^2 + r^2\right)^2} = \frac{18v^2}{13\sqrt{3}r^2} \tag{7.68}$$

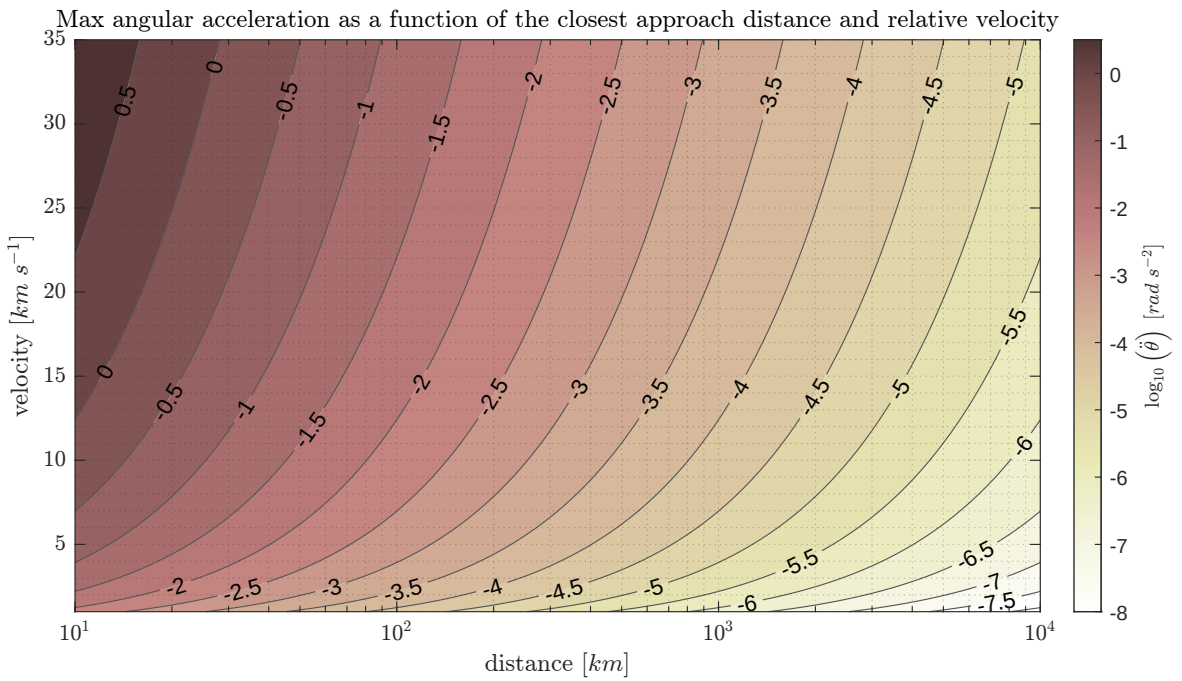

Figure 7.3: This figure shows the maximum angular acceleration required to track an asteroid during a fly-by based on the relative velocity and closest approach distance. The maximum angular acceleration is found by solving for $\ddot{\varphi}_{max} = \ddot{\varphi}\left(t : \dddot{\varphi}\left(t\right) = 0\right)$, which is found by taking the second derivative of the observation angle φ with respect to time.

The maximum required slew rate can also be expressed in the closest approach distance and relative velocity. This happens at $t = 0$ or the moment of the closest approach.

$$\dot{\varphi}\left(0\right) = -\frac{rv}{v^2(0)^2 + r^2} = -\frac{v}{r} \tag{7.69}$$

For this thesis, it is assumed that the expected relative fly-by velocity in the worst case is $35\,\mathrm{km\,s^{-1}}$. This results in a maximum angular acceleration requirement of approximately $0.01\,\mathrm{mrad\,s^{-1}}$. The asteroid tracking motion can be tracked by using the identical transformations as used for the LVLH frame tracking. The MRP representation for the asteroid tracking orientation can then be obtained from the polar asteroid tracking orientation by first calculating the quaternion that represents the rotation from the inertia frame to the asteroid tracking frame:

$$\begin{aligned} q_w &= \tfrac{1}{2}\sqrt{2 + 2\left(\hat{e}_x \cdot \hat{x} + \hat{e}_y \cdot \hat{y}\right)} \\ q_x &= \frac{\left(\hat{e}_y \cdot \hat{z} - \hat{e}_x \cdot \hat{y}\right)}{\sqrt{2 + 2\left(\hat{e}_x \cdot \hat{x} + \hat{e}_y \cdot \hat{y}\right)}} \\ q_y &= \frac{\left(\hat{e}_x \cdot \hat{z} - \hat{e}_y \cdot \hat{x}\right)}{\sqrt{2 + 2\left(\hat{e}_x \cdot \hat{x} + \hat{e}_y \cdot \hat{y}\right)}} \\ q_z &= \tfrac{1}{2}\sqrt{2 + 2\left(\hat{e}_x \cdot \hat{x} - \hat{e}_y \cdot \hat{y}\right)} \end{aligned} \tag{7.70}$$

In this case $\hat{e}_x = \begin{bmatrix}\cos\varphi & \sin\varphi & 0\end{bmatrix}^\top$, $\hat{e}_y = \begin{bmatrix}-\sin\varphi & \cos\varphi & 0\end{bmatrix}^\top$, and $\hat{e}_z = \begin{bmatrix}0 & 0 & 1\end{bmatrix}^\top$. The MRP for the asteroid tracking frame orientation can then be found using:

$$\vec{\psi} = \frac{\begin{bmatrix}q_x & q_y & q_z\end{bmatrix}^\top}{1 + q_w}$$

Finally, the angular velocity vector of the asteroid tracking frame can be expressed as:

$$\vec{\omega} = \begin{bmatrix} 0 & 0 & \dot{\varphi} \end{bmatrix}^\top \tag{7.71}$$

And the angular acceleration vector of the asteroid tracking frame can be expressed as:

$$\dot{\vec{\omega}} = \begin{bmatrix} 0 & 0 & \ddot{\varphi} \end{bmatrix}^\top \tag{7.72}$$

7.5.1. Lyaponov's direct method controller

Lyaponov's direct method controller as described in the Earth tracking section is used also to track the asteroid. The main reason for this is that higher-order time derivatives of the motion of the asteroid can be included in the controller. The torque of the reaction wheels is thus described as:

$$\vec{T} = -W_{z,w}^{-1}\vec{\omega} \times J_s\vec{\omega} - W_{z,w}^{-1}\vec{\omega} \times \vec{h}_w - W_{z,w}^{-1}K_1\left(C_{\mathcal{R}}^{\mathcal{B}}\,\dot{\vec{\omega}}_r - \vec{\omega} \times C_{\mathcal{R}}^{\mathcal{B}}\,\vec{\omega}_r\right) + W_{z,w}^{-1}K_2\delta\vec{\omega} + W_{z,w}^{-1}K_3\delta\psi$$

7.6. Summary

In this chapter, a method is presented to find a thruster placement to perform momentum dumping or reaction wheel desaturation maneuvers with RCTs to answer research question RQ2.2. In Biggs and Fournier [46] the minimal required number of fixed thrusters that can instantaneously control every axis of rotation in both directions is argued to be four. However, it is investigated in this thesis if three RCTs are also possible. This thesis presents a thruster placement optimization method to solve the thruster configuration optimization problem to maximize the angular accelerations around every axis of rotation while generating minimal disturbances around other axes of rotation. This optimization method can be applied to any satellite geometry and inertia by using a super-ellipsoid approximation of the satellite's surface. This way a thruster can be parameterized by a longitude, co-latitude, and two thrust angles relative to the satellite surface. The thruster allocations for each axis of rotation are also optimized together with the thruster placement to find a complete solution for both the control allocation, thruster position, and direction for all RCTs.

Next, to answer research question RQ3, a detumbling case is made for detumbling using only reaction wheels, using reaction wheels and magnetorquers, and using reaction wheels and RCTs. For the control algorithm, an LQR algorithm is chosen because it can handle a non-linear system by linearizing the kinematic and dynamic equations and it focuses on performance rather than stability. The CubeSat must be able to detumble when the satellite is spinning at 30 deg/s in any axis of rotation. If the results show that the CubeSat can stabilize without saturating the reaction wheels then MR-AOCS-2 is considered to be verified.

Then, to answer research question RQ2, a reaction wheel desaturation case is formulated using an LQR algorithm as well. The CubeSat must be able to desaturate the reaction wheels when these are saturated in any reaction wheel in both positive and negative directions. The results for the different desaturation cases can then be used to answer research question RQ2.

Finally, to track the Earth and a NEA at a distance of 10,000 km to verify requirement MR-AOCS-3 and answer research question RQ3, an LC algorithm using only the reaction wheels is presented because it can deal with the non-linear nature of the EOM. Simulating the performance of the CubeSat for a relative velocity of $35\,\mathrm{km\,s^{-1}}$ with respect to the NEA at the closest approach and the tracking of the Earth in SSGTO leads to an answer to research question RQ3.

8

Attitude control and desaturation simulation results

To answer the research questions RQ2, RQ2.2, and RQ3 the framework for rotational kinematics and dynamics of a satellite as presented in chapter 6 combined with the control algorithms and RCT thruster configuration optimization method as presented in chapter 7 were simulated for the selected satellite subsystems and RCT propulsion system for desaturation and detumbling as presented in chapter 1 and chapter 2.

RQ2: What is a feasible design for a propulsion system to desaturate reaction wheels for an autonomous 6U satellite near-Earth asteroid fly-by mission starting from a super synchronous geostationary transfer orbit for 5 years?

RQ2.2: What number of thrusters, their position, and direction are required to perform momentum dumping maneuvers?

RQ3: What is a feasible design for an attitude control system including a control algorithm for an autonomous 6U satellite near-Earth asteroid fly-by mission starting from a super synchronous geostationary transfer orbit?

The satellite model described in Figure 8.1 including approximated inertia data and center of mass using Matlab was used to simulate the attitude of the 6U CubeSat.

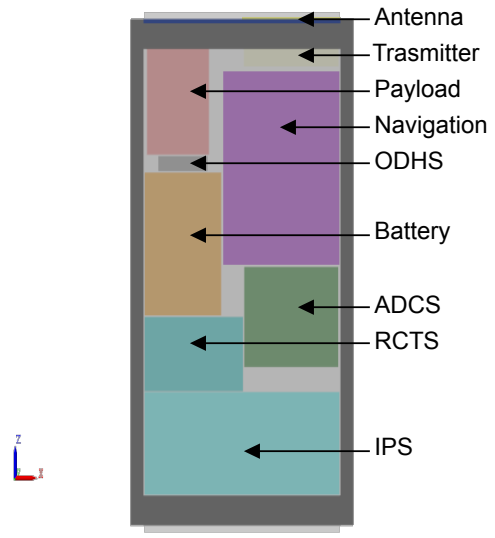

(a) Satellite configuration front view.

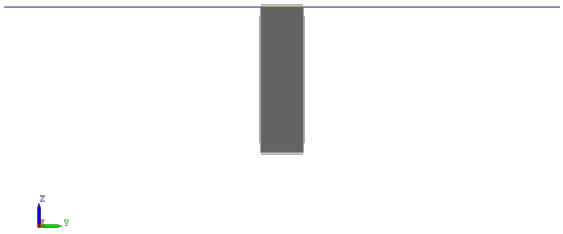

(b) Satellite configuration side view.

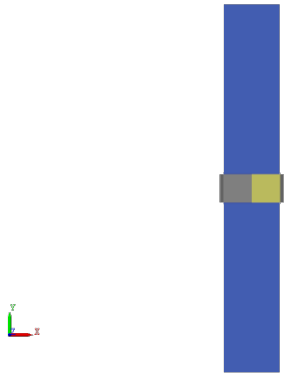

(c) Satellite configuration top view.

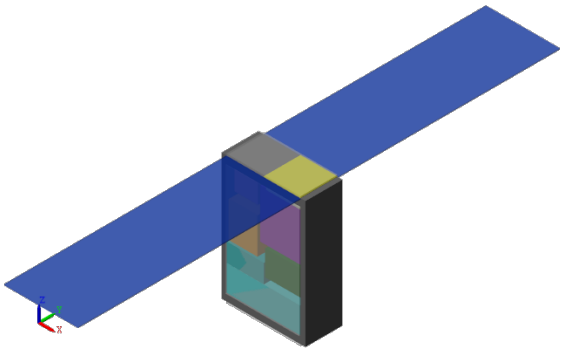

(d) Satellite configuration isometric view.

Figure 8.1: This figure displays the complex and detailed design of a 6U satellite, purposefully designed for a near-Earth asteroid exploration fly-by mission. The intricate CubeSat configuration has been simulated using MATLAB's "simscape" toolbox to determine the satellite's center of mass and inertia. Abbreviations used in the detailed view (a) are onboard data handling system (ODHS), reaction control thruster system (RCTS), attitude determination and control system (ADCS), and interplanetary propulsion system (IPS).

The detailed design of a 6U satellite presented in Figure 8.1 modeled in MATLAB's "simscape" toolbox resulted in the following inertia (including static reaction wheels) and center of mass:

$$J_s = \begin{bmatrix} 0.261522993033346 & -1.18099695051684 \times 10^{-18} & 0.00178386237212245 \\ -1.18099695051684 \times 10^{-18} & 0.181700297095600 & -2.85458768324159 \times 10^{-18} \\ 0.00178386237212245 & -2.85458768324159 \times 10^{-18} & 0.171663828901755 \end{bmatrix} \text{kg m}^{-2} \tag{8.1}$$

Table 8.1: Center of mass of the detailed 6U satellite measured from the geometric center of the 6U satellite.

Variable	Result
x_{COM} (m)	0.00169854561309273
y_{COM} (m)	0
z_{COM} (m)	-0.0403683027374510

8.1. Reaction control thruster optimal configuration

In chapter 7, a method is presented to find a thruster placement to perform momentum dumping or reaction wheel desaturation maneuvers with RCTs to answer research question RQ2.2.

RQ2.2: What number of thrusters, their position, and direction are required to perform momentum dumping maneuvers?

In this section, the results of a thruster placement optimization method to solve the thruster configuration optimization problem to maximize the angular accelerations around every axis of rotation while generating minimal disturbances around other axes of rotation are presented. Furthermore, both three RCTs and four RCTs configurations were investigated.

8.1.1. Problem setup

This optimization method was applied to the detailed CubeSat design as presented in chapter 5 and its inertia and center of mass were found by using MATLAB's "simscape" toolbox to model the CubeSat. By using a super-ellipsoid approximation of the satellite's surface the position and fixed direction of the thrusters were parameterized by only four parameters. Namely, a longitude, co-latitude, and two thrust angles relative to the satellite surface. The super-ellipsoid was made by solving for the super-ellipsoid surface function $\left(\left(\frac{x}{A}\right)^r + \left(\frac{y}{B}\right)^r\right)^{r/t} + \left(\frac{z}{C}\right)^t = 1$ with the following parameters: $A = 0.1\,\text{m}$, $B = 0.05\,\text{m}$, $C = 0.15\,\text{m}$, $r = t = 8$, and a sufficient ν from trial and error was found to be 1×10^4.

8.1.2. Optimizer setup

A particle swarm optimization method was used because the design parameters do not contain integers and it was expected that this method converges better to a global minimum than other methods such as the genetic algorithm method. The solution of the particle swarm optimization method was then used as an initial guess for a Levenberg-Marquardt local optimization method to find a true local minimum. The particle swarm optimizer used had a swarm size of $100 \times 30 = 3,000$ for three RCTs or $100 \times 40 = 4,000$ for four RCTs which is 100 times the number of design parameters. This number was selected to increase the likelihood to find the global minimum. The co-latitude and longitude were bound to the complete surface of the CubeSat for the optimization script. The RCT direction vector was bounded by the thrust angles such that they could never be chosen to point through the surface of the CubeSat. And finally, the thrust allocation parameters are bounded between zero and one such that the thrusters cannot fire in a negative direction or exceed 100% thrust.

8.1.3. Optimal reaction control thruster configuration result for three thrusters

The optimization did not find a solution that sufficiently maximizes the angular accelerations produced by the thrusters in any direction while minimizing the unwanted angular accelerations in other directions.

Since no proper solution could be found no comment can be made on the efficiency of the found configuration because the objective and penalties converged to a minimum that does not have near zero unwanted angular accelerations in other directions.

This configuration resulted in the following thrust allocations of the three RCTs for the six angular

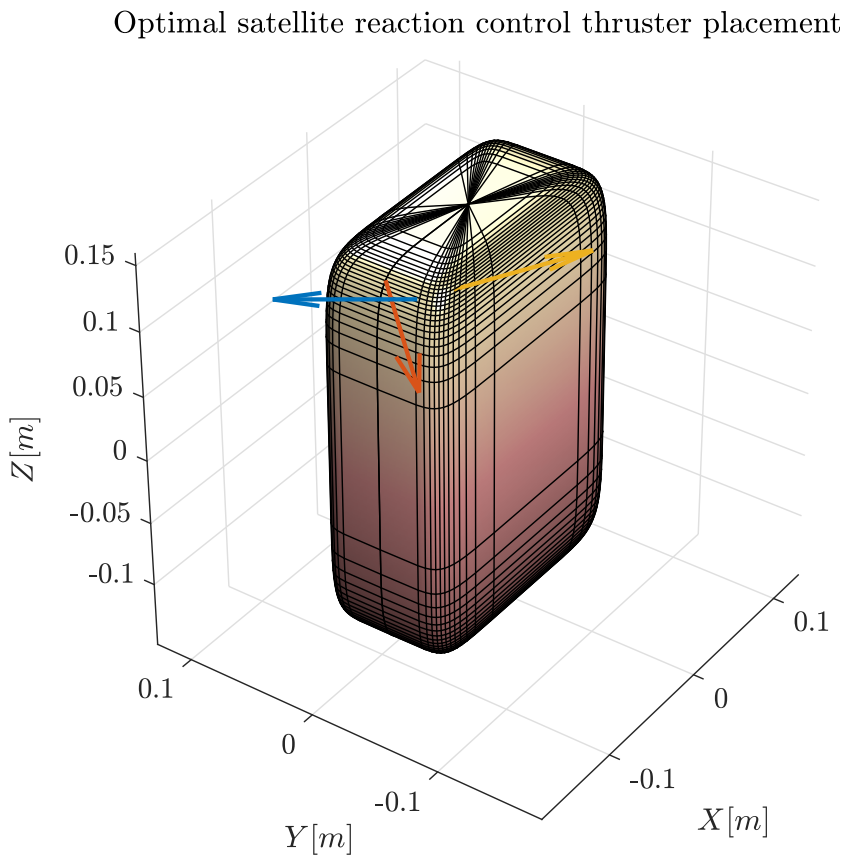

Figure 8.2: Optimal reaction control thrusters configuration for three thrusters. A feasible solution could not be found to prevent undesired angular accelerations while simultaneously generating acceleration along a specific axis of rotation.

velocities:

$$A_u = \begin{bmatrix} \vec{u}^{\top}_{M_x} \\ \vec{u}^{\top}_{M_y} \\ \vec{u}^{\top}_{M_z} \\ \vec{u}^{\top}_{-M_x} \\ \vec{u}^{\top}_{-M_y} \\ \vec{u}^{\top}_{-M_z} \end{bmatrix} = \begin{bmatrix} 0.0000 & 1.0000 & 1.0000 \\ 0.0000 & 0.0000 & 1.0000 \\ 0.0000 & 1.0000 & 1.0000 \\ 1.0000 & 0.0000 & 0.0000 \\ 1.0000 & 1.0000 & 0.0000 \\ 1.0000 & 0.0000 & 0.0000 \end{bmatrix} \tag{8.2}$$

And these thrust allocations produced the following angular velocities:

$$\begin{bmatrix} \dot{\vec{\omega}}^{\top}_{M_x} \\ \dot{\vec{\omega}}^{\top}_{M_y} \\ \dot{\vec{\omega}}^{\top}_{M_z} \\ \dot{\vec{\omega}}^{\top}_{-M_x} \\ \dot{\vec{\omega}}^{\top}_{-M_y} \\ \dot{\vec{\omega}}^{\top}_{-M_z} \end{bmatrix} = \begin{bmatrix} 0.9314 & 0.0342 & 0.8536 \\ 0.4325 & 0.8006 & 0.4732 \\ 0.9314 & 0.0342 & 0.8536 \\ -0.5679 & -0.5365 & -0.5354 \\ -0.0690 & -1.3030 & -0.1550 \\ -0.5679 & -0.5365 & -0.5354 \end{bmatrix} \text{rad s}^{-2} \tag{8.3}$$

From the results, it can be seen that no pure angular accelerations can be made in any axis of rotation using the three RCTs in the current configuration. Therefore, a configuration using three RCTs is not considered to be feasible which is in line with the expectations from papers such as Biggs and Fournier [46].

8.1.4. Optimal reaction control thruster configuration result

The optimization found a solution that sufficiently maximizes the angular accelerations produced by the thrusters in any direction while minimizing the unwanted angular accelerations in other directions. It is however still unknown if this solution is close to the true global optimum. This can only be verified if the Pareto front is investigated which is not done in this thesis due to a lack of computing power.

Furthermore, the results show that the thrusters' directions, positions, and thrust allocations are closely related to the produced angular acceleration around the desired axis of rotation and unwanted angular acceleration in other rotation directions. The thrusters must be oriented such that a linear combination of the thrusters is able to produce pure angular accelerations along all the axes of rotation.

From the results, it can be seen four thrusters placed at the top of the 6U CubeSat are a possible feasible solution. Also, the placed solar panels do not interfere with the placed thrusters. This model however does lack the incorporation of the RCTs thruster head mass in the inertia calculation of the CubeSat and assumes that all the mass is inside of the selected secondary propulsion system, the GOMSpace NanoProp CGP3. This then answers research question RQ2.2.

For future work, the multiple-objective optimization problem can be better formalized to incorporate penalties for thrusting near sensors or through external solar panels. Another suggestion is to look for a Pareto front that contains multiple sets of solutions instead of a single solution. That way a designer can select a solution that might be less optimal but has a more desirable outcome.

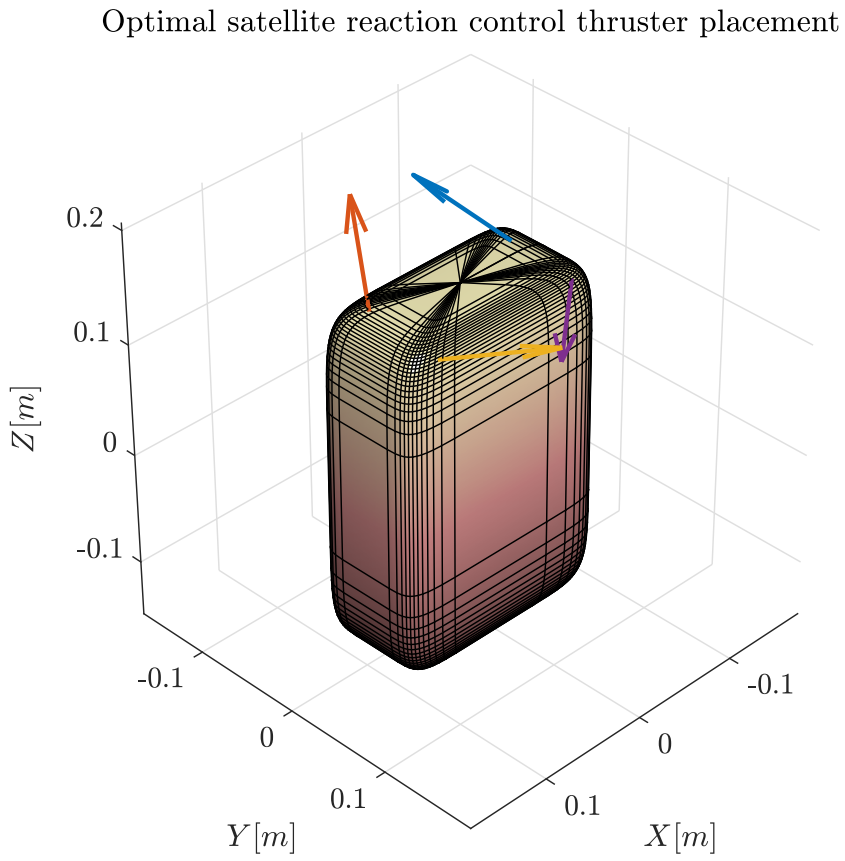

Figure 8.3: Optimal reaction control thrusters configuration. The four reaction control thrusters are placed on a super ellipsoid that approximates the surface of a 6U CubeSat. Then the angular accelerations are optimized using a particle swarm optimization method for each axis of rotation which results in the following configuration.

Table 8.2: The found optimal reaction control thrusters placement parameters.

Variable	Result
Reaction control thruster 1	
v_1 (rad)	-3.11221256059610
w_1 (rad)	1.36122881071411
$\theta_{d,1}$ (rad)	-1.04599638197860
$\phi_{d,1}$ (rad)	-0.898167370686014
Reaction control thruster 2	
v_2 (rad)	-0.117909260610473
w_2 (rad)	1.29805723594228
$\theta_{d,2}$ (rad)	-1.03493964975417
$\phi_{d,2}$ (rad)	1.04669003731763
Reaction control thruster 3	
v_3 (rad)	1.26856851829831
w_3 (rad)	0.763284048213187
$\theta_{d,3}$ (rad)	0.291168122240135
$\phi_{d,3}$ (rad)	0.973986528051412
Reaction control thruster 4	
v_4 (rad)	2.00818476159327
w_4 (rad)	0.870408004189103
$\theta_{d,4}$ (rad)	0.637906486015526
$\phi_{d,4}$ (rad)	-1.01889265526861

This configuration resulted in the following thrust allocations for the six angular velocities:

$$A_u = \begin{bmatrix} \vec{u}_{M_x}^\top \\ \vec{u}_{M_y}^\top \\ \vec{u}_{M_z}^\top \\ \vec{u}_{-M_x}^\top \\ \vec{u}_{-M_y}^\top \\ \vec{u}_{-M_z}^\top \end{bmatrix} = \begin{bmatrix} 0.980709 & 1.000000 & 0.081063 & 0.006865 \\ 1.000000 & 0.043077 & 0.196581 & 0.798584 \\ 1.000000 & 0.060275 & 0.991845 & 0.088340 \\ 0.130156 & 0.056975 & 0.974589 & 1.000000 \\ 0.011111 & 1.000000 & 0.855413 & 0.150965 \\ 0.048925 & 1.000000 & 0.024792 & 0.944823 \end{bmatrix} \tag{8.4}$$

And these thrust allocations produced the following angular velocities:

$$\begin{bmatrix} \dot{\vec{\omega}}_{M_x}^\top \\ \dot{\vec{\omega}}_{M_y}^\top \\ \dot{\vec{\omega}}_{M_z}^\top \\ \dot{\vec{\omega}}_{-M_x}^\top \\ \dot{\vec{\omega}}_{-M_y}^\top \\ \dot{\vec{\omega}}_{-M_z}^\top \end{bmatrix} = \begin{bmatrix} 0.000798 & 0.000000 & 4.065758 \times 10^{-20} \\ 2.786738 \times 10^{-19} & 0.001130 & 2.710505 \times 10^{-19} \\ -6.776263 \times 10^{-21} & 5.421011 \times 10^{-20} & 0.000680 \\ -0.000777 & 5.421011 \times 10^{-20} & -5.421011 \times 10^{-20} \\ 3.252607 \times 10^{-19} & -0.001233 & 0.000000 \\ 1.0842022 \times 10^{-19} & -1.76183 \times 10^{-19} & -0.000729 \end{bmatrix} \text{rad s}^{-2} \tag{8.5}$$

8.2. Satellite detumbling

To answer research question RQ3 the detumbling of a 6U CubeSat in SSGTO has to be simulated for the different designs presented in chapter 2 and chapter 7, and the RCTs design found in Section 8.1 was simulated.

RQ3: What is a feasible design for an attitude control system including a control algorithm for an autonomous 6U satellite near-Earth asteroid fly-by mission starting from a super synchronous geostationary transfer orbit?

In chapter 7, three methods for the detumbling of a satellite are presented which are LQR controllers using reaction wheels only, using RCTs and reaction wheels, and using magnetorquers and reaction wheels. These three methods were simulated for six different scenarios in an SSGTO starting at the perigee to demonstrate their detumbling capabilities. In order to comply with MR-AOCS-2, the objective of the AOCS system was to both detumble the satellite and desaturate the reaction wheels from the maximum expected tip-off rate of $0.524\,\text{rad}\,\text{s}^{-1}$ in any direction until the angular velocities of the satellite's body and reaction wheels are close to zero.

MR-AOCS-2: The attitude and orbital control system shall be able to detumble the spacecraft after orbit injection.

8.2.1. Scenarios setup

Six scenarios were simulated for each detumbling method. All scenarios started at the perigee of the SSGTO as specified in chapter 1. The orientation of the satellite started at $\psi = \begin{bmatrix} 0 & 0 & 0 \end{bmatrix}^\top$ and the satellite's reaction wheels had an angular velocity of zero. In each scenario, the starting angular velocities are zero in all axes except for one axis, which starts at a positive or negative $0.524\,\text{rad}\,\text{s}^{-1}$. This led to six unique variations. All these scenarios were simulated with a control interval rate of 1 second for a total maneuver duration of 1 hour. The used ADCS was the ClydeSpace iADCS400 with three RW400 reaction wheels. It can produce reaction wheel torques up to $8\,\text{mN}\,\text{m}$, magnetic moments of up to 0.5 in X/Y-directions and 0.4 in Z-direction $\text{A}\,\text{m}^2$, and maximum wheel angular velocities of up to $523.6\,\text{rad}\,\text{s}^{-1}$. The GOMSpace Nanoprop CGP3 was used for the RCTs with a maximum thrust of $1\,\text{mN}$ and specific impulse up to $110\,\text{s}$.

8.2.2. Results of detumbling using reaction wheels only and a linear quadratic regulator

The following results were obtained for the simulation of detumbling using reaction wheels only. In Figure 8.4 it can be seen that detumbling using only reaction wheels is not possible because tip-off rates in the X-direction result in reaction wheel angular velocities larger than $523.59\,\text{rad}\,\text{s}^{-1}$ or 5000 rpm which is above the maximum allowed angular velocity of the ClydeSpace RW400 reaction wheel. Thus, a control algorithm that involves only reaction wheels did not meet the requirement MR-AOCS-2. To conclude, this means that RCTs or magnetorquers are required in the detumbling phase to keep the reaction wheels from saturating.

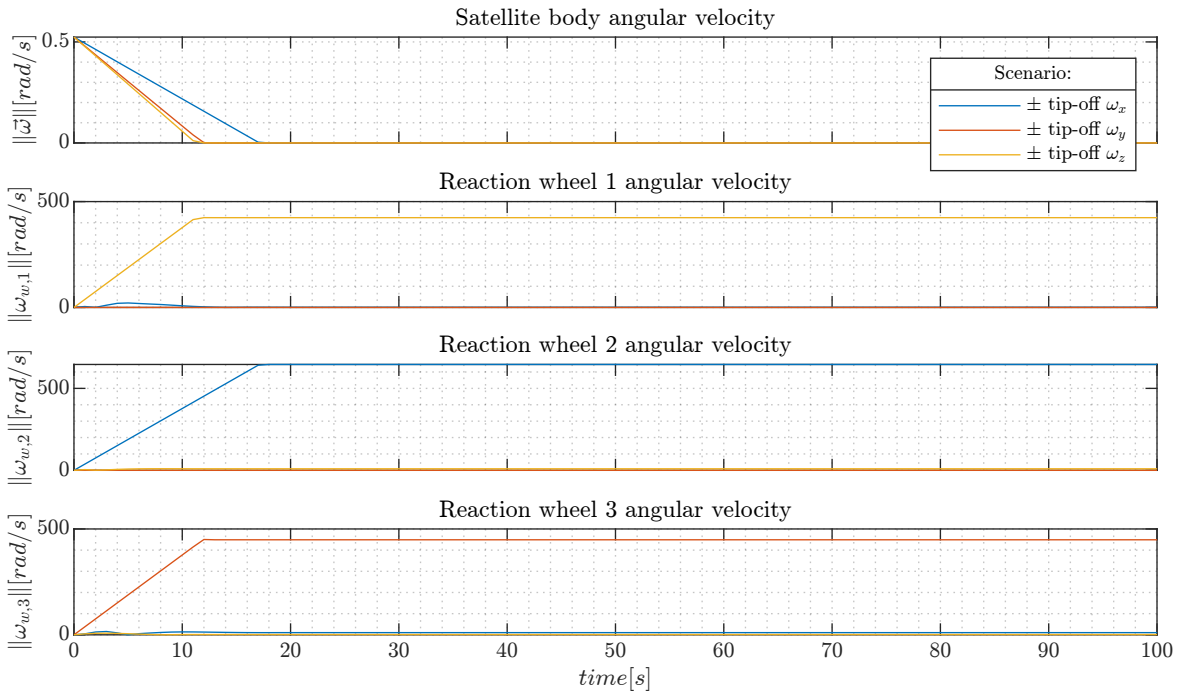

Figure 8.4: Detumbling of the satellite using only reaction wheels.

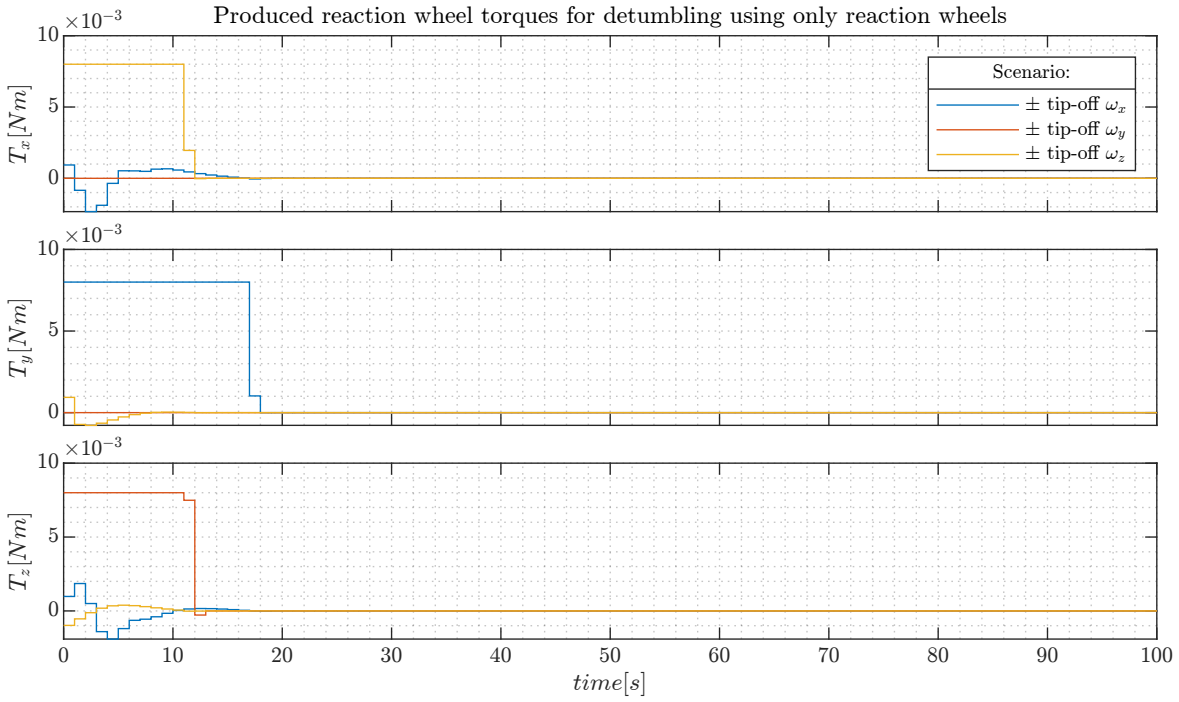

Figure 8.5: Reaction wheel torques for the detumbling of the satellite using only reaction wheels.

8.2.3. Results of detumbling using reaction control thrusters and reaction wheels

The following results were obtained for the simulation of detumbling using reaction wheels and RCTs. In Table 8.3 it can be seen that for the worst scenario of the six scenarios, a maximum propellant mass of $1.438\,\mathrm{g}$ was used to detumble the satellite starting from a tip-off rate of $\omega_x = +0.524\,\mathrm{rad\,s^{-1}}$. With

respect to the GOMSpace Nanoprop CGP3's available propellant mass, which is $50\,\mathrm{g}$, this is only 2.9%. Therefore a system that consists of four RCTs and three reaction wheels is considered to be a feasible option for desaturation. From Figure 8.6 and Figure 8.7 it can be seen that the detumbling algorithm kept the reaction wheels from 'charging' or spinning. However, it can be seen that the reaction wheels are not changing their angular velocities very smoothly which can be an issue. The built-in controller of the reaction wheels controls the speed of the reaction wheels and not the torque which makes fast-changing angular velocities challenging. To conclude, a control algorithm that involves RCTs and reaction wheels combined with an LQR control algorithm did meet the requirement MR-AOCS-2. For research question RQ3, this indicates that RCTs and reaction wheels combined with an LQR controller can be part of a feasible design for an ACS. However, the LQR controller design as it is now can be challenging for the built-in reaction wheel controller.

Table 8.3: Propellant mass used by the reaction control thrusters for detumbling.

Scenario	Used propellant
$\omega_x = +0.524\,\mathrm{rad\,s^{-1}}$	$1.438\,\mathrm{g}$
$\omega_y = +0.524\,\mathrm{rad\,s^{-1}}$	$0.795\,\mathrm{g}$
$\omega_z = +0.524\,\mathrm{rad\,s^{-1}}$	$1.081\,\mathrm{g}$
$\omega_x = -0.524\,\mathrm{rad\,s^{-1}}$	$1.356\,\mathrm{g}$
$\omega_y = -0.524\,\mathrm{rad\,s^{-1}}$	$0.876\,\mathrm{g}$
$\omega_z = -0.524\,\mathrm{rad\,s^{-1}}$	$1.085\,\mathrm{g}$

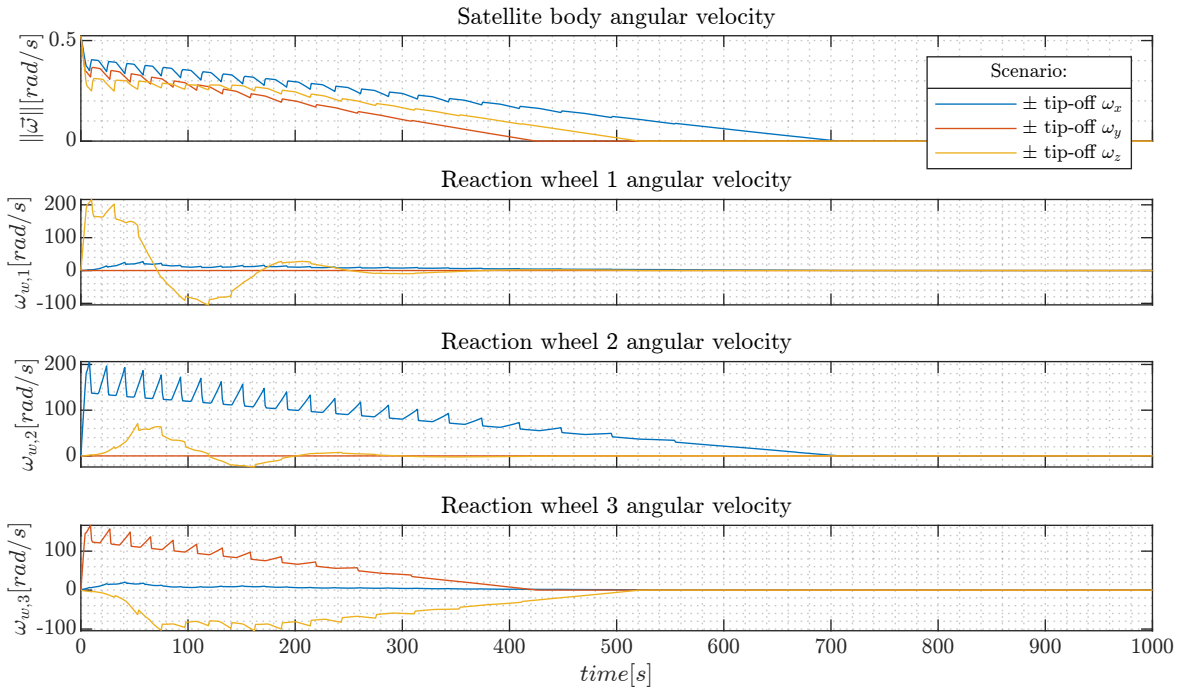

Figure 8.6: Detumbling of the satellite using only reaction wheels and reaction control thrusters.

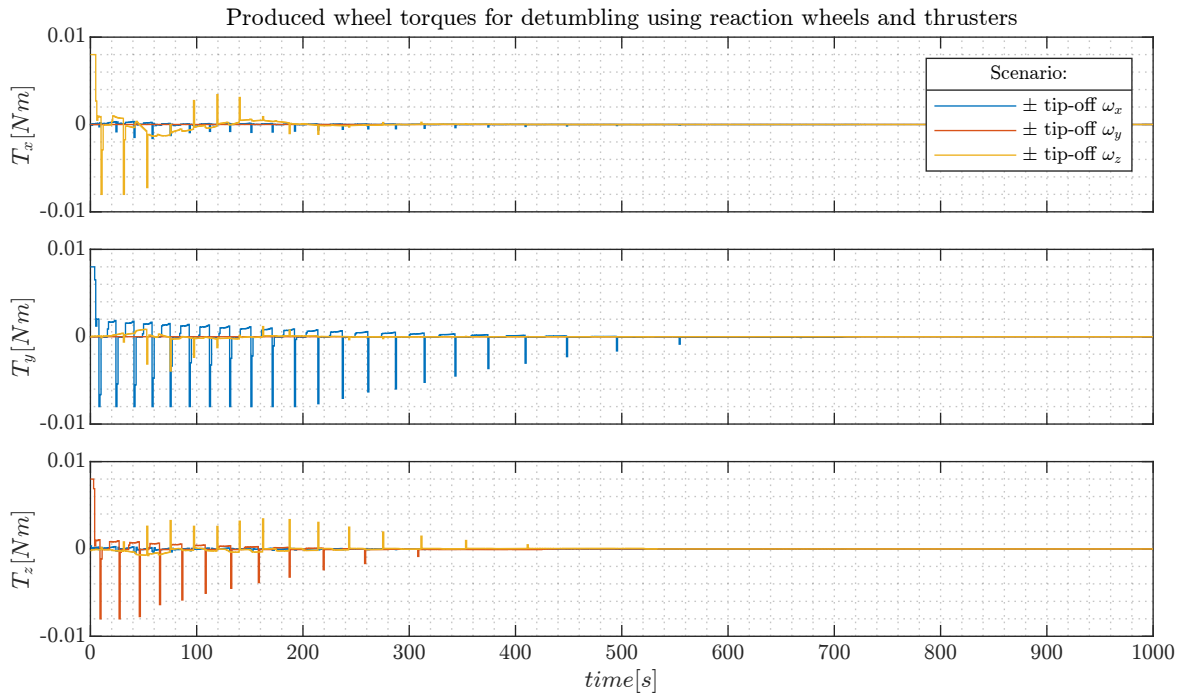

Figure 8.7: Reaction wheel torques for the detumbling of the satellite using reaction wheels and reaction control thrusters.

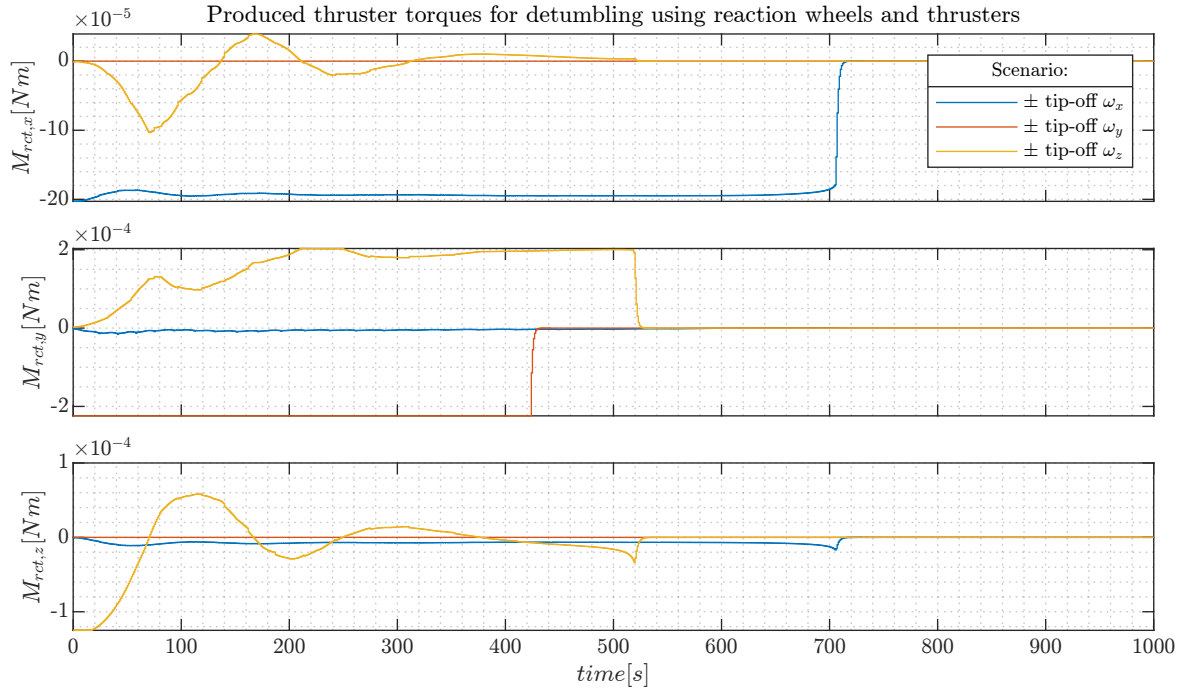

Figure 8.8: Reaction control thrusters torques for the detumbling of the satellite using reaction wheels and reaction control thrusters.

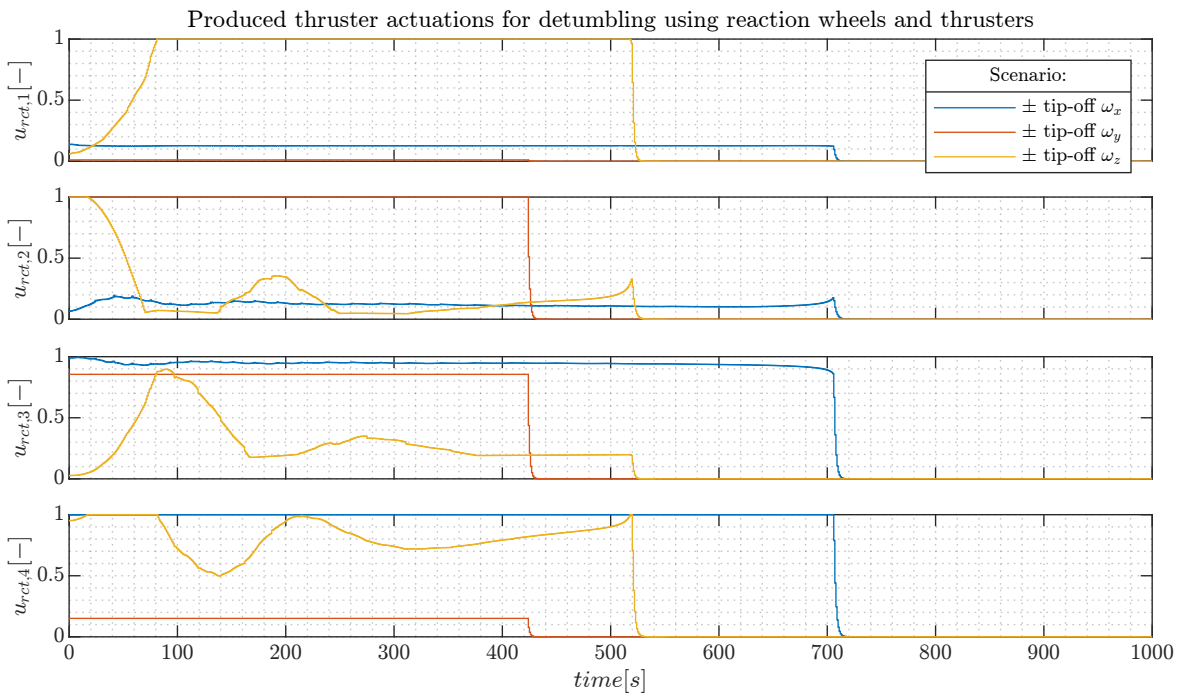

Figure 8.9: Reaction control thrusters throttle for the detumbling of the satellite using reaction wheels and reaction control thrusters.

8.2.4. Result of detumbling using reaction wheels and magnetic torquers

The following results were obtained for the simulation of detumbling using reaction wheels and magnetic torquers. During simulating it was observed that it takes a lot of time to detumble the satellite using both reaction wheels and magnetic torquers until the angular velocities are close to zero and the reaction wheels are desaturated. Therefore, it was decided to only simulate one scenario. It can be seen that after 50 hours, the satellite's angular velocities were brought close to zero from the reaction wheel torques. It can be seen in Figure 8.11 that the magnetic torquers were unable to desaturate the reaction wheels within 50 hours. Assuming that, in every orbital revolution, a similar portion of the reaction wheels' angular momenta can be decreased it can be concluded that a complete desaturation of the reaction wheels will take many days if not weeks to succeed. Due to the high elliptical nature of the SSGTO orbit, this will lead to a significantly more harsh radiation environment over the complete duration of the mission. This leads to the need for a larger radiation shield. Furthermore, assuming the ClydeSpace iADCS400 contains two MTQ400(0.5) magnetic torquers of $44\,$g and one MTQ400(0.4) $34.5\,$g, $122.5\,$g of extra propellant could be added to the CubeSat for detumbling and desaturation. And finally, the magnetic torquers significantly decrease in power efficiency for higher altitudes as can be seen in the results. Since the CubeSat mission has the objective to escape an Earth orbit as fast and efficiently as possible the magnetic torquers cannot be optimally used.

In conclusion, the results demonstrate that meeting requirement MR-AOCS-2 is feasible by limiting wheel saturation and utilizing multiple orbital revolutions to fully detumble and desaturate reaction wheels. However, regarding research question RQ3, the potential extra time required for detumbling renders a design consisting of magnetic torquers and reaction wheels combined with an LQR controller impractical due to added mass of a radiation shield and the mass of magnetic torquers. Therefore, it can be inferred that a CubeSat without magnetic torquers and extra propellant for detumbling and desaturation would be a more optimal solution.

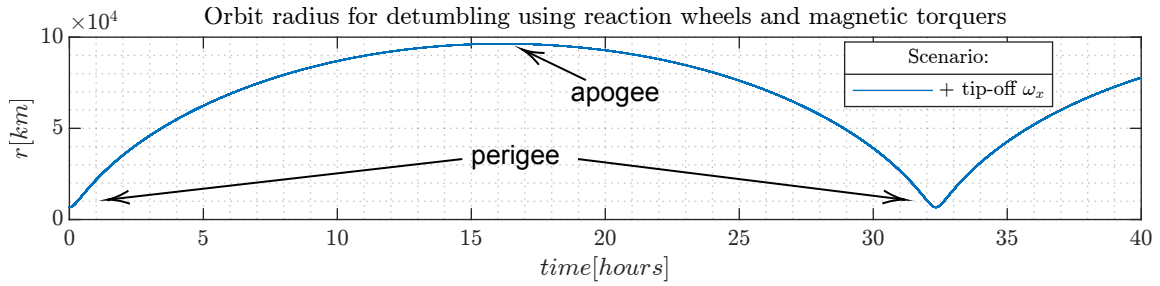

Figure 8.10: Orbital radius of the satellite during detumbling using magnetic torquers and reaction wheels.

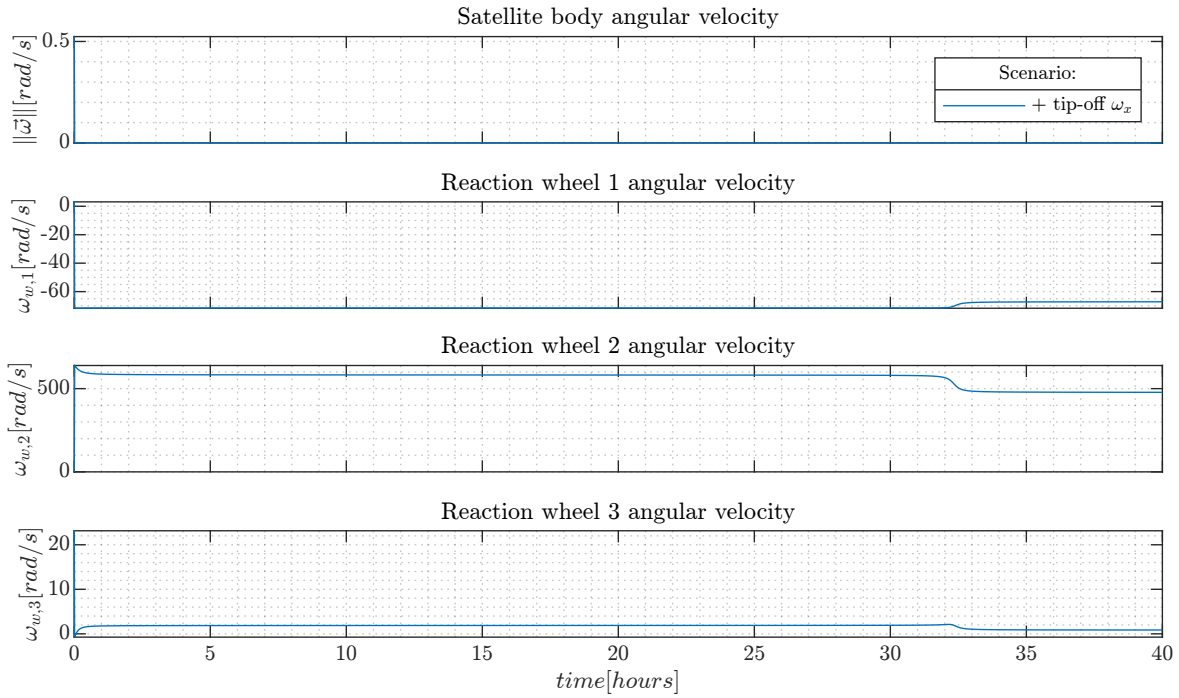

Figure 8.11: This figure shows The angular velocities of the satellite and reaction wheels during the satellite's detumbling process using a combination of reaction wheels and magnetic torquers in combination with a linear quadratic regulator. The effectiveness of this control method can be observed in the graph as the satellite's angular velocity is swiftly reduced. However, a drawback of this setup is evident as the second reaction wheel becomes saturated and the setup is only capable of decreasing its angular momentum by 10-20% per orbital revolution. Consequently, the satellite may need to desaturate its reaction wheels for up to 400 hours or 2 weeks in extreme cases to completely desaturate.

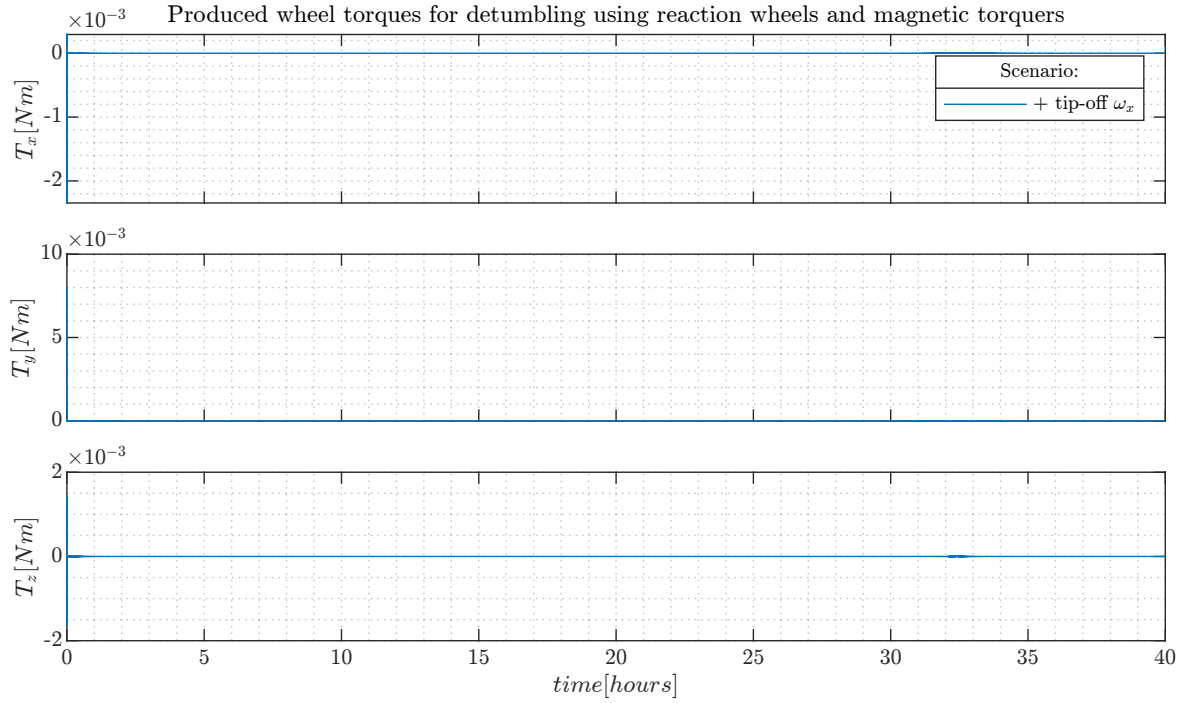

Figure 8.12: The produced reaction wheel torques for detumbling the satellite using reaction wheel and magnetic torquers.

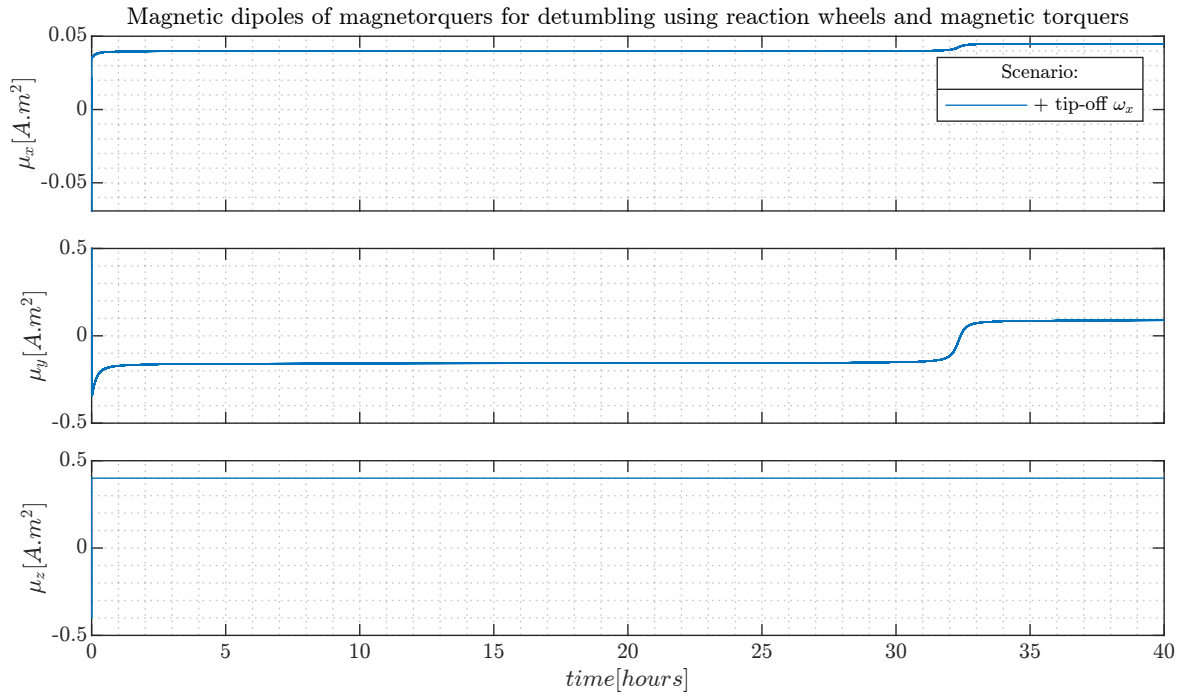

Figure 8.13: The produced magnetic torquer dipoles for detumbling the satellite using reaction wheel and magnetic torquers. It can be observed that the magnetic torquers are producing magnetic dipoles when a strong magnetic field is absent (, which is when the satellite is in high altitude regions as can be seen in Figure 8.10). This means that the current control algorithm is not power efficient in producing torque using magnetic torquers.

8.3. Reaction wheel desaturation

The desaturation of the reaction wheels was only demonstrated using RCTs because based on the result of the detumbling simulation using magnetic torquers, the decision was made not to simulate a distinct scenario for desaturating the reaction wheels with magnetic torquers. This is due to the fact that the simulated scenario produced similar starting conditions to those required for a desaturation demonstration. The reaction wheels combined with RCTs already showed some promising results for the case of detumbling. Therefore, the desaturation of the reaction wheels was only simulated using RCTs for six different scenarios similar to the detumbling.

8.3.1. Desaturation using magnetic torquers

From the results of the detumbling of the satellite using magnetic torquers and reaction wheels, it can be observed that only 10-20% of the angular momentum of one of the reaction wheels could be decreased per orbital revolution. In the worst case, this means that the satellite must desaturate its reaction wheels for approximately 400 hours or 2 weeks to reach an acceptable level. As mentioned in the results for the detumbling of a satellite using magnetic torquers, it is therefore less optimal to incorporate magnetic torquers in the CubeSat design. The most important reason for this is twofold: firstly, a thicker radiation shield is required, and secondly, the magnetic torquers themselves add extra mass.

8.3.2. Desaturation using reaction control thrusters

The scenarios started with one reaction wheel which was completely saturated in one direction with an angular velocity of $523.6\,\mathrm{rad\,s^{-1}}$. The angular velocities of the satellite and the orientation were set to zero. Again a very low maximum propellant mass of $1.179\,\mathrm{g}$ was required to completely desaturate the reaction wheels if one reaction wheel was fully saturated. The simulation shows that the designed RCTs setup could successfully desaturate the reaction wheels.

In conclusion, to answer the research question RQ2, the design as presented in Section 8.1 can be considered as feasible to detumble the reaction wheels because the results in this section show that this RCT system design waS able to completely desaturate the reaction wheels if one reaction wheel was fully saturated.

However, nothing can be said about the total required propellant for desaturation and detumbling from the desaturation and detumbling simulations alone. For future work, it is recommended that a complete mission is simulated including expected disturbance torques to better estimate the required propellant.

Table 8.4: Propellant mass used by the reaction control thrusters for desaturation.

Scenario	Used propellant
$\omega_{w,1} = +523.6\,\mathrm{rad\,s^{-1}}$	$1.179\,\mathrm{g}$
$\omega_{w,2} = +523.6\,\mathrm{rad\,s^{-1}}$	$1.161\,\mathrm{g}$
$\omega_{w,3} = +523.6\,\mathrm{rad\,s^{-1}}$	$0.927\,\mathrm{g}$
$\omega_{w,1} = -523.6\,\mathrm{rad\,s^{-1}}$	$1.182\,\mathrm{g}$
$\omega_{w,2} = -523.6\,\mathrm{rad\,s^{-1}}$	$1.094\,\mathrm{g}$
$\omega_{w,3} = -523.6\,\mathrm{rad\,s^{-1}}$	$1.022\,\mathrm{g}$

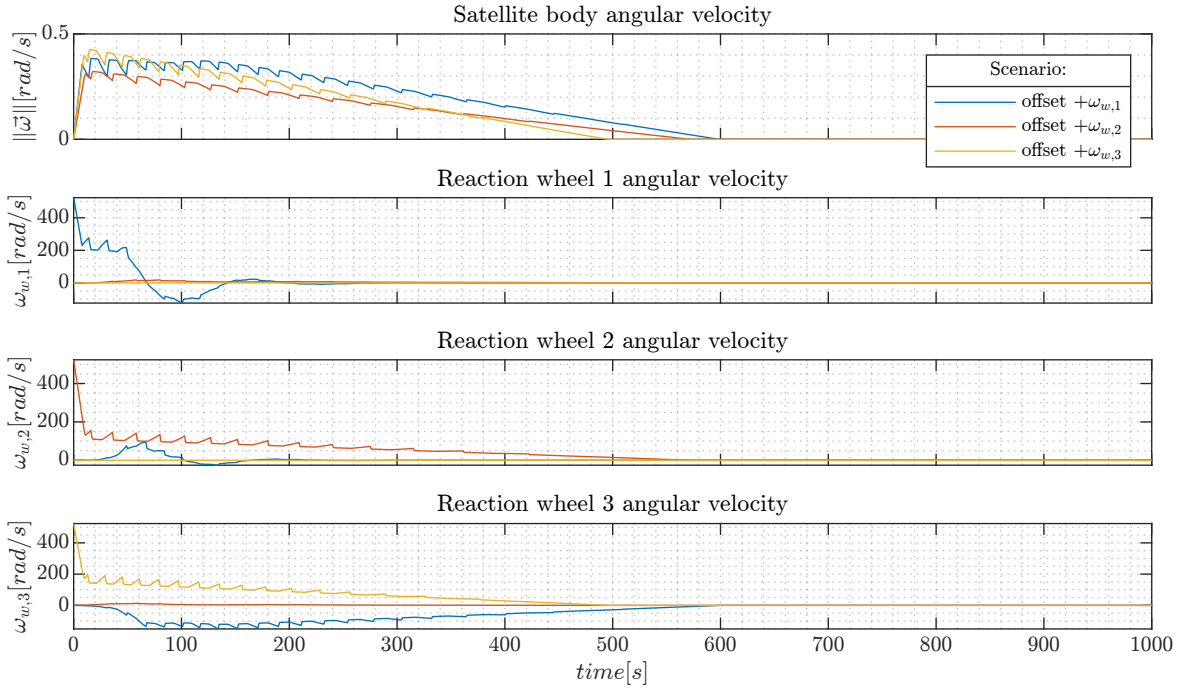

Figure 8.14: Desaturation of the satellite's reaction wheels using reaction control thrusters.

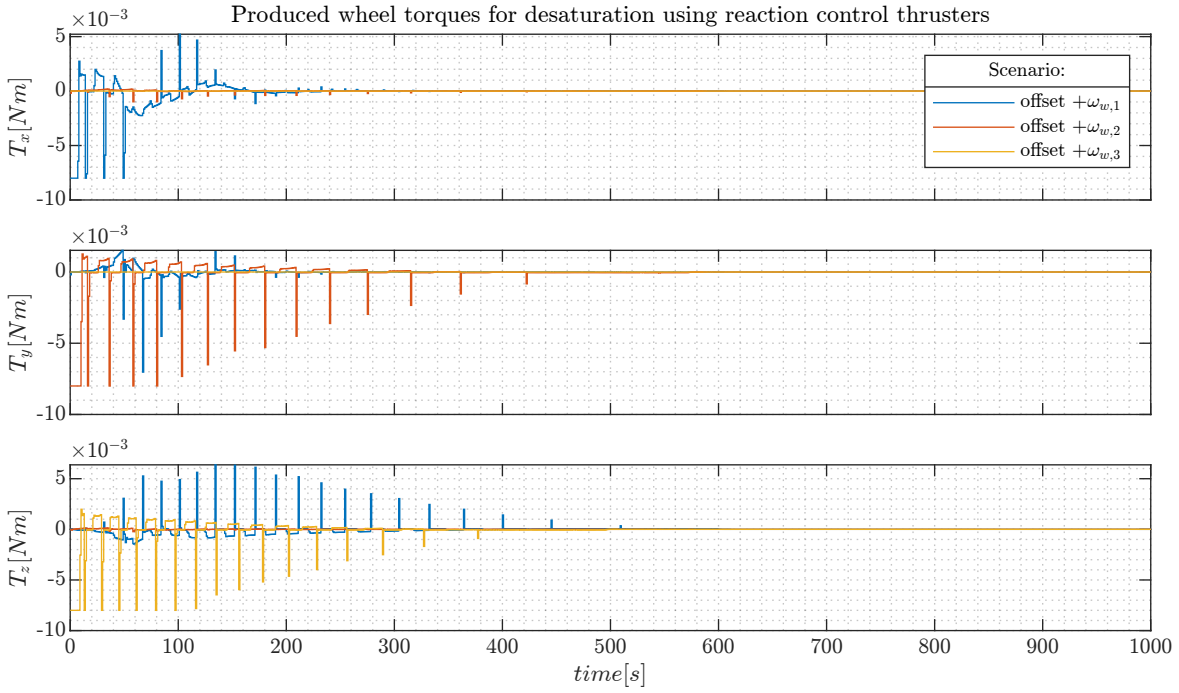

Figure 8.15: Reaction wheel torques for the desaturation of the satellite using reaction wheels and reaction control thrusters.

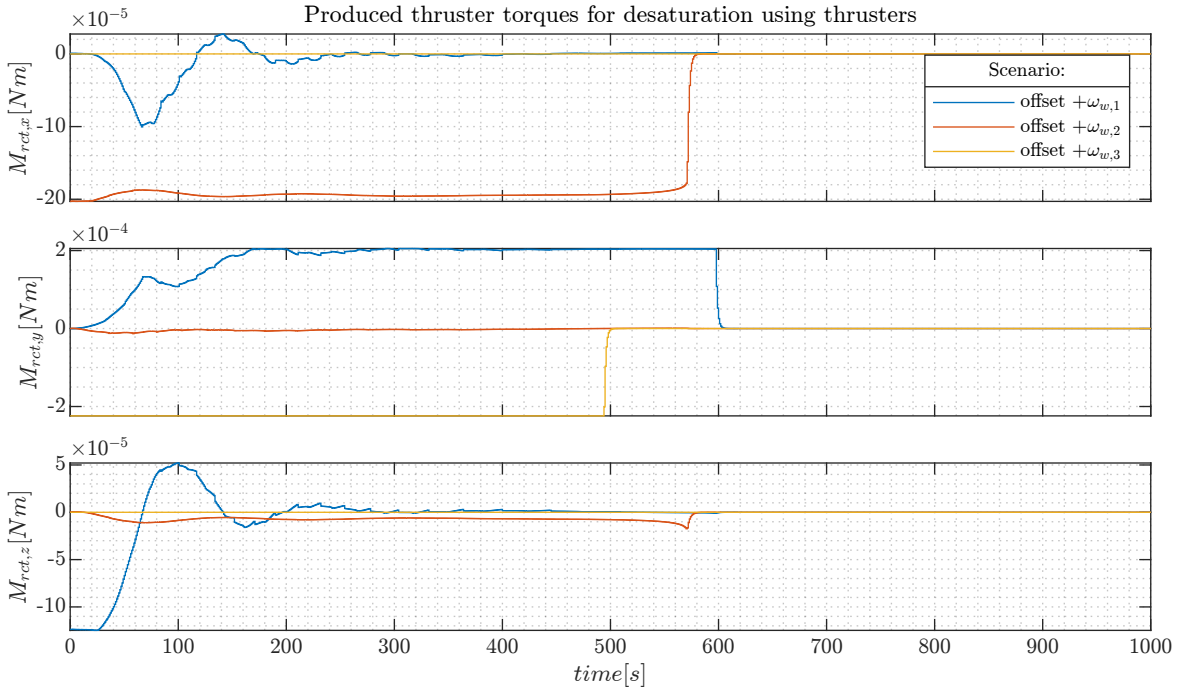

Figure 8.16: Reaction control thrusters torques for the desaturation of the satellite using reaction wheels and reaction control thrusters.

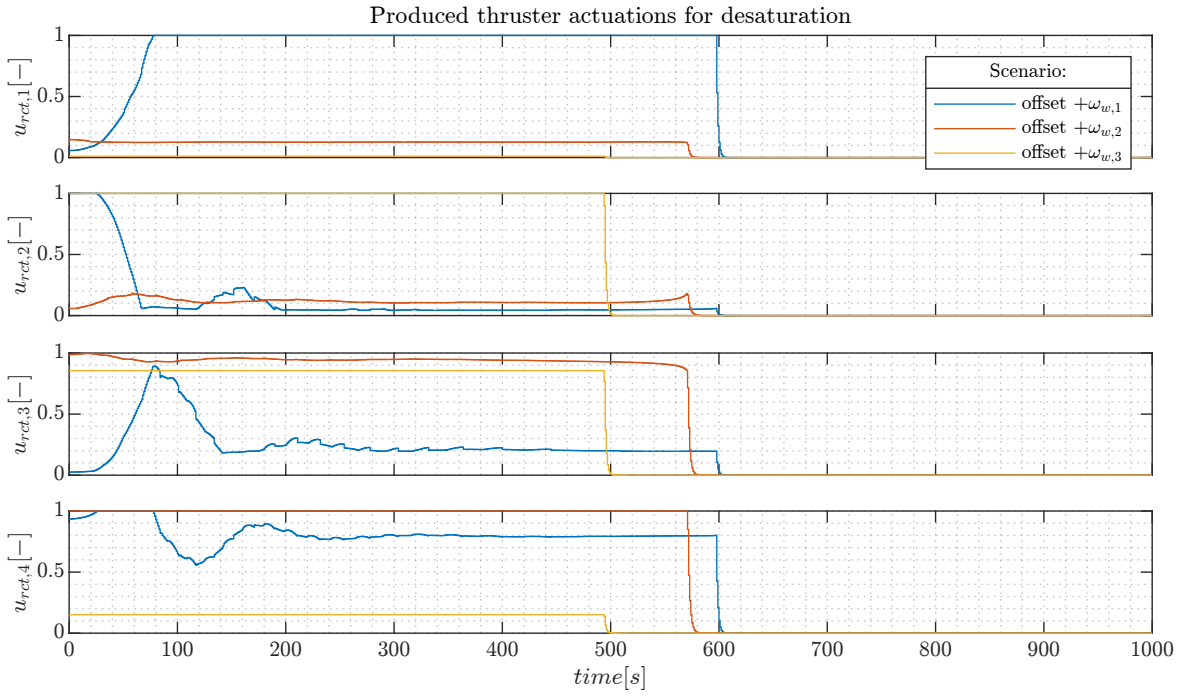

Figure 8.17: Reaction control thrusters throttle for the desaturation of the satellite using reaction wheels and reaction control thrusters.

8.4. Results for tracking the optimal thrusting direction in Earth orbit using reaction wheels and Lyapunov control

To simulate if the AOCS system is able to track the optimal heuristic thrusting law found in chapter 4 for an Earth escape trajectory, one orbit revolution was simulated. This simulation was necessary to prove that requirement MR-SC-1 can be fulfilled and the selected design was feasible for the mission as was required to answer research question RQ3.

MR-SC-1: The satellite shall be able to fly-by a near-Earth asteroid at a closest approach distance of 10,000 km within 5 years.

From chapter 7, the control algorithm selected is an LC method that only uses the reaction wheels. For the simulation, the orientation of the satellite starts aligned with the inertial reference frame with no angular velocity and no angular momenta in the reaction wheels. The Lyapunov gains were set to scalar values instead of gain matrices of $K_1 = 1 \times 10^{-3}$, $K_2 = 0.2$, and $K_3 = 0.15$. These gains were selected from tuning by hand. Figure 8.19 and Figure 8.18 show the initial stabilization actions that were obtained from the first 200 seconds of simulation. The initial corrections did not saturate the reaction wheels, which means that the maneuver was possible. From Figure 8.22 it can be observed that the satellite was able to track the optimal Earth escape thrusting direction from chapter 4 which is $\hat{v}$ or the direction of the orbital velocity. However, Figure 8.23 does show that the satellite deviated from the optimal angular velocity of the optimal thrusting direction. This might be due to precession mutation, and the change in angular momentum in the reaction wheels that are not present in the reference optimal thrusting direction's frame motion. In other words, the optimal thrusting direction's frame motion does not account for the non-linear effects that are present in the satellite attitude model.

In conclusion, the results demonstrate that the reaction wheels combined with an LC controller were able to track the optimal thrusting direction required to escape the SSGTO around Earth. This design can thus be considered feasible in the theme of research question RQ3.

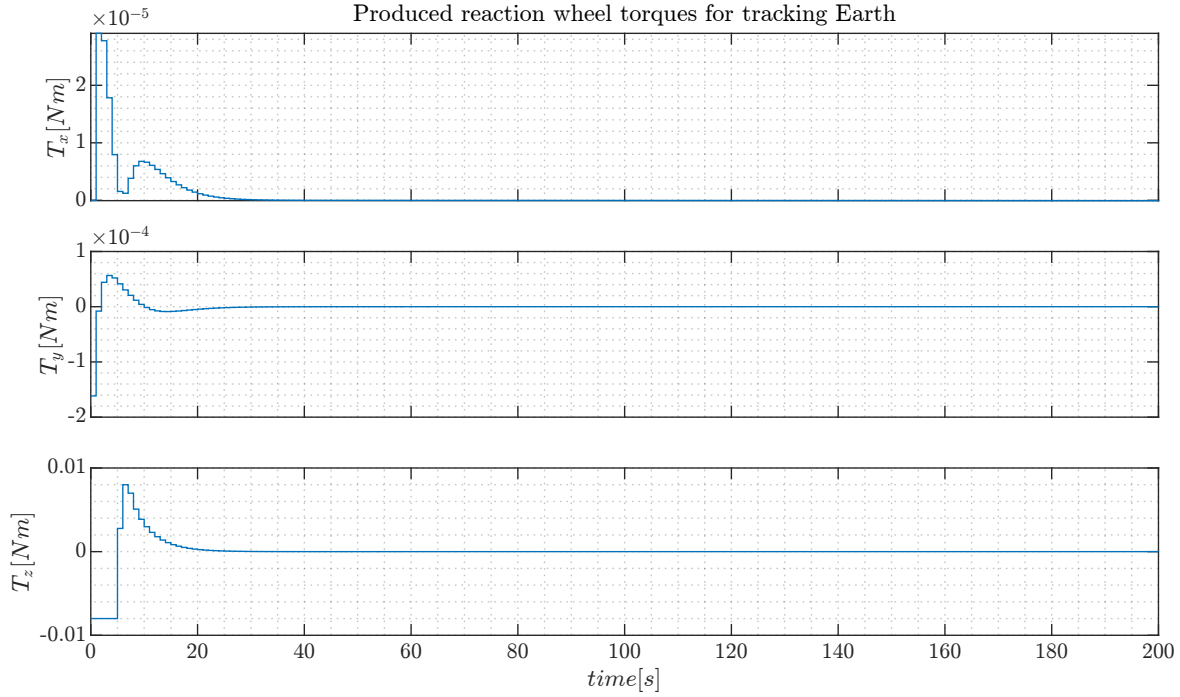

Figure 8.18: Tracking optimal Earth escape attitude reaction wheel torques for the first 200 seconds.

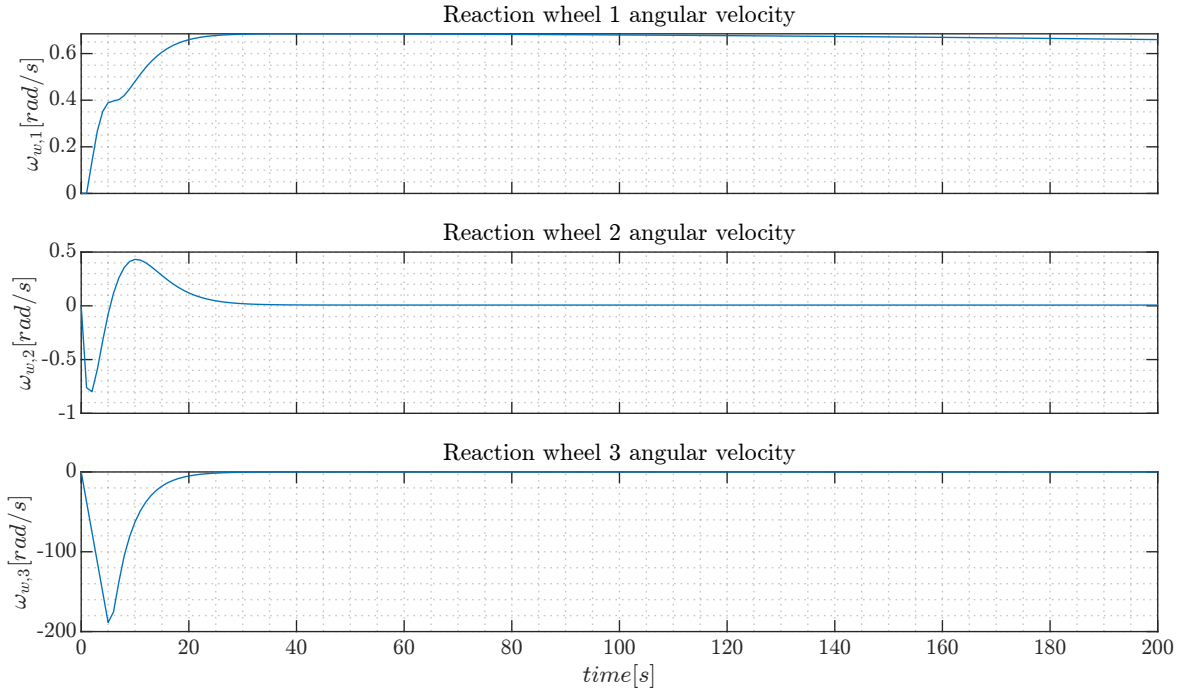

Figure 8.19: Tracking optimal Earth escape attitude reaction wheel angular velocities for the first 200 seconds.

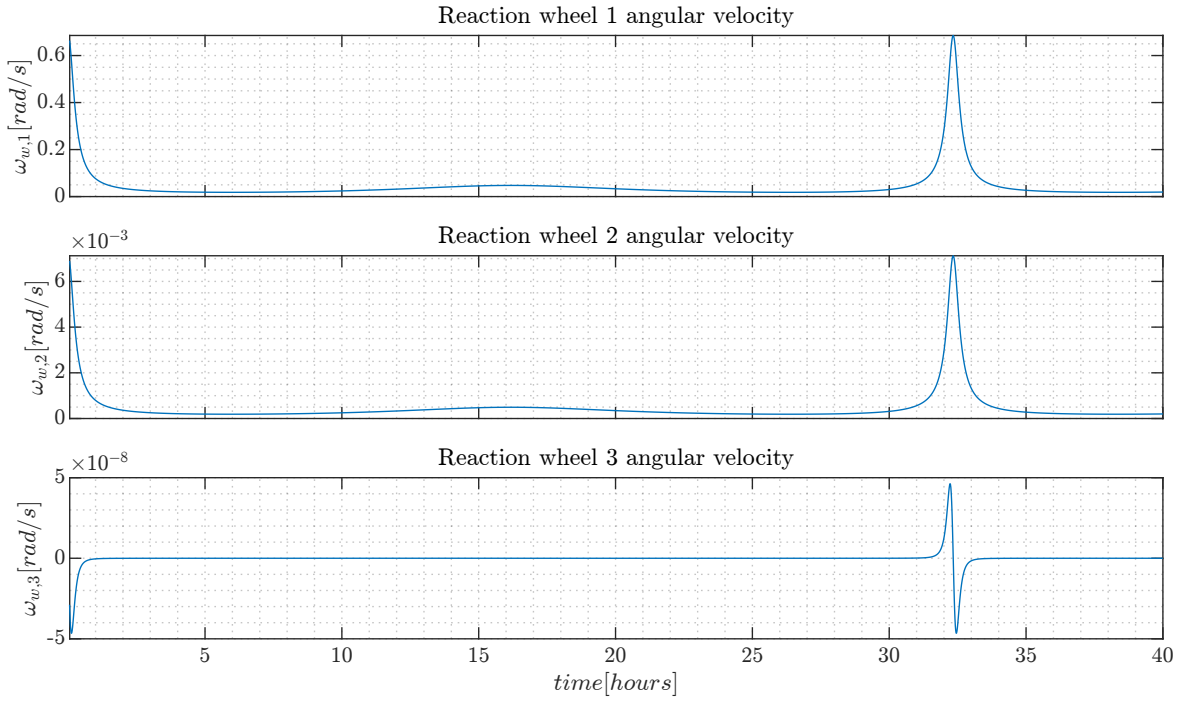

Figure 8.20: Tracking optimal Earth escape attitude reaction wheel angular velocities for one orbital revolution.

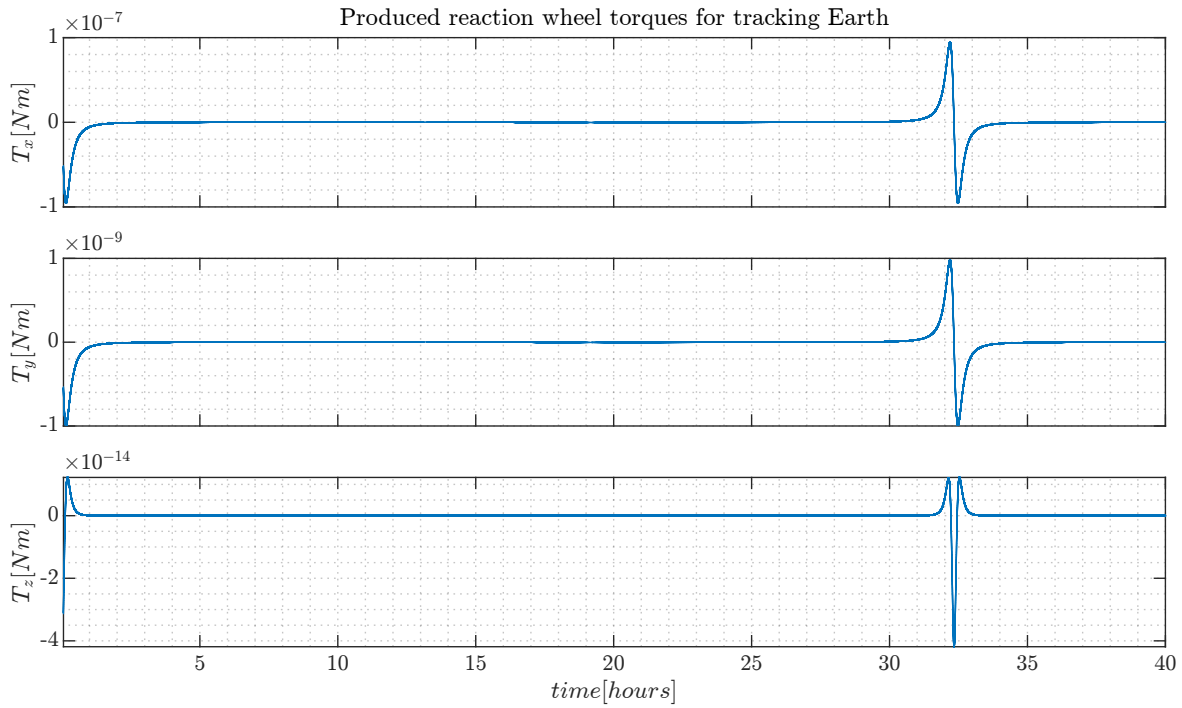

Figure 8.21: Tracking optimal Earth escape attitude reaction wheel torques for one orbital revolution.

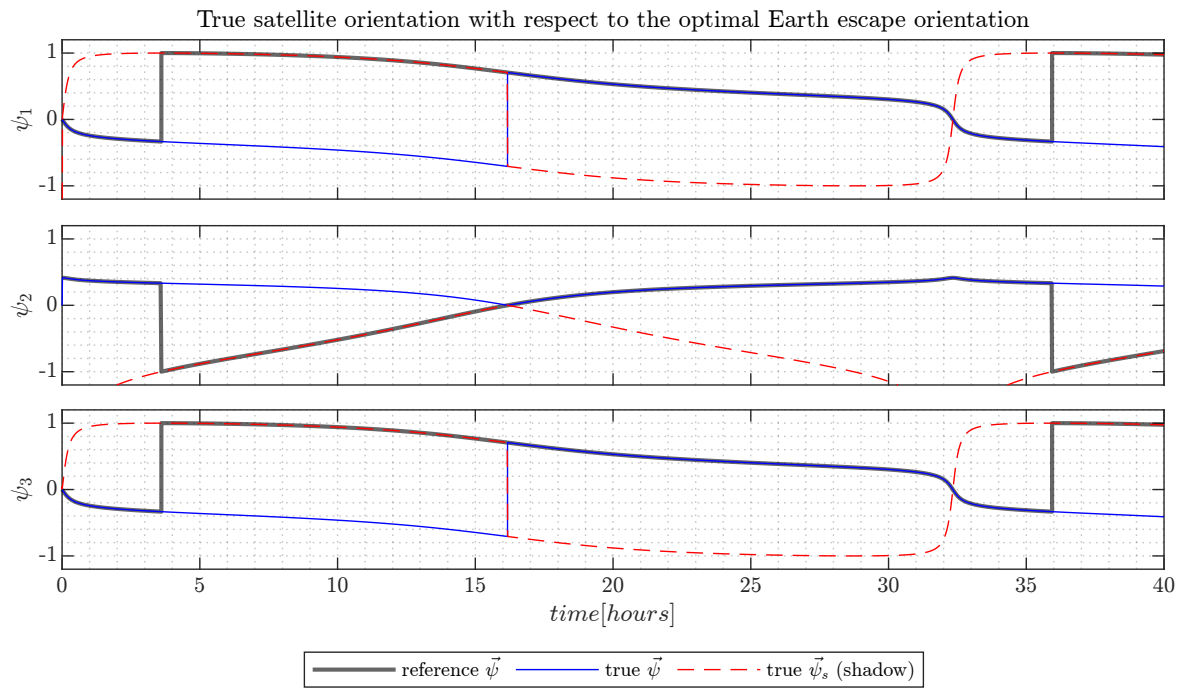

Figure 8.22: Tracking optimal Earth escape attitude orientation for one orbital revolution.

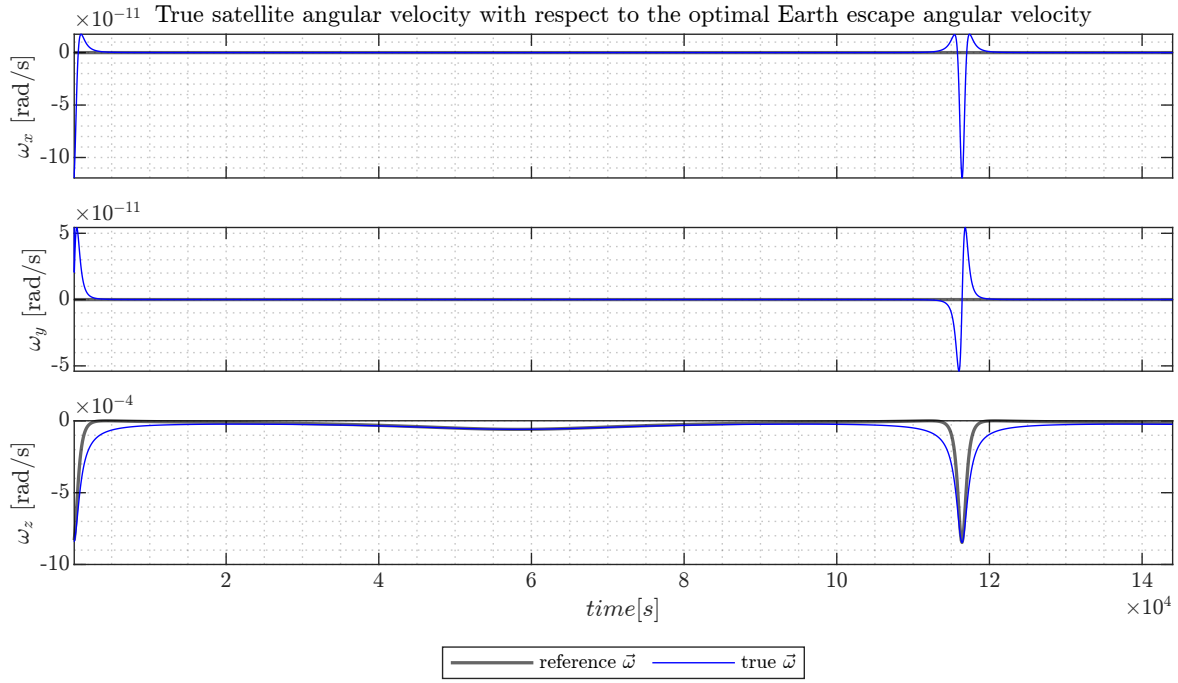

Figure 8.23: Tracking optimal Earth escape attitude angular velocity for one orbital revolution.

8.5. Result for the tracking of an asteroid using reaction wheels and Lyapunov control

To verify the requirement MR-AOCS-3 and answer research question RQ3, an LC algorithm using only the reaction wheels, as selected in chapter 7, was simulated.

MR-AOCS-3: The attitude and orbital control system shall be able to track the near-Earth asteroid at a distance of 10,000 km.

The simulation demonstrated the performance of the CubeSat for a relative velocity of $35\,\mathrm{km\,s^{-1}}$ with respect to a NEA at a closest approach distance of $10\,000\,\mathrm{km}$. The Lyapunov gains were set to scalar values instead of gain matrices of $K_1 = 1 \times 10^{-3}$, $K_2 = 0.2$, and $K_3 = 0.15$. These gains were selected from tuning by hand. For the simulation, the orientation of the satellite starts aligned with a non-rotating inertial reference frame and no residual angular momenta in the reaction wheels were present. The results show that the selected design for the asteroid tracking mission phase was able to successfully track the asteroid at a distance of $10\,000\,\mathrm{km}$ and a relative velocity of $35\,\mathrm{km\,s^{-1}}$. Furthermore, a maximal torque of only $1.5 \times 10^{-6}\,\mathrm{N\,m}$ was required to perform the maneuver. Therefore, the current design had a significant torque margin for closer approaches and higher relative velocities.

In conclusion, the asteroid tracking simulation verifies that, with this design, mission requirement MR-AOCS-3 can be met for relative velocity up to at least $35\,\mathrm{km\,s^{-1}}$. This indicates that this design can be incorporated into a feasible ACS design, which answers research question RQ3.

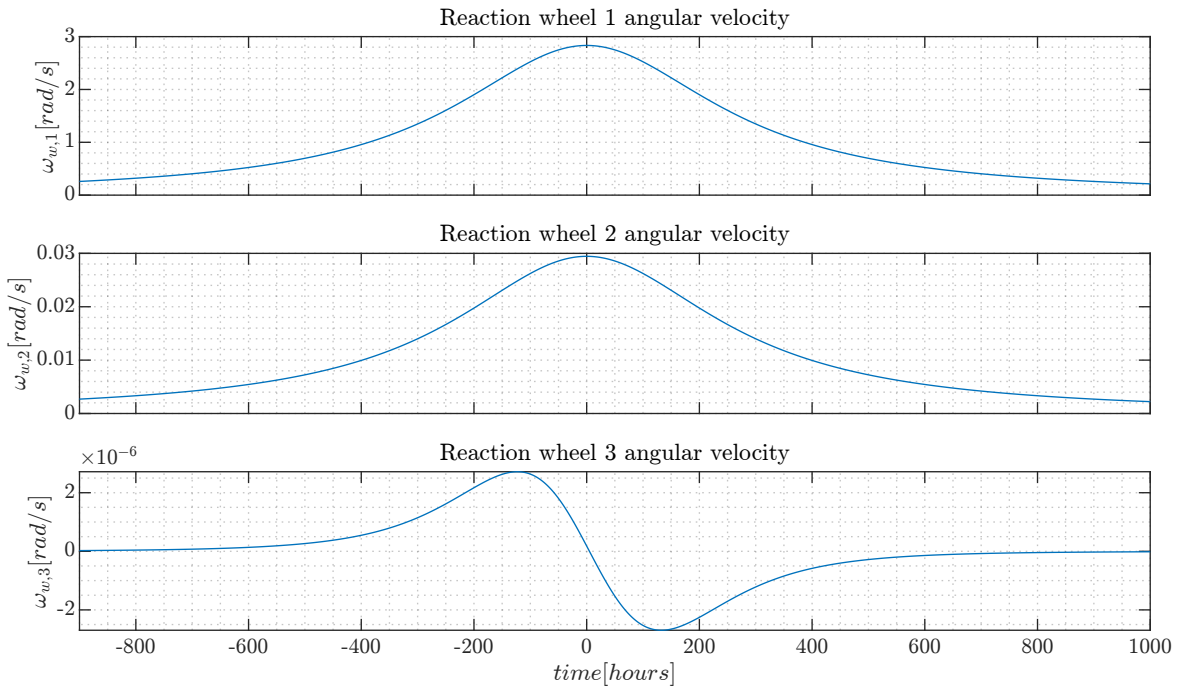

Figure 8.24: The reaction wheel angular velocities for tracking an asteroid at a distance of $10\,000$ km and a relative velocity of $35\,\mathrm{km\,s^{-1}}$.

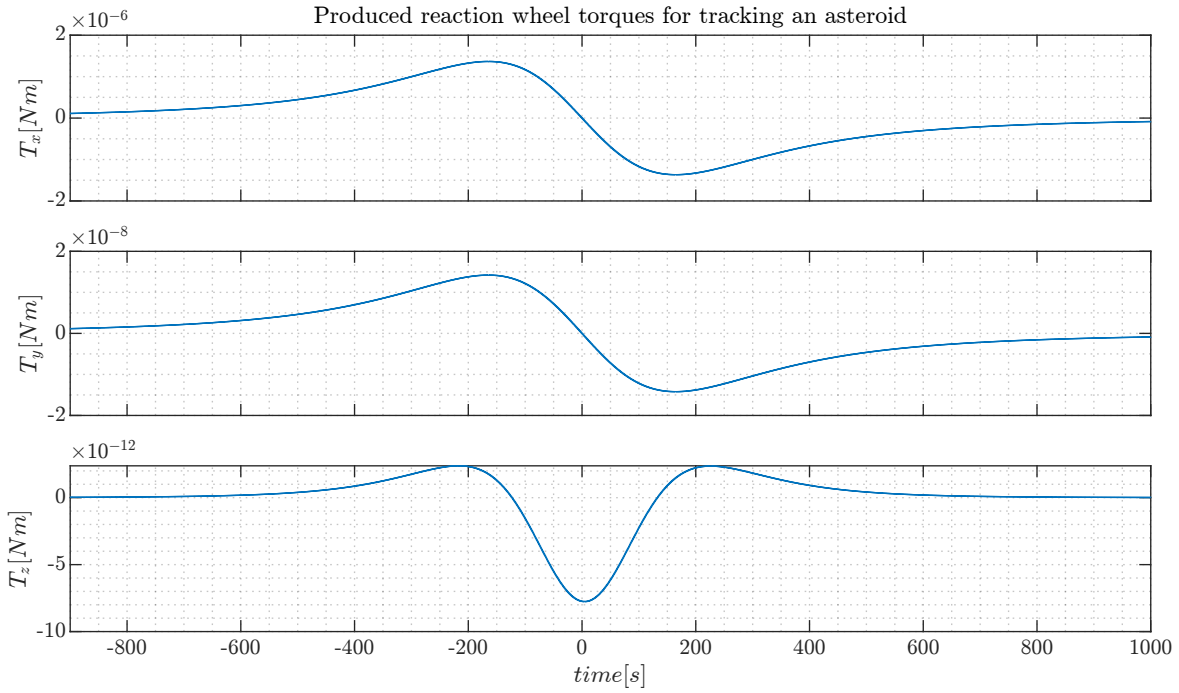

Figure 8.25: The reaction wheel torques for tracking an asteroid at a distance of $10\,000$ km and a relative velocity of $35\,\mathrm{km\,s^{-1}}$.

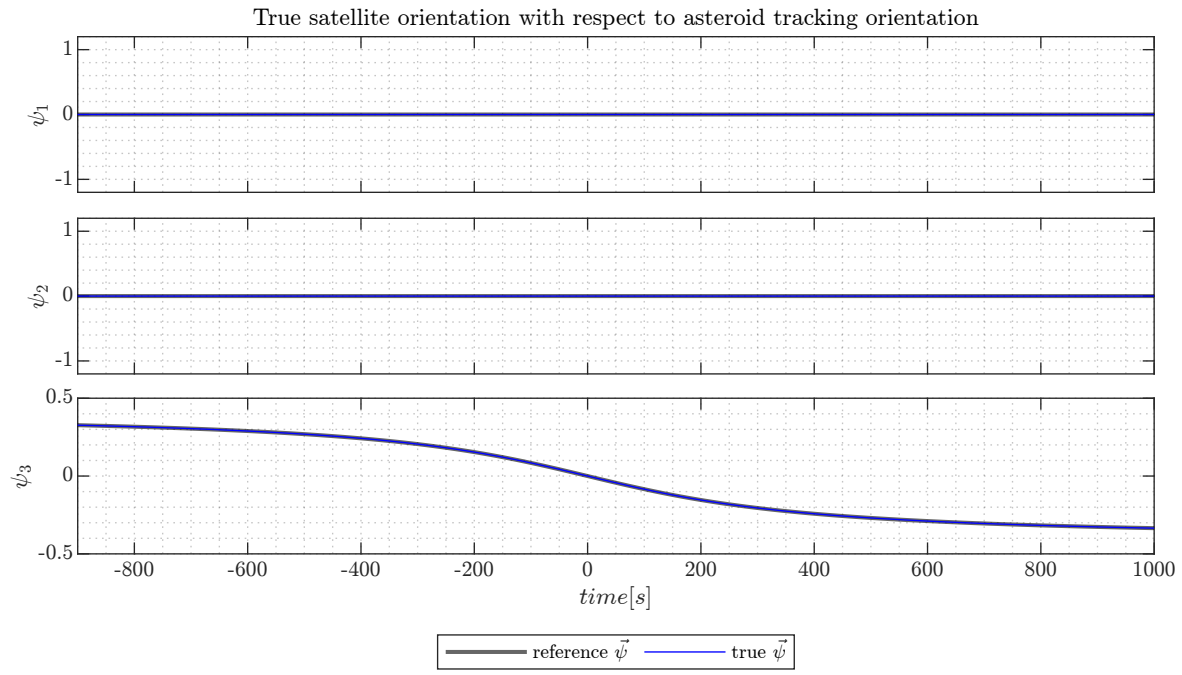

Figure 8.26: The true satellite orientation with respect to the perfect tracking orientation for an asteroid at a distance of $10\,000$ km and a relative velocity of $35\,\mathrm{km\,s^{-1}}$.

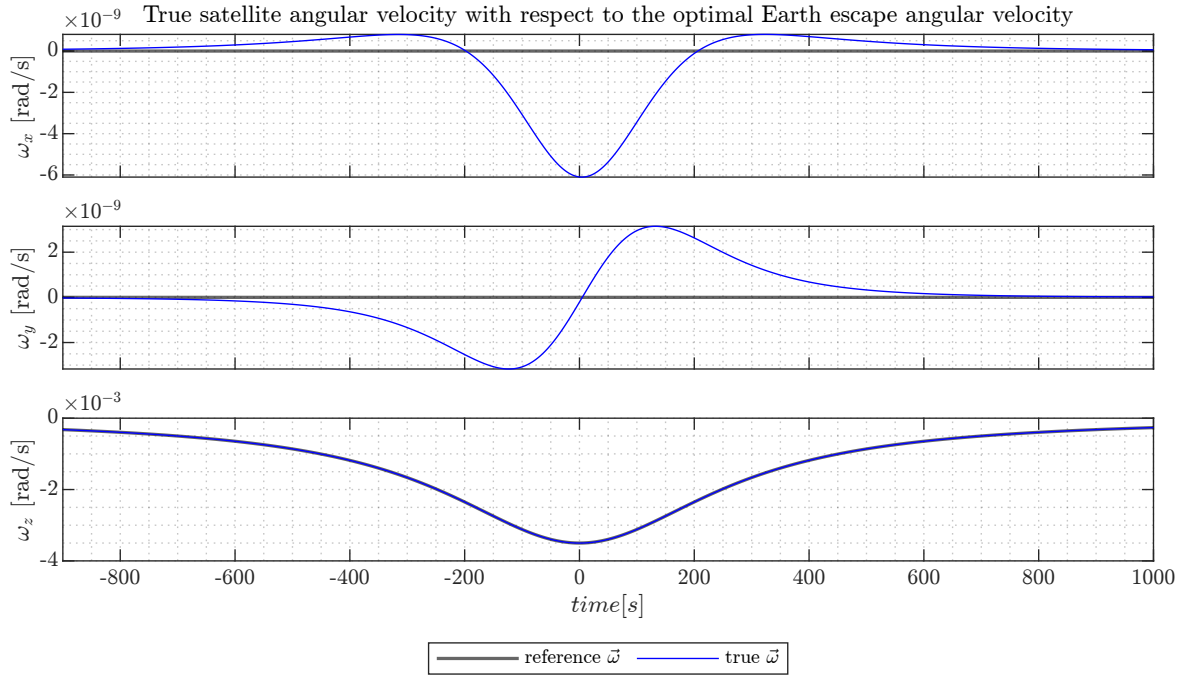

Figure 8.27: The true satellite angular velocity with respect to the perfect tracking angular velocity for an asteroid at a distance of $10\,000$ km and a relative velocity of $35\,\mathrm{km\,s^{-1}}$.

8.6. Summary

To answer the research questions RQ2, RQ2.2, and RQ3 the framework for rotational kinematics and dynamics of a satellite as presented in chapter 6 combined with the control algorithms and RCT thruster configuration optimization method as presented in chapter 7 were simulated for the selected satellite

subsystems and RCT propulsion system for desaturation and detumbling as presented in chapter 1 and chapter 2.

The first research question that is answered in this chapter is RQ2.2.

RQ2.2: What number of thrusters, their position, and direction are required to perform momentum dumping maneuvers?

From the results of the RCT thruster configuration optimization method as presented in chapter 7 it can be said that a minimum of four fixed thrusters can control every axis of rotation in both positive and negative directions at a moment in time. This then enables momentum-dumping maneuvers in every direction. The results show that for this particular CubeSat design a thruster placement at the top of the satellite in each corner was found favored to control each axis of rotation. Moreover, it avoids thrusting against the solar panels. Next, a three thrusters configuration was found to be unable to control each axis of rotation without generating unwanted angular velocities in other axes of rotation and thus found to be unfeasible. Finally, the results show that the four thrusters' directions, positions, and thrust allocations are closely related to the produced angular acceleration around the desired axis of rotation and unwanted angular acceleration in other rotation directions. The thrusters must be oriented such that a linear combination of the thrusters is able to produce pure angular accelerations along all the axes of rotation.

From the results simulation of the found RCT system of research question RQ2.2 in combination with an LQR controller for reaction wheel desaturation research question RQ2 was answered.

RQ2: What is a feasible design for a propulsion system to desaturate reaction wheels for an autonomous 6U satellite near-Earth asteroid fly-by mission starting from a super synchronous geostationary transfer orbit for 5 years?

Based on the simulation results, it can be concluded that the GOMSpace Nanoprop CGP3 propulsion system, which consists of four RCTs and an LQR controller placed on top of the CubeSat, is a feasible design for desaturating reaction wheels during the CubeSat mission. The simulation demonstrated that a maximum of 1.179 grams of propellant was required to desaturate any of the reaction wheels starting from an angular velocity magnitude of 0.524 radians per second. Moreover, these desaturation maneuvers were completed within a mere 10 minutes. Compared to magnetic torquers, which require several days to accomplish the same desaturation, the RCTs design is also deemed feasible in terms of duration.

Finally combining the selected design and their results RQ3 can be answered.

RQ3: What is a feasible design for an attitude control system including a control algorithm for an autonomous 6U satellite near-Earth asteroid fly-by mission starting from a super synchronous geostationary transfer orbit?

In chapter 1 the ClydeSpace iADCS400 with RW400 reaction wheels and MTQ400 magnetic torquers was selected in combination with the GOMSpace Nanoprop CGP3 propulsion system selected in chapter 2. These systems in combination with the selected control algorithms for the different mission phases of chapter 7 were simulated in this chapter to verify if they met the requirements specifically relevant for the ACS which are requirements MR-SC-1, MR-AOCS-2, and MR-AOCS-3.

MR-SC-1: The satellite shall be able to fly-by a near-Earth asteroid at a closest approach distance of 10,000 km within 5 years.

In chapter 7 the iADCS400's reaction wheels combined with an LC controller were selected to verify that the ACS is able to orient the satellite such that it points in the direction of the optimal thrusting law. From the results, it can be observed that this design was able to meet the rotational control part of requirement MR-SC-1 because it can steer the system in the correct direction during the Earth escape trajectory, which requires the highest torquers.

Next, during the complete fly-by trajectory, the reaction wheels must be desaturated in case of increasing angular momenta due to disturbance torques or thrust misalignment. Based on the simulation results, it can be concluded that the GOMSpace Nanoprop CGP3 propulsion system, which consists of four RCTs and an LQR controller placed on top of the CubeSat, is a feasible design for desaturating reaction wheels during the CubeSat mission.

MR-AOCS-2: The attitude and orbital control system shall be able to detumble the spacecraft after orbit injection.

For the detumbling of the satellite after orbital injection, three designs were simulated starting from tip-off rates of $0.524\,\text{rad}\,\text{s}^{-1}$. The first is a design that consists of only reaction wheels and an LQR controller. The second is a design that consists of RCTs, reaction wheels, and an LQR controller. And the third is a design that consists of proportional controlled magnetic torquers, and reaction wheels controlled by an LQR controller. From the results, it was concluded that the design that consists of only reaction wheels would fail because the reaction wheels saturate before detumbling occurs. The design that consists of RCTs and reaction wheels was able to detumble within 700 seconds using a maximum of 1.438 grams of propellant. The design that consists of magnetic torquers and reaction wheels was able to detumble but could not desaturate the reaction wheels within one orbital revolution. The results indicate that it could take a week to completely desaturate the reaction wheels. Regarding research question RQ3, the potential extra time required for complete detumbling and desaturation renders a design consisting of magnetic torquers and reaction wheels combined with an LQR controller impractical due to added mass required for a thicker radiation shield due to longer exposure to the harsh radiation environment of the SSGTO. And the added mass of magnetic torquers lead to an extra 122.5 grams. Therefore, it can be concluded that a CubeSat without magnetic torquers and extra propellant for detumbling and desaturation using RCTs would be the better solution.

MR-AOCS-3: The attitude and orbital control system shall be able to track the near-Earth asteroid at a distance of 10,000 km.

In chapter 7 the iADCS400's reaction wheels combined with an LC controller were selected to verify that the ACS is able to orient the satellite such that it points a payload in the direction of the asteroid. The asteroid tracking simulation verifies that, with this design, mission requirement MR-AOCS-3 can be met for a relative velocity up to at least $35\,\text{km}\,\text{s}^{-1}$. This indicates that this design can be incorporated into a feasible ACS design.

To conclude and answer research question RQ3, a feasible design for an ACS including a control algorithm is the iADCS400 without magnetic torquers combined with an LC controller for asteroid tracking and steering the satellite during its fly-by trajectory. And for detumbling and reaction wheel desaturation, the design incorporates the GOMSpace Nanoprop CGP3 propulsion system with four thrusters including an LQR controller.

9

Conclusion

One of the next decades' most challenging and interesting objectives is the exploration of NEAs. The main reasons for this deep interest are related to scientific exploration [1], planetary protection [2], and in situ resource utilization [3, Part 5]. For these missions, Casini, Fodde, Monna, *et al.* [1] proposes the use of autonomous CubeSats for NEA exploration missions starting from an SSGTO. The most important reason for this is threefold: firstly, autonomy decreases the costs of the mission ground segment. Secondly, the utilization of CubeSat components leads to standardization and an even further reduction in the total mission cost. And thirdly, SSGTOs are preferred for CubeSats due to their high orbital energy and commercial nature as they are often used by larger satellites which can be used as a low-cost piggyback ride. According to Casini, Fodde, Monna, *et al.* [1], one of the biggest challenges of NEA autonomous CubeSat missions is the design of the AOCS which leads to the focus of this master thesis.

Since there is a need and proven interest in NEA exploration missions using an autonomous CubeSat and one of the main challenges that have to be solved is to design an AOCS for these missions, the goal of this thesis is to design an AOCS for an autonomous 6U CubeSat NEA fly-by mission starting from an SSGTO within 5 years by simulating different combinations of COTS components. As stated in the introduction, a feasible combination for the AOCS consists of a propulsion system for interplanetary travel and reaction wheels desaturation, and an ACS consisting of reaction wheels and optionally magnetic torquers. Therefore, to fulfill the thesis goal, three main research questions are formulated in the introduction with one or two sub-research questions each. The first research question RQ1 focuses on the design of a feasible propulsion system for interplanetary travel by selecting and customizing COTS propulsion systems. The second research question RQ2 focuses on the desaturation of reaction wheels and if needed, attitude corrections. Finally, the third research question focuses on the ACS system required to perform the different critical mission phases such as detumbling, the Earth escape phase, and the tracking of a NEA at a distance of 10,000 km. In this final chapter, the thesis goal is fulfilled by combining the answers to the research questions to formulate a feasible design for an AOCS for the described mission. This then concludes the master thesis.

9.1. Propulsion system for interplanetary travel

Research question RQ1 focuses on a feasible propulsion system selection from customized COTS propulsion systems for interplanetary travel starting from SSGTO. However before, this research question can be answered RQ1.1 and RQ1.2 have to be answered first. RQ1.1 focuses on the SOTA propulsion systems that meet the requirements for an interplanetary trip to a NEA within 5 years for a 6U CubeSat. Next, RQ1.2 focuses on a practical framework to simulate a fuel-efficient trajectory to a NEA to verify if the selected propulsion systems in RQ1.1 are feasible.

RQ1.1: What state-of-the-art propulsion systems meet the requirements for a near-Earth asteroid fly-by mission?

In chapter 2 it is elaborated that in an ideal scenario, the propulsion system should have a high specific impulse, high thrust, low power consumption, low mass, and a small volume. A high specific impulse is necessary to maneuver to a distant target like a NEA with the available propellant, but a sufficient maximum thrust is required to maneuver to the destination within the 5-year constraint. However, most systems tend to have an inverse correlation between high thrust and high specific impulse. Two branches of possible solutions for an interplanetary propulsion system are identified. The first branch consists of low-thrust propulsion systems that make use of a high specific impulse. It is beneficial for the propulsion system to have a high specific impulse, as it allows for more efficient use of propellant regardless of other factors. From this branch, nine outliers of potentially feasible propulsion type groups, with an emphasis on a high thrust and high specific impulse, were selected. The second branch, namely high-thrust propulsion systems, capitalizes on the advantage of greater propellant efficiency gained by a spacecraft when using more of its propellant near the perigee. Since a high-thrust propulsion system is able to use more of its propellant close to the perigee when the orbital velocity is at its maximum, a larger change in escape velocity can be achieved with the same amount of propellant. Five propulsion systems were selected for this branch based on their high specific impulse and thrust properties: two bi-propellant systems, one mono-propellant system, and two solid propulsion systems.

From the results of the practical framework to simulate a fuel-efficient trajectory in chapter 5 it can be concluded that the selected high-thrust propulsion systems, Tethers Unlimited's HYDROS-C, Dawn Aerospace's B1, Bradford ECAPS's 22N HPGP, DSSP's CDM-1, and THiokol's STAR G4, do not gain enough propellant efficiency from firing near the perigee to be competitive for ambitious NEAs such as asteroid 2012BX34. They require at least 7.5 kg of the total mass of a 12 kg CubeSat. The interplanetary propulsion systems 22N HPGP, CDM-1, and STAR G4 are promising for the selected asteroid 2020QN1 since they only require 4.1 kg of the satellite to be allocated to the propulsion system. By considering the reduced flight time required for these high-thrust propulsion systems (less than half a year), the radiation shielding required can be greatly decreased. As a result, these systems can fall within the same total mass range as the low-thrust propulsion systems, which only require 3 to 4 kg of shielding. IIn terms of volume, high-thrust systems for asteroid 2020QN1 would require approximately 2U to 3U, and up to approximately 3U to 4U for asteroid 2012BX34, based on the propellant densities of $1.81\,\mathrm{kg\,L^{-1}}$ for LMP-103S, $2.0\,\mathrm{kg\,L^{-1}}$ for AP/HTPB, and approximately $1.8\,\mathrm{kg\,L^{-1}}$ for TP-H-3399. This is larger than the volumes required for low-thrust systems, which typically use propellants with densities that are two to five times higher than those used by high-thrust systems, and only require 2U to 3U.

It can be concluded that for an ambitious NEA fly-by mission, such as a fly-by mission to asteroid 2012BX34, low-thrust propulsion systems with a high specific impulse are currently the better option. However, for low-thrust high-specific impulse propulsion systems, it can be inferred that Enpulsion's IFM

Nano and CU Aerospace's FPPT-1.6 propulsion systems are not suitable for a fly-by mission to asteroid 2012BX34 due to the fact that they will exceed the maximum mission duration of 5 years. However, for specific targets such as asteroids 2020QN1 and 163693, the IFM Nano system would be the preferred choice. Additionally, Safran's PPS-X00, EDB Fakel's SPT-70M, and JPL's MaSMi are also not viable options as they demand an excessive total propulsion system mass for a 12 kg 6U CubeSat. In most cases, over half of the CubeSat's mass has to be allocated to the interplanetary propulsion system, which exceeds the available mass. However, ThrustMe's NPT30-I2 RF, Alameda Applied Sciences Corp.'s Metal Plasma Thruster, Busek's BIT-3 RF, and Enpulsion's IFM Micro can be considered for a fly-by mission to a NEA based on their compliance with the 5-year maximum mission duration and least required propulsion system mass. These systems have total propulsion system masses ranging from 4 to 6 kilograms, making them suitable for a 12 kg 6U CubeSat. It can be concluded that without ESA mass margins, these systems are able to meet the requirements. Considering all the results, ThrustMe's NPT30-I2 RF gridded-ion thruster is the system with the smallest total mass for the majority of considered targets and a closest approach distance of under 10,000 km within a 5-year period.

RQ1.2: What is a practical framework to simulate a fuel-efficient trajectory to a near-Earth asteroid within 5 years?

A practical framework to simulate a fuel-efficient trajectory to a NEA within 5 years starting from an SSGTO consists of two main parts. An astrodynamics model and an optimal control approach. In chapter 3 it is concluded that an astrodynamics model split up into two parts, an Earth escape trajectory and an interplanetary cruise is most practical. It separates the Earth escape trajectory, which is a many-revolution problem, from the interplanetary cruise which is considered to have relatively low orbital revolutions. This enables the selection of the most suitable astrodynamics models for each mission phase.

For the Earth escape trajectory a geocentric non-rotating reference frame combined with SC is considered most practical because SC is considered to be more stable for numerical integration which is required for a many-revolution problem. A geocentric non-rotating reference frame is considered the better option because it leads to the simplest kinematics compared to topocentric frames or geocentric rotating frames. In order to verify if a propulsion system can get a satellite from SSGTO to a NEA only perturbations with a magnitude of at least 1% of the Earth's gravitational attraction are included. From the magnitudes of the different perturbing forces as given in Wakker [36] can be concluded that only atmospheric drag and the Earth's gravitational J_2 zonal harmonic effect must be included.

For the interplanetary trajectory, which is considered to be a few orbital revolutions problem, it is concluded that CSV provides the simplest mathematical expressions and enough numerical integration stability. The reference frame for this mission phase does not have a particular preference. However, to use NASA's SPICE toolbox the heliocentric 'ECLIPJ2000' reference frame can be considered in combination with a time definition in epochs or seconds past J2000. No perturbing forces are included in the interplanetary trajectory. Only the Sun, assumed to be at the barycenter, is included in the interplanetary trajectory model. This is done because perturbing forces and other complexities made the selected optimal control approach not converge. Furthermore, since the goal of the practical framework is to prove the feasibility which leads to a propellant mass estimate and an approximate mission duration, this is acceptable.

In chapter 4 two optimal control approaches are described that are combined with the astrodynamics model, resulting in a practical framework to simulate both low-thrust and high-thrust propulsion systems. A COV-based single-shooting indirect method to optimize low-thrust fly-by trajectories to NEAs

is proposed and demonstrated in the results. This approach combines PSO and Levenberg-Marquardt optimization techniques to determine a fuel-efficient trajectory. An indirect optimal control method is practical to compare different propulsion systems because it rewrites the problem to a TPBVP which guarantees that a fuel-efficient trajectory is found if the boundary conditions are met. This makes it ideal for comparison because it eliminates the factor that one system converged to a sub-optimal solution.

In addition, a second approach for high-thrust trajectories is described that involves a single-shooting TPBVP. This strategy minimizes the required initial escape velocity from Earth to the NEA and the closest approach distance to the target asteroid, making it suitable for high-thrust systems.

Both approaches are patched to an Earth escape trajectory starting at the perigee of the SSGTO that utilizes a full-throttle heuristic thrusting law that is always fired in the direction of the satellite's orbital velocity. For high-thrust systems that can be restarted, only a region near the perigee is used for thrusting because it maximizes the efficiency of the propellant. The key difference is that the low-thrust trajectory has a final Earth escape condition that leads to an Earth escape velocity of zero and the high-thrust trajectory stops when the Earth escape velocity matches the found required escape velocity to fly by the NEA.

From the results in chapter 5 it can be concluded that the practical framework as presented in chapter 3 and chapter 4 leads to a trajectory that meets the requirements for a NEA fly-by mission. For future mission designs, this practical framework can be used as a preliminary design tool to estimate the required propellant mass and mission duration for a selected propulsion system, total satellite mass, fly-by target, and starting orbit. This enables researchers and designers to make fast decisions without the need for a computer cluster. For future work, the practical framework can be changed to incorporate gravity assists as well as dual propulsion systems that make use of both the efficiency gain a propulsion system gets from firing near the perigee during Earth escape and a low-thrust, high-specific impulse propulsion system to fly by a target after Earth escape. Furthermore, a practical framework to simulate a fuel-efficient rendezvous mission can be made by changing the boundary conditions of this framework. This then enables researchers and designers to also design a propulsion system for these missions without the need for a computer cluster. The practical framework presented in this work is focused on designing trajectories for a single NEA target. In future work, researchers could expand the framework to consider trajectories to multiple targets, or to optimize trajectories that visit multiple targets. This would enable the design of more complex and versatile missions. Finally, the practical framework presented in this work is optimized for fuel efficiency, but it may not necessarily be a robust or resilient design. In future work, researchers could explore how to optimize trajectories for factors such as safety, reliability, or redundancy, in addition to fuel efficiency.

RQ1: What is a feasible design for a propulsion system for interplanetary travel to perform an autonomous 6U satellite near-Earth asteroid fly-by mission starting from a super synchronous geostationary transfer orbit within 5 years?

From the feasible propulsion systems of research question RQ1.1, the system that required the least mass and volume for asteroid 2012BX34, ThrustMe's NPT30-I2 RF, was simulated in more detail. From the results, an adaptation of ThrustMe's NPT30-I2 RF gridded ion propulsion system including 4.810 kg of solid iodine propellant with a volume of 0.983U is a feasible design for a propulsion system for interplanetary travel to perform an autonomous 6U satellite fly-by mission to an ambitious NEA target such as asteroid 2012BX34 starting from an SSGTO within 5 years. The total mass and volume excluding margins of the CubeSat are 5.527U and 13.041 kg. This means the propulsion system exceeds the required mass of 12 kg. However, if the 12 kg requirement for a 6U CubeSat is considered to be

a guideline for CubeSat missions that depends on the dispenser that ejects the satellite into its orbit, then larger masses can occasionally be considered by a designer on a mission-specific basis. Apart from the mass requirements, this interplanetary propulsion system meets the mission requirements as presented in the introduction and meets additional ESA margin philosophy for propulsion system verification simulations. This conclusion means that these CubeSat missions are a possibility and do not necessarily require a launch vehicle that brings these satellites into a heliocentric orbit. A deep space mission for NEAs is possible for a 6U satellite starting from SSGTO.

9.2. Propulsion system for reaction wheel desaturation

Research question RQ2 focuses on a feasible propulsion system design for the desaturation of the onboard reaction wheels. Before a design can be made first research questions RQ2.1 and RQ2.2 have to be answered. RQ2.1 focuses on the current SOTA for micro-propulsion systems that are able to perform reaction wheel desaturation and possibly other attitude control maneuvers. RQ2.2 then focuses on the required number of thrusters, their position, direction, and allocations to desaturate the reaction wheels. In order to verify the design of RQ2.2 a framework to simulate the attitude of the CubeSat. This framework is formulated when answering research question RQ3.1.

RQ2.1: What state-of-the-art propulsion systems meet the requirements for the desaturation of reaction wheels for a CubeSat near-Earth asteroid fly-by mission?

There are a couple of options to generate a torque to counteract the momentum dumping of the reaction wheels which are: Thrust vectoring the main propulsion system such that the thrust misalignment with the satellite's center of mass creates a torque, actuating multiple main propulsion modules in a combination that the force imbalance in the center of mass leads to torque, and using a secondary propulsion system of multiple thrusters purely for attitude control. Thrust vectoring is discarded as an option because it is considered outside of the thesis scope, using multiple main thrusters is also discarded because there is not enough volume to fit enough main thrusters to also control the three axes of rotation. This leaves the thesis with only one possible solution which is the use of a secondary propulsion system purely for the rotational actions.

An optimal desaturation propulsion system is low-mass, propellant efficient, low-volume, low-power, and has a low minimum impulse bit. Additionally, the thrusters must be compact and simple in design to allow for placement in various positions and orientations on the CubeSat. For the RCT system, GomSpace Nanoprop CGP3 and VACCO the end-mounted standard MiPS 0.44U are selected as possible options for the desaturation of the reaction wheels because they have the greatest impulse-to-total mass ratio. For impulse requirements in the range of 50-150 Ns, the Nanoprop CGP3 is the better option of the two. Above 150 Ns MiPS 0.44U can be used. Both these systems do not have the downside of using cold/hot gas propulsion which is that the thrust profile is decreasing over time because their propellants are stored as liquids. The pressure of the propellants comes from the vapor pressure of these propellants which means the pressure is not decreasing as long as there is still propellant in the liquid form available in the tank. Furthermore, in contrast to other systems, cold and warm gas systems present a simple and effective solution. These systems have low dry mass and volume, making precise orientation and placement possible. Their simplicity allows for ease of control and their thruster heads can be placed in various positions and orientations on the CubeSat [4]. An alternative approach involves utilizing the interplanetary propulsion system's propellant for the desaturation of reaction wheels. However, for low-thrust interplanetary propulsion systems, this approach is not deemed to be competitive. RCTs utilizing indium, iodine, or xenon warm gas are expected to have specific impulses ranging from

10 to 30 seconds (as demonstrated by the I2T5 Cold Iodine Thruster and the MEPSI Xenon cold gas thruster in CANX-2). Although such a system eliminates the need for an additional propellant storage tank, the low specific impulse diminishes its overall benefit. To conclude, depending on the required total impulse GomSpace Nanoprop CGP3 and VACCO the end-mounted standard MiPS 0.44U are the better options that are currently available for the described mission.

RQ2.2: What number of thrusters, their position, and direction are required to perform momentum dumping maneuvers?

In Biggs and Fournier [46] the minimal required number of fixed thrusters that can instantaneously control every axis of rotation in both directions is argued to be four. The results in this thesis show that for three fixed thrusters no solution could be found that controls every axis of rotation independently which strengthens this theory. This thesis presents a fixed thruster placement optimization method to solve the thruster configuration optimization problem to maximize the angular accelerations around every axis of rotation while generating minimal disturbances around other axes of rotation. This optimization method can be applied to any cuboid satellite geometry, such as a CubeSat, and inertia by using a super-ellipsoid approximation of the satellite's surface. This way a thruster can be parameterized by a longitude, co-latitude, and two thrust angles relative to the satellite surface. The thruster allocations for each axis of rotation are also optimized together with the thruster placement to find a complete solution for both the control allocation, thruster position, and direction for all four RCTs. This model however does lack the incorporation of the RCTs thruster head mass in the inertia calculation of the CubeSat and assumes that all the mass is inside of the selected secondary propulsion system, the GOMSpace NanoProp CGP3.

From the results, it can be seen that four thrusters placed at the top of the 6U CubeSat are a possible feasible solution. Also, the solar panels do not interfere with the placed thrusters. This then answers research question RQ2.2.

To improve the formulation of the optimal thruster configuration problem, future work could consider incorporating penalties for thrusting near sensitive areas such as sensors or through external solar panels. This would ensure that the chosen thruster configuration not only meets performance requirements but also minimizes potential damage or interference with other subsystems. This could be done through the use of additional constraints or objectives in the optimization problem. Additionally, future work could explore the use of more advanced optimization techniques such as multi-objective optimization or machine learning algorithms to further improve the efficiency and effectiveness of the optimization process. Another suggestion for future work is to search for a Pareto front that includes multiple sets of solutions instead of just a single solution. By doing so, a designer can choose a solution from the Pareto front that may be less optimal but has a more favorable outcome. This approach allows for a more flexible and personalized design process, which can lead to better mission success.

RQ2: What is a feasible design for a propulsion system to desaturate reaction wheels for an autonomous 6U satellite near-Earth asteroid fly-by mission starting from a super synchronous geostationary transfer orbit for 5 years?

Combining the found solution for the optimal RCTs configuration with the selected secondary propulsion system for desaturation, the GOMSpace NanoProp CGP3, RQ2 can be answered.

Based on the simulation results of the framework developed to answer research question RQ3, it can be concluded that the GOMSpace Nanoprop CGP3 propulsion system, consisting of four RCTs and an LQR controller placed on top of the CubeSat, is a feasible design for desaturating reaction

wheels during the CubeSat mission. The simulation demonstrated that a maximum of 1.179 grams of propellant was required to desaturate any of the reaction wheels starting from an angular velocity magnitude of 0.524 radians per second. Moreover, these desaturation maneuvers were completed within a mere 10 minutes.

9.3. Attitude control system design including control algorithm

The final and third research question RQ3 focuses on the attitude determination and control system including a control algorithm to detumble, track the asteroid, and correct the orientation of the satellite. Before this research question can be answered a framework to simulate the different critical mission phases must be formulated. This is done by answering research question RQ3.1.

RQ3.1: What is a practical framework to simulate the attitude of a CubeSat?

In chapter 6, the rotational dynamics in a non-rotating reference frame are described in MRPs. MRPs are selected because they reduce the number of parameters required to describe a rotation to only three parameters whereas quaternions have four and direction cosine rotations even have 9 parameters to describe a single rotation. Euler angles and RPs also require three parameters to describe a single rotation. The downside of using Euler or RPs is that they have singularities for some angles whereas direction cosine rotations and quaternions do not have singularities for any rotation. MRPs also have singularities but these can be mitigated by switching to the shadow component of the MRPs when the norm of the MRP or shadow MRP exceeds 1. The shadow of an MRP describes the same rotation but in the opposite direction.

The choice of the reference frame and rotational parameterization in MRPs are further used in combination with rigid body dynamics to simulate the attitude of the satellite for different scenarios that demonstrate the feasibility of the RCT system and ACS. Rigid body dynamics are considered sufficient to demonstrate the capabilities of the ACS.

RQ3: What is a feasible design for an attitude control system including a control algorithm for an autonomous 6U satellite near-Earth asteroid fly-by mission starting from a super synchronous geostationary transfer orbit?

To formulate a feasible design for an ACS including control algorithms and the available RCT system for desaturation, four mission operations are simulated. Detumbling, desaturation of reaction wheels as can be seen in the answer to RQ2, tracking the optimal thrusting direction in Earth orbit, and tracking the asteroid during the scientific acquisition phase. For the ACS system, the iADCS400 from ClydeSpace is selected because it is designed for a 6U CubeSat of approximately 12 kg. For detumbling, three designs are tested. Namely, detumbling using only reaction wheels, using the iADCS400's magnetic torquers and reaction wheels, and using RCTs and reaction wheels. All of these systems use an LQR controller because it prioritizes performance over stability and can handle non-linear systems such as the attitude of the satellite.

The results show that detumbling using only reaction wheels is not possible because the wheels saturate before detumbling occurs. Detumbling using magnetic torquers is possible, but that leaves the reaction wheels with a residual angular momentum. For the desaturation of reaction wheels, magnetic torquers do not pose a valuable option because they require weeks to desaturate the reaction wheels, add extra mass, and only work in low altitudes which do not occur most of the time in SSGTO. Finally, detumbling using RCTs and reaction wheels is a feasible solution. Only 2.9% of the 50 grams

of available propellant of the GOMSpace Nanoprop CGP3 is required to detumble the satellite and desaturate the reaction wheels. RCTs and reaction wheels combined with an LQR controller are therefore considered feasible for detumbling.

For the tracking of the optimal thrusting direction in Earth orbit, a system consisting of only reaction wheels combined with an LC controller is simulated. The results show that the reaction wheels combined with an LC controller are able to track the optimal thrusting direction required to escape the SSGTO around Earth. This design can thus be considered feasible.

For the tracking of the asteroid during scientific acquisition, a system consisting of only reaction wheels combined with an LC controller is simulated. The asteroid tracking simulation verifies that the design is able to track an asteroid at a closest approach distance of $10\,000$ km and for a relative velocity up to at least $35\,\mathrm{km\,s^{-1}}$. This shows that this design can be incorporated into a feasible ACS design.

9.4. A feasible design for an attitude and orbital control system

Combining the answers found for all the research questions, an AOCS system design can be formulated. The goal of the thesis is to design an AOCS for an autonomous 6U satellite NEA fly-by mission starting from an SSGTO by simulating different combinations of COTS components. As mentioned in the introduction, a feasible combination is a combination of a propulsion system for interplanetary travel, desaturation of reaction wheels and orbital corrections, and an ACS. For interplanetary travel, a customized ThrustMe NPT30-I2 including 4.850 kilograms of iodine is considered feasible because it meets the requirements and extra ESA mass margins for a propulsion system verification simulation. For reaction wheel desaturation and detumbling, the GOMSpace Nanoprop CGP3 in combination with the found RCT configuration of RQ2 and an LQR controller is considered a feasible option because it is able to detumble the CubeSat and desaturate the reaction wheels using 2% - 3% of propellant. And it is assumed that the total impulse of the perturbing torques does not exceed the total impulse of the RCT propulsion system. Finally from the answer to research question RQ3, ClydeSpace's iADCS400 in combination with an LC controller can be considered a feasible option for the tracking of the optimal thrusting law in Earth orbit and the NEA during scientific acquisition. The goal of this master's thesis is accomplished by creating a final design for an AOCS that can carry out an autonomous 6U satellite NEA fly-by mission starting from an SSGTO within 5 years, achieved by merging all the subsystem designs. This AOCS design can be considered a starting point for the standardization of these systems in future missions.

For future research, it is recommended to investigate the possibility of thrust vectoring for CubeSats to both desaturate the reaction wheels and travel to a NEA simultaneously. Secondly, the influence of the total mission duration on the TID should be further investigated for these missions because it directly relates to the required thickness of the radiation shield which adds a significant mass to the satellite. Linking the propulsion system design for the interplanetary trajectory to the radiation shield mass can lead to more optimal designs. Thirdly, this thesis found that high-thrust systems were less competitive for the selected ambitious NEA targets, even with the propellant efficiency gain from using most of the propellant near the perigee. However, a viable alternative could be a dual propulsion system that combines a solid propulsion system utilizing the propellant efficiency gained from thrusting near the perigee and reducing mission time, with an electric propulsion system that handles the rest of the interplanetary trajectory. This approach can reduce mission duration significantly and compensate for the imprecise nature of solid propulsion with the precision of electrical propulsion.

References

[1] S. Casini, I. Fodde, B. Monna, A. Cervone, and E. Gill, "Novel 3U stand-alone cubesat architecture for autonomous near earth asteroid fly-by," *Aerospace*, vol. 8, no. 1, pp. 1–28, 2021, ISSN: 22264310. DOI: 10.3390/aerospace8010009.

[2] V. Reddy, M. S. Kelley, D. Farnocchia, *et al.*, "Near-Earth asteroid 2012 TC4 observing campaign: Results from a global planetary defense exercise," *Icarus*, vol. 326, no. February, pp. 133–150, 2019, ISSN: 10902643. DOI: 10.1016/j.icarus.2019.02.018. [Online]. Available: https://doi.org/10.1016/j.icarus.2019.02.018.

[3] P. Michel, F. E. DeMeo, W. F. Bottke, and R. Dotson, *Asteroids IV*. Tucson, AZ, USA: University of Arizona Press, 2015, ISBN: 9780816532131.

[4] NASA, "State - of - the - Art Small Spacecraft Technology," *NASA Technical Report*, no. October, NASA/TP–2020–5 008 734, 2021. [Online]. Available: https://www.nasa.gov/sites/default/files/atoms/files/soa_2021_1.pdf.

[5] S. Casini, A. Cervone, B. Monna, and P. Visser, "LINE-OF-SIGHT NAVIGATION OBSERVABILITY ANALYSIS FOR NEAR-EARTH ASTEROIDS EXPLORATION WITH CUBESAT," *73rd International Astronautical Congress*, 2022. [Online]. Available: https://iafastro.directory/iac/archive/browse/IAC-22/B4/IP/73063/.

[6] EoPortal, *PROCYON*, 2022. [Online]. Available: https://directory.eoportal.org/web/eoportal/satellite-missions/p/procyon.

[7] V. Franzese, F. Topputo, F. Ankersen, and R. Walker, "Deep-Space Optical Navigation for M-ARGO Mission," *The Journal of the Astronautical Sciences*, vol. 68, no. 4, pp. 1034–1055, Dec. 2021, ISSN: 0021-9142. DOI: 10.1007/s40295-021-00286-9. [Online]. Available: https://link.springer.com/10.1007/s40295-021-00286-9.

[8] European Cooperation for Space Standardization, *ECSS-E-ST-10-04C Rev.1 Space environment*. ESA Requirements and Standards Office ESTEC, 2020, p. 208.

[9] ——, *Methods for the calculation of radiation received and its effects, and a policy for design margins*, November. 2008, pp. 1–218, ISBN: 978-3-319-41506-2.

[10] J. Lightholder, D. R. Thompson, J. Castillo-Rogez, and C. Basset, "Near Earth Asteroid Scout CubeSat Science Data Retrieval Optimization Using Onboard Data Analysis," in *2019 IEEE Aerospace Conference*, vol. 2019-March, IEEE, Mar. 2019, pp. 1–7, ISBN: 978-1-5386-6854-2. DOI: 10.1109/AERO.2019.8742190. [Online]. Available: https://ieeexplore.ieee.org/document/8742190/.

[11] E. Turan, S. Speretta, and E. Gill, "Autonomous navigation for deep space small satellites: Scientific and technological advances," *Acta Astronautica*, vol. 193, pp. 56–74, Apr. 2022, ISSN: 0094-5765. DOI: 10.1016/J.ACTAASTRO.2021.12.030.

[12] S. I. Sheikh, D. J. Pines, P. S. Ray, K. S. Wood, M. N. Lovellette, and M. T. Wolff, "Spacecraft Navigation Using X-Ray Pulsars," *Journal of Guidance, Control, and Dynamics*, vol. 29, no. 1, pp. 49–63, Jan. 2006, ISSN: 0731-5090. DOI: 10.2514/1.13331. [Online]. Available: https://arc.aiaa.org/doi/10.2514/1.13331.

[13] J. Yim, J. Crassidis, and J. Junkins, "Autonomous orbit navigation of interplanetary spacecraft," in *Astrodynamics Specialist Conference*, Reston, Virigina: American Institute of Aeronautics and Astronautics, Aug. 2000, pp. 53–61. DOI: 10.2514/6.2000-3936. [Online]. Available: https://arc.aiaa.org/doi/10.2514/6.2000-3936.

[14] G. Flandin, B. Polle, B. Frapard, P. Vidal, C. Philippe, and T. Voirin, "Vision based navigation for planetary exploration," *Advances in the Astronautical Sciences*, vol. 133, pp. 277–296, 2009, ISSN: 00653438.

[15] J. Taylor, *Deep Space Communications*, J. Taylor, Ed. Hoboken: Wiley, Jul. 2016, ISBN: 9781119169024. DOI: 10.1002/9781119169079. [Online]. Available: https://onlinelibrary.wiley.com/doi/book/10.1002/9781119169079.

[16] Endurosat, *Endurosat specifications*, 2022. [Online]. Available: https://www.endurosat.com/products (visited on 07/11/2022).

[17] AAC Clyde Space, *XANT*, 2021. [Online]. Available: https://www.aac-clyde.space/wp-content/uploads/2021/10/PULSAR-XANT.pdf (visited on 08/01/2022).

[18] Tether Unlimited, *SWIFT-XTX*, 2022. [Online]. Available: https://www.tethers.com/wp-content/uploads/2022/04/SWIFT-XTX.pdf (visited on 07/28/2022).

[19] General Dynamics, *X-band Small Deepspace*, 2019. [Online]. Available: https://gdmissionsystems.com/-/media/General-Dynamics/Space-and-Intelligence-Systems/PDF/small-deep-space-transponder-datasheet.ashx?la=en&hash=1A2E96BE0D9C0C29BD281963680DABDBEAE0E465 (visited on 07/28/2022).

[20] JPL, *Iris V2*, 2015. [Online]. Available: https://www.nasa.gov/sites/default/files/atoms/files/brochure_irisv2_201507.pdf (visited on 07/28/2022).

[21] IQ-Spacecom, *XLINK-X Transceiver*, 2021. [Online]. Available: https://www.iq-spacecom.com/images/downloads/XLink-X_Datasheet_072022.pdf (visited on 07/28/2022).

[22] AAC Clyde Space, *Pulsar-XTX*, 2021. [Online]. Available: https://www.aac-clyde.space/wp-content/uploads/2021/10/PULSAR-XTX.pdf (visited on 07/28/2022).

[23] Jet Propulsion Laboratory, "DSN Telecommunications Link Design Handbook DSN Telecommunications Link Design Handbook," no. 810-005, 2000. [Online]. Available: https://deepspace.jpl.nasa.gov/dsndocs/810-005/.

[24] AAC Clyde Space, *HT CP400.85*, 2021. [Online]. Available: https://www.aac-clyde.space/wp-content/uploads/2021/10/HT_CP400.85.pdf (visited on 08/05/2022).

[25] C. Longo and S. Rickman, "Method for the Calculation of Spacecraft Umbra and Penumbra Shadow Terminator Points," *NASA Technical Paper*, vol. 1, no. April, p. 41, 1995.

[26] AAC Clyde Space, *RW400 Datasheet*, 2021. [Online]. Available: https://www.aac-clyde.space/wp-content/uploads/2021/11/RW400.pdf (visited on 01/23/2023).

[27] Isispace, *6-Unit CubeSat Structure*, 2018. [Online]. Available: https://www.isispace.nl/product/6-unit-cubesat-structure/ (visited on 09/07/2022).

[28] Gomspace, *6U structure datasheet*, 2022. [Online]. Available: https://gomspace.com/UserFiles/Subsystems/datasheet/gs-ds-nanostructure-6u-11.pdf (visited on 09/07/2022).

[29] AAC Clyde Space, *Datasheet Zaphod*, 2020. [Online]. Available: https://www.aac-clyde.space/wp-content/uploads/2021/11/AAC_DataSheet_Zaphod.pdf (visited on 08/07/2022).

[30] Spacemind, *SM Structures Specification sheet*, 2020. [Online]. Available: https://www.npcspacemind.com/app/download/7215327359/SM_STRUCTURES_DATASHEET_2020.pdf?t=1591361681 (visited on 09/07/2022).

[31] A. Menicucci, A. Cervone, S. Speretta, E. Bertels, and F. Topputo, "The Radiation Environment and effects analysis of the LUMIO Mission," in *Proceedings of the International Astronautical Congress, IAC*, vol. C2, 2021, pp. 25–29, ISBN: 9781713843085.

[32] NASA, "Small Sats State of the Art," *Small Spacecraft Technology*, 2020. [Online]. Available: https://www.nasa.gov/sites/default/files/atoms/files/2020soa_final.pdf.

[33] A. R. Tummala and A. Dutta, "An overview of Cube-Satellite propulsion technologies and trends," *Aerospace*, vol. 4, no. 4, pp. 1–30, 2017, ISSN: 22264310. DOI: 10.3390/aerospace4040058.

[34] D. M. Goebel and I. Katz, "Fundamentals of Electric Propulsion: Ion and Hall Thrusters," *Fundamentals of Electric Propulsion: Ion and Hall Thrusters*, pp. 1–507, 2008. DOI: 10.1002/9780470436448.

[35] ESA, "Margin philosophy for science assessment studies," pp. 1–11, 2012.

[36] K. F. Wakker, *Fundamentals of Astrodynamics*. Delft, The Netherlands: Institutional Repository Library Delft University of Technology, 2015, ISBN: 9789461864192. DOI: 10.1007/978-3-319-09444-1_1.

[37] D. Morante, M. S. Rivo, and M. Soler, "A survey on low-thrust trajectory optimization approaches," *Aerospace*, vol. 8, no. 3, 2021, ISSN: 22264310. DOI: 10.3390/aerospace8030088.

[38] R. Chai, A. Savvaris, A. Tsourdos, S. Chai, and Y. Xia, "A review of optimization techniques in spacecraft flight trajectory design," *Progress in Aerospace Sciences*, vol. 109, no. December 2018, p. 100 543, Aug. 2019, ISSN: 03760421. DOI: 10.1016/j.paerosci.2019.05.003. [Online]. Available: https://doi.org/10.1016/j.paerosci.2019.05.003%20https://linkinghub.elsevier.com/retrieve/pii/S037604211830191X.

[39] F. Jiang, H. Baoyin, and J. Li, "Practical techniques for low-thrust trajectory optimization with homotopic approach," *Journal of Guidance, Control, and Dynamics*, vol. 35, no. 1, pp. 245–258, 2012, ISSN: 15333884. DOI: 10.2514/1.52476.

[40] C. A. Kluever, "Optimal low-thrust, Earth-Moon trajectories," Ph.D. dissertation, Iowa State University, Digital Repository, Ames, 1993. DOI: 10.31274/rtd-180813-9731. [Online]. Available: https://lib.dr.iastate.edu/rtd/10466/.

[41] R. Bertrand and R. Epenoy, "New smoothing techniques for solving bang-bang optimal control problems - Numerical results and statistical interpretation," *Optimal Control Applications and Methods*, vol. 23, no. 4, pp. 171–197, 2002, ISSN: 01432087. DOI: 10.1002/oca.709.

[42] A. E. Bryson and Y.-C. Ho, *Applied Optimal Control*. Routledge, 1975, ISBN: 9781315137667. DOI: 10.1201/9781315137667. [Online]. Available: https://www.taylorfrancis.com/books/9781351465922.

[43] B. Wie, *Space Vehicle Dynamics and Control, Second Edition*, Second Edi. Reston ,VA: American Institute of Aeronautics and Astronautics, Jan. 2008, p. 970, ISBN: 978-1-56347-953-3. DOI: 10.2514/4.860119. [Online]. Available: https://arc.aiaa.org/doi/book/10.2514/4.860119.

[44] M. D. Shuster, "A survey of Attitude Representations," Johns Hopkins University Applied Physics Laboratory, Laurel, Tech. Rep., 1993, p. 79. [Online]. Available: http://malcolmdshuster.com/Pub_1993h_J_Repsurv_scan.pdf.

[45] M. Navabi and M. Barati, "Mathematical modeling and simulation of the earth's magnetic field: A comparative study of the models on the spacecraft attitude control application," *Applied Mathematical Modelling*, vol. 46, pp. 365–381, Jun. 2017, ISSN: 0307904X. DOI: 10.1016/j.apm.2017.01.040. [Online]. Available: https://linkinghub.elsevier.com/retrieve/pii/S0307904X1730046X.

[46] J. D. Biggs and H. Fournier, "Neural-Network-Based Optimal Attitude Control Using Four Impulsive Thrusters," *Journal of Guidance, Control, and Dynamics*, vol. 43, no. 2, pp. 299–309, Feb. 2020, ISSN: 1533-3884. DOI: 10.2514/1.G004226. [Online]. Available: https://arc.aiaa.org/doi/10.2514/1.G004226.

[47] A. H. Barr, "Superquadrics and Angle-Preserving Transformations," *IEEE Computer Graphics and Applications*, vol. 1, no. 1, pp. 11–23, Jan. 1981, ISSN: 0272-1716. DOI: 10.1109/MCG.1981.1673799. [Online]. Available: http://ieeexplore.ieee.org/document/1673799/.

[48] Á. Romero-Calvo, J. D. Biggs, and F. Topputo, "Attitude control for the Lumio Cubesat in deep space," *Proceedings of the International Astronautical Congress, IAC*, vol. 2019-Octob, no. October, 2019, ISSN: 00741795.

[49] A. Shaiju and I. R. Petersen, "Formulas for Discrete Time LQR, LQG, LEQG and Minimax LQG Optimal Control Problems," *IFAC Proceedings Volumes*, vol. 41, no. 2, pp. 8773–8778, 2008, ISSN: 14746670. DOI: 10.3182/20080706-5-KR-1001.01483. [Online]. Available: http://dx.doi.org/10.3182/20080706-5-KR-1001.01483%20https://linkinghub.elsevier.com/retrieve/pii/S1474667016403629.

[50] J. L. Junkins and H. Schaub, *Analytical Mechanics of Space Systems, Second Edition*. Reston ,VA: American Institute of Aeronautics and Astronautics, Jan. 2009, ISBN: 978-1-60086-721-7. DOI: 10.2514/4.867231. [Online]. Available: https://arc.aiaa.org/doi/book/10.2514/4.867231.

[51] P. Tsiotras, "Passivity approach to attitude stabilization using nonredundant kinematic parameterizations," in *Proceedings of the IEEE Conference on Decision and Control*, vol. 1, IEEE, 1995, pp. 515–520, ISBN: 0-7803-2685-7. DOI: 10.1109/cdc.1995.478944. [Online]. Available: http://ieeexplore.ieee.org/document/478944/.

[52] J. Wertz, D. Everett, and J. Puschell, *Space Mission Engineering - The New SMAD*, 1st ed., ser. Space Technology Library, Vol. 28. Microcosm Press, 2011, ISBN: 9781881883159.

A

Satellite communication

In this appendix chapter, the different noise sources for RF communication with the Deep space network are worked out in detail.

A.1. Data encoding

Before data can be sent it is almost always encoded to make more efficient use of a communication channel. As a limit, the well-known Shannon-Hartley theorem can be used which states that the maximum channel capacity C in bits per second can be formulated as:

$$C = B \log_2 (1 + SNR) \tag{A.1}$$

where B is the signal bandwidth and SNR is the signal-to-noise ratio. This maximum channel capacity, as described by the Shannon-Hartley theorem, cannot be reached for a signal due to errors caused by the channel noise. If better encoding strategies are used, the true channel capacity will be closer to the maximum channel capacity. The downside, however, is that higher-rank encoding strategies lead to a decrease in the maximum channel capacity because more bits are required per symbol sent. Some encoding schemes are uncoded code, Reed-Solomon code, convolutional Code, and turbo codes. The trade-off between these coding schemes is done based on coding gain, bandwidth, latency, and the error floor. Where the coding gain is the difference between the uncoded code SNR and the encoded SNR, bandwidth is the required signal bandwidth to reach the desired symbol rate, and latency is the delay between the moment a data packet is sent and the moment the data is received by the ground station, and the error floor is a phenomenon encountered in coding schemes such as turbo code where the bit error rate as a function of the SNR does not decrease as quickly anymore due to a decrease in the SNR. Of these four trade-off criteria, only the coding gain and bandwidth are important for the data transfer back to Earth, because the system does not need to be low latency, and the important effect of the error floor is already taken when calculating the required signal bandwidth [23].

Deep-space communication often uses turbo code since deep-space communication will encounter significant channel noise which produces a relatively high error rate. If the error rate of a signal is too high, significant chunks of data can be lost and a proper connection cannot be established. To limit the scope of this thesis, a turbo code with a symbol per bits coding rate of 1/6 and an information block

size of 8920 bits is used. This means that for every 6 bits 1 symbol will be sent. And data is sent in chunks of 8920 bits which produces a code block length of 53544 bits after encoding. This is the highest supported coding gain and should lead to the lowest bit error rate [23].

A.2. Downlink

After the data is encoded, it will be modulated and then send using an antenna. This signal is then received by a ground station antenna and converted back to the actual information stream. In Figure 1.2 a schematic of the radio communication between a satellite and a ground station is shown including common signal losses.

As can be seen in Figure 1.2, the downlink from a satellite to a ground station is done by using a transmitter that sends a radio signal using an antenna to a ground station antenna. This signal is then converted back to digital data in a receiver. A downlink is 'closed' if the received signal power, which is also referred to as the carrier power, is more than the system noise power at the ground station. The calculation of the carrier power can be simplified to a summation if all the losses and gains are converted to decibels. The received power of a signal can then be obtained by adding the different losses and gains which occur during the data transmission and conversion losses [52]:

$$P_{RX} = P_{TX} + G_{TX} + G_{RX} - L_{TX} - L_{RX} - L_{fs} - L_{atm} - L_{p,TX} - L_{p,RX} - DCL \tag{A.2}$$

where P_{RX} is the received power, P_{TX} the transmitted power, G_{TX} the transmitted gain, G_{RX} the receiver gain, L_{TX} the losses between transmitter and antenna, L_{RX} the losses between the receiving antenna and receiver, L_{fs} the power loss in free space, L_{atm} the power loss due to the atmosphere, L_p the loss due to the pointing error of the antennas and DCL is the data conversion loss which is the signal power loss due to modulation/demodulation.

A.3. Ground antenna gain

For deep space missions, the Deep Space Network (DSN) is generally used for communication. An alternative is to establish communication with other satellites present in the Earth's orbit but this is considered to be beyond the topic of this thesis. The DSN is a network of different antennas situated at three locations which are approximately 120 degrees in longitude apart. The DSN can be grouped by antenna size 26, 34, and 70 meters in diameter [52]. As a reference, only the 34-meter beam-wave guide (BWG) antenna is used. The gain for these antennas is given in Jet Propulsion Laboratory [23] and follows the empiric relation:

$$G_{RX}(\theta) = G_0 + G_1(\theta - \gamma)^2 \tag{A.3}$$

Where G_0 and G_1 are gain coefficients in dBi and θ is the elevation angle in deg and γ is the angle offset in deg.

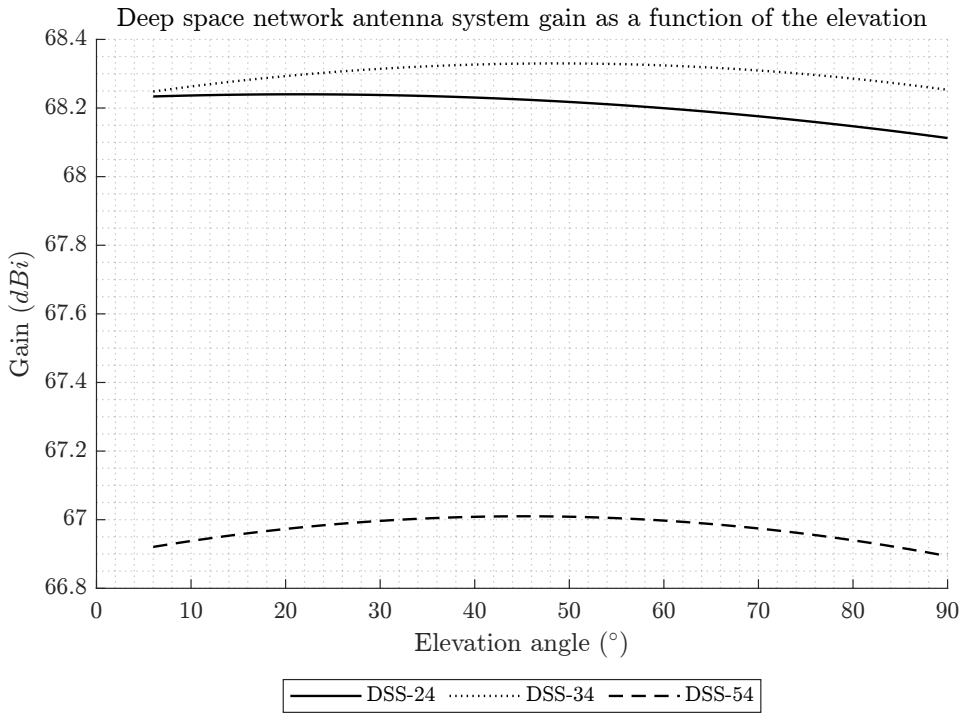

Figure A.1: The figure displays the gain of Deep Space Network's 34-meter Beam Waveguide Antenna Systems located in Goldstone (DSS-24), Canberra (DSS-34), and Madrid (DSS-54) as a function of the elevation angle. This information is crucial for designing and optimizing the communication systems of deep space missions that rely on these antennas for data transmission and reception.

Table A.1: The table displays the gain parameters of the Deep Space Network's 34-meter Beam Waveguide Antenna Systems located in Goldstone (DSS-24), Canberra (DSS-34), and Madrid (DSS-54). These gain parameters are essential for designing and optimizing communication systems for deep space missions that rely on these antennas for data transmission and reception [23].

Antenna system	G_0 (dBi)	G_1 (dBi)	γ (deg)
DSS-24	68.24	0.000027	21.28
DSS-34	68.33	0.000045	48.64
DSS-54	67.01	0.000058	45.25

A.4. Free space path and atmospheric losses

The free space path loss comes from the spreading of the radio frequency signal as the signal moves through free space. The free space path loss $FSPL$ can be described by the following formula [52]:

$$FSPL = \left(\frac{4\pi df}{c}\right)^2 \tag{A.4}$$

where d is the distance in meters between the transmitting and receiving antenna, f is the radio frequency in Hz and c is the speed of light which is $299\,792\,458\,\mathrm{m\,s^{-1}}$. The free space path loss in dB can then be found using:

$$L_{fs} = 10\log_{10}(FSPL) \tag{A.5}$$

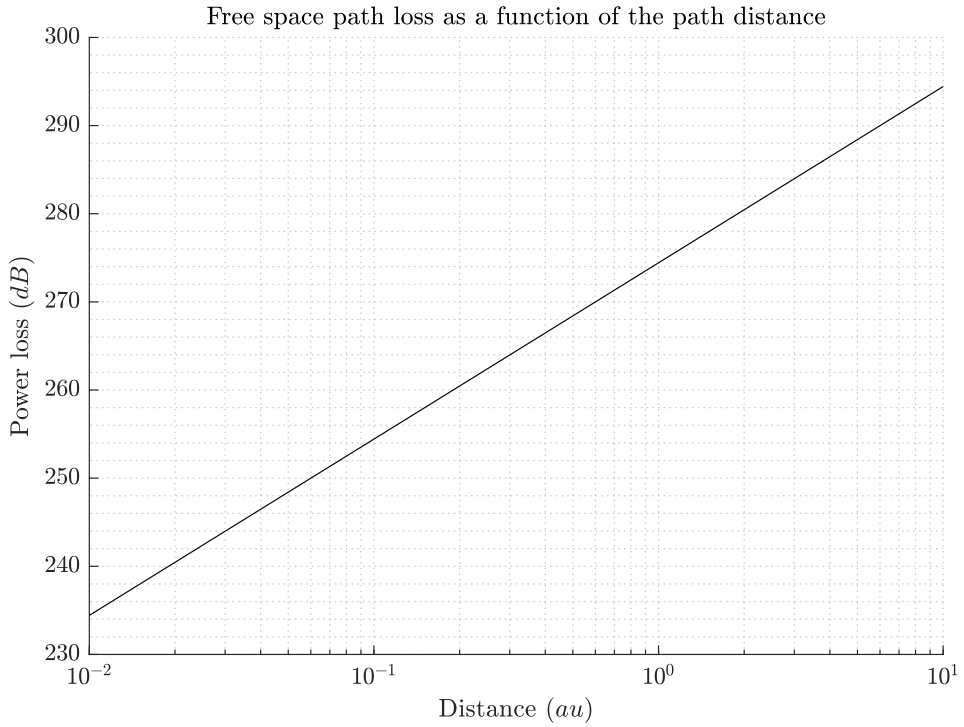

Figure A.2: The figure depicts the free space path loss as a function of the distance between the satellite antenna and the ground station antenna, measured in astronomical units. The information presented in the figure is critical for designing and optimizing communication systems for satellite missions that rely on ground station antennas for data transmission and reception. The figure provides a clear representation of the relationship between distance and free space path loss, aiding in the selection and utilization of appropriate communication systems for different satellite missions.

Since the satellite has to penetrate the Earth's atmosphere, there is also an atmospheric loss which has to be taken into account. The loss due to the atmosphere for X-band systems to the different antennas in Goldstone (DSS-24), Canberra (DSS-34), and Madrid (DSS-54) can be approximated using [23]:

$$L_{atm} = \frac{A_{zen}}{\sin\theta} \tag{A.6}$$

where A_{zen} is the zenith atmospheric attenuation which can be seen in Table A.2 in dB and θ the elevation angle in deg.

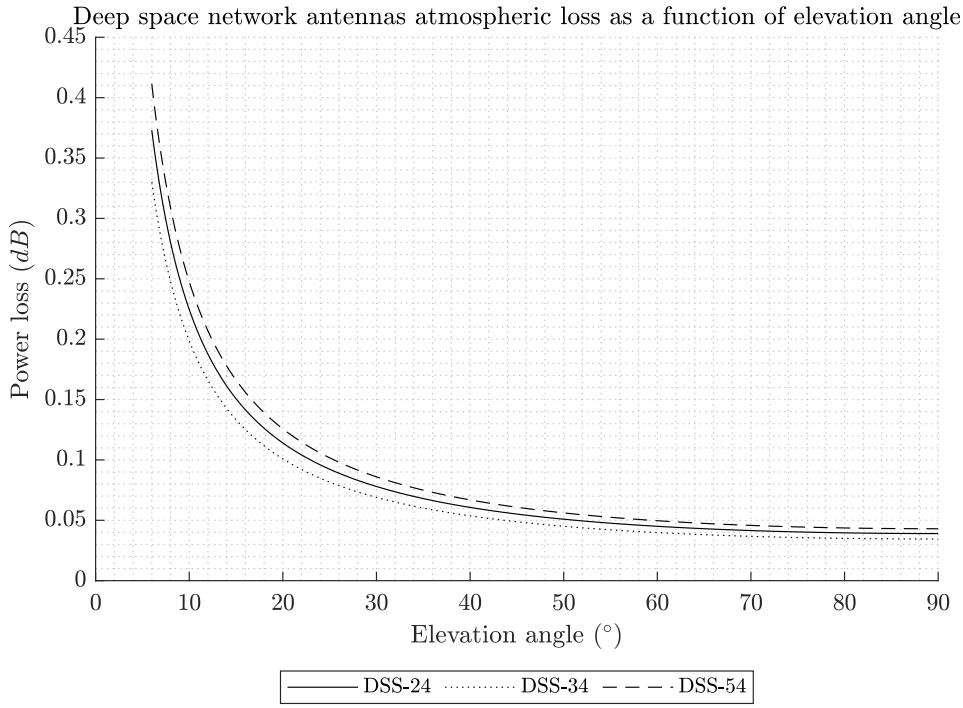

Figure A.3: The figure illustrates the X-band power losses in the Deep Space Network's 34-meter antenna systems located in Goldstone (DSS-24), Canberra (DSS-34), and Madrid (DSS-54) due to atmospheric effects. The losses are depicted as a function of the elevation angle between $6°$ and $90°$, assuming average clear weather conditions with a CD value of 0.25. This information is essential for designing and optimizing communication systems for deep space missions that rely on these antennas for data transmission and reception. The figure provides a clear representation of the power losses caused by atmospheric effects at different elevation angles, aiding in the selection and utilization of appropriate communication systems for specific deep space missions.

A.5. System noise

The system noise at the ground station receiver depends fully on the operational system noise temperature. The noise in electronics depends on the temperature of the components. This temperature then results in a uniformly distributed noise. This relation is also known as the Johnson-Nyquist noise which can be expressed as:

$$N = k_B T \tag{A.7}$$

where N is the noise spectral density in $\mathrm{W\,Hz^{-1}}$, k_B the Boltzmann constant equal to $1.380\,649 \times 10^{-23}\,\mathrm{J\,K^{-1}}$ and T the noise temperature in K.

The system noise temperature can be found using the following equation as given in Jet Propulsion Laboratory [23]:

$$T_{op}(\theta) = T_1 + T_2 e^{-a\theta} + T_{atm}(\theta) + T'_{CMB}(\theta) \tag{A.8}$$

Where T_1, T_2 and a are antenna-microwave noise temperature parameters which can be seen in Table A.2,θ is the elevation angle, T_{atm} is the atmospheric noise contribution and T'_{CMB} is the effective cosmic background noise.

The atmospheric noise contribution can be found using [23]:

$$T_{atm}(\theta) = 255 + 25 \times CD \left(1 - 10^{-L_{atm}(\theta)/10}\right) \tag{A.9}$$

where CD is the cumulative distribution of the weather which is between 0 for clear weather and 0.99 for heavy rain (it is assumed that CD = 0.25 which is average clear weather) and L_{atm} is the atmospheric

attenuation in dB. Further, the effective cosmic background noise can be found using [23]:

$$T'_{CMB}(\theta) = T_{CMB} \times 10^{-L_{atm}(\theta)/10} \tag{A.10}$$

where T_{CMB} is the cosmic background temperature of $2.725\,\mathrm{K}$, L_{atm} is the atmospheric attenuation in dB and T'_{CMB} is the effective cosmic background temperature.

The power of the system noise in milliwatt decibels over a bandwidth can be found by combining the Johnson-Nyquist noise, the found operating noise temperature of the DSN antenna, and the operation bandwidth using the following equation:

$$P_{noise} = 10\log_{10}\left(\frac{k_B T_{op}(\theta)}{1\mathrm{mW}}\right) + 10\log_{10}(B) \tag{A.11}$$

where k_B is the Boltzmann constant equal to $1.380\,649 \times 10^{-23}\,\mathrm{J\,K^{-1}}$, T_{op} is the operational noise temperature in K and B is the operation bandwidth in Hz.

Table A.2: The table displays the noise temperature parameters of the Deep Space Network's 34-meter Beam Waveguide Antenna Systems located in Goldstone (DSS-24), Canberra (DSS-34), and Madrid (DSS-54) under average clear weather conditions with a CD value of 0.25. These noise temperature parameters are crucial for designing and optimizing communication systems for deep space missions that rely on these antennas for data transmission and reception [23].

Antenna system	**T_1 (K)**	**T_2 (K)**	**a (-)**	**Yearly average zenith atmospheric attenuation (dB)**
DSS-24	26.04	5.2	0.05	0.039
DSS-34	24.88	20	0.16	0.045
DSS-54	26.04	25.72	12.0	0.043

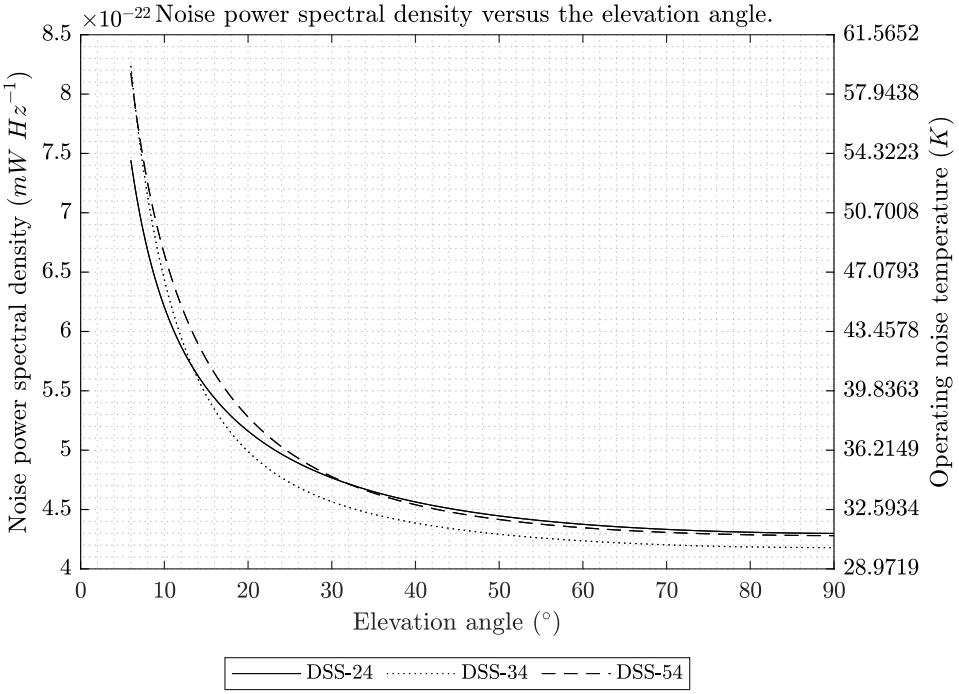

Figure A.4: The figure shows the system noise spectral density of the Deep Space Network's antenna systems located in Goldstone (DSS-24), Canberra (DSS-34), and Madrid (DSS-54) under average clear weather conditions with a CD value of 0.25, as a function of elevation angle. System noise spectral density is a crucial parameter that affects the performance, quality, and reliability of communication systems in deep space missions. The figure provides a clear representation of the noise spectral density at different elevation angles, which is essential for designing and optimizing communication systems for specific deep space missions.

A.6. Pointing error losses

In an ideal situation both the transmitting and receiving antennas have no pointing error. In Jet Propulsion Laboratory [23] an equation from empirical data is given that described the gain loss of a signal as a function of the pointing error and the antenna's half-power beam width:

$$L_p = 10 \log_{10} \left(e^{\left(\frac{2.773 {\theta_e}^2}{HPBW^2} \right)} \right) \tag{A.12}$$

where L_p is the signal gain loss in dBi, θ_e is the pointing error in deg and $HPBW$ is the antenna's Half-Power Beam Width in deg.

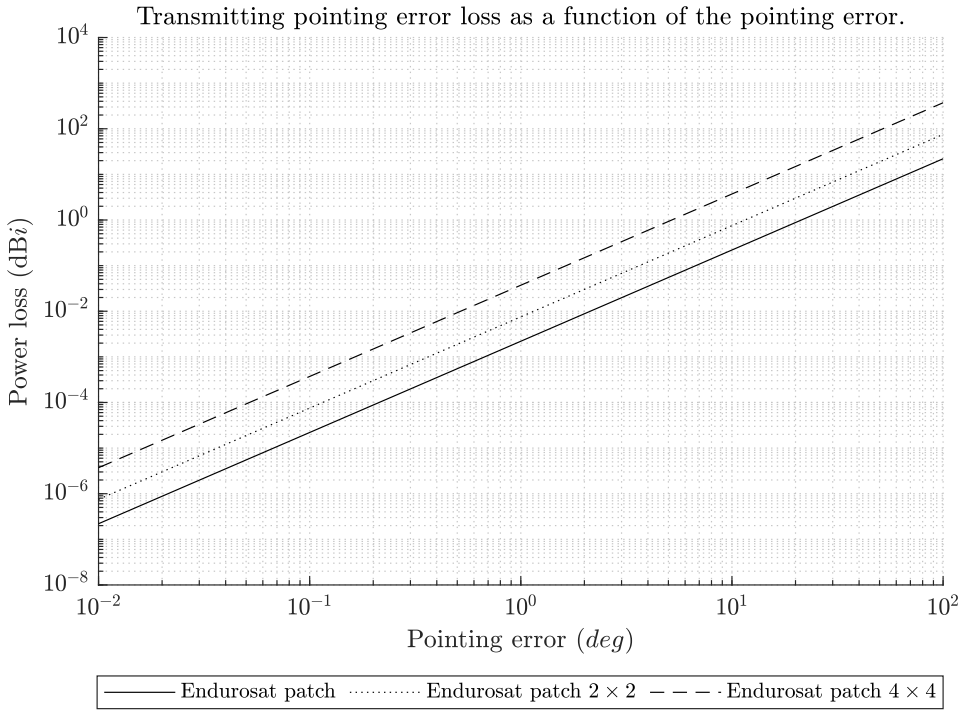

Figure A.5: The figure illustrates the transmitting pointing error loss as a function of pointing error for various antennas. The graph clearly indicates that a pointing error of 10 degrees results in a power loss of approximately 3 dBi or less. The transmitting pointing error loss is a critical factor affecting the performance of communication systems, especially for deep space missions. The figure provides important insights into the pointing error requirements for different antennas and their corresponding power losses, enabling the selection of the appropriate antenna for a given mission.

The DSN receiving antennas also have pointing error losses. If the conical scan function of the DSN antennas is used, Jet Propulsion Laboratory [23] recommends a power loss of 0.1 dB due to the pointing error of the DSN antenna.

B

Attitude parameters derivations

B.1. Derivation of direction cosine kinematics

the direction cosine matrix can also be time-variant, thus the change in orientation can be defined using a direction cosine. Consider two frames $\mathcal{N}$ and $\mathcal{B}$ which move relative to each other by the angular velocity vector $\vec{\omega}^{\mathcal{B}}_{\mathcal{N}\mathcal{B}}$ which is expressed in frame $\mathcal{B}$:

$$\vec{\omega}^{\mathcal{B}}_{\mathcal{N}\mathcal{B}} = \omega_1 \hat{b}_1 + \omega_2 \hat{b}_2 + \omega_3 \hat{b}_3 \tag{B.1}$$

$\vec{\omega}^{\mathcal{B}}_{\mathcal{N}\mathcal{B}}$ causes rotations of the $\mathcal{B}$ frame such that:

$$\dot{\hat{b}} = \vec{\omega}^{\mathcal{B}}_{\mathcal{N}\mathcal{B}} \times \hat{b}$$

$$\begin{bmatrix} \dot{\hat{b}}_1 \\ \dot{\hat{b}}_2 \\ \dot{\hat{b}}_3 \end{bmatrix} = - \begin{bmatrix} 0 & -\omega_3 & \omega_2 \\ \omega_3 & 0 & -\omega_1 \\ -\omega_2 & \omega_1 & 0 \end{bmatrix} \begin{bmatrix} \hat{b}_1 \\ \hat{b}_2 \\ \hat{b}_3 \end{bmatrix} \tag{B.2}$$

By taking the time derivative of the direction cosine matrix definition in Equation 6.1 the following relation can be found:

$$\frac{\mathrm{d}}{\mathrm{d}t} \left\{ \begin{bmatrix} \hat{n}_1 \\ \hat{n}_2 \\ \hat{n}_3 \end{bmatrix} \right\} = \frac{\mathrm{d}}{\mathrm{d}t} \left\{ C^{\mathcal{N}}_{\mathcal{B}} \begin{bmatrix} \hat{b}_1 \\ \hat{b}_2 \\ \hat{b}_3 \end{bmatrix} \right\}$$

$$\begin{bmatrix} 0 \\ 0 \\ 0 \end{bmatrix} = \dot{C}^{\mathcal{N}}_{\mathcal{B}} \begin{bmatrix} \hat{b}_1 \\ \hat{b}_2 \\ \hat{b}_3 \end{bmatrix} + C^{\mathcal{N}}_{\mathcal{B}} \begin{bmatrix} \dot{\hat{b}}_1 \\ \dot{\hat{b}}_2 \\ \dot{\hat{b}}_3 \end{bmatrix} \tag{B.3}$$

Note that $\frac{\mathrm{d}}{\mathrm{d}t} \left\{ \begin{bmatrix} \hat{n}_1 & \hat{n}_2 & \hat{n}_3 \end{bmatrix}^\top \right\} = 0$ because from the definition of the inertial reference frame, $\mathcal{N}$ is time-invariant so its axes are time-invariant.

Combining Equation B.2 with Equation B.3 can be expressed as:

$$\begin{bmatrix} 0 \\ 0 \\ 0 \end{bmatrix} = \dot{C}^{\mathcal{N}}_{\mathcal{B}} \begin{bmatrix} \hat{b}_1 \\ \hat{b}_2 \\ \hat{b}_3 \end{bmatrix} - C^{\mathcal{N}}_{\mathcal{B}} \begin{bmatrix} 0 & -\omega_3 & \omega_2 \\ \omega_3 & 0 & -\omega_1 \\ -\omega_2 & \omega_1 & 0 \end{bmatrix} \begin{bmatrix} \hat{b}_1 \\ \hat{b}_2 \\ \hat{b}_3 \end{bmatrix} \tag{B.4}$$

Defining the skew symmetric matrix in Equation B.4 as:

$$\Omega_{\mathcal{NB}}^{\mathcal{B}} = \begin{bmatrix} 0 & -\omega_3 & \omega_2 \\ \omega_3 & 0 & -\omega_1 \\ -\omega_2 & \omega_1 & 0 \end{bmatrix} \tag{B.5}$$

The following relation can then be obtained:

$$\begin{gathered} \left[\dot{C}_{\mathcal{B}}^{\mathcal{N}} - C_{\mathcal{B}}^{\mathcal{N}}\,\Omega_{\mathcal{NB}}^{\mathcal{B}}\right] \begin{bmatrix} \hat{b}_1 \\ \hat{b}_2 \\ \hat{b}_3 \end{bmatrix} = \begin{bmatrix} 0 \\ 0 \\ 0 \end{bmatrix} \\ \dot{C}_{\mathcal{B}}^{\mathcal{N}} - C_{\mathcal{B}}^{\mathcal{N}}\,\Omega_{\mathcal{NB}}^{\mathcal{B}} = 0 \\ \dot{C}_{\mathcal{B}}^{\mathcal{N}} = C_{\mathcal{B}}^{\mathcal{N}}\,\Omega_{\mathcal{NB}}^{\mathcal{B}} \end{gathered} \tag{B.6}$$

From the relation ${\Omega_{\mathcal{NB}}^{\mathcal{B}}}^{\top} = -\,\Omega_{\mathcal{NB}}^{\mathcal{B}}$ the found expression for $\dot{C}_{\mathcal{B}}^{\mathcal{N}}$ can also be expressed as:

$$\dot{C}_{\mathcal{B}}^{\mathcal{N}} = -\,\Omega_{\mathcal{NB}}^{\mathcal{B}}\,C_{\mathcal{B}}^{\mathcal{N}} \tag{B.7}$$

This relation is known as the kinematic differential equation for the direction cosine matrix $C_{\mathcal{B}}^{\mathcal{N}}$.

B.2. Derivation of quaternion kinematics

The kinematic equations for quaternions can be found by starting with the equations in Equation 6.5. This results in:

$$\omega_1 = 2\left(\dot{q}_1 q_4 + \dot{q}_2 q_3 - \dot{q}_3 q_2 - \dot{q}_4 q_1\right) \tag{B.8a}$$

$$\omega_2 = 2\left(\dot{q}_2 q_4 + \dot{q}_3 q_1 - \dot{q}_1 q_3 - \dot{q}_4 q_2\right) \tag{B.8b}$$

$$\omega_3 = 2\left(\dot{q}_3 q_4 + \dot{q}_1 q_2 - \dot{q}_2 q_1 - \dot{q}_4 q_3\right) \tag{B.8c}$$

Finally differentiating Equation 6.11 gives the final equation:

$$0 = 2\left(\dot{q}_1 q_1 + \dot{q}_2 q_2 + \dot{q}_3 q_3 + \dot{q}_4 q_4\right) \tag{B.9}$$

Combining Equation B.8 and Equation B.9 gives the differential equations for the quaternions in matrix form as:

$$\begin{bmatrix} \omega_1 \\ \omega_2 \\ \omega_3 \\ 0 \end{bmatrix} = 2 \begin{bmatrix} q_4 & q_3 & -q_2 & -q_1 \\ -q_3 & q_4 & q_1 & -q_2 \\ q_2 & -q_1 & q_4 & -q_3 \\ q_1 & q_2 & q_3 & q_4 \end{bmatrix} \begin{bmatrix} \dot{q}_1 \\ \dot{q}_2 \\ \dot{q}_3 \\ \dot{q}_4 \end{bmatrix} \tag{B.10}$$

Since the matrix in Equation B.10 is orthonormal the inverse is equal to the transpose which so $\dot{\vec{q}}, \dot{q}_4$ can easily be rewritten in terms of $\vec{\omega}$:

$$\begin{bmatrix} \dot{q}_1 \\ \dot{q}_2 \\ \dot{q}_3 \\ \dot{q}_4 \end{bmatrix} = \frac{1}{2} \begin{bmatrix} q_4 & -q_3 & q_2 & q_1 \\ q_3 & q_4 & -q_1 & q_2 \\ -q_2 & q_1 & q_4 & q_3 \\ -q_1 & -q_2 & -q_3 & q_4 \end{bmatrix} \begin{bmatrix} \omega_1 \\ \omega_2 \\ \omega_3 \\ 0 \end{bmatrix} \tag{B.11}$$

which can be further simplified to:

$$\begin{bmatrix} \dot{q}_1 \\ \dot{q}_2 \\ \dot{q}_3 \\ \dot{q}_4 \end{bmatrix} = \frac{1}{2} \begin{bmatrix} 0 & \omega_3 & -\omega_2 & \omega_1 \\ -\omega_3 & 0 & \omega_1 & \omega_2 \\ \omega_2 & -\omega_1 & 0 & \omega_3 \\ -\omega_1 & -\omega_2 & -\omega_3 & 0 \end{bmatrix} \begin{bmatrix} q_1 \\ q_2 \\ q_3 \\ q_4 \end{bmatrix} \tag{B.12}$$

This expression can be rewritten to:

$$\dot{\vec{q}} = \tfrac{1}{2} \left(q_4 \vec{\omega} - \vec{\omega} \times \vec{q} \right) \tag{B.13a}$$

$$\dot{q}_4 = -\tfrac{1}{2} \vec{\omega}^\top \vec{q} \tag{B.13b}$$

where $\vec{q} = \begin{bmatrix} q_1 & q_2 & q_3 \end{bmatrix}^\top$, $\vec{\omega} = \begin{bmatrix} \omega_1 & \omega_2 & \omega_3 \end{bmatrix}^\top$ and $\omega \times \vec{q}$ comes from:

$$\vec{\omega} \times \vec{q} = \begin{bmatrix} 0 & -\omega_3 & \omega_2 \\ \omega_3 & 0 & -\omega_1 \\ -\omega_2 & \omega_1 & 0 \end{bmatrix} \begin{bmatrix} q_1 \\ q_2 \\ q_3 \end{bmatrix} \tag{B.14}$$

B.3. Modified Rodrigues Parameters properties and identities

B.3.1. Shadow component

MRPs have some interesting properties for inverse rotations. The inverse rotation in MRPs can namely be expressed as:

$$\vec{\psi}^{-1} = -\vec{\psi} \tag{B.15}$$

Furthermore, every rotation in MRPs has a shadow component that results in an identical direction cosine but rotates the frame in the opposite direction. The shadow component can be expressed as [44]:

$$\vec{\psi}_s = -\frac{\vec{\psi}}{\|\vec{\psi}\|^2} \tag{B.16}$$

and the opposite transformation is identical and can be expressed as:

$$\vec{\psi} = -\frac{\vec{\psi}_s}{\|\vec{\psi}_s\|^2} \tag{B.17}$$

To deal with singularities, it is common practice to switch to the shadow component of the MRP vector when the norm of the MRP exceeds a value. this guarantees that a rotation does not come near the singularity for rotations at π. For this thesis, the following switching rule will be used when solving the system of equations in MRPs:

$$\begin{aligned} &\text{if } \|\vec{\psi}\| > 1, \quad &&\text{then } \vec{\psi} = \vec{\psi}_s \\ &\text{if } \|\vec{\psi}_s\| > 1, \quad &&\text{then } \vec{\psi}_s = \vec{\psi} \end{aligned} \tag{B.18}$$

B.3.2. Tracking of a frame using modified Rodrigues parameters

To find the rotation from one rotated frame $\mathcal{C}$ to another rotated frame $\mathcal{D}$ the direction cosines can be used such that the rotation from $\mathcal{C} \rightarrow \mathcal{D}$ can be found by rotating $\mathcal{C}$ back to the Newtonian inertial reference frame $\mathcal{N}$ or $\mathcal{C} \rightarrow \mathcal{N}$ and then rotate from $\mathcal{N} \rightarrow \mathcal{D}$. For further reference, this means that:

$$C_{\mathcal{C}}^{\mathcal{D}} \equiv C_{\mathcal{N}}^{\mathcal{D}} \, C_{\mathcal{C}}^{\mathcal{N}} \tag{B.19}$$

Or

$$C_{\mathcal{C}}^{\mathcal{D}} \equiv \left[C_{\mathcal{D}}^{\mathcal{N}} \right]^\top C_{\mathcal{C}}^{\mathcal{N}} \tag{B.20}$$

Using Equation 6.26 the difference $\delta\vec{\psi}$ between the current reference frame $\vec{\phi}$ and the desired reference frame $\vec{\phi}_r$ in MRPs can be expressed as:

$$\delta\vec{\psi} = \frac{\left(1 - \left\|-\vec{\psi}_r\right\|^2\right)\vec{\psi} + \left(1 - \left\|\vec{\psi}\right\|^2\right) - \vec{\psi}_r - 2\vec{\psi} \times -\vec{\psi}_r}{1 + \left\|\vec{\psi}\right\|^2\left\|-\vec{\psi}_r\right\|^2 - 2\vec{\psi}\cdot -\vec{\psi}_r} \tag{B.21}$$

where $\vec{\psi}$ is the true state of the rigid body and $\vec{\psi}_r$ is the desired reference state. Notice that $\vec{\psi}_r$ has negative signs in front of it because the rotation from the body to the inertial reference frame to the desired reference frame has to be found, which is a composition of the true rotation and the inverse of the rotation of the desired reference frame.

Since MRPs have shadow components that describe the same orientation using an opposite rotation, these shadow components should also be checked. For a particular case, the shadow component MRP rotation error could smaller than the MRP rotation error. Therefore, if $\|\delta\vec{\psi}_s\| < \|\delta\vec{\psi}\|$ then the MRP rotation error that is considered will be $\delta\vec{\psi}_s$ instead of $\delta\vec{\psi}$.

To find a similar expression for $\delta\dot{\vec{\psi}}$ recall Equation 6.31 from the rigid body kinematics such that $\delta\dot{\vec{\psi}}$ can be expressed as:

$$\delta\dot{\vec{\psi}} = G\left(\delta\vec{\psi}\right)\delta\vec{\omega} \tag{B.22}$$

where

$$G\left(\delta\vec{\psi}\right) = \tfrac{1}{2}\left[\mathbb{I}_{3\times3} + Q\left(\delta\vec{\psi}\right) + \delta\vec{\psi}\delta\vec{\psi}^{\top} - \tfrac{1}{2}\left(1 + \delta\vec{\psi}^{\top}\delta\vec{\psi}\right)\mathbb{I}_{3\times3}\right]$$

and where

$$Q\left(\delta\vec{\psi}\right) = \begin{bmatrix} 0 & -\delta\psi_3 & \delta\psi_2 \\ \delta\psi_3 & 0 & -\delta\psi_1 \\ -\delta\psi_2 & \delta\psi_1 & 0 \end{bmatrix}$$

To find $\delta\vec{\omega}$, the angular rotations in the reference frame have to be rotated to the rigid body frame such that $\delta\vec{\omega}$ can be expressed as:

$$\delta\vec{\omega} = \vec{\omega} - [\vec{\omega}_r]_{\mathcal{B}} \tag{B.23}$$

or

$$\delta\vec{\omega} = \vec{\omega} - C_{\mathcal{R}}^{\mathcal{B}}\left(\delta\vec{\psi}\right)\vec{\omega}_r \tag{B.24}$$

where $[\vec{\omega}_r]_{\mathcal{R}}$ is the desired reference angular velocity defined in the desired orientation frame $\mathcal{R}$. In the special case that $\mathcal{R}$ and $\mathcal{B}$ are identical or $\delta\vec{\psi} = 0$ then $C_{\mathcal{R}}^{\mathcal{B}}\left(\delta\vec{\psi}\right) = \mathbb{I}_{3\times3}$ such that:

$$\delta\vec{\omega} = \vec{\omega} - \vec{\omega}_r \tag{B.25}$$

this is however almost never the case unless the orientation of the satellite does not have to be controlled.

Using Equation B.7 and taking the time derivative of $\delta\vec{\omega}$, $\delta\dot{\vec{\omega}}$ can be found:

$$\begin{aligned}
\delta\dot{\vec{\omega}} &= \frac{\mathsf{d}\vec{\omega}}{\mathsf{d}t} - \frac{\mathsf{d}\left(C_{\mathcal{R}}^{\mathcal{B}}\left[\vec{\omega}_r\right]_{\mathcal{R}}\right)}{\mathsf{d}t} \\
\delta\dot{\vec{\omega}} &= \dot{\vec{\omega}} - C_{\mathcal{R}}^{\mathcal{B}}\left[\dot{\vec{\omega}}_r\right]_{\mathcal{R}} - \dot{C}_{\mathcal{R}}^{\mathcal{B}}\left[\vec{\omega}_r\right]_{\mathcal{R}} \\
\delta\dot{\vec{\omega}} &= \dot{\vec{\omega}} - \left[\dot{\vec{\omega}}_r\right]_{\mathcal{B}} + \Omega\, C_{\mathcal{R}}^{\mathcal{B}}\left[\vec{\omega}_r\right]_{\mathcal{R}} \\
\delta\dot{\vec{\omega}} &= \dot{\vec{\omega}} - \left[\dot{\vec{\omega}}_r\right]_{\mathcal{B}} + \Omega\left[\vec{\omega}_r\right]_{\mathcal{B}}
\end{aligned} \tag{B.26}$$

or

$$\delta\dot{\vec{\omega}} = \dot{\vec{\omega}} - C_{\mathcal{R}}^{\mathcal{B}}\left(\delta\vec{\psi}\right)\left[\dot{\vec{\omega}}_r\right]_{\mathcal{R}} + \omega \times C_{\mathcal{R}}^{\mathcal{B}}\left(\delta\vec{\psi}\right)\left[\vec{\omega}_r\right]_{\mathcal{R}} \tag{B.27}$$

Again if $\mathcal{R}$ and $\mathcal{B}$ are identical then $C_{\mathcal{R}}^{\mathcal{B}}\left(\delta\vec{\psi}\right) = \mathbb{I}_{3\times 3}$ such that:

$$\left[\delta\dot{\vec{\omega}}\right]_{\mathcal{B}} = \dot{\vec{\omega}} - \dot{\vec{\omega}}_r + \vec{\omega}\times\vec{\omega}_r \tag{B.28}$$

B.3.3. Identity 1

An important identity often used in MRPs is [44]:

$$\begin{aligned}
\vec{\psi}^{\top} G\left(\vec{\psi}\right) &= \tfrac{1}{2}\vec{\psi}^{\top}\left[\mathbb{I}_{3\times 3} + Q\left(\vec{\psi}\right) + \vec{\psi}\vec{\psi}^{\top} - \tfrac{1}{2}\left(1+\vec{\psi}^{\top}\vec{\psi}\right)\mathsf{I}_{3\times 3}\right] \\
&\ldots = \tfrac{1}{2}\vec{\psi}^{\top}\left[\left(1+\vec{\psi}\vec{\psi}^{\top}\right) - \tfrac{1}{2}\left(1+\vec{\psi}^{\top}\vec{\psi}\right)\right] \\
&\ldots = \tfrac{1}{2}\vec{\psi}^{\top}\left[\tfrac{1}{2}\left(1+\vec{\psi}^{\top}\vec{\psi}\right)\right] \\
\vec{\psi}^{\top} G\left(\vec{\psi}\right) &= \tfrac{1}{4}\vec{\psi}^{\top}\left(1+\vec{\psi}^{\top}\vec{\psi}\right)
\end{aligned} \tag{B.29}$$

where $\vec{\psi}^{\top}\mathbb{I}_{3\times 3} = \vec{\psi}^{\top}$ and $\vec{\psi}^{\top} Q\left(\vec{\psi}\right) = 0$.

C

Extra relations for low-thrust interplanetary propulsion systems

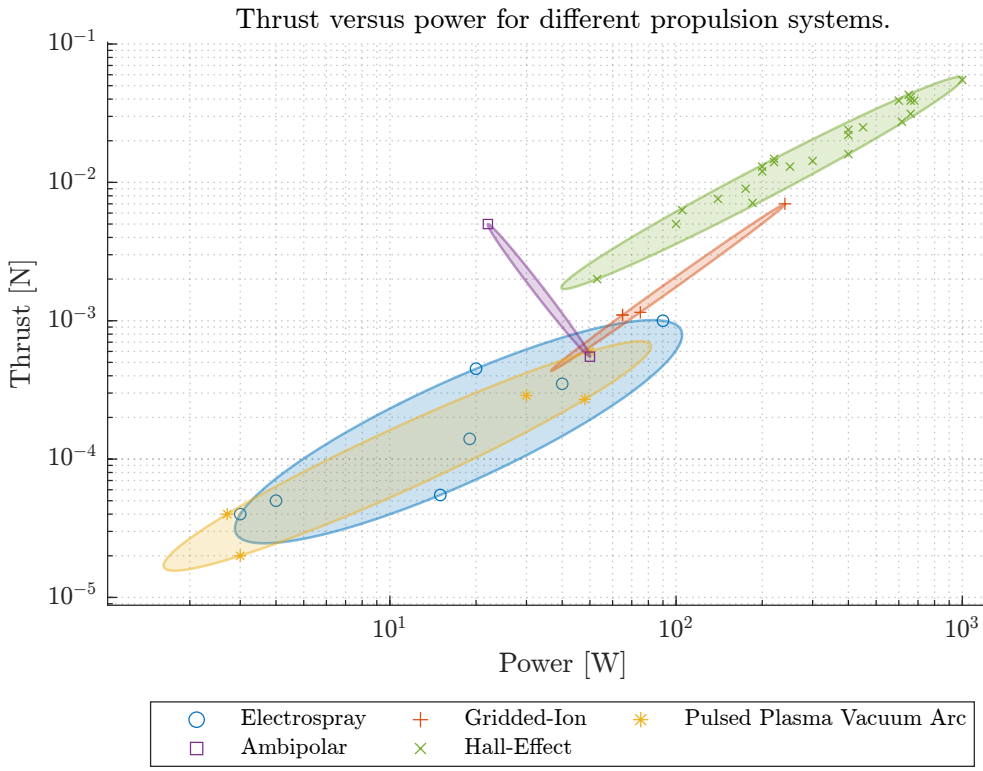

Figure C.1: The required electrical power for the maximum thrust at maximum specific impulse for different propulsion system types. It can be seen that most system types follow the same logarithmic trend, except for ambipolar which has a system that compromises specific impulses for lower required power. Also, Gridded-Ion and Hall-Effect systems tend to use more power than other systems.

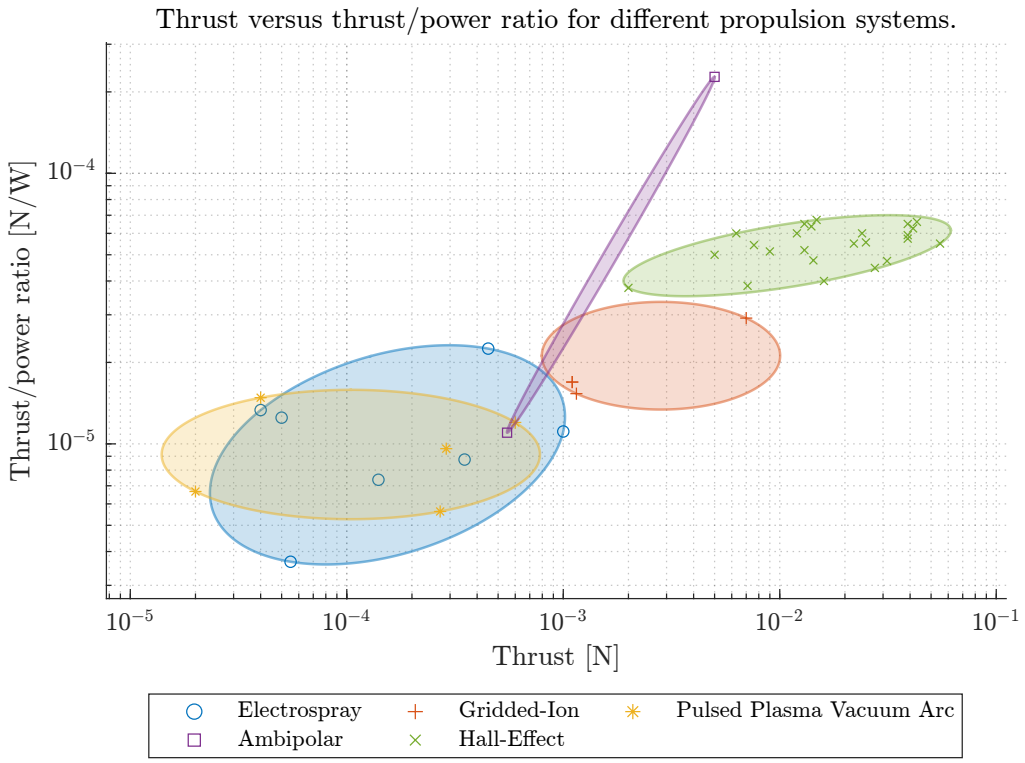

Figure C.2: This figure shows the relationship between thrust and thrust power ratios for different propulsion system types.

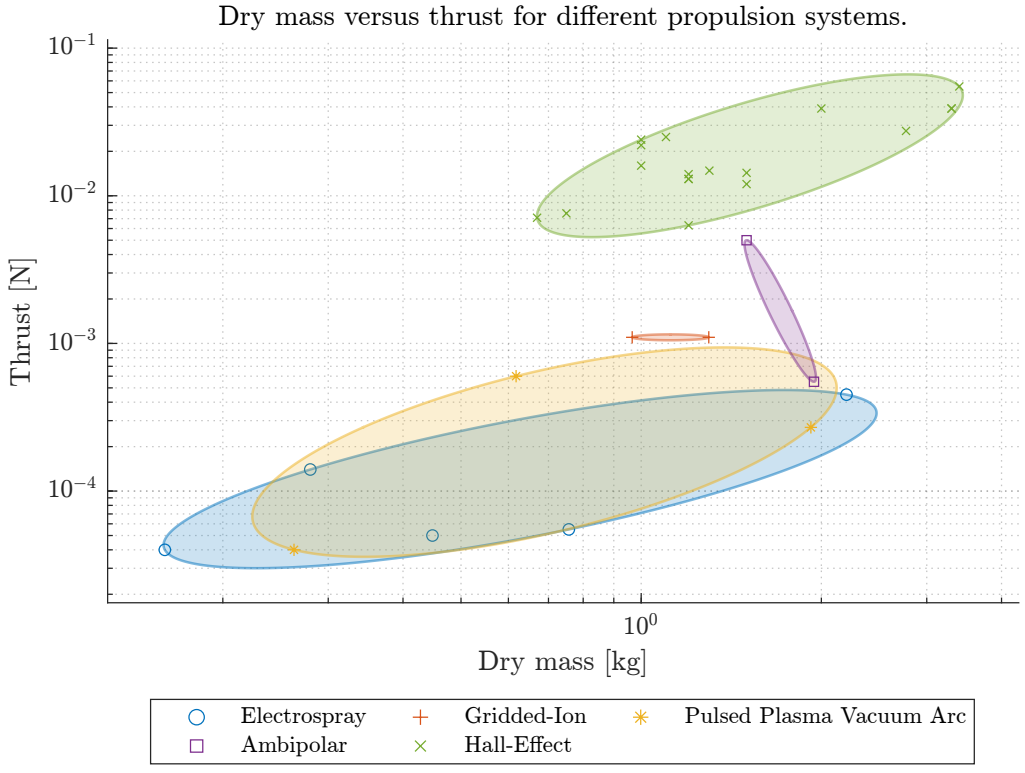

Figure C.3: This figure shows the relationship between thrust and dry mass for different propulsion system types.

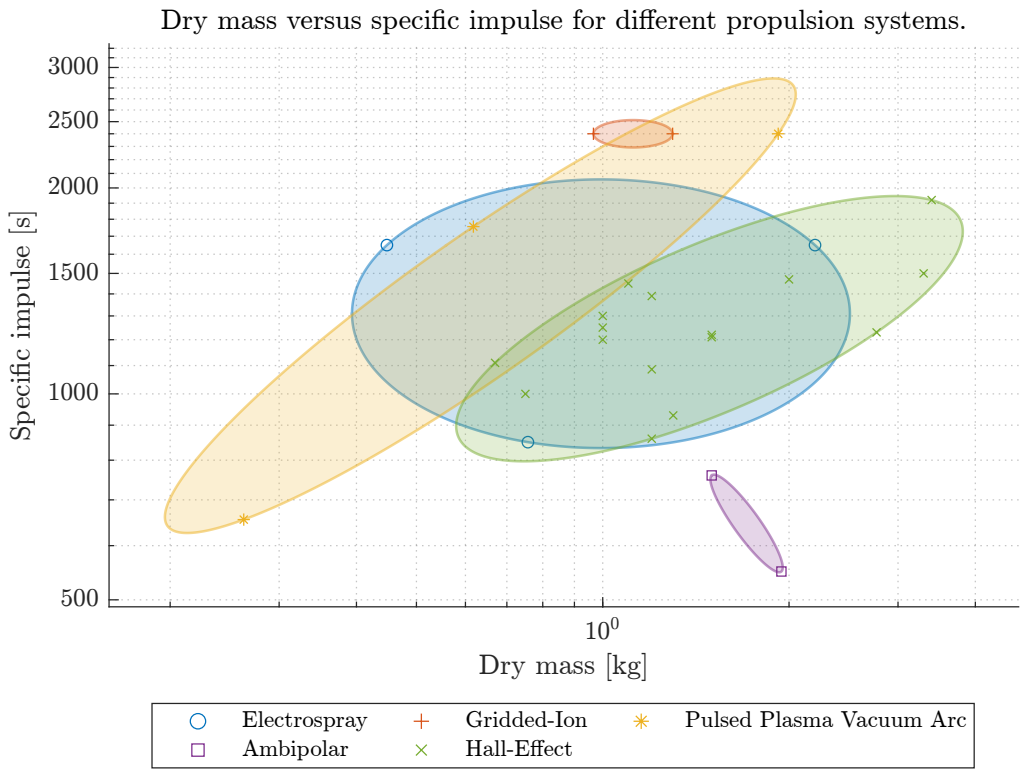

Figure C.4: This figure shows the relation between specific impulse and dry mass for different propulsion system types.

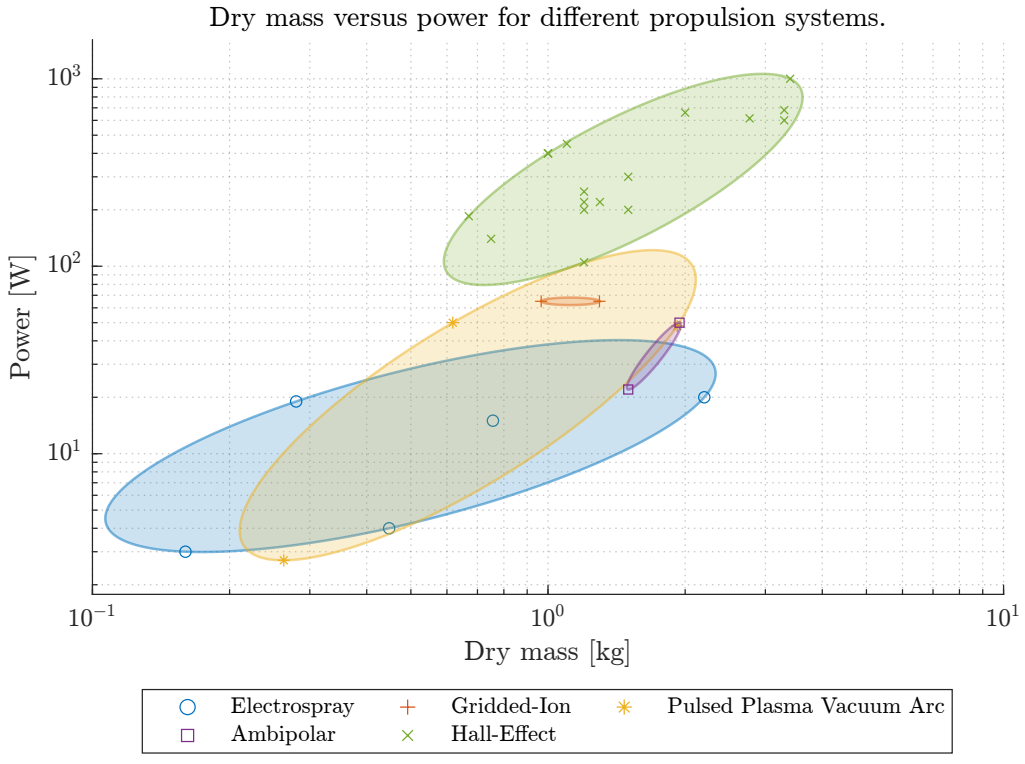

Figure C.5: This figure shows the relation between power and dry mass for different propulsion system types.

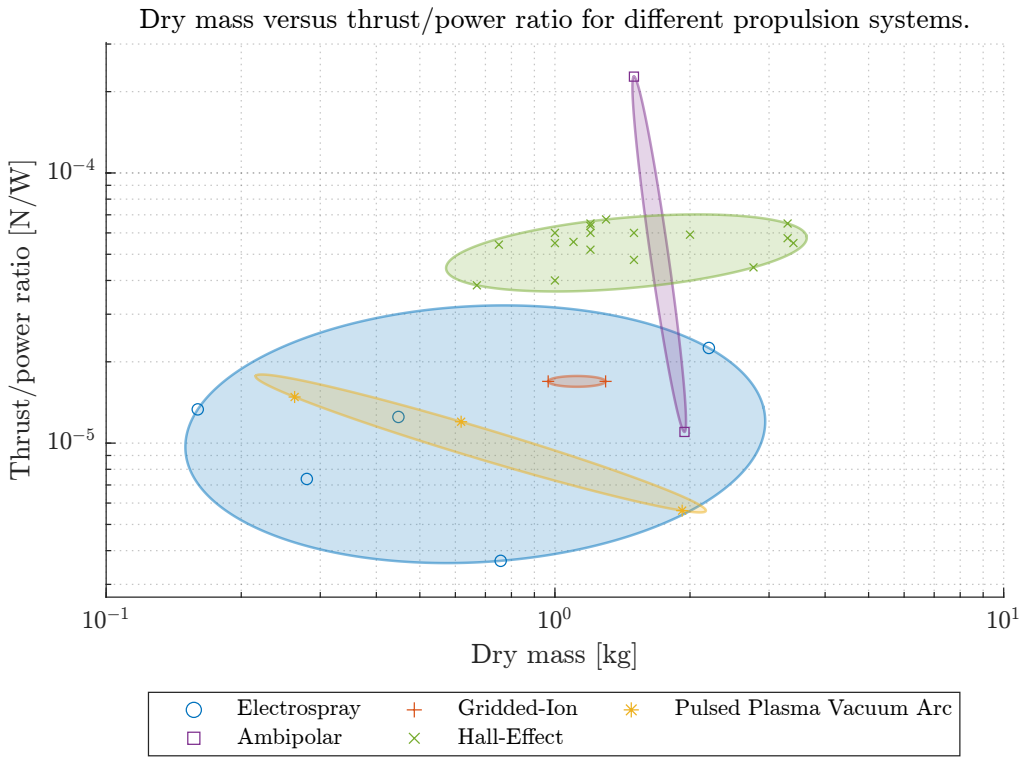

Figure C.6: This figure shows the relation between thrust-to-power ratio and dry mass for different propulsion system types.

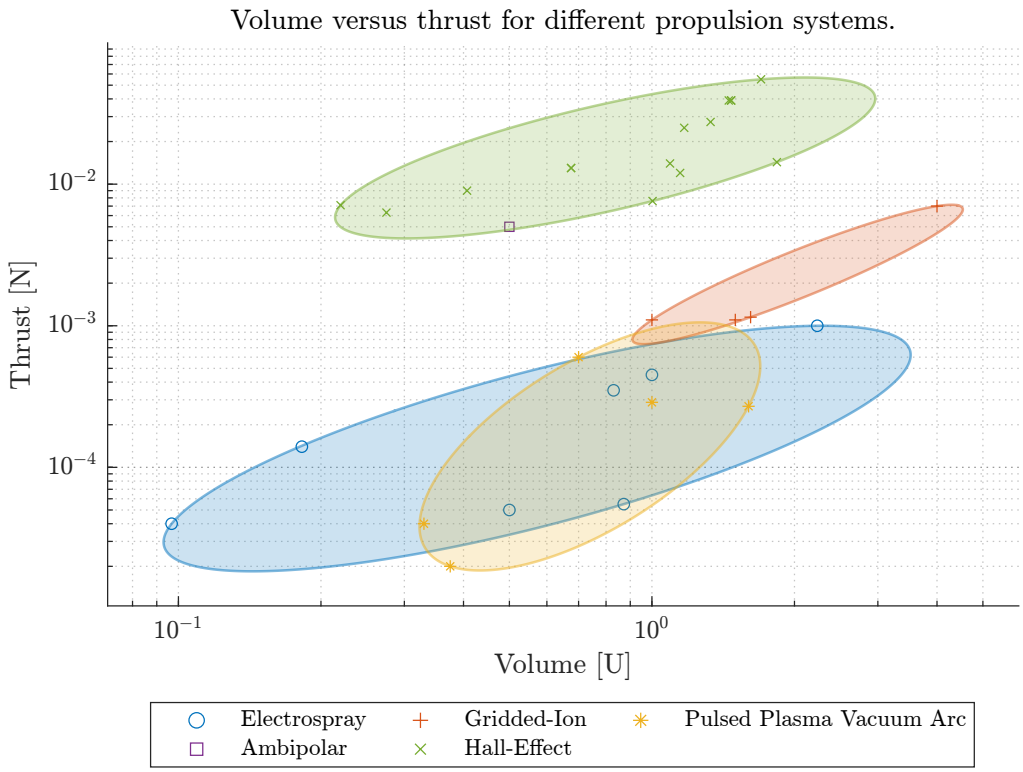

Figure C.7: This figure shows the relation between volume and thrust for different propulsion system types.

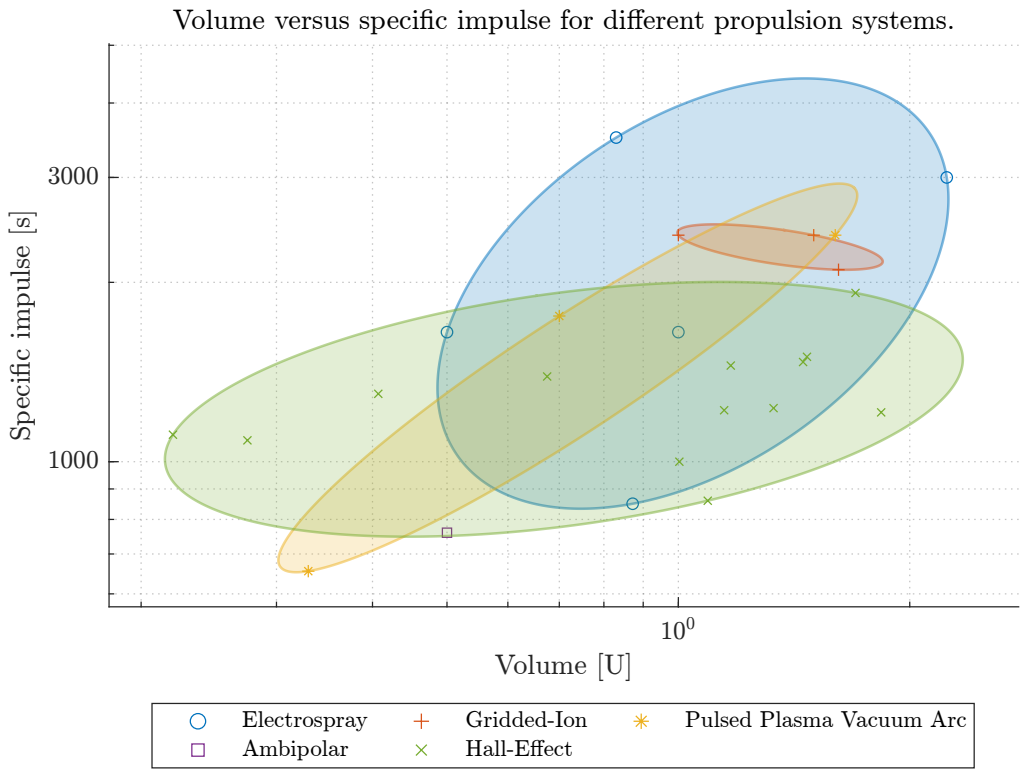

Figure C.8: This figure shows the relation between specific impulse and volume for different propulsion system types.

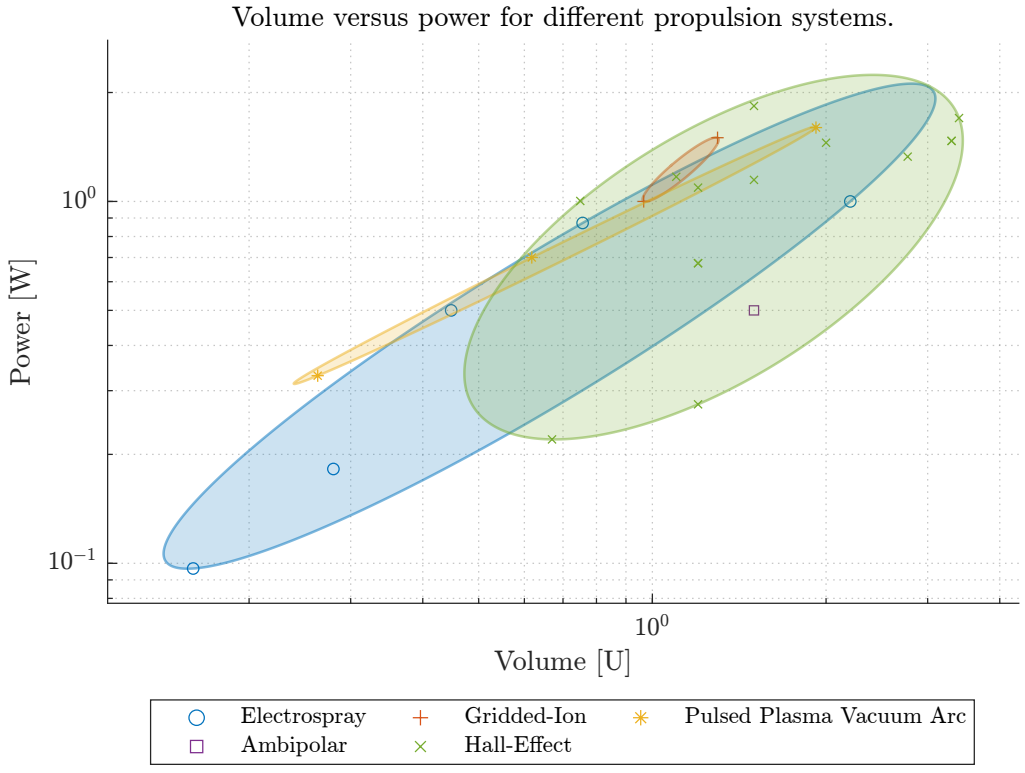

Figure C.9: This figure shows the relation between volume and power for different propulsion system types.

D

Extra relations for reaction control thruster propulsion systems

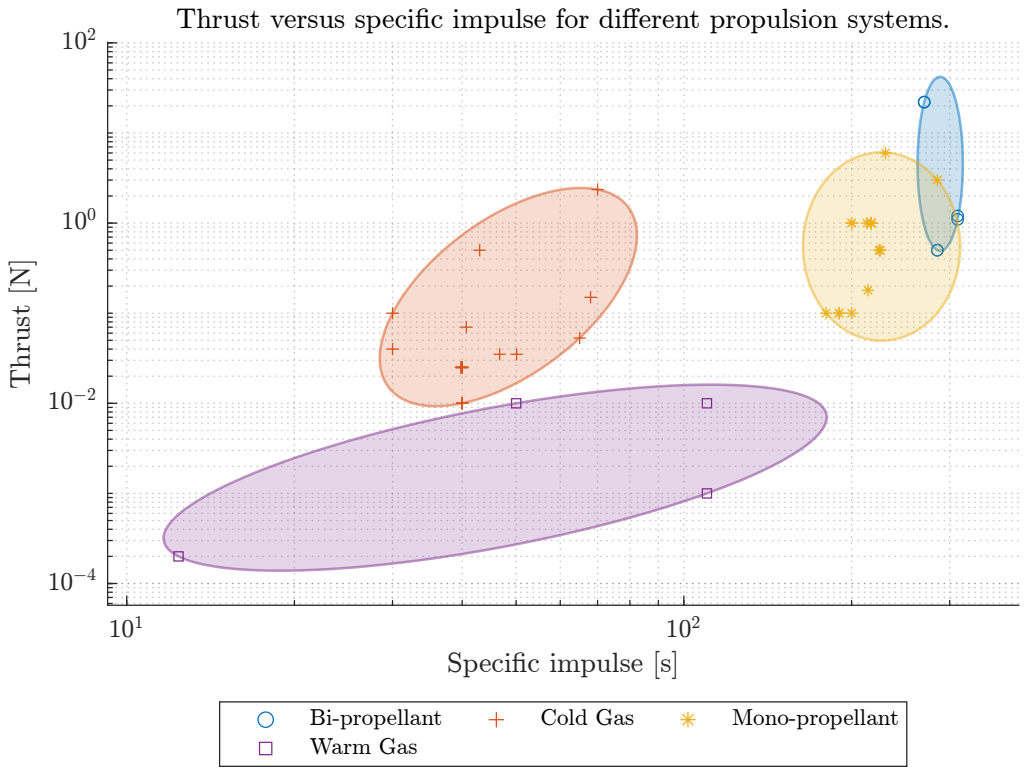

Figure D.1: This figure shows the relation between specific impulse and thrust for different reaction control propulsion system types.

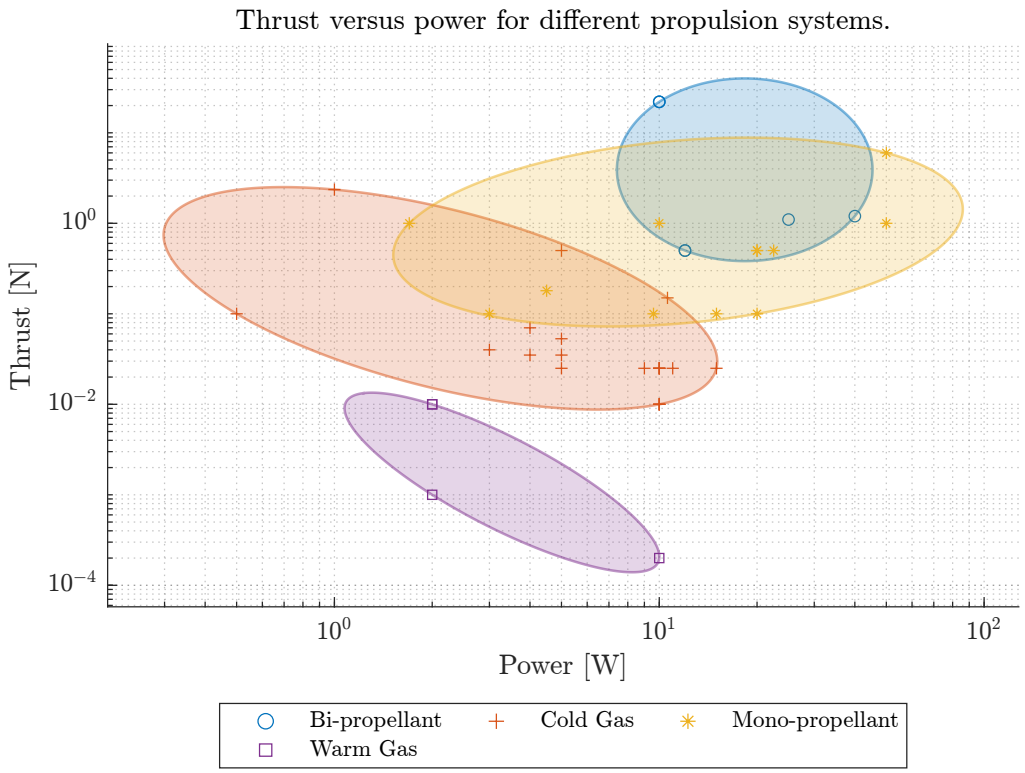

Figure D.2: This figure shows the relation between power and thrust for different reaction control propulsion system types.

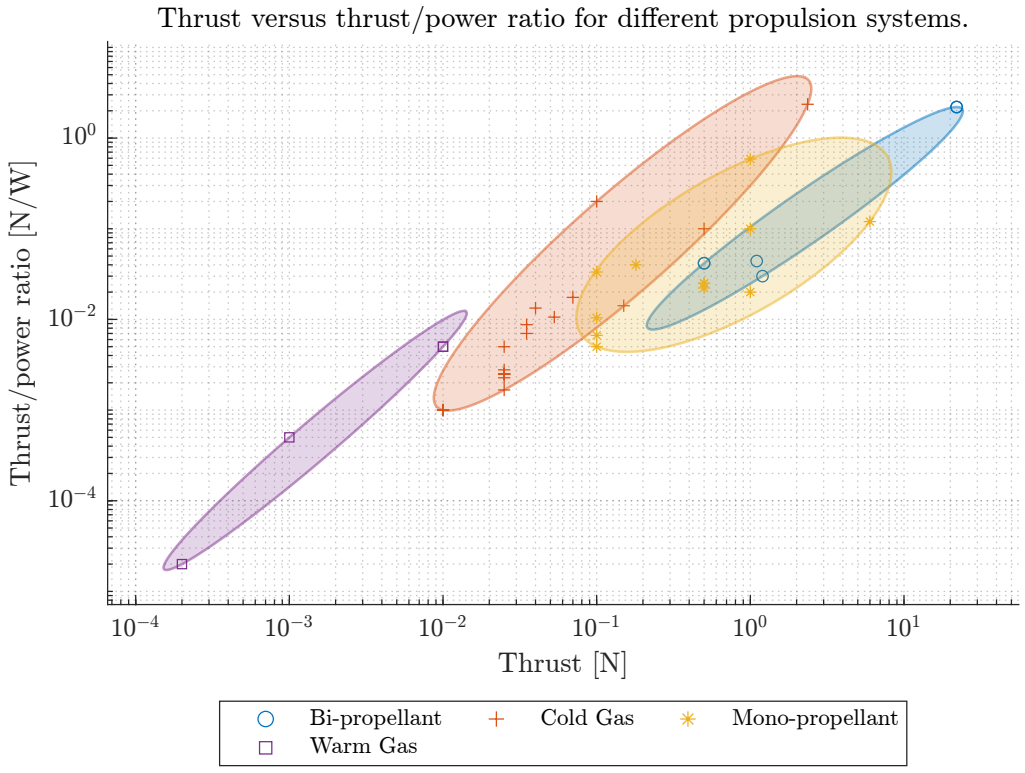

Figure D.3: This figure shows the relation between thrust and thrust power ratios for different reaction control propulsion system types.

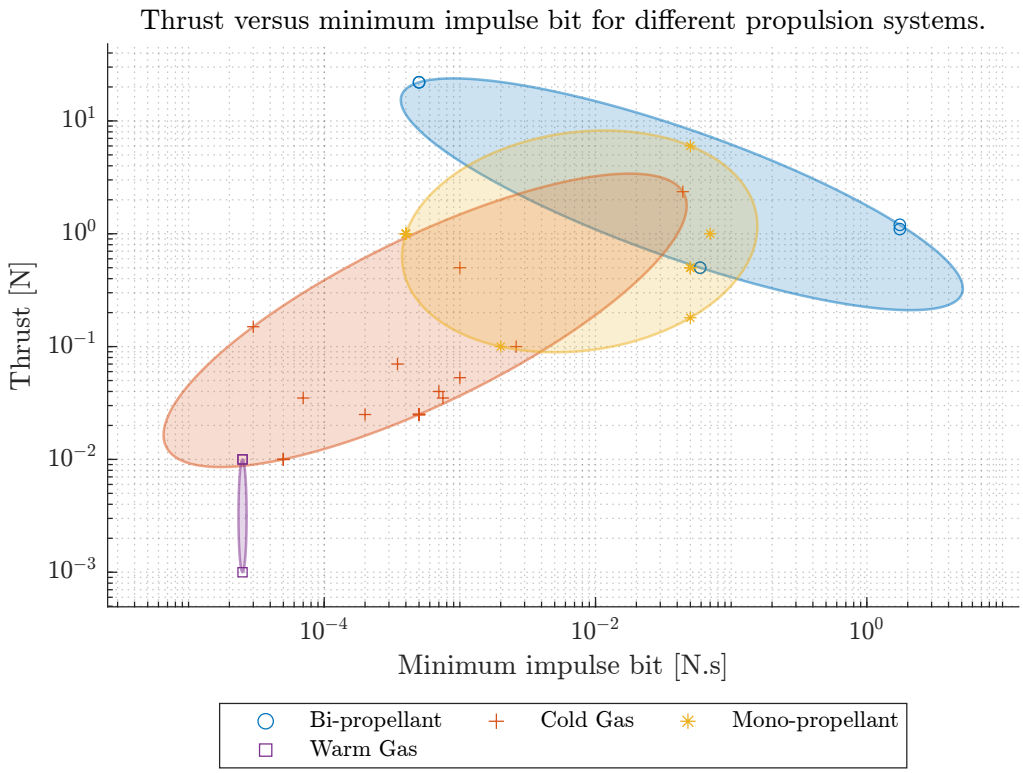

Figure D.4: This figure shows the relation between thrust and minimum impulse bit for different reaction control propulsion system types.

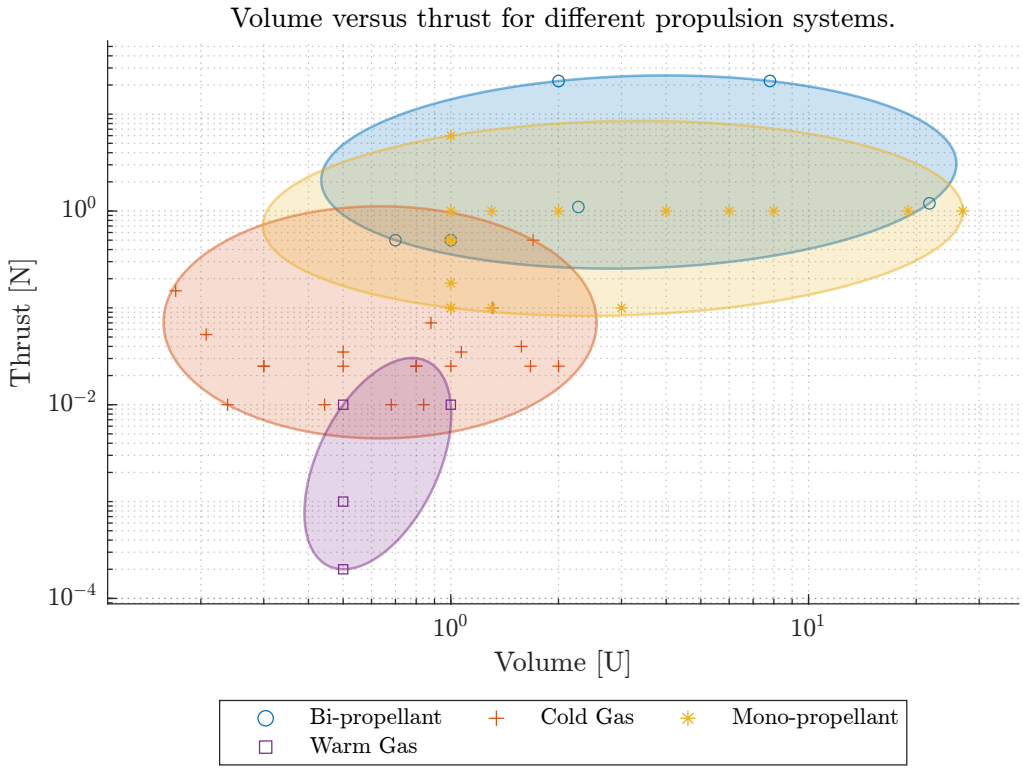

Figure D.5: This figure shows the relation between thrust and volume for different reaction control propulsion system types.

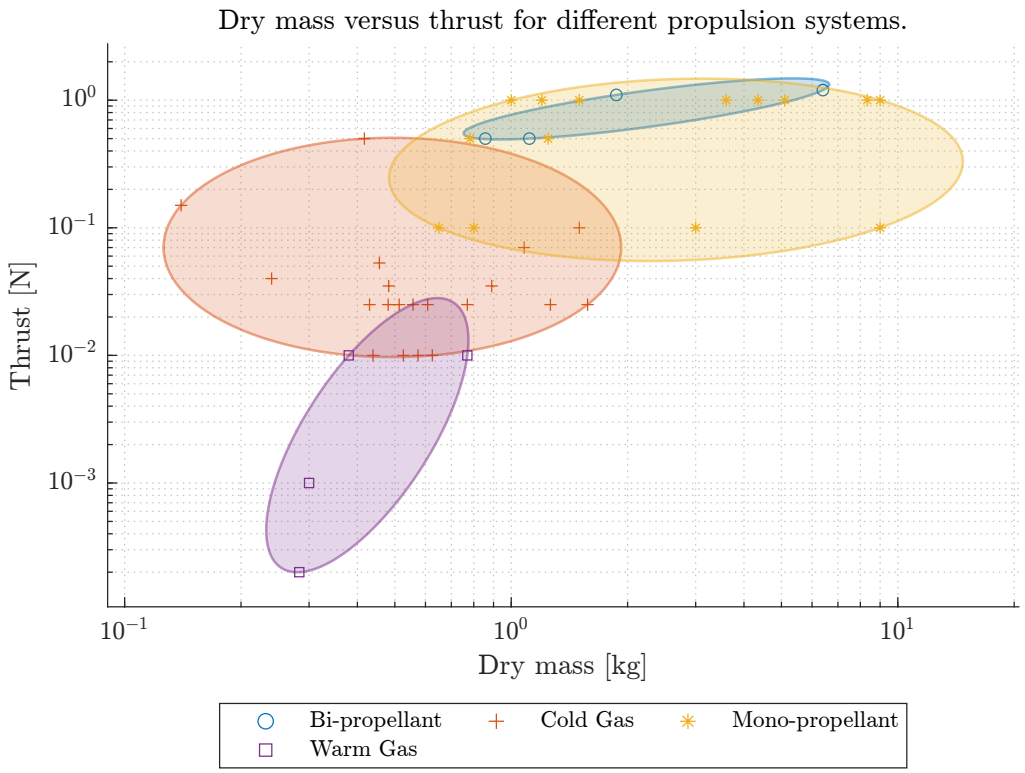

Figure D.6: This figure shows the relation between thrust and dry mass for different reaction control propulsion system types.

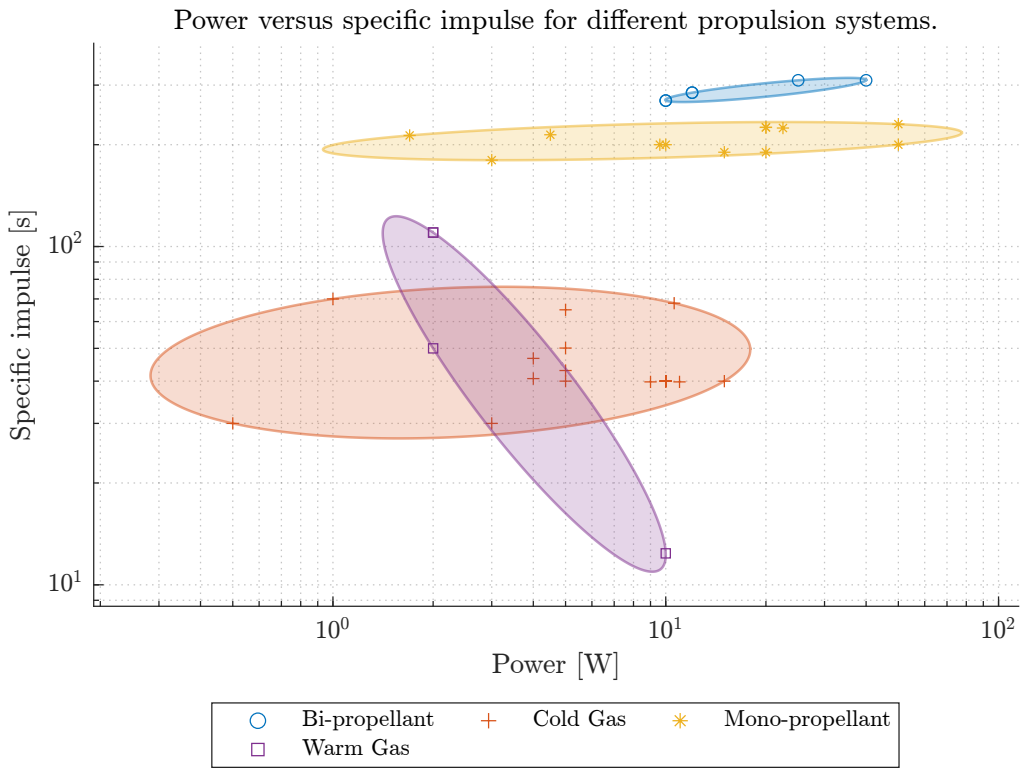

Figure D.7: This figure shows the relation between power and specific impulse for different reaction control propulsion system types.

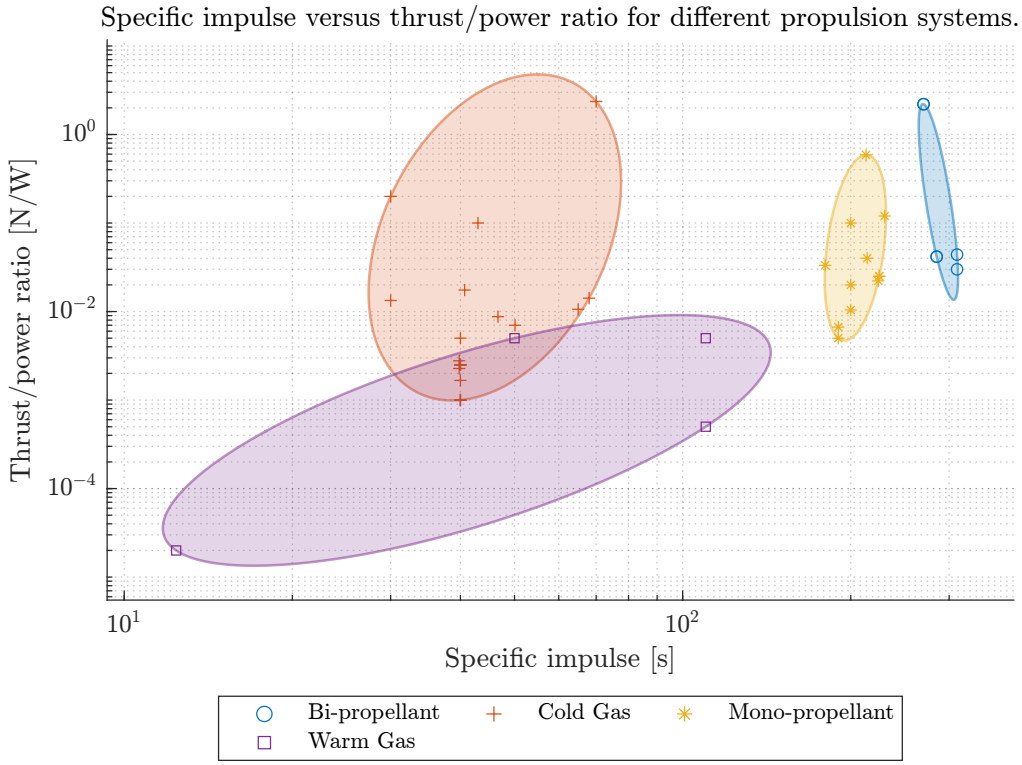

Figure D.8: This figure shows the relation between thrust-to-power ratio and specific impulse for different reaction control propulsion system types.

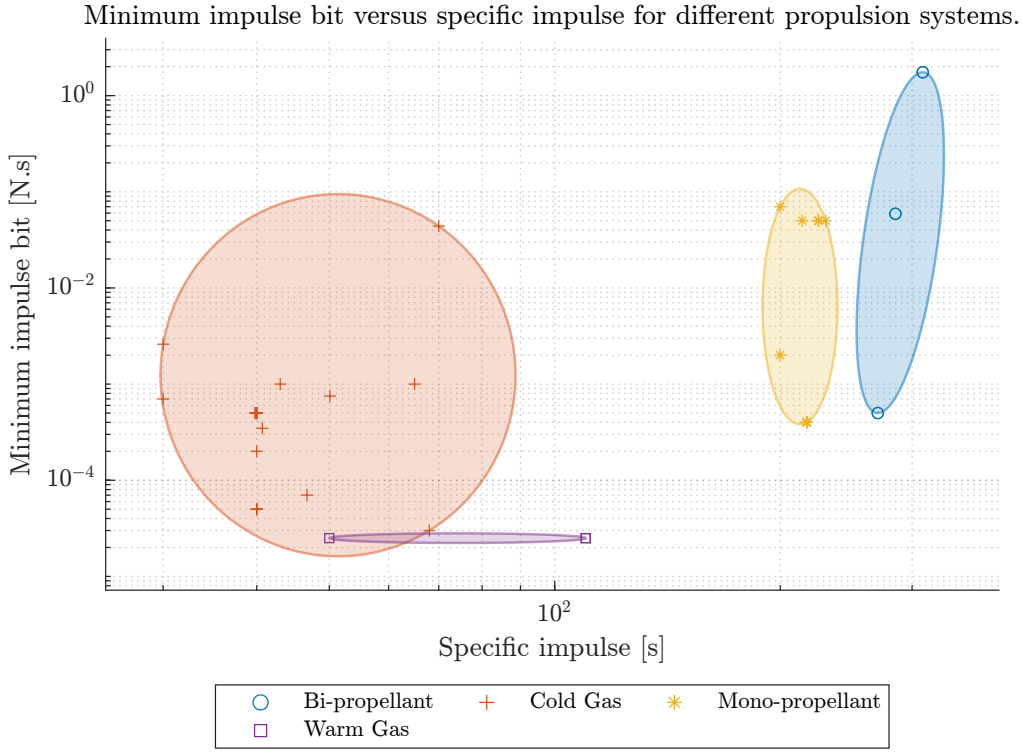

Figure D.9: This figure shows the relation between minimum impulse bit and specific impulse for different reaction control propulsion system types.

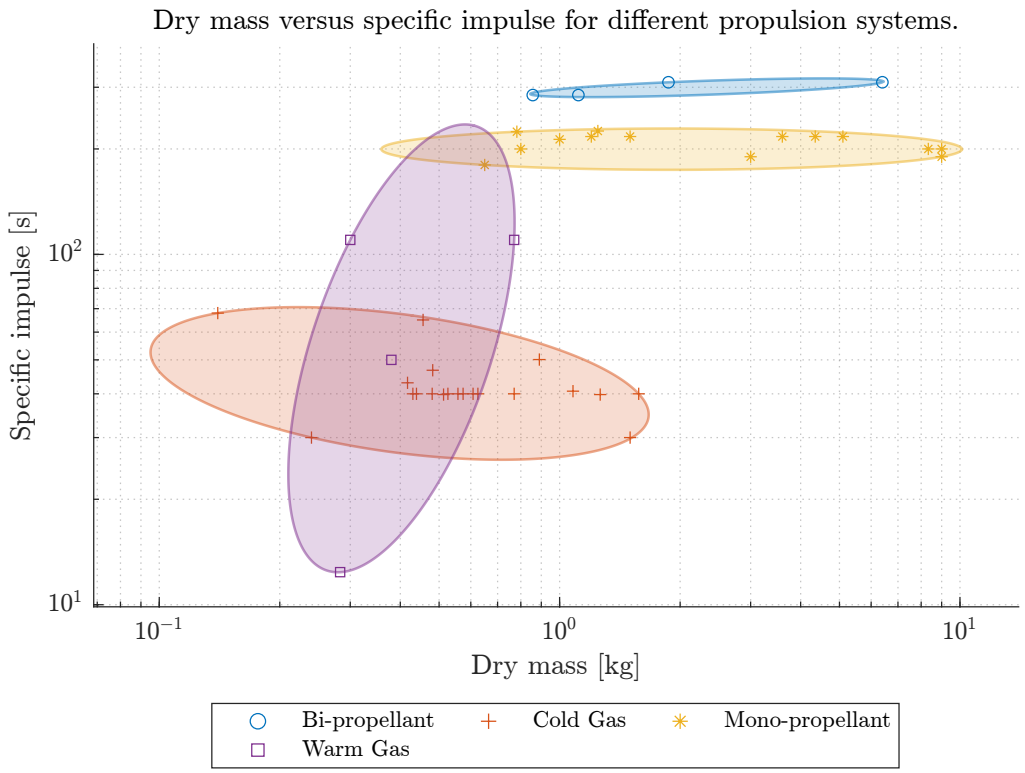

Figure D.10: This figure shows the relation between dry mass and specific impulse for different reaction control propulsion system types.

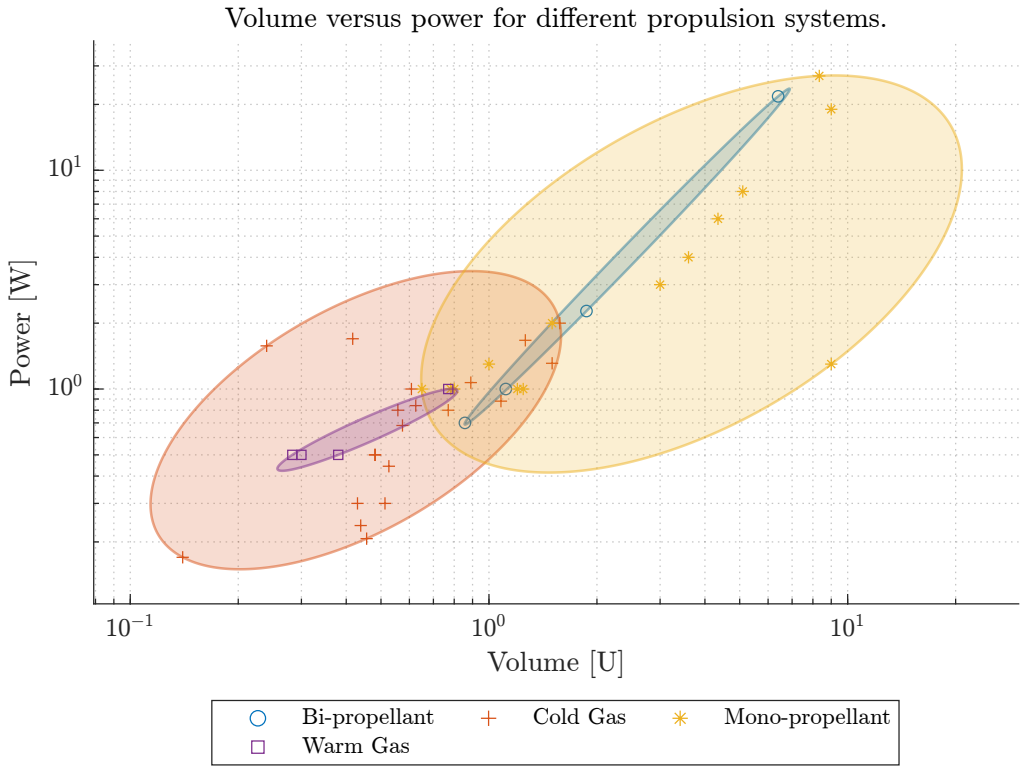

Figure D.11: This figure shows the relation between power and volume for different reaction control propulsion system types.

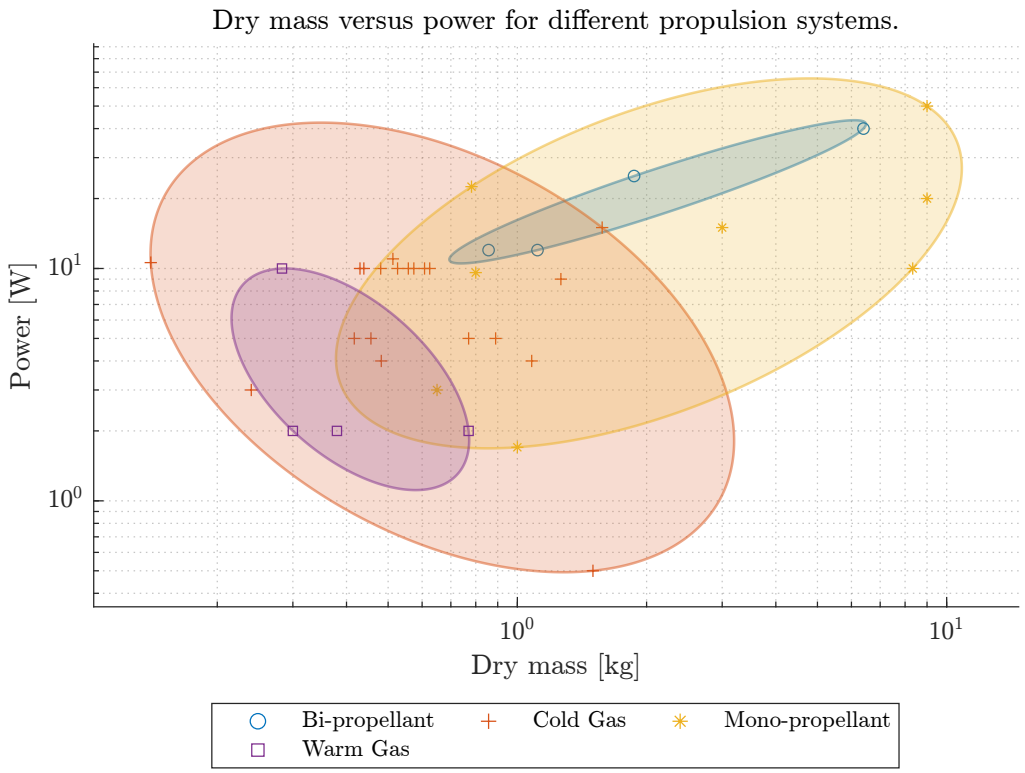

Figure D.12: This figure shows the relation between power and dry mass for different reaction control propulsion system types.

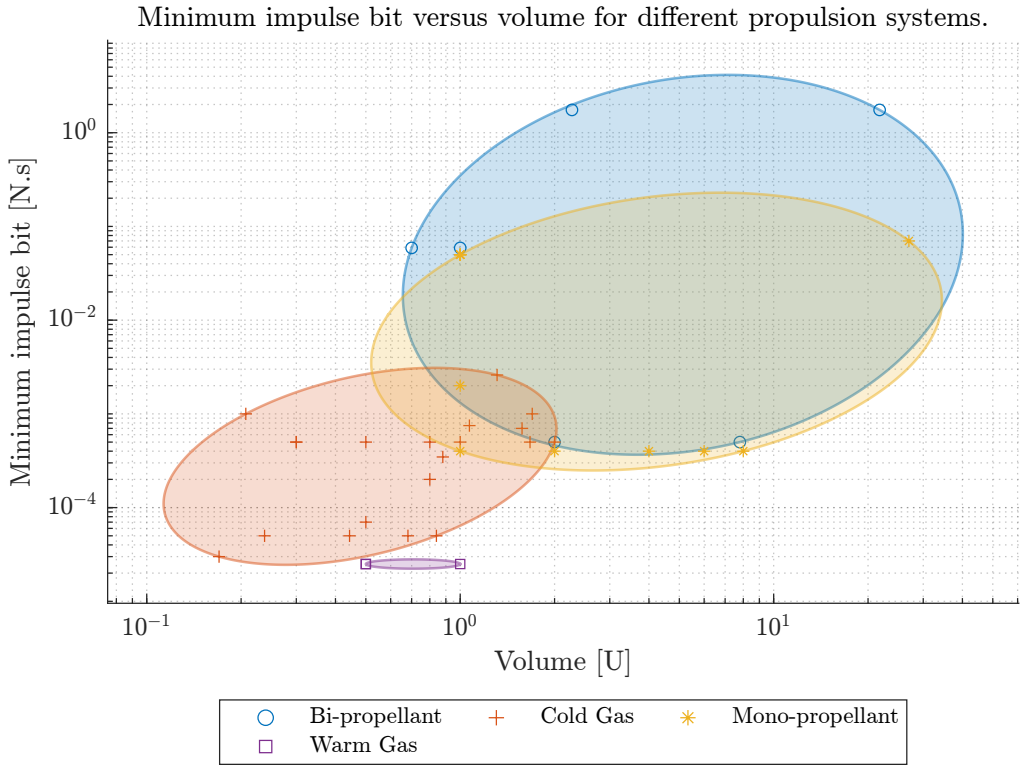

Figure D.13: This figure shows the relation between minimum impulse bit and volume for different reaction control propulsion system types.

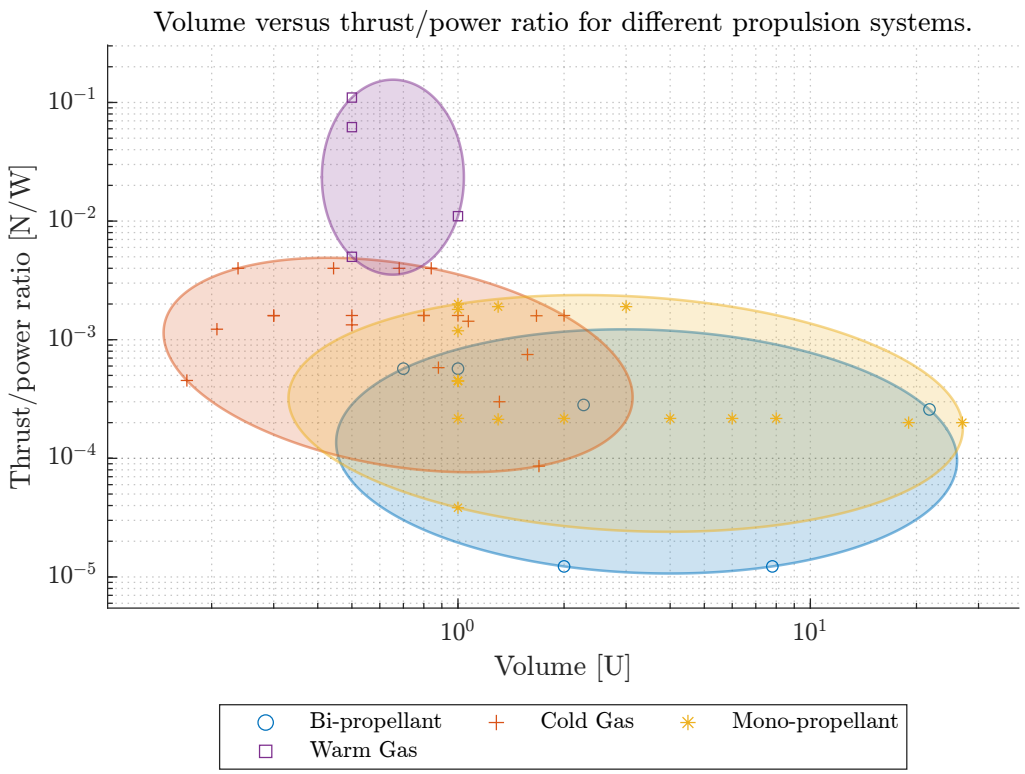

Figure D.14: This figure shows the relation between volume and thrust-to-power ratio for different reaction control propulsion system types.

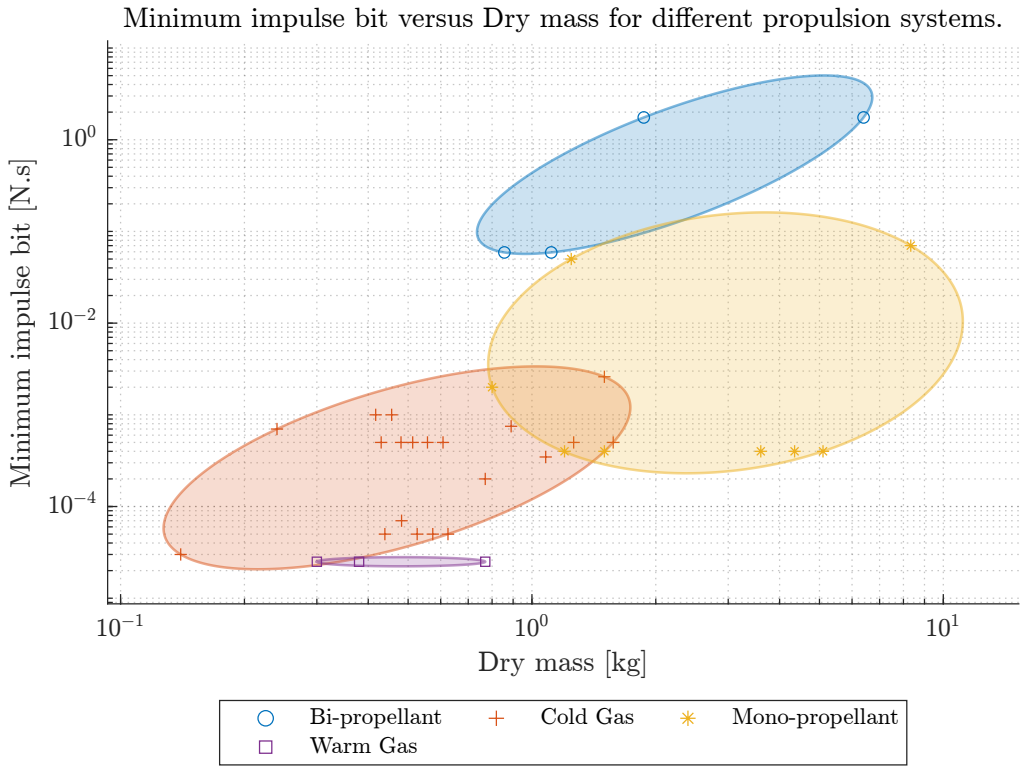

Figure D.15: This figure shows the relation between minimum impulse bit and dry mass for different reaction control propulsion system types.

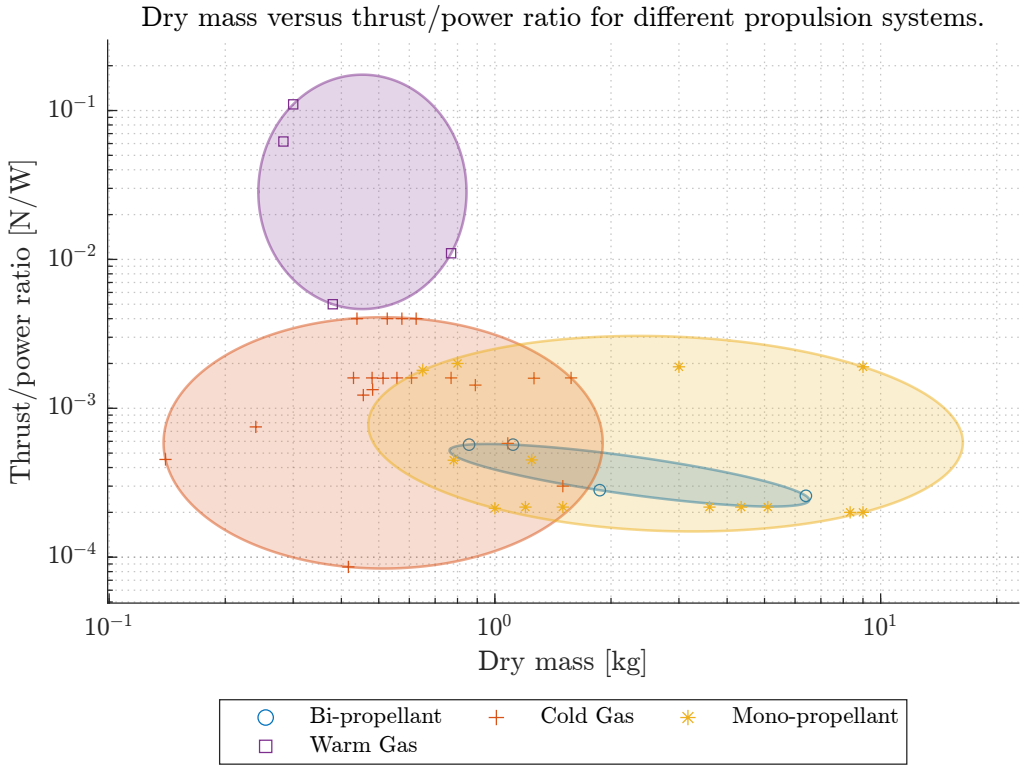

Figure D.16: This figure shows the relation between dry mass and thrust-to-power ratio for different reaction control propulsion system types.

E

Low-thrust trajectory cases results

Table E.1: Low-thrust system results for the fly-by mission to Asteroid 2020QN1.

System	Start Date	ToF (days)	Propellant mass (kg)	System dry mass (kg)	Distance (km)
PPS-X00 (1x)	Jul 28 09:14:35 2029	159.6	3.7966	3.2000	1.247×10^{-6}
SPT-70M (1x)	Sep 08 16:14:08 2029	117.3	3.9350	2.0000	2.513×10^{-5}
MaSMi (1x)	Jun 11 17:06:09 2029	206.2	3.2645	3.4000	3.505×10^{4}
NPT30-I2 RF (2x)	Sep 29 11:38:02 2028	461.5	2.4493	2.5940	4.094×10^{-6}
Metal Plasma Thruster (2x)	Apr 03 11:32:33 2028	640.5	3.4131	1.2360	3.671×10^{-6}
BIT-3 RF (1x)	Mar 08 07:06:50 2028	666.7	3.0180	1.2800	1.466×10^{-6}
IFM Micro (1x)	Aug 28 14:20:16 2027	859.4	2.3082	2.6000	2.326×10^{-6}
IFM Nano (2x)	Jul 12 23:09:03 2026	1271.0	1.9456	1.3600	7.299×10^{-7}
FPPT-1.6 (1x)	Nov 12 09:09:29 2021	2974.6	2.9196	1.9210	7.098×10^{5}
NPT30-I2 RF (1x)	Jan 30 18:04:20 2028	704.2	2.7375	1.297	3.012×10^{-6}

Table E.2: Low-thrust system results for the fly-by mission to Asteroid 163693.

System	Start Date	ToF (days)	Propellant mass (kg)	System dry mass (kg)	Distance (km)
PPS-X00 (1x)	Apr 03 17:34:40 2031	553.2676	8.0781	3.2000	1.256×10^{7}
SPT-70M (1x)	Nov 19 20:32:28 2030	688.1441	4.7612	2.0000	1.819×10^{7}
MaSMi (1x)	Dec 23 07:45:11 2031	289.6770	7.3662	3.4000	1.688×10^{7}
NPT30-I2 RF (2x)	Nov 01 13:08:28 2029	1071.5	3.1640	2.5940	8.300×10^{-3}
Metal Plasma Thruster (2x)	Sep 01 23:03:47 2029	1132.0	4.4767	1.2360	7.765×10^{3}
BIT-3 RF (1x)	Aug 14 12:41:23 2029	1150.5	3.9577	1.2800	5.694×10^{3}
IFM Micro (1x)	Jun 21 15:26:29 2028	1569.4	3.4137	2.6000	3.533×10^{4}
IFM Nano (2x)	Jan 23 16:12:59 2028	1719.3	2.8513	1.3600	1.052×10^{6}
FPPT-1.6 (1x)	Jan 15 12:05:26 2024	3188.5	3.0321	1.9210	2.226×10^{7}
NPT30-I2 RF (1x)	Jul 30 19:02:05 2029	1165.20	3.6424	1.297	4.8344×10^{3}

Table E.3: Low-thrust system results for the fly-by mission to Asteroid 2017WV13.

System	Start Date	ToF (days)	Propellant mass (kg)	System dry mass (kg)	Distance (km)
PPS-X00 (1x)	Apr 24 09:49:04 2931715 2032	160.5909	8.9888	3.2000	3.750×10^{2}
SPT-70M (1x)	Apr 18 07:37:05 2032	166.6826	8.8780	2.0000	4.631×10^{2}
MaSMi (1x)	Jul 05 15:17:32 2031	454.3628	4.3245	3.4000	5.439×10^{2}
NPT30-I2 RF (2x)	Oct 02 17:17:24 2030	730.2796	4.4111	2.5940	8.832×10^{4}
Metal Plasma Thruster (2x)	Jun 18 13:57:41 2029	1201.40	4.9835	1.2360	2.795×10^{-4}
BIT-3 RF (1x)	Jun 15 12:34:21 2029	1204.50	4.5937	1.2800	3.275×10^{-6}
IFM Micro (1x)	Mar 13 11:53:17 2028	1663.50	3.6391	2.6000	1.009×10^{4}
IFM Nano (2x)	Dec 26 08:02:06 2026	2106.70	3.1786	1.3600	6.442×10^{-6}
FPPT-1.6 (1x)	Aug 13 16:46:12 2024	2971.30	2.9381	1.9210	3.804×10^{7}
NPT30-I2 RF (1x)	Oct 06 02:13:47 2027	1822.90	3.7442	1.297	2.397×10^{3}

Table E.4: Low-thrust system results for the fly-by mission to Asteroid 2012BX34.

System	Start Date	ToF (days)	Prop. mass (kg)	System dry mass (kg)	Volume (U)	Distance (km)
PPS-X00 (1x)	Feb 25 06:12:08 2031	157.7416	6.9547	3.2000	6.518	3.160×10^{-6}
SPT-70M (1x)	Mar 21 05:25:37 2031	133.7739	7.5232	2.0000	3.953	1.720×10^{-6}
MaSMi (1x)	Feb 04 01:57:41 2031	178.9183	6.0105	3.4000	3.170	1.975×10^{3}
NPT30-I2 RF (2x)	Nov 05 17:23:49 2029	634.2751	4.7191	2.5940	2.783	9.478×10^{-7}
Metal Plasma Thruster (2x)	Jan 30 08:22:46 2027	1644.7	5.3459	1.2360	1.888	3.111×10^{4}
BIT-3 RF (1x)	Jul 02 06:45:27 2027	1491.7	4.4616	1.2800	2.208	6.568×10^{-5}
IFM Micro (1x)	Jul 16 06:10:43 2027	1477.7	3.2745	2.6000	2.516	7.979×10^{6}
IFM Nano (2x)	Apr 16 20:38:12 2025	2291.0	3.8050	1.3600	2.141	6.217×10^{5}
FPPT-1.6 (1x)	Aug 15 14:20:10 2026	1812.4	1.7732	1.9210	2.047	6.804×10^{7}
NPT30-I2 RF (1x)	Nov 23 18:07:04 2027	1347.20	4.1446	1.297	1.748	2.0116×10^{-5}

E.1. PPS-X00 (1x)

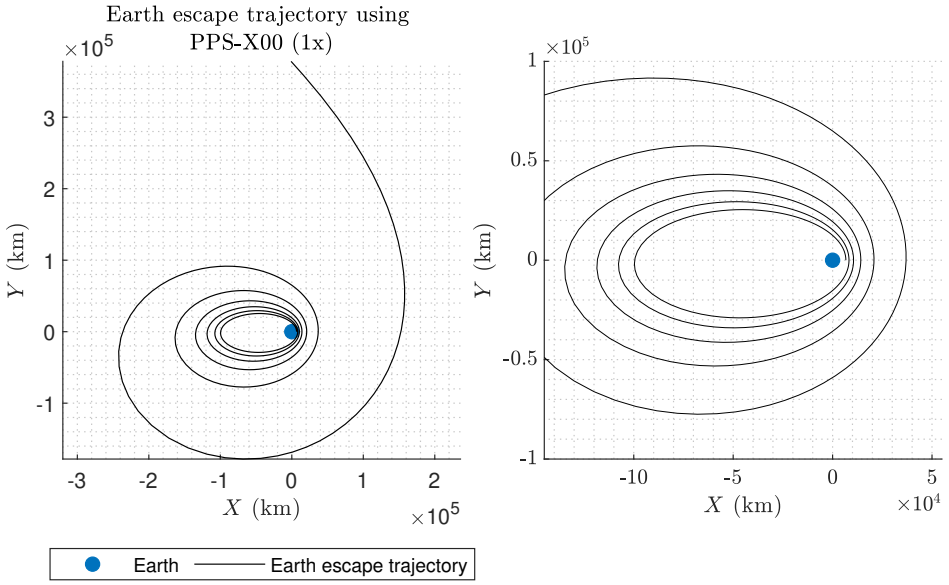

Figure E.1: Earth escape trajectory of the PPS-X00 propulsion system. The left-side figure contains the complete Earth escape trajectory and the right-side figure contains a zoomed-in Earth escape trajectory.

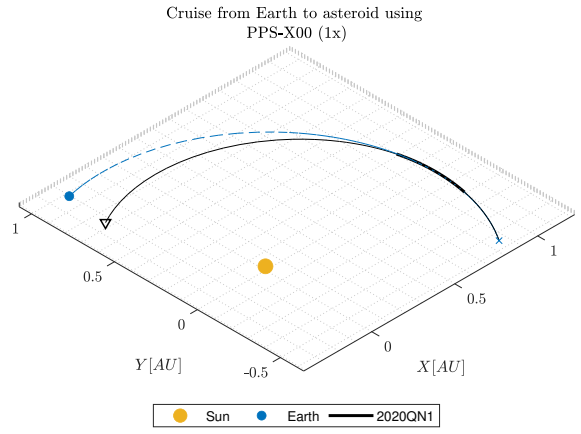

(a) Interplanetary cruise to 2020QN1. A successful fly-by trajectory could be found.

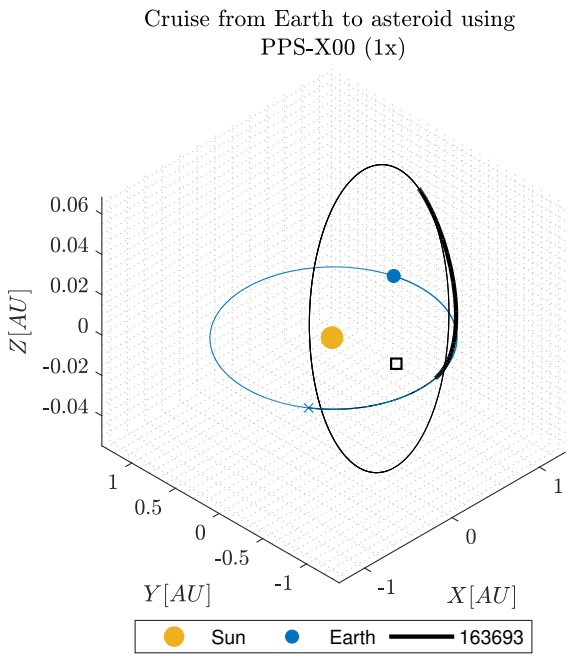

(b) Interplanetary cruise to 163693. No successful fly-by trajectory could be found.

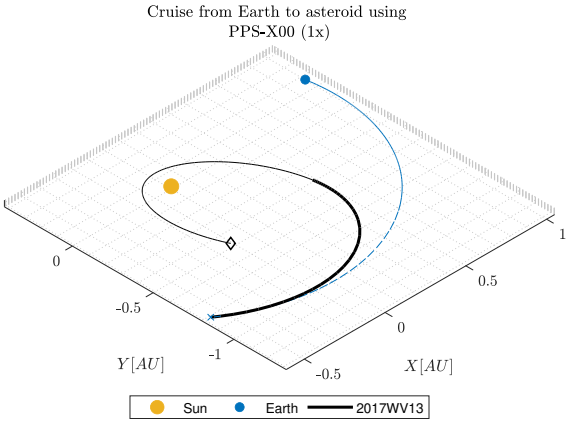

(c) No successful interplanetary trajectory for a fly-by mission to the celestial object 2017WV13 has been found. The propulsion system utilized a gravitationally assisted maneuver around the Sun to achieve the desired optimal trajectory. This trajectory brings the satellite dangerously close to the Sun, therefore it is considered unfeasible.

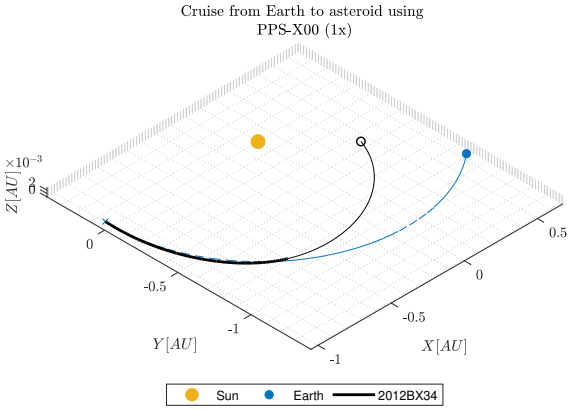

(d) Interplanetary cruise to 2012BX34. A successful fly-by trajectory could be found.

Figure E.2: Trajectories to the four specified objective asteroids using the PPS-X00 propulsion system. Thicker parts in the interplanetary trajectory indicate that the system is thrusting at full throttle and thinner parts indicate the system is not thrusting.

E.2. SPT-70M (1x)

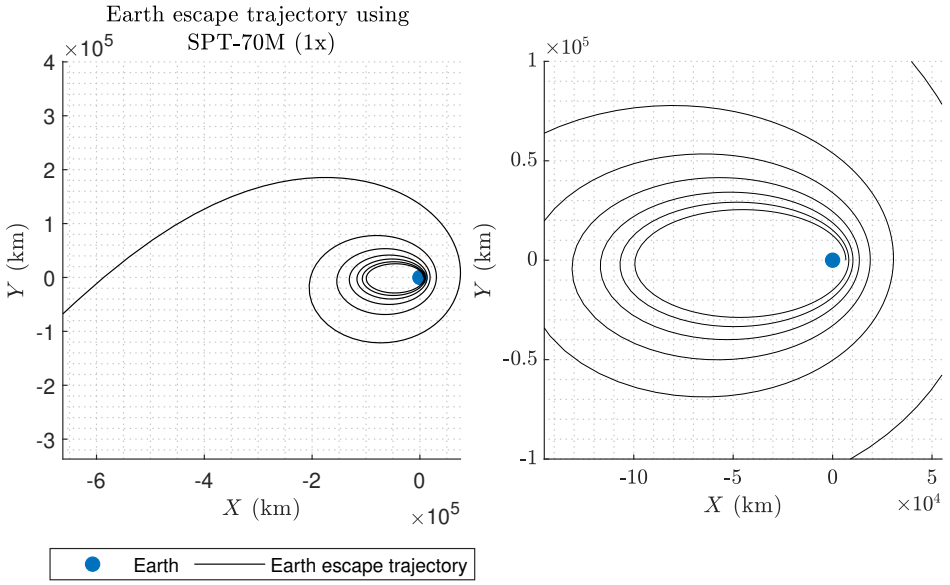

Figure E.3: Earth escape trajectory of the SPT-70M propulsion system. The left-side figure contains the complete Earth escape trajectory and the right-side figure contains a zoomed-in Earth escape trajectory.

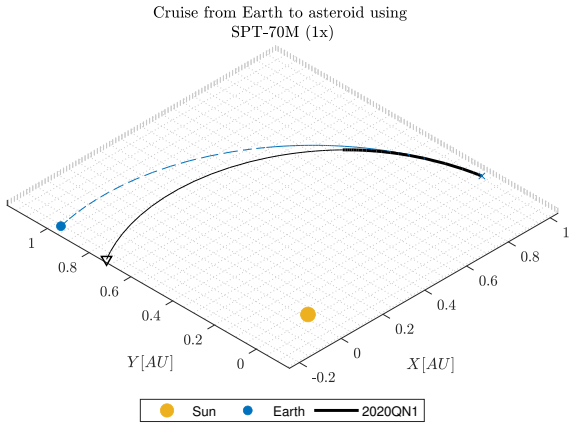

(a) Interplanetary cruise to 2020QN1. A successful fly-by trajectory could be found.

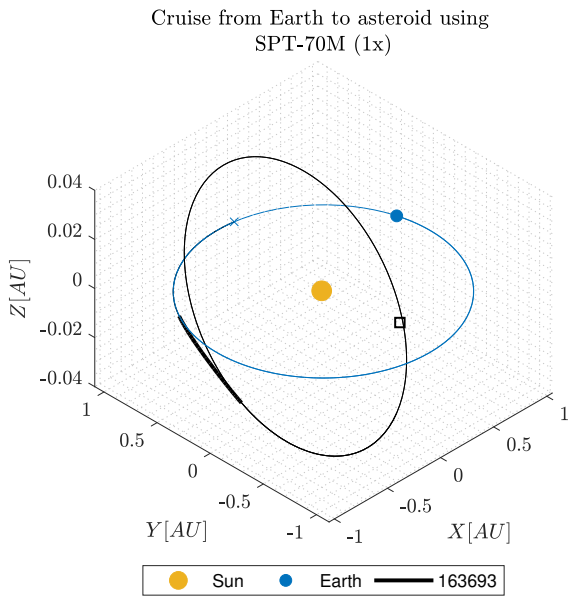

(b) Interplanetary cruise to 163693. No successful fly-by trajectory could be found.

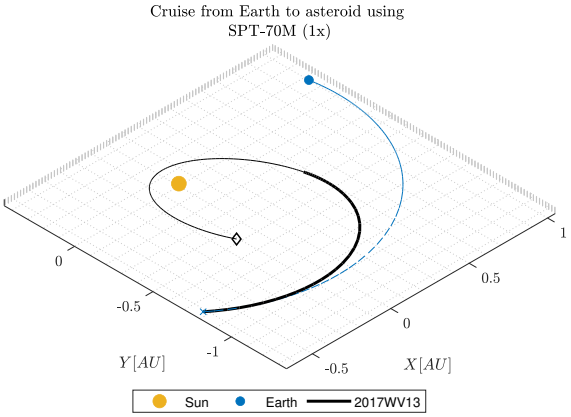

(c) No successful interplanetary trajectory for a fly-by mission to the celestial object 2017WV13 has been found. The propulsion system utilized a gravitationally assisted maneuver around the Sun to achieve the desired optimal trajectory. This trajectory brings the satellite dangerously close to the Sun, therefore it is considered unfeasible.

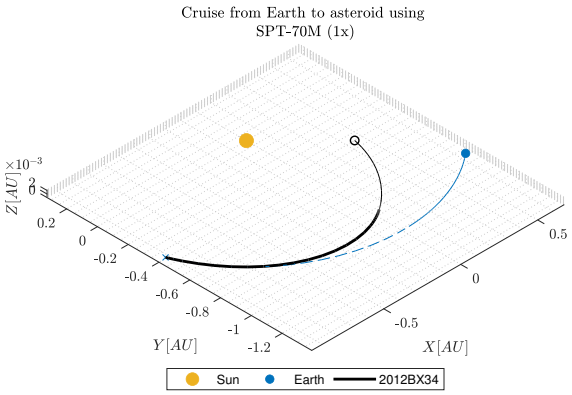

(d) Interplanetary cruise to 2012BX34. A successful fly-by trajectory could be found.

Figure E.4: Trajectories to the four specified objective asteroids using the SPT-70M propulsion system. Thicker parts in the interplanetary trajectory indicate that the system is thrusting at full throttle and thinner parts indicate the system is not thrusting.

E.3. MaSMi (1x)

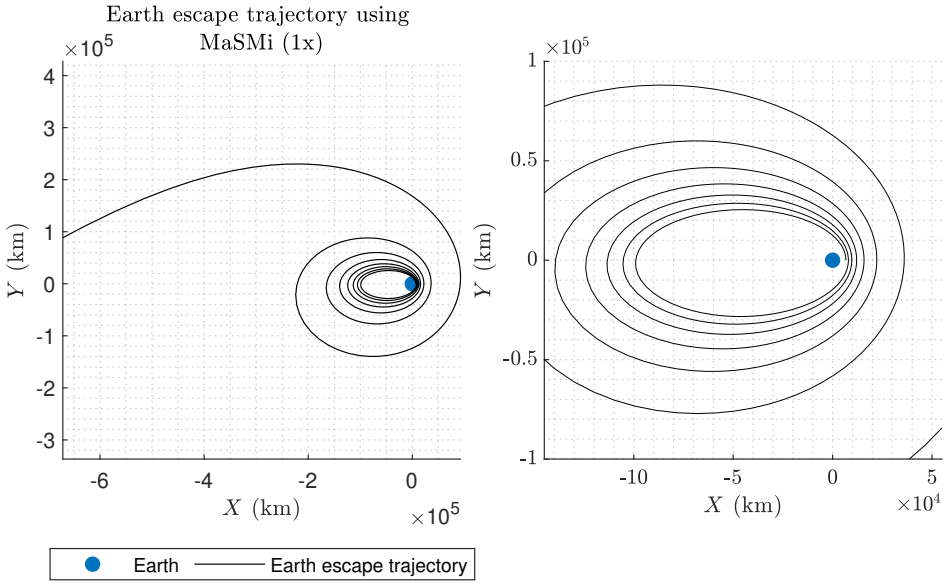

Figure E.5: Earth escape trajectory of the MaSMi propulsion system. The left-side figure contains the complete Earth escape trajectory and the right-side figure contains a zoomed-in Earth escape trajectory.

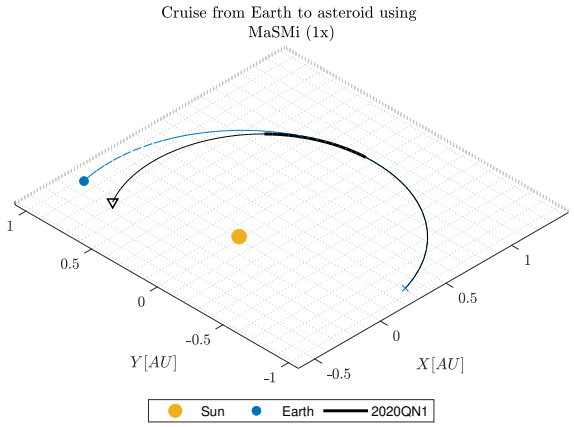

(a) Interplanetary cruise to 2020QN1. A successful fly-by trajectory could be found.

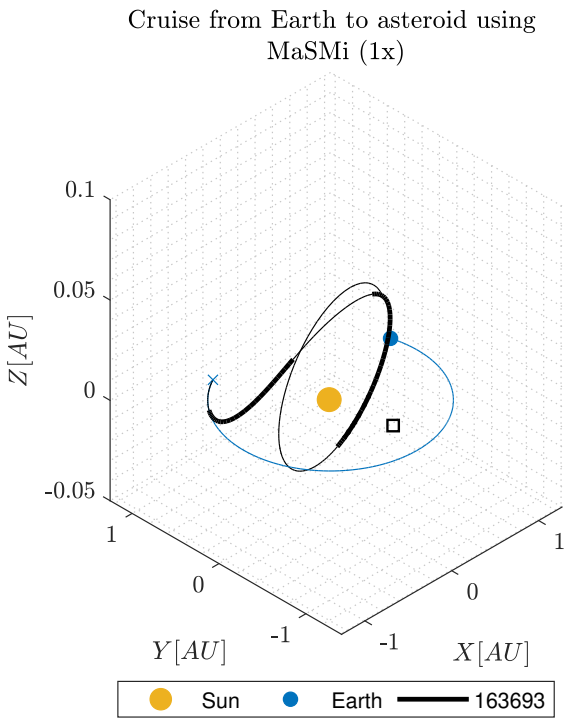

(b) Interplanetary cruise to 163693. No successful fly-by trajectory could be found.

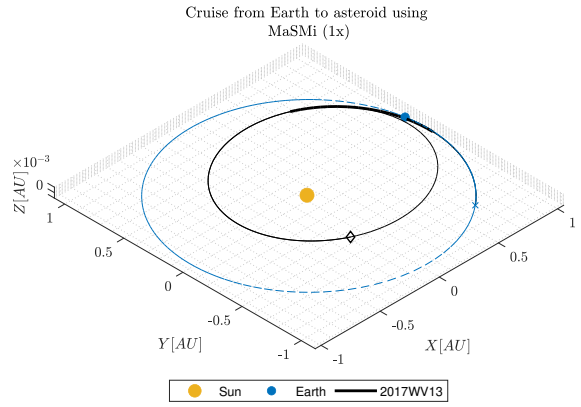

(c) A successful interplanetary trajectory for a fly-by mission to the celestial object 2017WV13 could be found. Compared to PPS-X00 and SPT-70M the MasMi solution does not require a gravitationally assisted maneuver around the Sun.

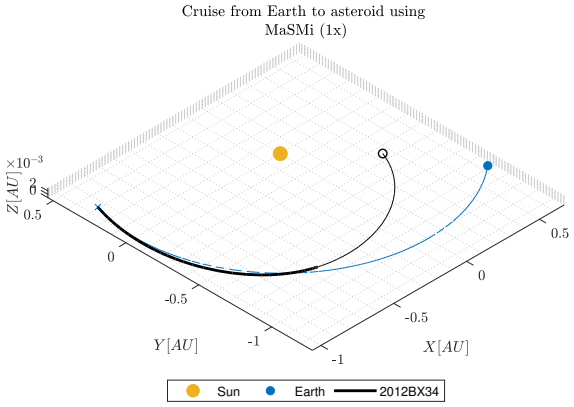

(d) Interplanetary cruise to 2012BX34. A successful fly-by trajectory could be found.

Figure E.6: Trajectories to the four specified objective asteroids using the MaSMi propulsion system. Thicker parts in the interplanetary trajectory indicate that the system is thrusting at full throttle and thinner parts indicate the system is not thrusting.

E.4. NPT30-I2 RF (2x)

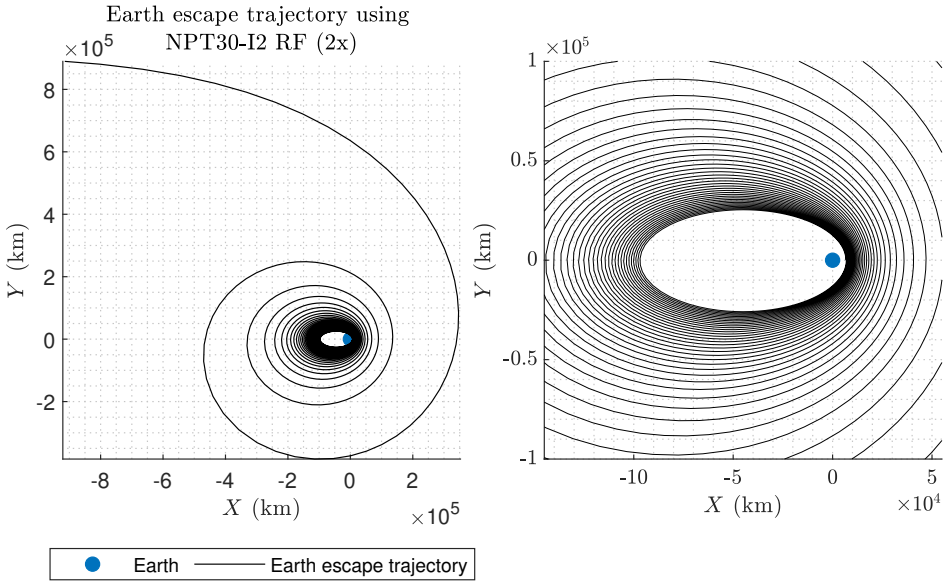

Figure E.7: Earth escape trajectory of the NPT30-I2 RF propulsion system. The left-side figure contains the complete Earth escape trajectory and the right-side figure contains a zoomed-in Earth escape trajectory.

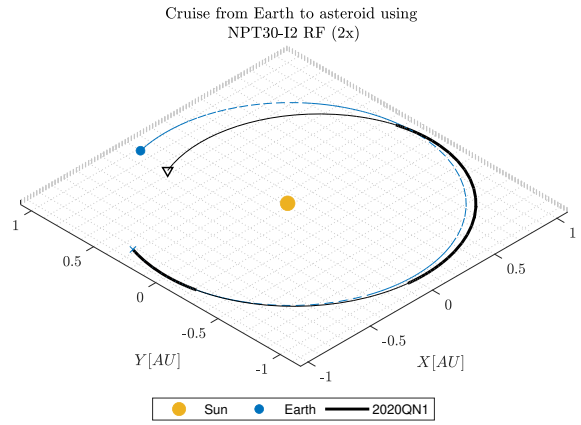

(a) Interplanetary cruise to 2020QN1. A successful fly-by trajectory could be found.

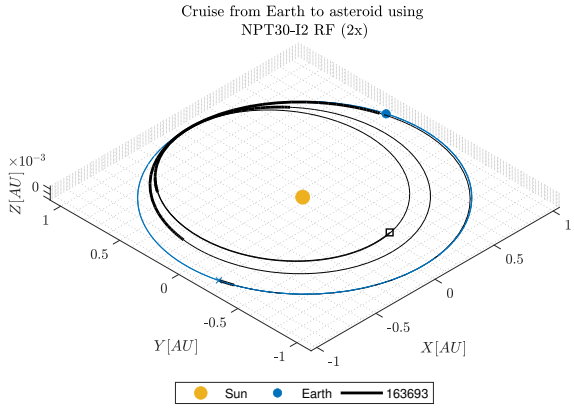

(b) Interplanetary cruise to 163693. A successful fly-by trajectory could be found.

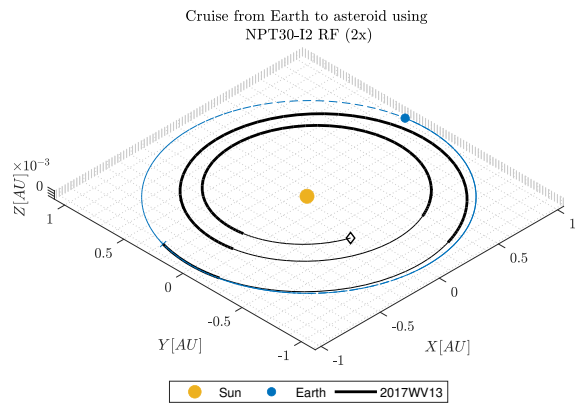

(c) A successful interplanetary trajectory for a fly-by mission to the celestial object 2017WV13 could be found.

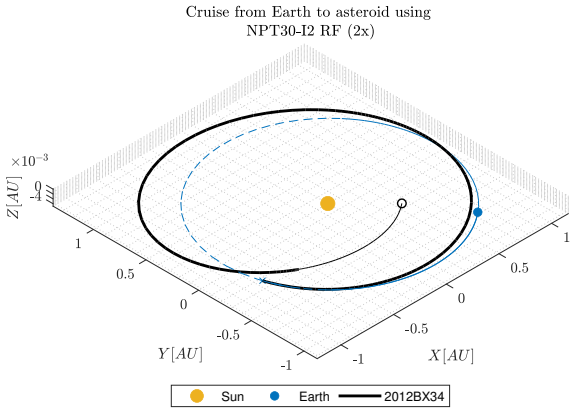

(d) Interplanetary cruise to 2012BX34. A successful fly-by trajectory could be found.

Figure E.8: Trajectories to the four specified objective asteroids using the NPT30-I2 RF propulsion system. Thicker parts in the interplanetary trajectory indicate that the system is thrusting at full throttle and thinner parts indicate the system is not thrusting.

E.5. Metal Plasma Thruster (2x)

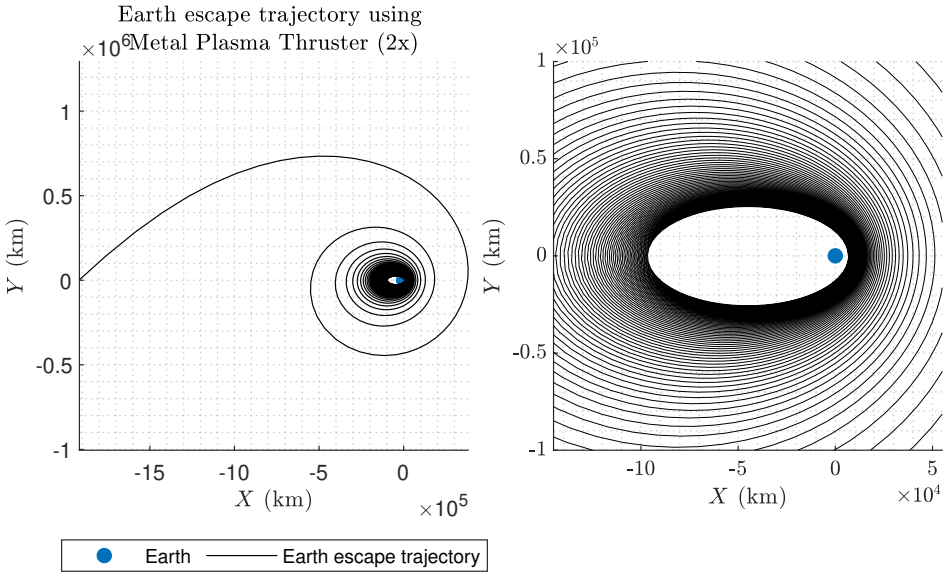

Figure E.9: Earth escape trajectory of the Metal Plasma Thruster propulsion system. The left-side figure contains the complete Earth escape trajectory and the right-side figure contains a zoomed-in Earth escape trajectory.

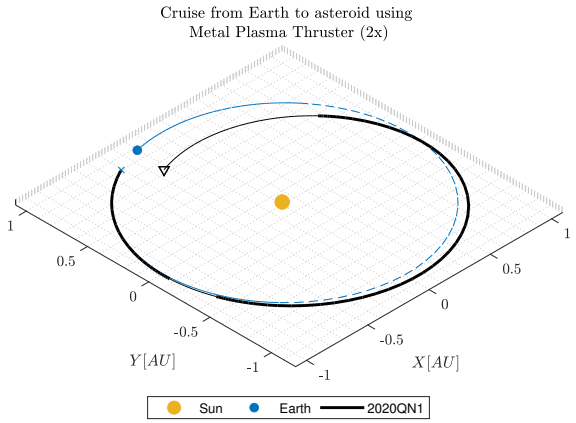

(a) Interplanetary cruise to 2020QN1. A successful fly-by trajectory could be found.

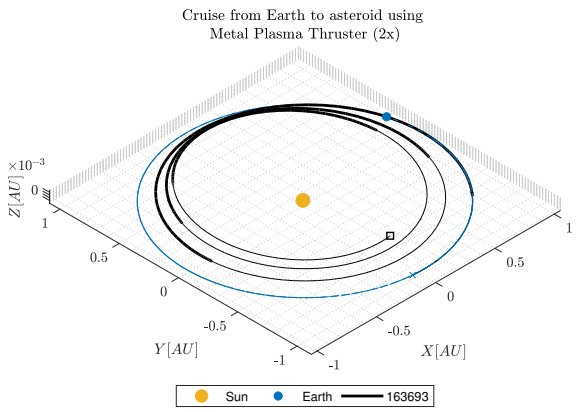

(b) Interplanetary cruise to 163693. A successful fly-by trajectory could be found.

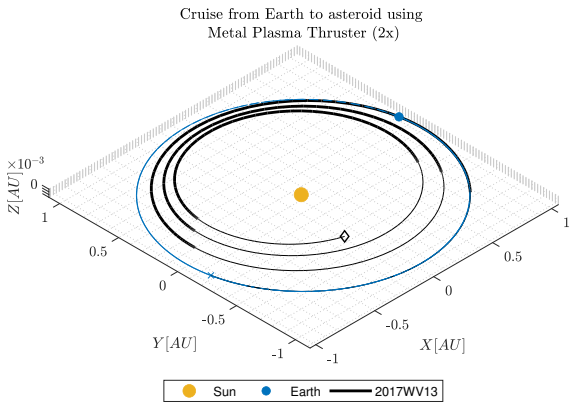

(c) A successful interplanetary trajectory for a fly-by mission to the celestial object 2017WV13 could be found.

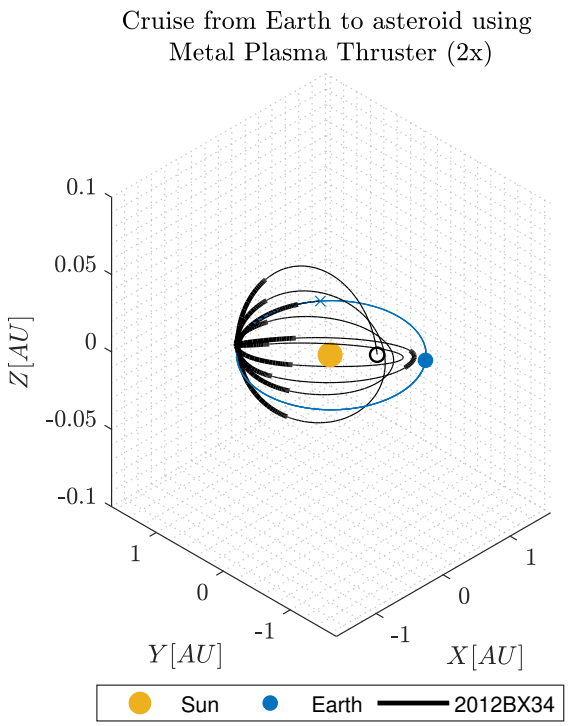

(d) Interplanetary cruise to 2012BX34. A successful fly-by trajectory could be found.

Figure E.10: Trajectories to the four specified objective asteroids using the Metal Plasma Thruster propulsion system. Thicker parts in the interplanetary trajectory indicate that the system is thrusting at full throttle and thinner parts indicate the system is not thrusting.

E.6. BIT-3 RF (1x)

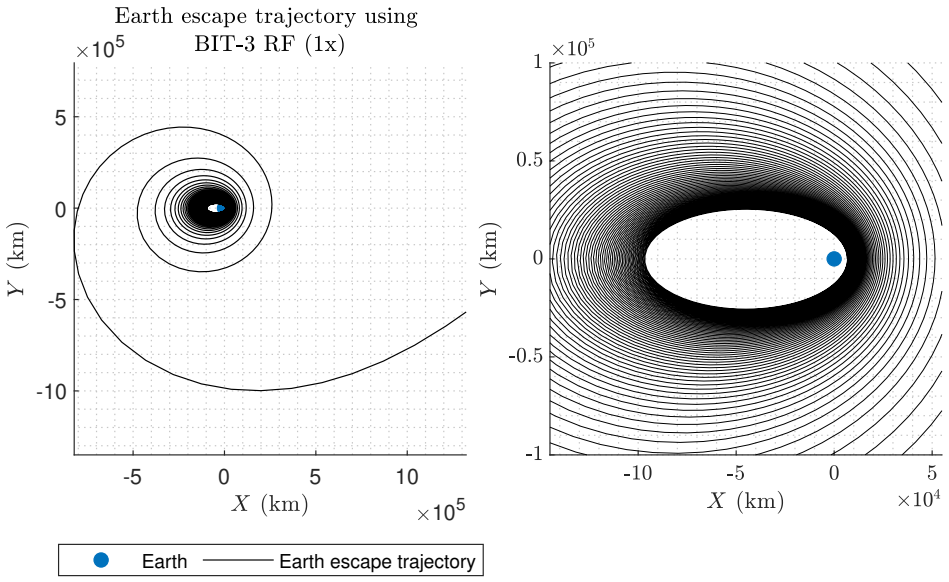

Figure E.11: Earth escape trajectory of the BIT-3 RF propulsion system. The left-side figure contains the complete Earth escape trajectory and the right-side figure contains a zoomed-in Earth escape trajectory.

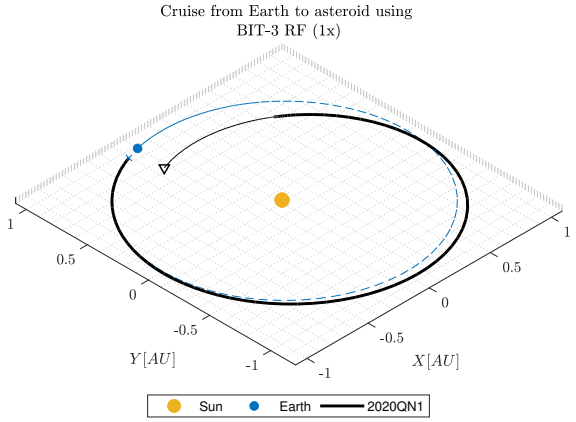

(a) Interplanetary cruise to 2020QN1. A successful fly-by trajectory could be found.

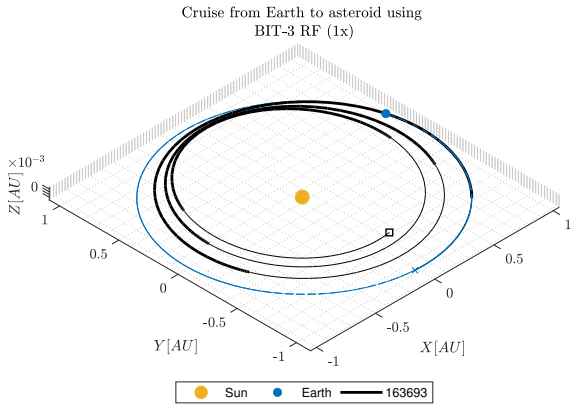

(b) Interplanetary cruise to 163693. A successful fly-by trajectory could be found.

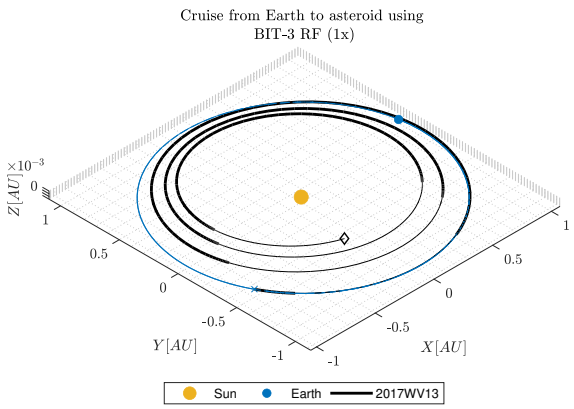

(c) A successful interplanetary trajectory for a fly-by mission to the celestial object 2017WV13 could be found.

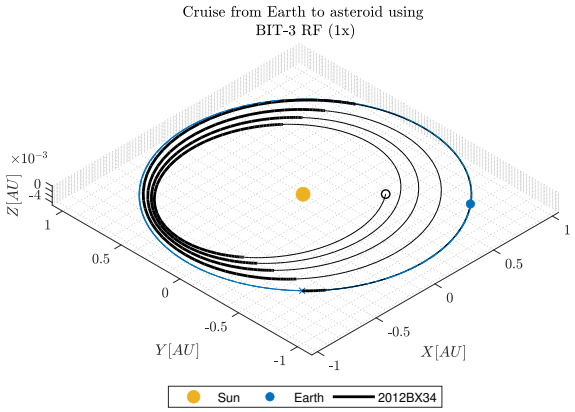

(d) Interplanetary cruise to 2012BX34. A successful fly-by trajectory could be found.

Figure E.12: Trajectories to the four specified objective asteroids using the BIT-3 RF propulsion system. Thicker parts in the interplanetary trajectory indicate that the system is thrusting at full throttle and thinner parts indicate the system is not thrusting.

E.7. IFM Micro (1x)

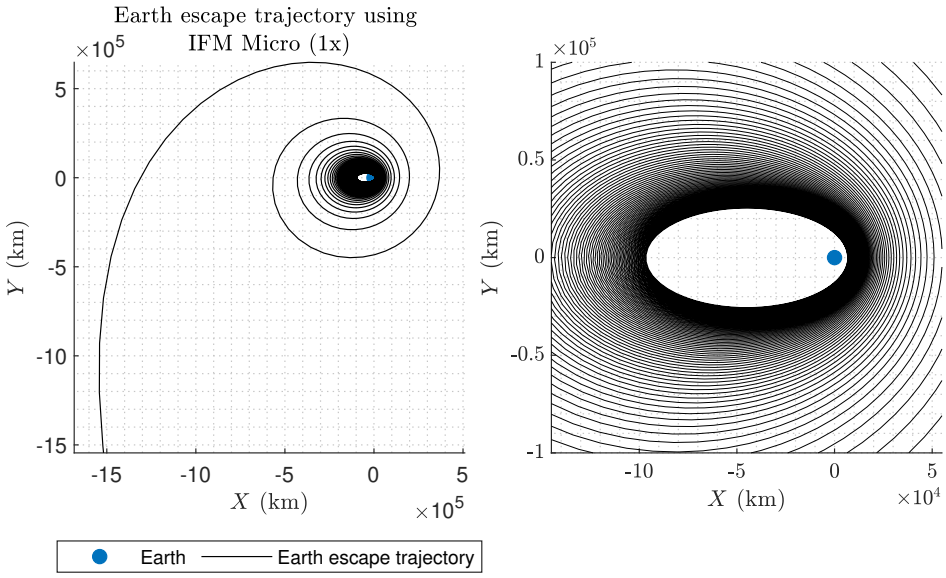

Figure E.13: Earth escape trajectory of the IFM Micro propulsion system. The left-side figure contains the complete Earth escape trajectory and the right-side figure contains a zoomed-in Earth escape trajectory.

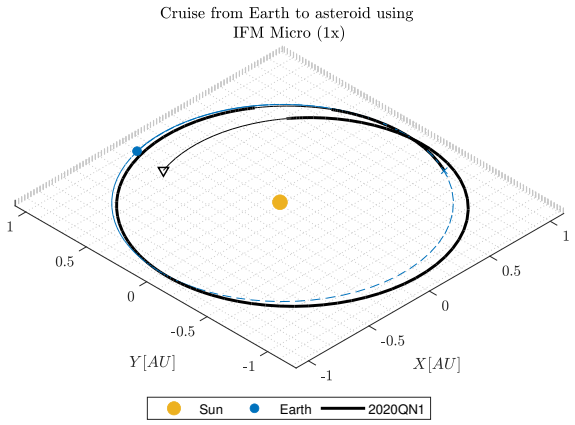

(a) Interplanetary cruise to 2020QN1. A successful fly-by trajectory could be found.

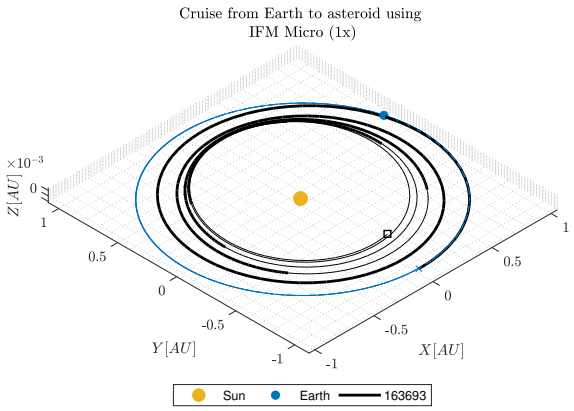

(b) Interplanetary cruise to 163693. A successful fly-by trajectory could be found.

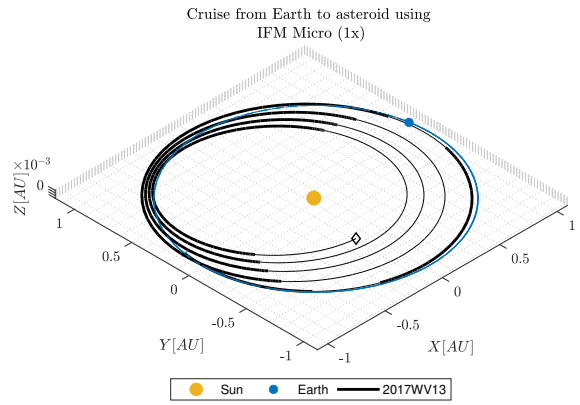

(c) A successful interplanetary trajectory for a fly-by mission to the celestial object 2017WV13 could be found..

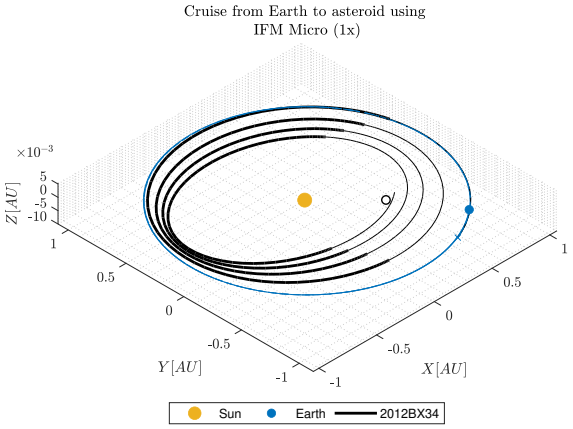

(d) Interplanetary cruise to 2012BX34. A successful fly-by trajectory could be found.

Figure E.14: Trajectories to the four specified objective asteroids using the IFM Micro propulsion system. Thicker parts in the interplanetary trajectory indicate that the system is thrusting at full throttle and thinner parts indicate the system is not thrusting.

E.8. IFM Nano (2x)

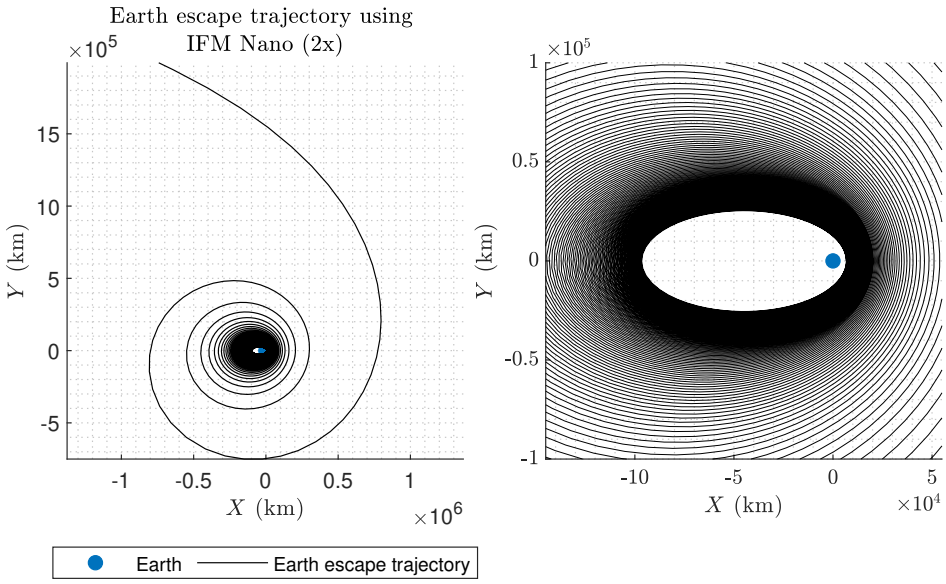

Figure E.15: Earth escape trajectory of the IFM Nano propulsion system. The left-side figure contains the complete Earth escape trajectory and the right-side figure contains a zoomed-in Earth escape trajectory.

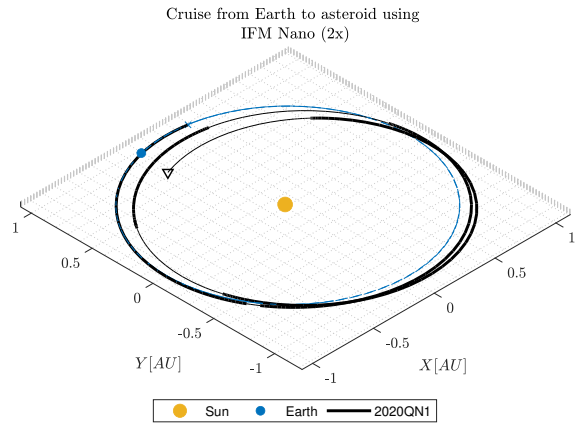

(a) Interplanetary cruise to 2020QN1. A successful fly-by trajectory could be found.

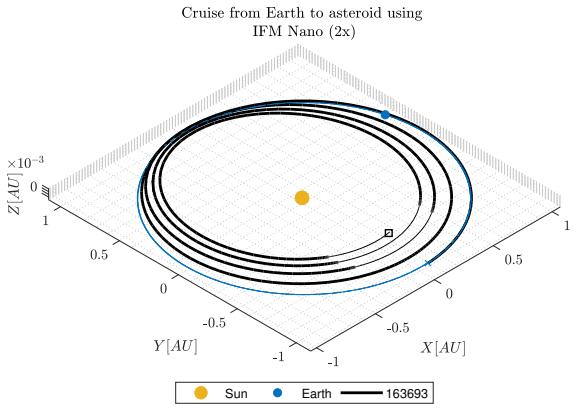

(b) Interplanetary cruise to 163693. A successful fly-by trajectory could be found.

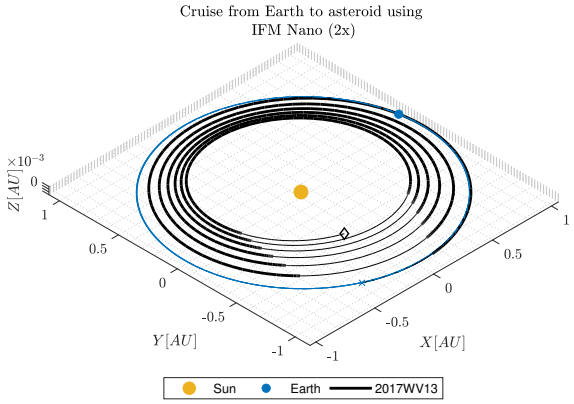

(c) A successful interplanetary trajectory for a fly-by mission to the celestial object 2017WV13 could be found.

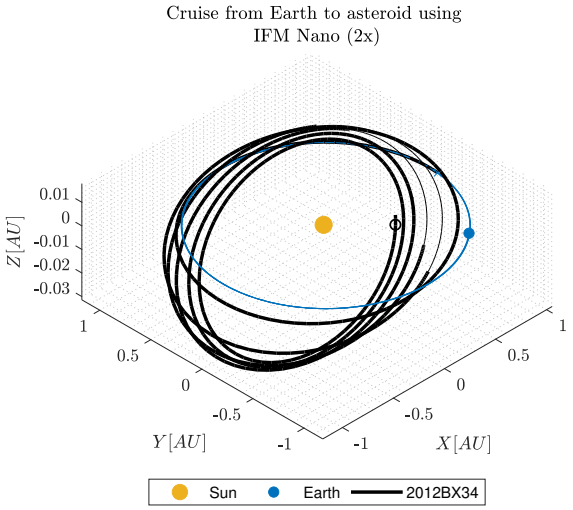

(d) Interplanetary cruise to 2012BX34. A successful fly-by trajectory could be found.

Figure E.16: Trajectories to the four specified objective asteroids using the IFM Nano propulsion system. Thicker parts in the interplanetary trajectory indicate that the system is thrusting at full throttle and thinner parts indicate the system is not thrusting.

E.9. FPPT-1.6 (1x)

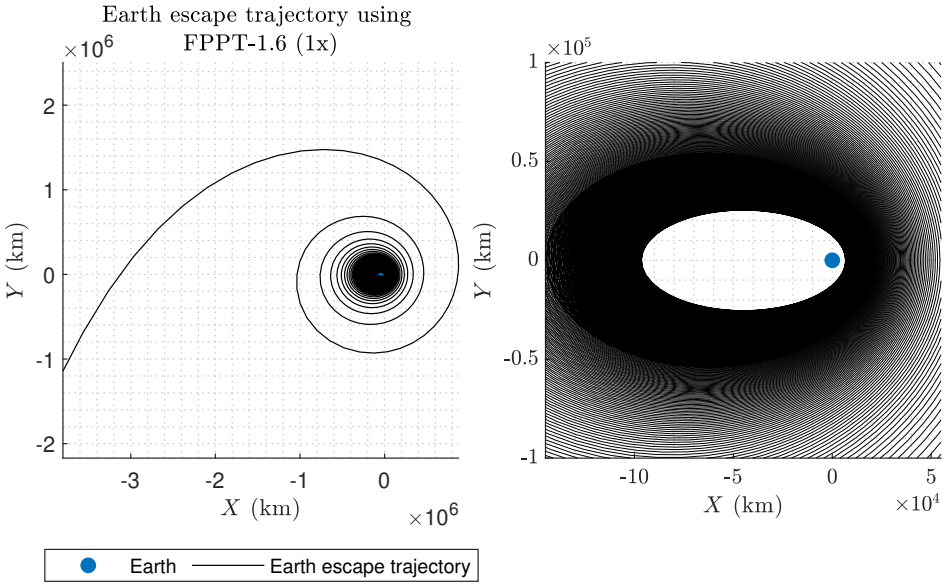

Figure E.17: Earth escape trajectory of the FPPT-1.6 propulsion system. The left-side figure contains the complete Earth escape trajectory and the right-side figure contains a zoomed-in Earth escape trajectory.

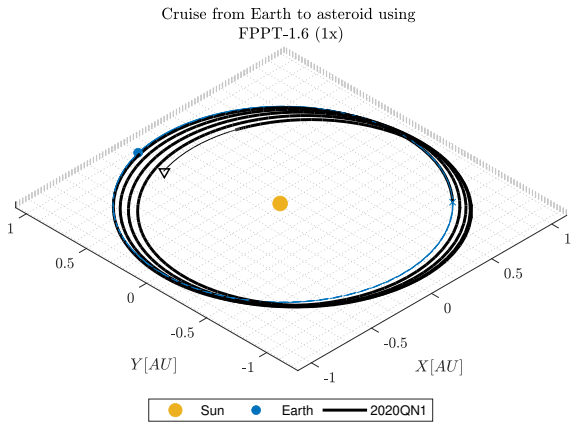

(a) Interplanetary cruise to 2020QN1. A successful fly-by trajectory could be found.

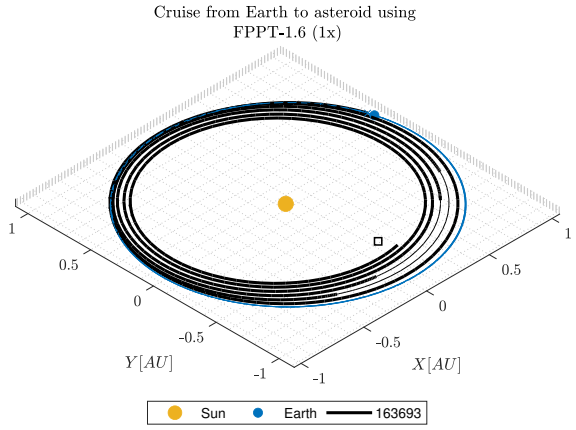

(b) Interplanetary cruise to 163693. No successful fly-by trajectory could be found.

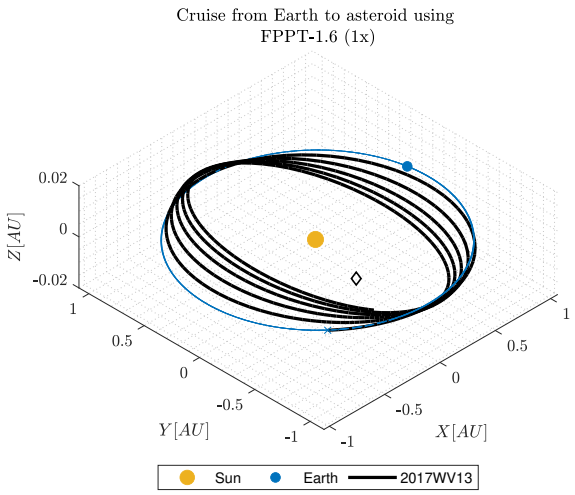

(c) No successful interplanetary trajectory for a fly-by mission to the celestial object 2017WV13 could be found.

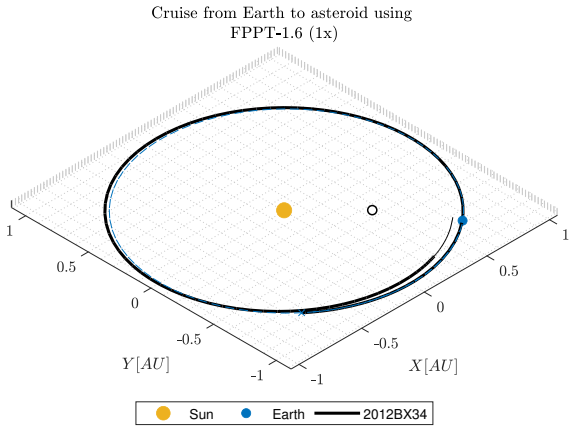

(d) Interplanetary cruise to 2012BX34. No successful fly-by trajectory could be found.

Figure E.18: Trajectories to the four specified objective asteroids using the FPPT-1.6 propulsion system. Thicker parts in the interplanetary trajectory indicate that the system is thrusting at full throttle and thinner parts indicate the system is not thrusting.

F

High-thrust trajectory cases results

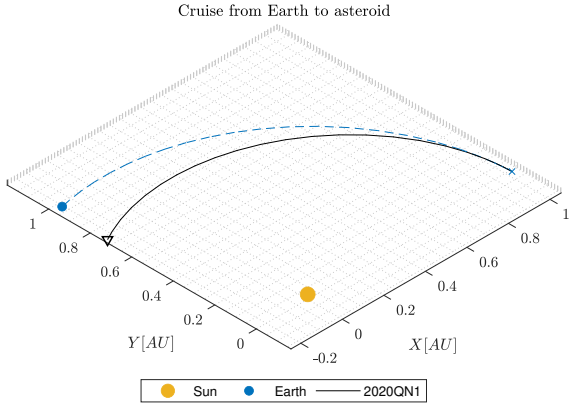

(a) Interplanetary cruise to 2020QN1. A successful fly-by trajectory could be found. A total Earth escape velocity of 3.4077 km/s was required.

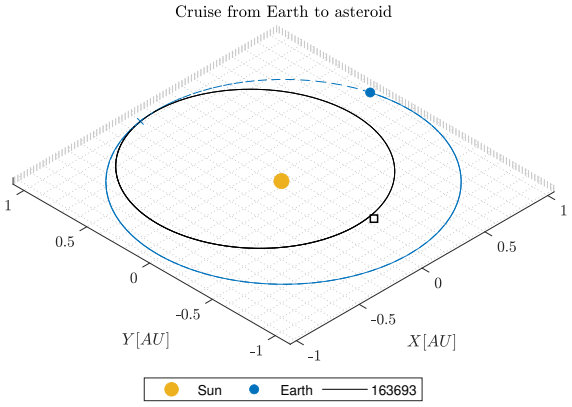

(b) Interplanetary cruise to 163693. No successful fly-by trajectory could be found. A total Earth escape velocity of 4.1384 km/s was required.

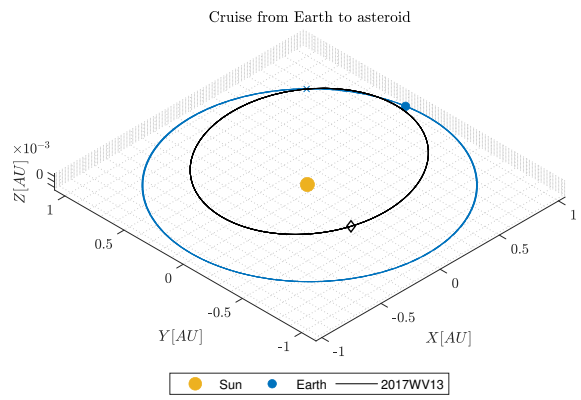

(c) A successful interplanetary trajectory for a fly-by mission to the celestial object 2017WV13 could be found. A total Earth escape velocity of 5.3016 km/s was required.

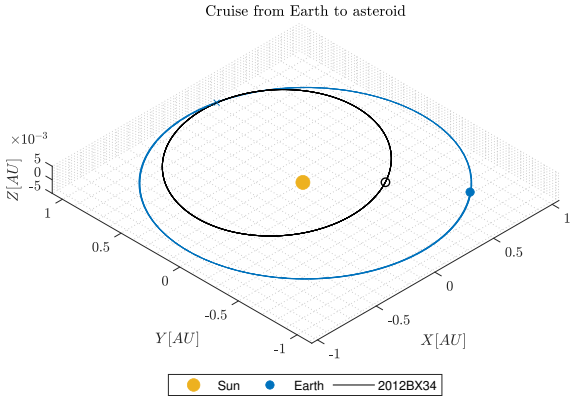

(d) Interplanetary cruise to 2012BX34. A successful fly-by trajectory could be found. A total Earth escape velocity of 6.3429 km/s was required.

Figure F.1: Trajectories to the four specified objective asteroids using the high thrust propulsion systems. These trajectories were found by optimizing the required escape velocity and direction. Some trajectories require multiple revolutions to reach the target asteroid which explains the longer mission duration for these missions.

F.1. HYDROS-C (1x)

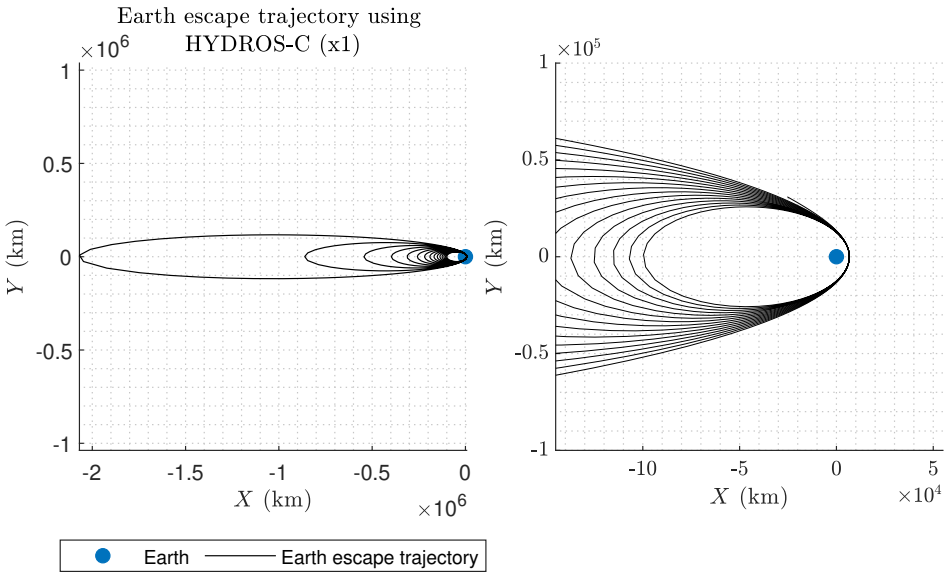

Figure F.2: Earth escape trajectory of the HYDROS-C propulsion system for asteroid 2020QN1. The left-side figure contains the complete Earth escape trajectory and the right-side figure contains a zoomed-in Earth escape trajectory.

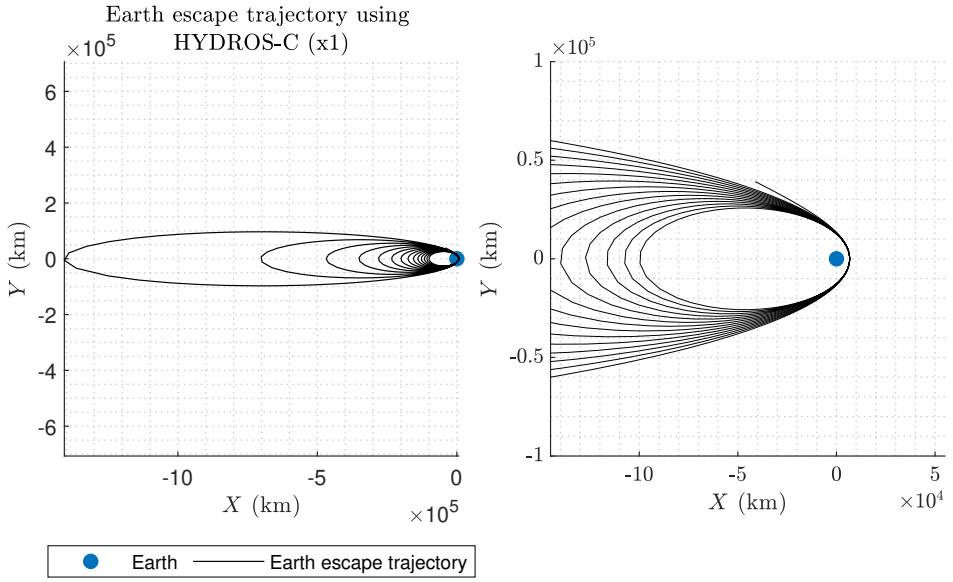

Figure F.3: Earth escape trajectory of the HYDROS-C propulsion system to asteroid 163693. The left-side figure contains the complete Earth escape trajectory and the right-side figure contains a zoomed-in Earth escape trajectory.

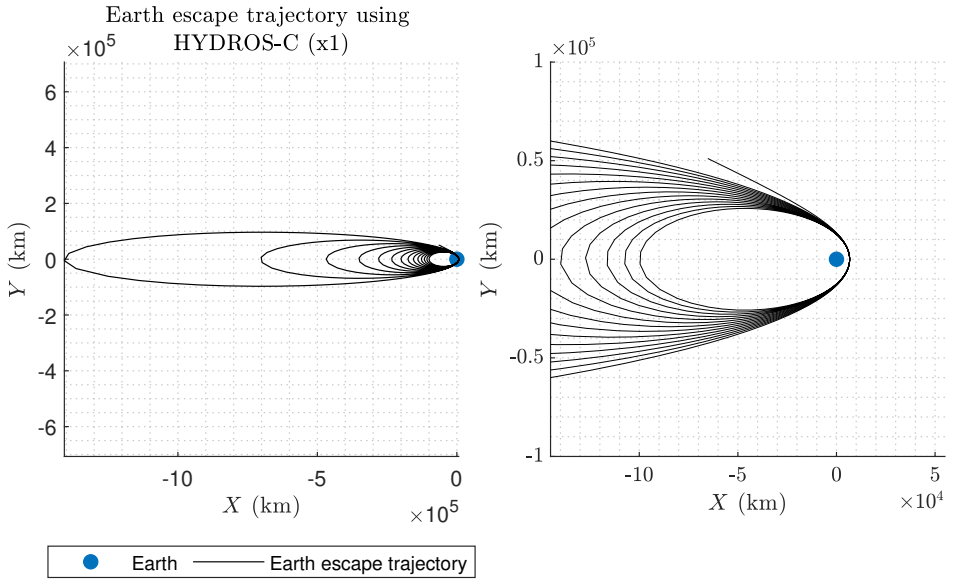

Figure F.4: Earth escape trajectory of the HYDROS-C propulsion system to asteroid 2017WV13. The left-side figure contains the complete Earth escape trajectory and the right-side figure contains a zoomed-in Earth escape trajectory.

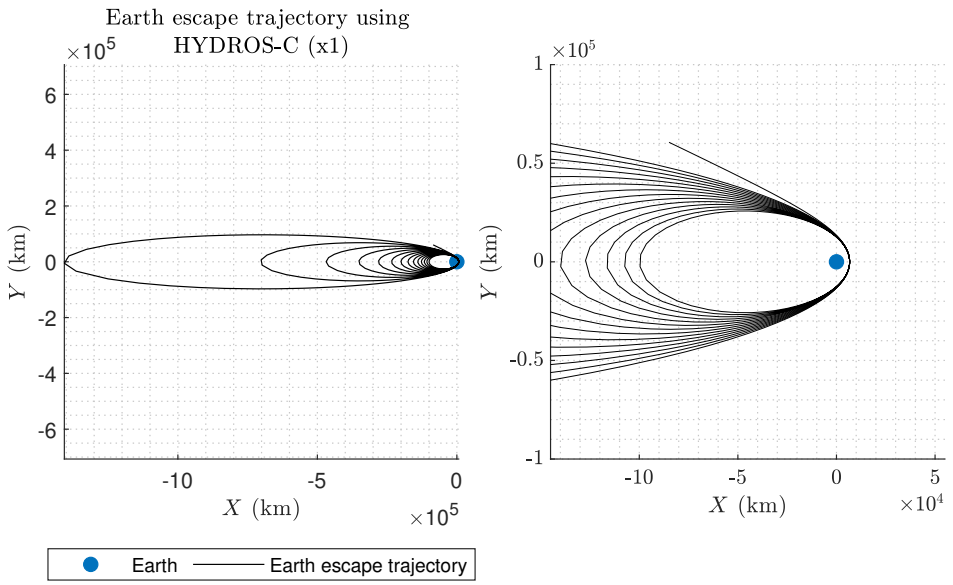

Figure F.5: Earth escape trajectory of the HYDROS-C propulsion system to asteroid 2012BX34. The left-side figure contains the complete Earth escape trajectory and the right-side figure contains a zoomed-in Earth escape trajectory.

F.2. B1 (1x)

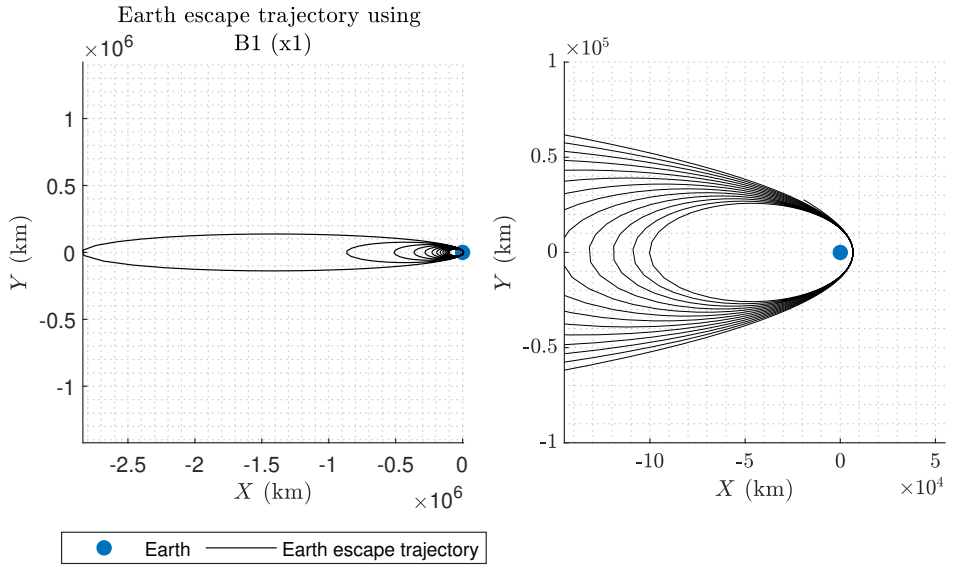

Figure F.6: Earth escape trajectory of the B1 propulsion system to asteroid 2020QN1. The left-side figure contains the complete Earth escape trajectory and the right-side figure contains a zoomed-in Earth escape trajectory.

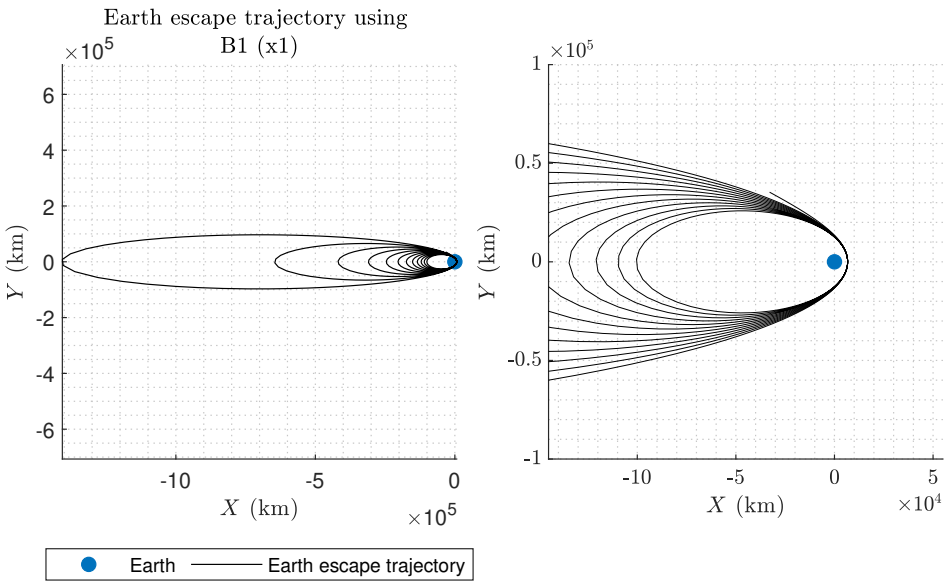

Figure F.7: Earth escape trajectory of the B1 propulsion system to asteroid 163693. The left-side figure contains the complete Earth escape trajectory and the right-side figure contains a zoomed-in Earth escape trajectory.

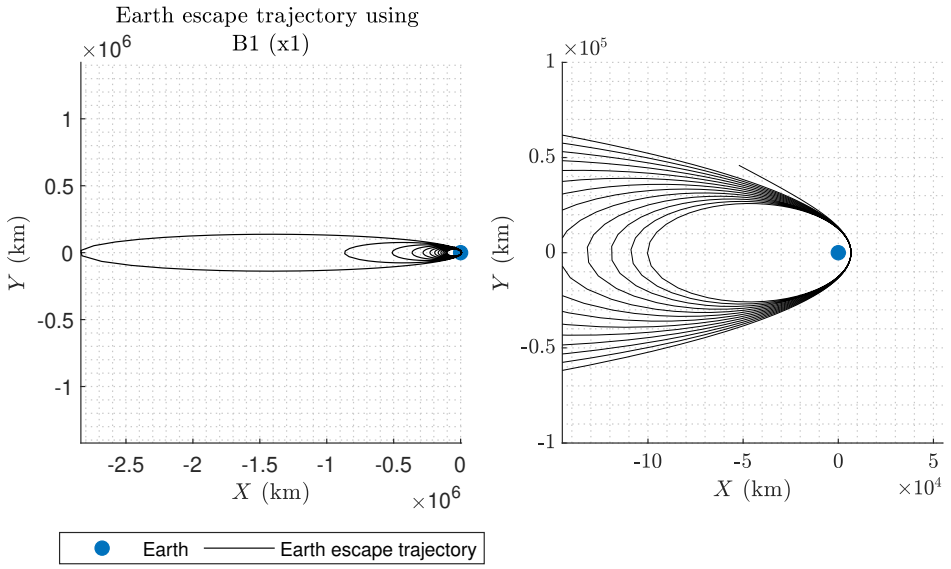

Figure F.8: Earth escape trajectory of the B1 propulsion system to asteroid 2017WV13. The left-side figure contains the complete Earth escape trajectory and the right-side figure contains a zoomed-in Earth escape trajectory.

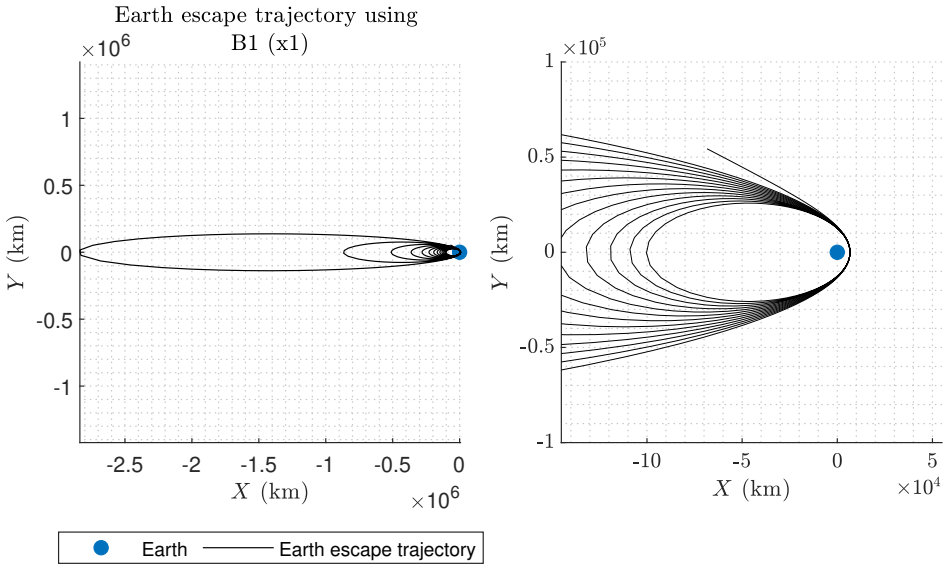

Figure F.9: Earth escape trajectory of the B1 propulsion system to asteroid 2012BX34. The left-side figure contains the complete Earth escape trajectory and the right-side figure contains a zoomed-in Earth escape trajectory.

F.3. 22 N HPGP (1x)

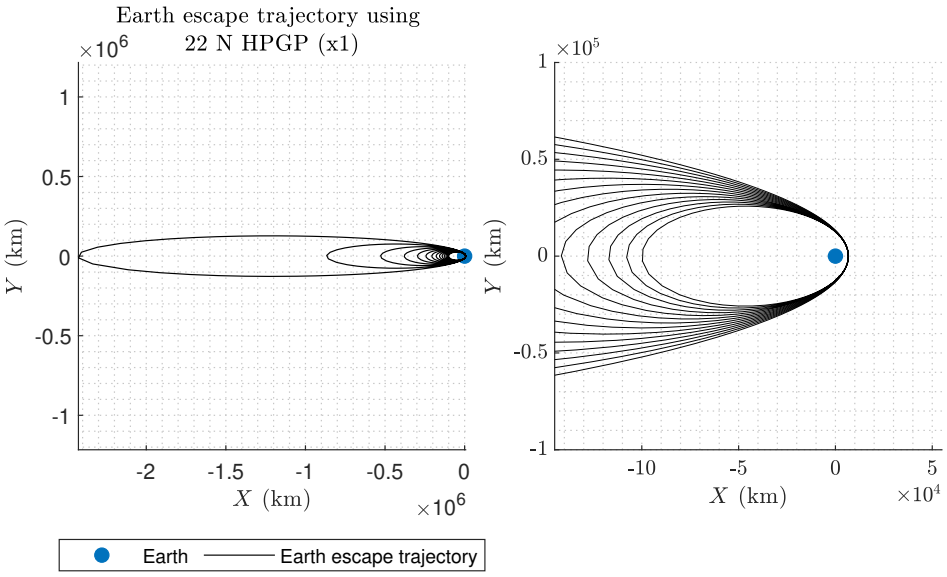

Figure F.10: Earth escape trajectory of the 22 N HPGP propulsion system to asteroid 2020QN1. The left-side figure contains the complete Earth escape trajectory and the right-side figure contains a zoomed-in Earth escape trajectory.

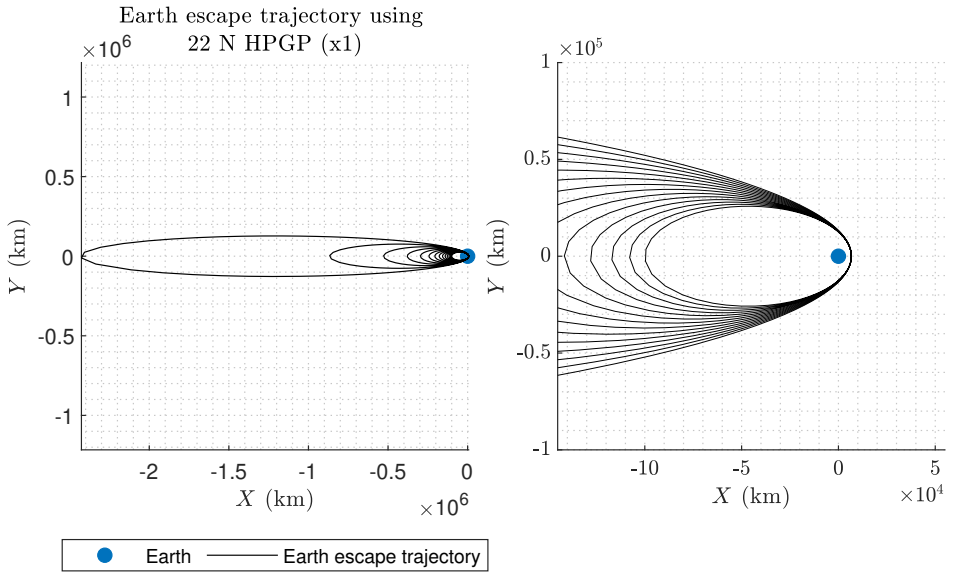

Figure F.11: Earth escape trajectory of the 22 N HPGP propulsion system to asteroid 163693. The left-side figure contains the complete Earth escape trajectory and the right-side figure contains a zoomed-in Earth escape trajectory.

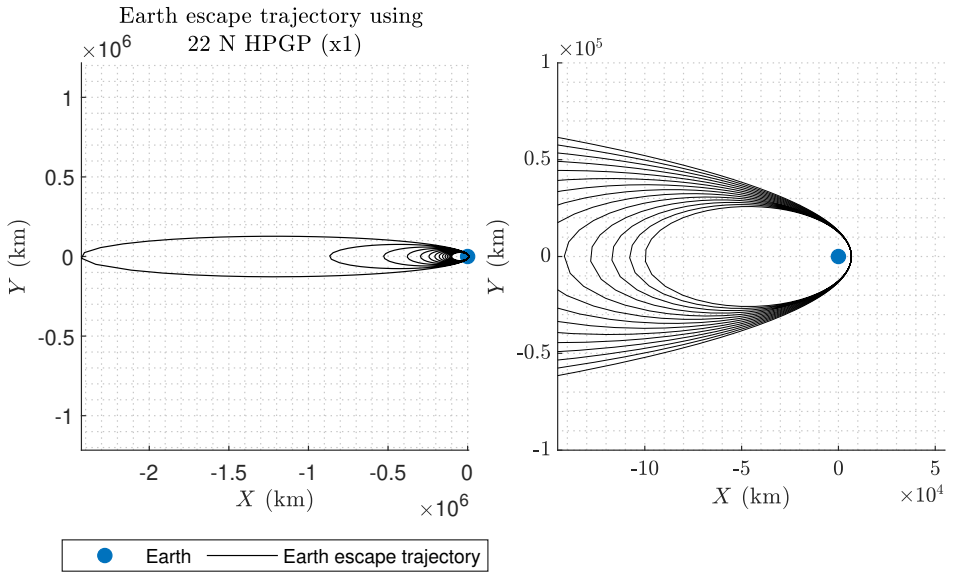

Figure F.12: Earth escape trajectory of the 22 N HPGP propulsion system to asteroid 2017WV13. The left-side figure contains the complete Earth escape trajectory and the right-side figure contains a zoomed-in Earth escape trajectory.

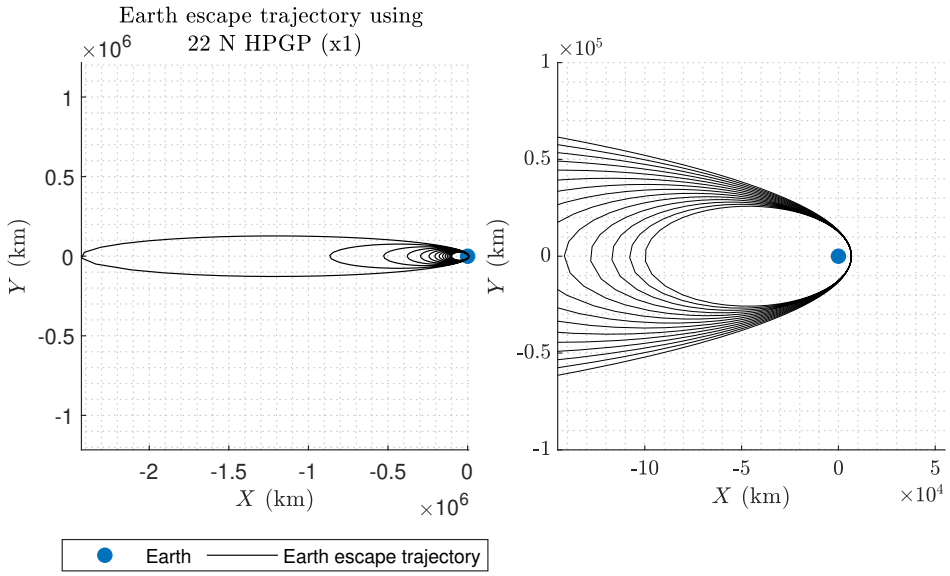

Figure F.13: Earth escape trajectory of the 22 N HPGP propulsion system to asteroid 2012BX34. The left-side figure contains the complete Earth escape trajectory and the right-side figure contains a zoomed-in Earth escape trajectory.

F.4. CDM-1 (1x)

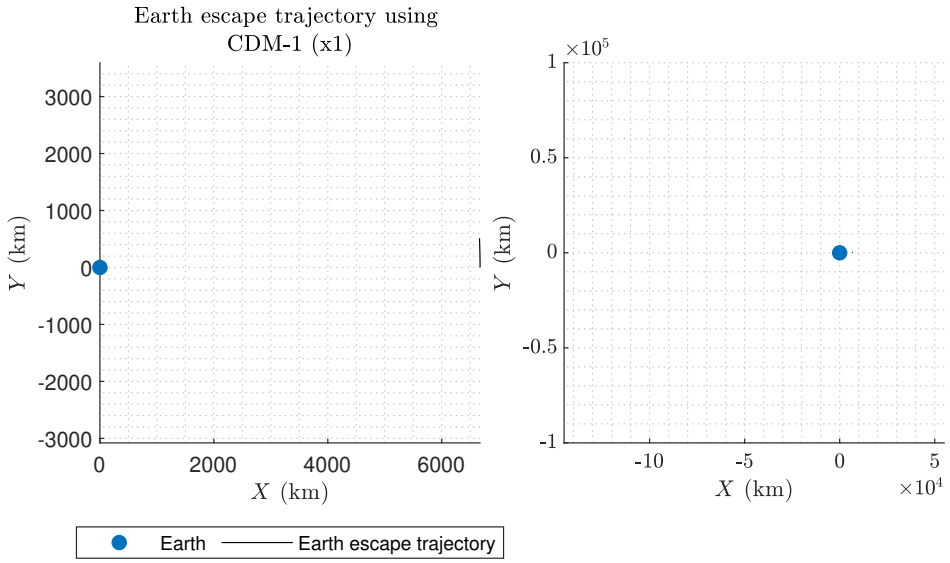

Figure F.14: Earth escape trajectory of the CDM-1 propulsion system to asteroid 2020QN1. The left-side figure contains the complete Earth escape trajectory and the right-side figure contains a zoomed-in Earth escape trajectory. The simulation is stopped after a short duration because the satellite already escapes with the required Earth escape velocity to fly by the target asteroid.

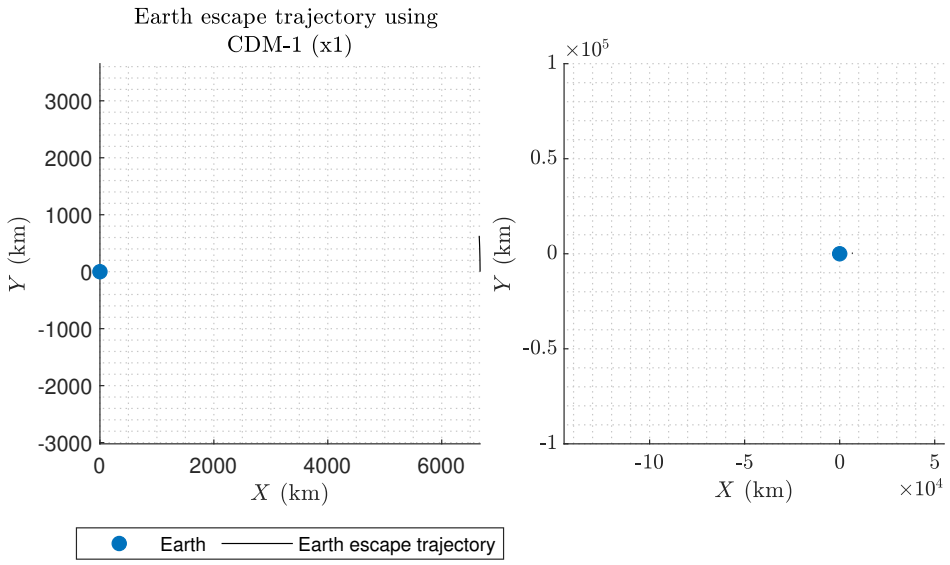

Figure F.15: Earth escape trajectory of the CDM-1 propulsion system to asteroid 163693. The left-side figure contains the complete Earth escape trajectory and the right-side figure contains a zoomed-in Earth escape trajectory. The simulation is stopped after a short duration because the satellite already escapes with the required Earth escape velocity to fly by the target asteroid.

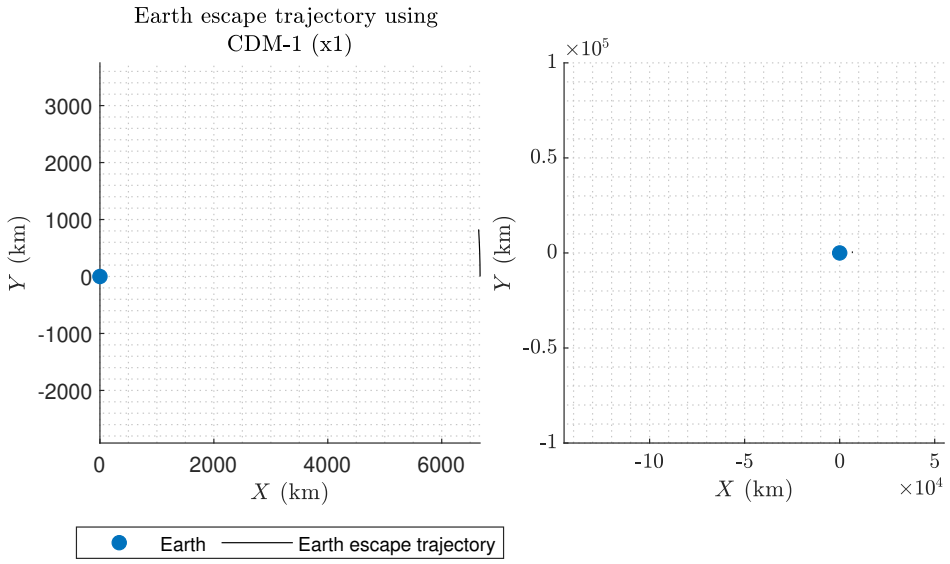

Figure F.16: Earth escape trajectory of the CDM-1 propulsion system to asteroid 2017WV13. The left-side figure contains the complete Earth escape trajectory and the right-side figure contains a zoomed-in Earth escape trajectory. The simulation is stopped after a short duration because the satellite already escapes with the required Earth escape velocity to fly by the target asteroid.

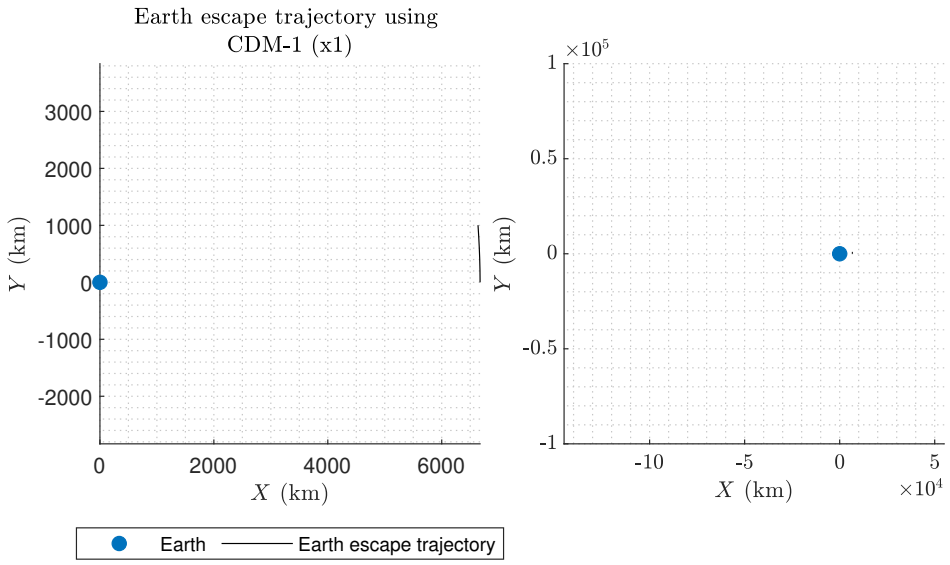

Figure F.17: Earth escape trajectory of the CDM-1 propulsion system to asteroid 2012BX34. The left-side figure contains the complete Earth escape trajectory and the right-side figure contains a zoomed-in Earth escape trajectory. The simulation is stopped after a short duration because the satellite already escapes with the required Earth escape velocity to fly by the target asteroid.

F.5. STAR 4G (1x)

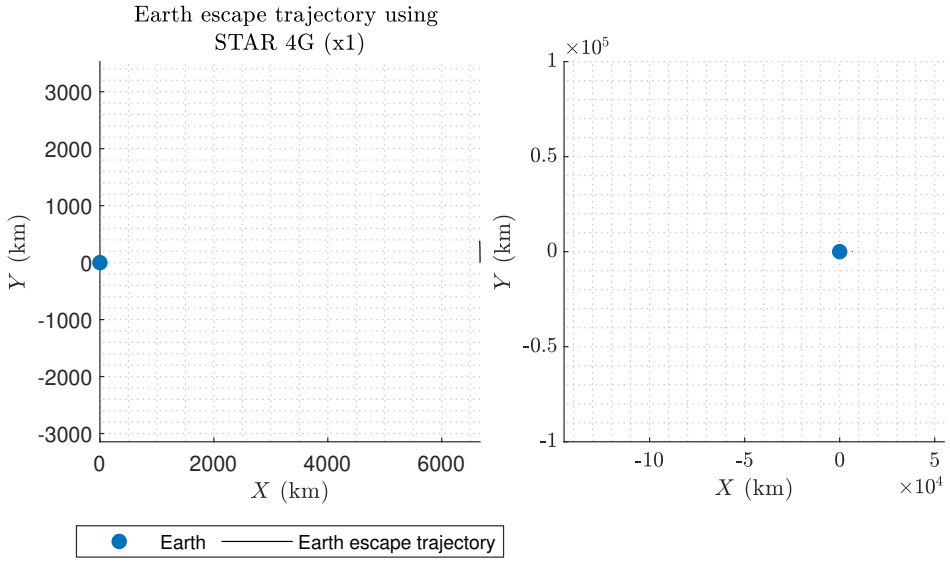

Figure F.18: Earth escape trajectory of the STAR 4G propulsion system to asteroid 2020QN1. The left-side figure contains the complete Earth escape trajectory and the right-side figure contains a zoomed-in Earth escape trajectory. The simulation is stopped after a short duration because the satellite already escapes with the required Earth escape velocity to fly by the target asteroid.

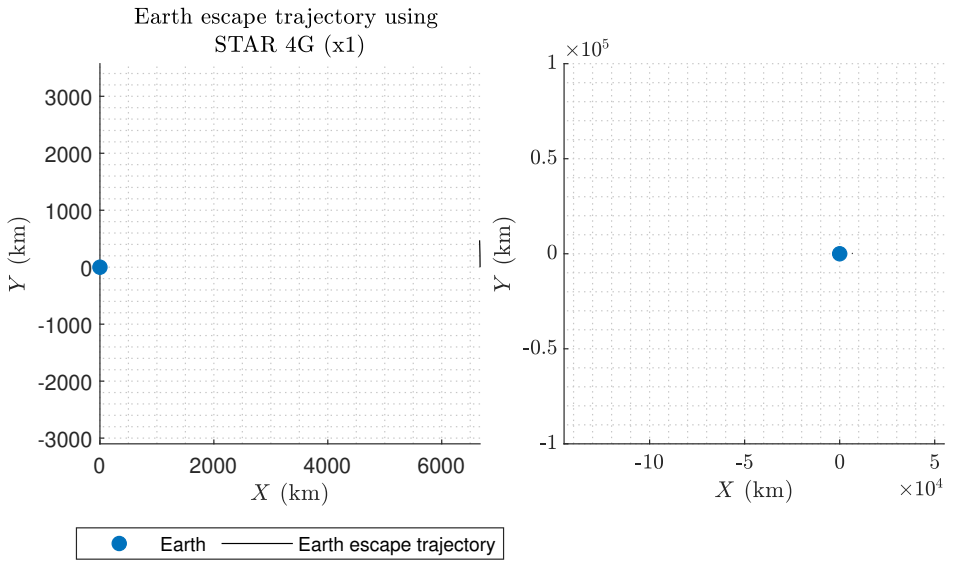

Figure F.19: Earth escape trajectory of the STAR 4G propulsion system to asteroid 163693. The left-side figure contains the complete Earth escape trajectory and the right-side figure contains a zoomed-in Earth escape trajectory. The simulation is stopped after a short duration because the satellite already escapes with the required Earth escape velocity to fly by the target asteroid.

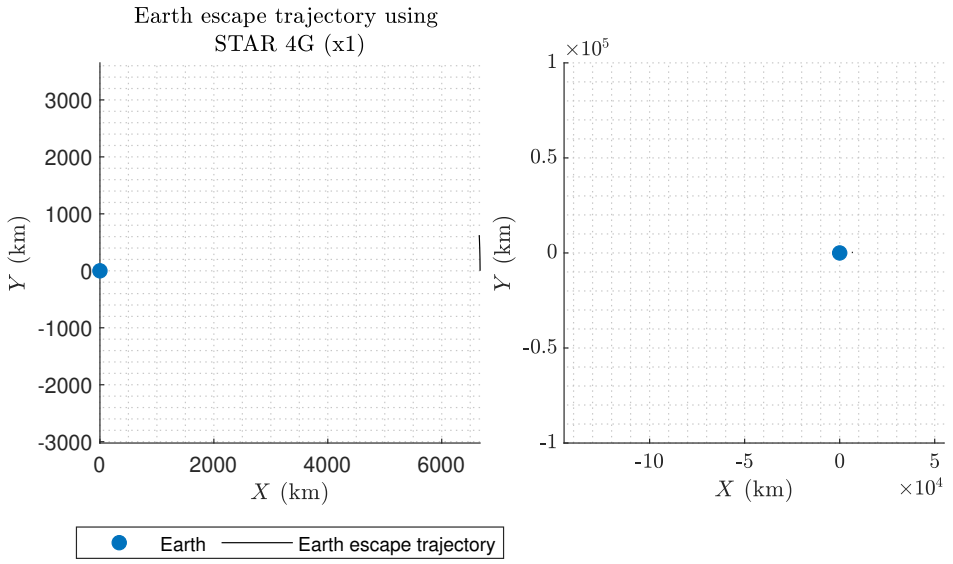

Figure F.20: Earth escape trajectory of the STAR 4G propulsion system to asteroid 2017WV13. The left-side figure contains the complete Earth escape trajectory and the right-side figure contains a zoomed-in Earth escape trajectory. The simulation is stopped after a short duration because the satellite already escapes with the required Earth escape velocity to fly by the target asteroid.

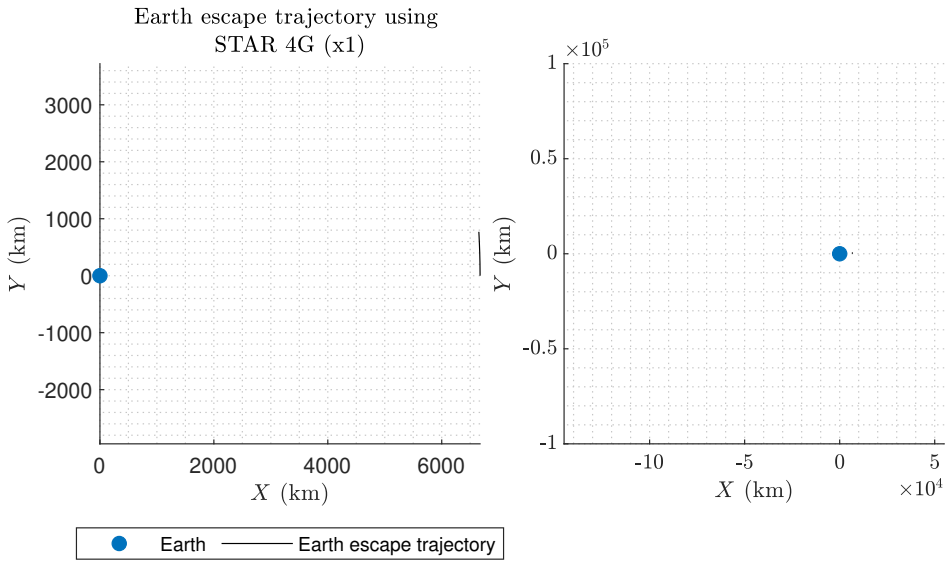

Figure F.21: Earth escape trajectory of the STAR 4G propulsion system to asteroid 2012BX34. The left-side figure contains the complete Earth escape trajectory and the right-side figure contains a zoomed-in Earth escape trajectory. The simulation is stopped after a short duration because the satellite already escapes with the required Earth escape velocity to fly by the target asteroid.